Geothermal Heat Recovery Under Heterogeneity of Porous Media, Transport and Fluid Properties

A thesis submitted to the University of Manchester for the degree of

Doctor of Philosophy

in the Faculty of Science and Engineering

2023

Amir Mohammad Norouzi

School of Engineering, Department of Chemical Engineering

Contents

Word Count: 34308 words

List of Figures

List of Tables

Abstract

Electricity and heat generation activities accounted for about 41% of the carbon dioxide (CO_2) emissions from burning fossil fuels in 2017. Therefore, developing low-carbon means of power generation and decarbonising the electricity and heat generation sectors are crucial steps in the transition to net zero. Geothermal energy is an adaptable and enormous resource, and when used in combination with carbon capture and storage can prevent CO_2 from reaching the atmosphere by sequestering it in saline aquifers located deep underground. CO_2 was introduced as an alternative working fluid in geothermal systems, defining the concept of CO_2-plume geothermal (CPG). Although scCO_2 has a lower heat capacity than water, its lower viscosity results in a lower pressure drop and higher production rates. Moreover, the naturally generated thermosiphon flow (resulting from the density gradient between the injection and the production well) almost removes the pumping requirements at the production well. However, there are a plethora of geochemical, thermophysical, and subsurface hydrogeological parameters that affect the efficiency of such systems. One of the main concerns about injecting CO_2 in saline aquifers is the geochemical reactions (specifically capillary-enhanced salt precipitation) that happen inside the aquifer and can damage the aquifer by reducing its permeability and increasing the pressure build-up near the injection well. Second is the geological uncertainty and heterogeneity that significantly affects the system performance. Last but not least, and arguably the most important, is the naturally-driven thermosiphon flow and power generation from the aquifer. The present work covers all these concerns in separate but coherent and integrated pieces of research, using a range of porous media and heat and mass transfer modelling studies. First, salt precipitation and the effect of capillary backflow are studied, and an analytical solution is provided to estimate the amount and extent of the precipitation when injecting CO_2 in a saline aquifer. Capillary pressure significantly affects the amount of precipitated salt and should not be ignored. Nevertheless, intense salt precipitation mainly occurs in a close area near the injection well. Therefore, its effects on the system's overall performance and power generation are insignificant. Second, using the developed codes and models, various 2D and 3D heterogeneous braided aquifer realisations are generated, and performance metrics are optimised by studying different affecting parameters. It is observed that heterogeneity significantly reduces the system performance by up to 75%. Finally, a direct CO_2 power plant is coupled with the well and aquifer models, and a comprehensive power generation sensitivity analysis is provided. This study has offered a more profound insight into the operation and functionality of CPG power systems and proposes recommendations on their feasibility, performance, and challenges.

Declaration

This thesis is an original work by Amir Mohammad Norouzi. I declare that no portion of the work referred to in the thesis has been submitted in support of an application for another degree or qualification of this or any other university or other institute of learning.

Copyright

The following four notes on copyright and the ownership of intellectual property rights must be included as written below:

i The author of this thesis (including any appendices and/or schedules to this thesis) owns certain copyright or related rights in it (the "Copyright") and s/he has given The University of Manchester certain rights to use such Copyright, including for administrative purposes.

ii Copies of this thesis, either in full or in extracts and whether in hard or electronic copy, may be made *only* in accordance with the Copyright, Designs and Patents Act 1988 (as amended) and regulations issued under it or, where appropriate, in accordance with licensing agreements which the University has from time to time. This page must form part of any such copies made.

iii The ownership of certain Copyright, patents, designs, trademarks and other intellectual property (the "Intellectual Property") and any reproductions of copyright works in the thesis, for example graphs and tables ("Reproductions"), which may be described in this thesis, may not be owned by the author and may be owned by third parties. Such Intellectual Property and Reproductions cannot and must not be made available for use without the prior written permission of the owner(s) of the relevant Intellectual Property and/or Reproductions.

iv Further information on the conditions under which disclosure, publication and commercialisation of this thesis, the Copyright and any Intellectual Property and/or Reproductions described in it may take place is available in the University IP Policy (see http://documents.manchester.ac.uk/DocuInfo.aspx?DocID=24420), in any relevant Thesis restriction declarations deposited in the University Library, The University Library's regulations (see http://www.library.manchester.ac.uk/about/regulations/) and in The University's policy on Presentation of Theses.

Acknowledgement

I would like to express my sincere gratitude to my caring supervisor, **Dr Masoud Babaei**, for his invaluable support, guidance, and planning through all levels of the project. Dr Babaei was more than a great leader and supervisor to me. His passion, selflessness, and caring character made him a wonderful friend and colleague. I was honoured to be a part of the *Unimus* research group and to work with such a great supervisor and team.

I am grateful to **Dr Vahid Niasar** for all his scientific discussions, support and valuable suggestions that improved the quality of this research and project. Also, special thanks to **Prof. Jon Gluyas** for his constructive support and thoughtful suggestions and for sharing some resources and data that are used in the present study. Additionally, I would like to thank my collaborators, **Dr Weon Shik Han** and **Dr Kue-Young Kim**, for their consultation and collaboration, which led to the production of Chapter 2 in this thesis. Also, I wish to thank **Prof. Larry Lake** for his constructive comments on the initial draft of Chapter 3 of this thesis. Also, I wish to extend my gratitude to **Dr Arash Rabbani**, **Dr Neil Fowler**, and **Dr Justin Ezekiel** for their help and support in modelling CO_2-plume geothermal aquifer and power plant, leading to Chapter 5 of this thesis, which is the fruit of this project. Thank you all for your support!

I would like to acknowledge the **President's Doctoral Scholar (PDS) Award 2020**, which provided me with the great opportunity to study at the University of Manchester.

Then, I would like to thank **my parents**, who endured my absence for several long years with patience while keeping their encouraging support to me following my dreams.

Last but not least, I would like to express my deepest gratitude to **my wife, Fatima,** who stood by me both in life and in my research. Her contribution to Chapter 5 of this thesis was invaluable, and none of this would have been possible without her selfless support and sacrifice.

Thank you all for your help and support through this journey.

Amir Mohammad Norouzi
Manchester
August 7, 2023

Chapter 1

Introduction

1.1 Preface

The importance of reducing CO_2 emissions has been recognised scientifically in the modern world. The COVID-19 pandemic and the resulting restrictions had a major impact on greenhouse emissions worldwide. For instance, in the UK, due to a greater number of individuals staying at home in 2020, household greenhouse gas emissions decreased by 10% when compared to the previous year [1]. Despite this, after the gradual reduction of limitations, the UK territorial greenhouse gas emissions increased from 405.5 to 424.5 million tonnes of carbon dioxide equivalent ($MtCO_2e$) from 2020 to 2021 [2, 3]. Emissions from the residential and energy supply sectors accounted for about 16% and 21% of total emissions in 2020, respectively [3]. Moreover, CO_2 - mainly resulting from burning fossil fuels - has the most extensive share of greenhouse emissions [3]. Therefore, developing low-carbon, eco-friendly, and cost-effective means of power generation and decarbonising the electricity and heat generation sectors are crucial steps to transition to net zero emissions.

Geothermal energy can supply the required heat demand and, when combined with carbon capture utilisation and storage (CCUS), can store significant amounts of CO_2 (10th of $MtCO_2$) in deep underground reservoirs for a relatively long period of time. For instance, adding 7-9 GW power carbon capture and storage plants to the UK's offshore wind will save about 18 $MtCO_2$ by reducing CO_2 emissions into the atmosphere [4]. Currently, solar and geothermal energy account for less than 5% (1100 thousand tonnes of oil equivalent) of the total renewable energy sources in the UK [3] (Fig. 1.1), while geothermal energy itself holds a potential higher than 100 GW_e [5, 6, 7]. The Durham Energy Institute has calculated that the UK has the potential of about 9.9×10^9 GWh available heat sources of up to depths of 9.5 km. Also, with the currently available technology of engineered geothermal systems, about 222 GW_e from depths of up to 6.5 km and 2280 MW_e from depths of 4.5 km are achievable [7]. Many locations around the world have access to low enthalpy resources, such as the hot sedimentary aquifers, and it is argued that the lack of high enthalpy resources is partly responsible for the limited growth of geothermal energy, especially in the UK [8]. CO_2-plume geothermal (CPG) can be the key to this problem as it requires low to medium enthalpy aquifers to perform. Therefore, it is hypothesised that CPG can meet the energy demands while contributing to reducing CO_2 emissions by storing considerable amounts of CO_2 in underground aquifers.

This thesis presents representative models of CPG systems considering important physical processes that take place when CO_2 is used to extract energy. I included the mutual dissolution of CO_2 and brine, geochemical reactions, capillary-driven backflow, CO_2 seques-

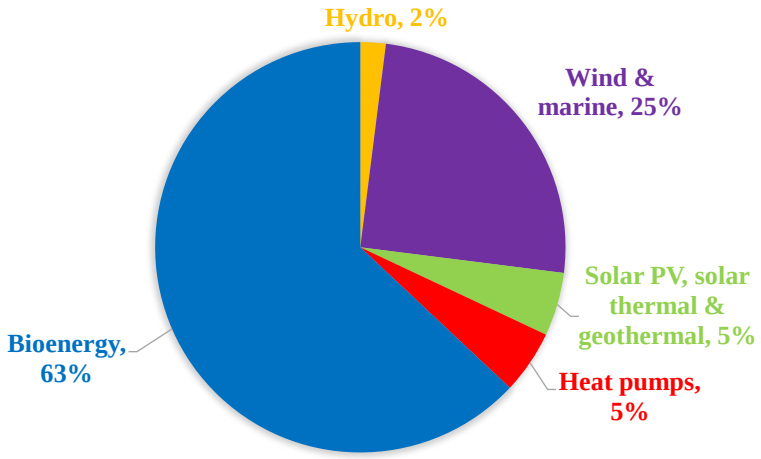

Figure 1.1: Renewable energy sources in the UK, 2021. The total amount of renewable used is 22495 thousand tonnes of oil equivalent (ktoe) [3]. Solar and geothermal energy together account for about 5% of the total renewables used in the UK.

tration, and aquifer thermal depletion. This thesis provides a good understanding of the potential, advantages, and problems of CPG systems and suggests mitigating solutions to make CPG a competitive option for CCUS. The thesis covers three main concerns about CPG, including salt precipitation, geological uncertainty, and net power generation. Each chapter includes a peer-reviewed and published journal article that has addressed one of the above-mentioned specific concerns about CPG. The first two papers mainly studied geochemical reactions and salt precipitation that happen inside the aquifer through numerical and analytical approaches. The third paper presented a performance optimisation of a CPG operating in a 2D heterogeneous fluvial aquifer. Finally, the fourth paper provided a detailed model for CPG, which includes coupled aquifer modelling, geochemical reactions, sequestration and cycle lifetime, well modelling, thermosiphon, optimisation, and power cycle analysis in 3D fluvial aquifers. The following sections provide details on the background, motivation, and outline of the research.

1.1.1 Background of geothermal energy and CPG

The term *'geothermal energy'* pertains to heat obtained from beneath the Earth's surface, encompassing depths ranging from a few meters to several kilometres. Generally, one or more injection and production well pairs are drilled to make a close/open loop fluid circuit. Then, cold fluid is injected at the injection well and absorbs the heat from the naturally-hot rock below the Earth's surface, and hot fluid returns to the surface. The produced hot fluid is either used for heating purposes or producing electricity through the concept of a *'heat*

engine' [9].

Geothermal energy production is more than a century years old, and the first geothermal plant was built in Larderello, Italy in 1904 [10]. Conventionally, water is used as the working fluid in geothermal systems. One of the most common types of geothermal systems is Groundwater Heat Pump (GWHP), which can operate with either a closed or an open loop water cycle as shown in Fig. 1.2. Geothermal heat is extracted by GWHPs using heat exchangers, which involve pipes inserted into the ground to circulate a working fluid in a *'closed loop'* system, or by pumping the groundwater in aquifers in *'open loop'* systems [11]. By using a heat pump, these systems convert low-grade heat from fluids into useful heat ($>$ 40 °C) for heating purposes [11]. Finally, the cold fluid is re-injected into the aquifer. GWHPs have the capability to provide heating, cooling, or a combination of both.

In the past decades, many researchers focused on GWHP systems and their development. One of the areas of interest was about the effects of thermal dispersivity on thermal plume dispersion and its effects on the thermal performance of the system [12, 13, 14, 15, 16]. Other researchers also developed GWHPs by focusing on different aspects, such as different design scenarios [17, 18], sensitivity analysis, modelling, and performance [19, 20, 21, 22], thermal impact assessment [23], and sustainability [24].

Another type of geothermal system is called Hot Dry Rock (HDR). Within this concept that was first developed by researchers at Los Alamos National Laboratory, deep (2.5 to 5 km) and low-permeable geothermal sources were the target. By increasing the pressure of the wells permeability was improved, and faults were reopened. Then, water was circulated through the permeability-enhanced reservoir and to the surface, and was used to produce electricity [25, 26]. This was almost the first time that low-permeable deep geothermal sources were used for energy extraction. Later, the term HDR was changed to Enhanced/Engineered Geothermal Systems (EGS) to emphasise more on the hydraulic fracturing and artificial permeability enhancement of the low-permeable field (Fig. 1.2) [11, 27]. CO_2 was later proposed as a working fluid for EGS systems to fracture the rocks, and these geothermal systems were referred to as CO_2-EGS systems [28, 29, 30].

Similar to GWHPs, many researchers worked on developing EGS systems and there are several recent review papers that scheme through the research works about EGS. Among these review papers, Li et al. [31] focused on reviewing the simulation mechanisms and design of EGS, Kumari et al. [32] reviewed the sustainable developments of EGS, and Zhu et al. [33] reviewed the mechanical responses of granite EGS systems. Finally, in 2019, Avanthi Isaka et al. [34] provided a comprehensive review of the utilisation of supercritical CO_2 ($scCO_2$) as

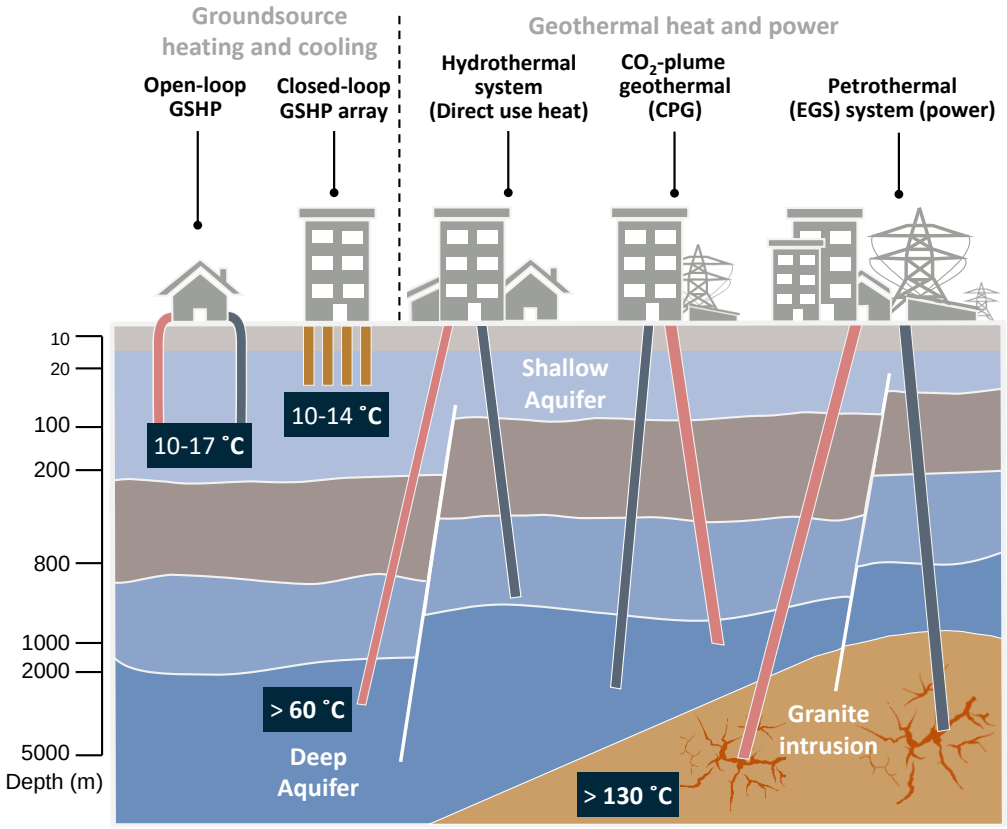

Figure 1.2: Geothermal energy technologies: ground source heat pump for relatively shallow depths, and hydrothermal systems, CPG, and engineered geothermal systems (also known as Hot Dry Rock or HDR) for deep geothermal sources (modified from [11]). Compared to EGS, CPG targets shallower aquifers with higher natural permeability.

the working fluid in EGS systems, showing that the attention of the geothermal researchers and engineers community has moved toward the utilisation of CO_2 in the last decade.

CO_2 was initially suggested as the working fluid by Brown [35] in 2000. He stated that the HDR concept can be more competitive by using CO_2 joined with CO_2 sequestration as it can store CO_2 and produce electricity. He also stated that CO_2 has some advantages compared to water, such as lower mineral solubility and the self-driven flow known as thermosiphon [35]. Finally, in 2009, Saar et al. [36] introduced the concept of CO_2-plume geothermal (CPG) and patented this idea. In this concept, CO_2 was used as the working fluid in low/medium enthalpy sedimentary aquifers, whereby heat and pressure energy were extracted from sedimentary basins that naturally had high permeability. The injection of CO_2 forms a large funnel-shaped plume inside the aquifer, which is why this concept is called CO_2-plume geothermal. A schematic of a CPG system and the parts of the operation that are the focus of this dissertation are shown in Fig. 1.3.

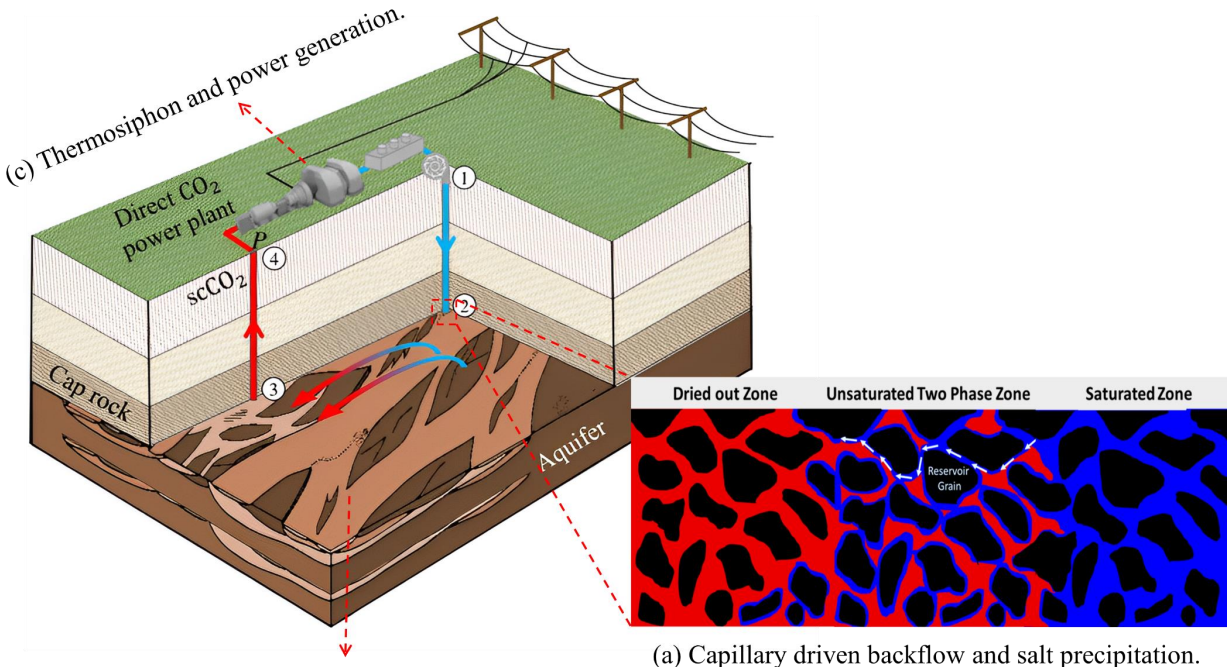

Figure 1.3: Schematic of the direct-CPG cycle and surface power plant (modified from [37] and [38]). Sections that are the focus of the present dissertation are (a) capillary-driven backflow and its effects on salt precipitation near the injection well. Here because of the water saturation gradient and the resulting capillary force water moves towards the injection well and then at the dry-out zone water evaporates and salt will remain; (b) fluvial heterogeneity and its effects on the performance of the CPG system. Fluvial channels form as a result of underground water passage through several years and the presence of these channels affects the CO_2 distribution and the system performance; and (c) thermosiphon and power generation, which is resulted from the CO_2 density gradient between the injection and production wells. In light of thermosiphon, CO_2 is self-produces at the production well and the need for pumping is greatly reduced.

In a CPG system, either the high pressure or the high temperature of the produced CO_2 can be used to produce electricity. In the case that the produced $scCO_2$ from the CPG directly enters an expansion turbine, its high pressure is used to produce electricity (direct-CO_2 expansion cycle). Conversely, the produced fluid can be used in an indirect cycle coupled with another cycle, such as an Organic Rankine Cycle (ORC), to transfer its heat to another secondary working fluid through a heat exchanger (known as the indirect CPG cycle). CPG is a different geothermal technology compared to other existing ones in many aspects [9]:

- CPG mainly uses CO_2 as its geologic working fluid.

- It targets low to medium enthalpy sedimentary basins instead of deep fractured networks used in EGS.
- CPG is relatively deep and uses sources at depths between 1.5 to 5 km.
- CPG is applicable for medium-range temperature aquifers and does not require hot reservoirs.
- It can produce electricity both through a direct and an indirect cycle.
- Great amounts of CO_2 will be stored and kept underground in CPG systems.

Moreover, using CO_2 as the working fluid offers several advantages. At depths beyond approximately 800 m under typical hydraulic conditions, CO_2 transitions into the supercritical phase, characterised by the absence of a clear distinction between gas and liquid phases. As a result, when CO_2 reaches the supercritical phase, it acquires a notable density and exhibits a low viscosity, rendering it an appealing option for extracting energy [39]. This lower viscosity, compared to water, results in a lower pressure drop within the reservoir and enables higher working mass flowrates. Additionally, the density of CO_2 is highly sensitive to temperature. As CO_2 is heated in the reservoir, its density decreases significantly. Therefore, at the production well, the bottomhole pressure is more than sufficient to self-produce CO_2 to the surface without requiring any pumping. In terms of the efficiency of heat removal from the aquifer, the heat capacity, density, and velocity of fluids under the same pressure gradient are important. It is claimed that when the depth exceeds 4 km, under typical geothermal gradients, water will be a more effective medium for carrying energy out of the aquifer compared to CO_2. However, for shallower aquifers with lower heat requirements, such as those below 100 °C, CO_2 is believed to be more efficient [39]. Despite these benefits, CPG is still a relatively new concept, and further investigation is necessary to address several concerns and problems before it can become commercially available. These concerns and drawbacks will be discussed in the following section.

1.2 Motivation

As mentioned, CPG is a relatively new technology and it requires further study and analysis. There are some challenges that a CPG system may have, including the possible water production at the initial stages of CPG that may result in a system performance reduction, additional imposed pressure drop, and the requirement of a pump/compressor to compensate

for this excess pressure drop due to water production at the initial stages of CPG. Another challenge could be the choice of turbine and compressor and their working condition. The phase condition of CO_2 at the exit of the turbine is very uncertain and it is closely located at the boundary of the supercritical phase and unsaturated two-phase regions, and this may cause problems with the turbine working condition. Additionally, the overall efficiency and lifetime of CPG systems are very uncertain and this has been highly overestimated in previous studies in this field. Besides these challenges, there are three major concerns about utilising CPG that can affect every aspect of a CPG system and are the focus of the present work. One of the main concerns is the geochemical reactions that happen between CO_2, brine, and rock, which results in minerals precipitation and dissolution inside the aquifer. Among these geochemical reactions, salt precipitation is of great importance as it is argued that it can significantly damage the reservoir and reduce its injectivity [40] (Fig. 1.3a). The second important concern is about the geological uncertainty and heterogeneity that is the nature of fluvial sedimentary aquifers (Fig. 1.3b). Less attention has been given to investigating the performance of CPG in a real, heterogeneous aquifer and its overall viability. Thirdly, are the CPG performance metrics, thermosiphon longevity, well patterns and spacing, optimum working flowrates, and power generation (Fig. 1.3c). All these concerns are directly related to the performance and energy output of a CPG system and should be clarified to pave the way for CPG to become commercially available and competitive. In this dissertation, it is tried to cover all these aspects in separate, but coherent and integrated pieces of research.

1.2.1 Flow and salt precipitation in the aquifer

To ensure the technical and economic feasibility of a CPG system that utilises CO_2 as the heat transmission fluid, various physics and considerations must be taken into account. CO_2-brine mutual solubilities and water vaporization are two phenomena that significantly impact the thermo-hydrodynamics of the injected CO_2 in the aquifer. Overlooking these factors can result in over- or underestimation of the system's feasibility. Other crucial phenomena that must be considered in a CPG system include geochemical reactions between CO_2, brine, and minerals, mineral dissolution/precipitation effects on reservoir porosity and permeability, capillary pressure and capillary backflow, and water vaporization due to the low water vapour pressure in the dry-out zone. Understanding the complexity of these interactions is essential for successfully implementing CPG systems in commercial applications. When CO_2 is injected into a sandstone aquifer, minerals like calcite, anorthite, kaolinite, and halite can

precipitate within the aquifer. These minerals' dissolution and precipitation reactions can affect the amount of CO_2 stored in the aquifer, reservoir injectivity, and CPG performance. Of these minerals, halite is the most crucial to consider, as its precipitation near the injection well can significantly impair the injectivity of the injection well.

To thoroughly study the effects of minerals (specifically salt) precipitation and investigate the extent that they can affect the CPG performance, two sub-projects are defined. In the first project, which formed Chapter 2, a complete sensitivity analysis on various parameters that affect minerals precipitation/dissolution and specifically the capillary-driven backflow inside the reservoir and the subsequently precipitated salt is performed. The study is done through numerical modellings (using the CMG-GEM compositional simulator) coupled with post-processing codes. In this sensitivity analysis, a new parameter (BEP) is also introduced that correlates the amount of the precipitated salt to brine backflow. Then, in the second project (Chapter 3), using an analytical approach based on the Buckley–Leverett theory, and the programming code developed for that, I was able to estimate the amount of the precipitated salt as well as the distance of the affected region in the reservoir, in presence of capillary-driven backflow.

1.2.2 Heterogeneity and geological uncertainty

Fluvial heterogeneity is a fundamental characteristic of sandstone aquifers [41]. It refers to the spatial variability of sedimentary properties and architecture within aquifers that have been influenced by ancient river systems. This heterogeneity results from the complex interplay of sediment supply, channel migration, and depositional processes. Different types of heterogeneity can be present in saline aquifers, including meandering, braided, and anabranching [42, 43, 44]. Heterogeneity can significantly impact the hydrological properties of sandstone aquifers, such as their porosity, permeability, and storage capacity. Moreover, the presence of fluvial channels in aquifers can significantly affect the flow pattern, CO_2 plume propagation, and performance metrics of a CPG system. Therefore, a thorough understanding of fluvial heterogeneity is essential for the accurate characterization and modelling of sandstone aquifers, particularly for the design of effective and sustainable CPG systems. While the effect of this parameter is significant, there has been no study that has taken this parameter into account in a CPG.

In this regard, the ubiquitous presence of various forms of heterogeneity in rock properties (porosity and permeability) which is inherent in subsurface porous media, is analysed through two defined projects. One of the main achievements of these projects is the development

of an in-house MATLAB code that can generate different 2D and 3D braided/meandering fluvial heterogeneous realisations of sandstone aquifers with high coefficients of variation ($C_V > 1$ [45]). Through this code, it is possible to generate different types of fluvial heterogeneity (braided and meandering) with control over channel number, width, thickness, and sinuosity. In the first project (Chapter 4), 2D braided aquifer realisations are used to study the performance metrics of a CPG system and suggest optimised working conditions. In the second project, which is the most complete model of a CPG system in a 3D heterogeneous aquifer (Chapter 5), different 3D realisations are generated, and the results are coupled with the surface power plant model, and a comprehensive study on every aspect of a CPG is performed.

1.2.3 CPG performance optimisation in heterogeneous reservoirs

It is important to establish the most efficient operational conditions for the CPG system. However, there are many parameters to be considered in this regard. The dominant parameters that affect the CPG system's performance include the spacing and patterns of the wells and the CO_2 injection rates. These parameters are optimised through numerous numerical simulations that are performed in 2D and 3D aquifers. The optimal well spacing is determined by evaluating the performance metrics of the CPG system in a 2D aquifer (Chapter 4). Subsequently, this optimised value is used to reduce the number of simulations required for the 3D cases, and then the CO_2 injection rate is optimised through the 3D models coupled with the power plant model (Chapter 5). This approach ensures a comprehensive study of every aspect of the CPG system and aids in determining the best operating conditions for an efficient and sustainable system.

1.2.4 Thermosiphon and net power generation

The thermosiphon effect and net power generation are critical factors to consider in a CPG system. Along with influencing parameters such as heterogeneity, other phenomena also significantly impact a CPG system's efficiency and power output. One such phenomenon is CO_2 plume propagation. Firstly, a minimum CO_2 saturation is required at the production well to have an annular flow inside the well (to maintain the thermosiphon effect) and to be able to use the produced fluid directly in a turbine. Also, it is important to always produce supercritical CO_2 at the surface. Therefore, the production temperature and pressure should not fall below critical values. These criteria define the lifetime of a CPG system. To

accurately calculate the net power output of a CPG system, a model is required, which considers the CPG lifetime as described combined with well and power plant models. Providing such a comprehensive model is the target of this dissertation in Chapter 5, in which a direct CO_2 expansion power plant is coupled with a CPG in a 3D heterogeneous aquifer. The provided model in this chapter includes the CO_2 density-driven thermosiphon flow, effects of a 3D heterogeneous aquifer, well modelling, direct power cycle, geochemical reactions, and performance optimisation in an integrated manner.

1.3 Thesis objectives

The detailed thesis objectives are summarised below:

- Investigating the extent and the effects of geochemical reactions on the reservoir injectivity and CPG performance.
- Studying the effective parameters on salt precipitation and capillary-driven backflow.
- Being able to analytically estimate the amount and the extent of salt precipitation when injecting CO_2 in a saline aquifer.
- Studying the effects of heterogeneity on CPG performance, lifetime, sequestration time, and thermosiphon longevity.
- Optimising CPG performance and net power output through an integrated aquifer, well, power plant model.

1.4 Thesis structure and publications

A combination of numerical modelling, analytical solutions, programming, and optimisation approaches have been used to investigate CPG systems further. The presented journal-format thesis comprises four peer-reviewed and published papers that are direct outcomes of the PhD project. The first two papers, forming chapters #2 and #3, are about geochemical reactions and capillary-enhanced salt precipitation that occur in CPG. The third and fourth papers, forming chapters #4 and #5, primarily focus on the effects of heterogeneity, power generation, and thermosiphon in CPG systems. All these papers have been peer-reviewed, published, and are available online. Chapter #6 provides a summary of the findings of the present dissertation and future research opportunities, and chapter #7 offers supplementary

descriptions and analyses for each of the preceding chapters. The papers that form this thesis are listed below:

1. **CO_2-plume geothermal processes: A parametric study of salt precipitation influenced by capillary-driven backflow**, **A. M. Norouzi**, M. Babaei, W. S. Han, K. Y. Kim, V. Niasar. *Chemical Engineering Journal vol.425, p.130031, (2021).*
   Link: https://www.sciencedirect.com/science/article/pii/S1385894721016168

2. **Analytical solution for predicting salt precipitation during CO_2 injection into saline aquifers in presence of capillary pressure. A. M. Norouzi**, V. Niasar, J. Gluyas, M. Babaei. *Water Resources Research, vol.58, no.6, p.e2022WR032612, (2022).*
   Link: https://agupubs.onlinelibrary.wiley.com/doi/full/10.1029/2022WR032612

3. **CO_2-plume geothermal in fluvial formations: A 2D numerical performance study using subsurface metrics and upscaling. A. M. Norouzi**, J. Gluyas, M. Babaei. *Geothermics, Vol.99, p.102287, (2022).*
   Link: https://www.sciencedirect.com/science/article/pii/S0375650521002443

4. **CO_2-plume geothermal: Power net generation from 3D fluvial aquifers. A. M. Norouzi**, F. Pouranian, A. Rabbani, N. Fowler, J. Gluyas, V. Niasar, J. Ezekiel, M. Babaei. *Applied Energy, Vol.332, p.120546, (2023).*
   Link: https://www.sciencedirect.com/science/article/pii/S0306261922018037

Chapter 2

CO_2-plume geothermal processes: A parametric study of salt precipitation influenced by capillary-driven backflow

This chapter is a modified version of the paper published in the '*Chemical Engineering Journal*'.

Authors: **A. M. Norouzi**, M. Babaei, W. S. Han, K. Y. Kim, V. Niasar. CO_2-plume geothermal processes: A parametric study of salt precipitation influenced by capillary-driven backflow. *Chemical Engineering Journal*, vol.425, p.130031, 2021.

2.1 Abstract

Utilising CO_2-plume geothermal systems allows both carbon dioxide storage (about 12% of the injected CO_2 –1.4 Mt– in this study) and geothermal heat exploitation by producing hot fluid. However, the commercial and technical feasibility aspects of such systems are major challenges to address. Salt precipitation is a common phenomenon that governs near-well damage and pressure build-up. Although various governing parameters affect the amount and the extent of salt precipitation, capillary-driven backflow is considered in a recent review paper by Miri and Hellevang [40] as a key mechanism that determines regimes of salt precipitation. As a result, a comprehensive sensitivity analysis is performed on a wide range of parameters, including relative permeability and capillary pressure curves; injection flow rate and temperature; and the reservoir's initial salinity, porosity, and temperature to underpin the role of capillary pressure and capillary-driven backflow on salt precipitation. Moreover, a backflow extent parameter (BEP) is defined, through which the brine backflow velocity profile is linked to salt precipitation. It is observed that capillary backflow significantly influences the pattern and enhances near-well salt precipitation. Also, BEP is found to have a semi-linear relation to the amount of the precipitated salt. Also, an increase in brine salinity (up to a critical value $\sim$ 175000 ppm for our simulations) resulted in a significant reduction in reservoir porosity and permeability surrounding the injection well. In addition, the imposed required pumping power is analysed, and an average (for all salinities) 20% increase of pumping power is required to keep the injection rate constant in the present study.

Keywords: CO_2 injection, Capillary backflow, Salt precipitation, Pumping power, CO_2-plume geothermal.

2.2 Introduction

2.2.1 CO_2 sequestration and salt precipitation

Through the last decade, climate change and global warming have alarmed the importance of carbon dioxide (CO_2) management and carbon footprint reduction [46]. One of the proposed solutions to CO_2 problem is the geological storage of CO_2 in various reservoirs, such as coal beds, deep and shallow saline aquifers, and depleted oil and gas reservoirs [47], which became a growing attraction for researchers during the last few years [48]. In addition to the carbon storage, CO_2 also can be used in enhanced oil recovery [49, 50, 51], enhanced gas recovery [52], and integrated sequestration-geothermal processes [53, 54].

Among the above-mentioned types of reservoirs, deep saline aquifers are the most practical candidates and have the largest storage capacity [55]. For non-isothermal flow in aquifers, in addition to carbon storage, heat extraction can also be considered. Generally, there are two approaches regarding CO_2 injection into geothermal systems. One is the enhanced geothermal system (EGS) where either CO_2 is used for hydrofracturing or is used as the transmission fluid [28, 29, 30], known as CO_2-EGS; through this approach, carbon storage is not the main objective. Secondly, there is the CO_2-plume geothermal system (CPG), in which CO_2 is injected into the aquifer to be stored and to act as a means to provide energy [53, 54, 56, 57, 58, 59]. Unlike EGS, the main objective of CPG operations is to maximize both the hot and high-pressure fluid production and CO_2 storage. Therefore, storage capacity, heat recovery factor, and injectivity are the factors that should be considered for the economic and technical feasibility of such systems [40].

Reservoir composition and geochemical reactions play important roles in the injectivity and trapping of CO_2 inside the reservoir [60]. As a result, to accurately simulate a reservoir, it is vital to consider them similar to the real field reservoirs in modelling. In this regard, Zhu et al. [61] numerically modelled and studied the long-term CO_2-brine-rock reactions in a sandstone reservoir and compared the results with measured data for natural analogue. In another comprehensive study, Nghiem et al. [62] provided a fully coupled solver that simulates minerals dissolution and precipitation for the CO_2 injection into an aquifer. Also, they included the main geochemical reactions for a CO_2-brine-rock system, as well as their chemical equilibrium constants. Among these reactions, the solid salt resulting from fluid-rock reactions was found to be of great importance. While injecting supercritical (sc) CO_2 into the reservoir, the formation water eventually evaporates, resulting in an increase in the dissolved salt concentration. As the amount of salt passes the solubility limit, solid salt precipitates and clogs the reservoir pores, which can significantly affect the reservoir's properties such as permeability and porosity as well as CO_2 injectivity. Consequently, the bottom-hole pressure increases and the pump requirement is necessarily increased. Miri and Hellevang [40] comprehensively reviewed the up-to-date knowledge regarding salt precipitation during CO_2 injection. Although there is still a dispute over the preponderant parameter that controls salt precipitation, in general, it is believed that the capillary force plays an important role in supplying fresh brine to the dry-out front, causing salt precipitation. However, according to the works reviewed in [40], only few research studies have considered the effect of capillary force and brine backflow on salt build-up.

To better demonstrate the importance of salt precipitation and the associated damages

at a reservoir, it is useful to summarise observations from field investigations. Baumann et al. [63] reported that salt precipitation occurred near the brine levels with the maximum halite saturation of 14.1% in the Ketzin CO_2 injection project; the reservoir's temperature and pressure were 35 °C and 7.5 MPa, respectively, and the brine salinity was 220 $g.L^{-1}$. In addition, Grude et al. [64] investigated CO_2 injection into the low permeable Tubåen sandstone formation where the temperature and pressure were 95 °C and 28 MPa, respectively. Through the time-lapse seismic survey, it was revealed that injectivity was reduced near the wellbore and pressure build-up was observed. Here, salt precipitation was suggested as a possible reason for these phenomena.

Through laboratory experiments, Nooraiepour et al. [65] tested CO_2 injection in shale caprocks to investigate whether salt can block CO_2 leakage pathways or not. The study revealed that solid salt had the potential to clog the fractures. Another experimental work by Muller et al. [66] reported a 16% salt precipitation with a subsequent reduction of the absolute permeability of about 40% in a sandstone core for carbon storage near Ketzin, Germany. Ott et al. [67] investigated the effects of salt precipitation during sc-CO_2 injection for enhanced oil recovery and gas disposal purposes and reported a 0.8% impairment in macroporosity. Similarly, Bacci et al. [68] reported a porosity reduction of about 3-5% and a permeability reduction of about 13-75%. In another work, Berntsen et al. [69] provided a medium-scale experimental study on salt precipitation near the injection well. Through X-ray computed tomography they observed that capillary backflow affects the water saturation near the wellbore and compensates for water evaporation by dry CO_2. There are other research studies in this regard that all focused on salt precipitation and its effects on the reservoir's permeability (Oh et al. [70], Tang et al. [71], and Kim et al. [72]).

Various numerical studies focused on salt precipitation in the CO_2 injection process and analysed the effects of different parameters on the amount of precipitation and CO_2 injectivity. For instance, Cui et al. [73], considered complex geochemical reactions, including halite, during CO_2 injection in a saline aquifer. Effects of various parameters were studied in this work. However, the sensitivity analysis was only performed for the pressure build-up at the injection well and the changes in other parameters were overlooked. It was observed that although salt precipitation might result in a significant pressure build-up, it was only limited to the vicinity of the injection well. In a more recent study, Parvin et al. [74] provided a formulation of the capillary-enhanced salt clogging of the pores near injection. Their model indicated that in the absence of capillary effect, salt precipitation still occurred, however, the magnitude of precipitation is a strong function of capillary pressure. The modelling is

carried out on one-dimensional 15 cm × 6 cm × 6 cm, with a total of 15 grid blocks only. In another recent work, Babaei [53] considered the effect of brine salinity and salt precipitation in reservoirs with closed and open boundary conditions and different well patterns, suggesting that increasing the number of wells can significantly reduce the maximum amount of the precipitated salt. Other older similar works can be referred to through the review paper provided by Miri and Hellevang [40].

2.2.2 Salt precipitation and capillary backflow

After CO_2 injection into the aquifer, three zones including a dry-out zone, a two-phase-flow zone, and a saturated zone can be defined (Fig. 2.1). Miri and Hellevang [40] proposed that salt can precipitate through different mechanisms such as water evaporation, capillary backflow and salt diffusion. It has been conjectured that brine backflow due to capillary pressure plays an important role in salt precipitation [40].

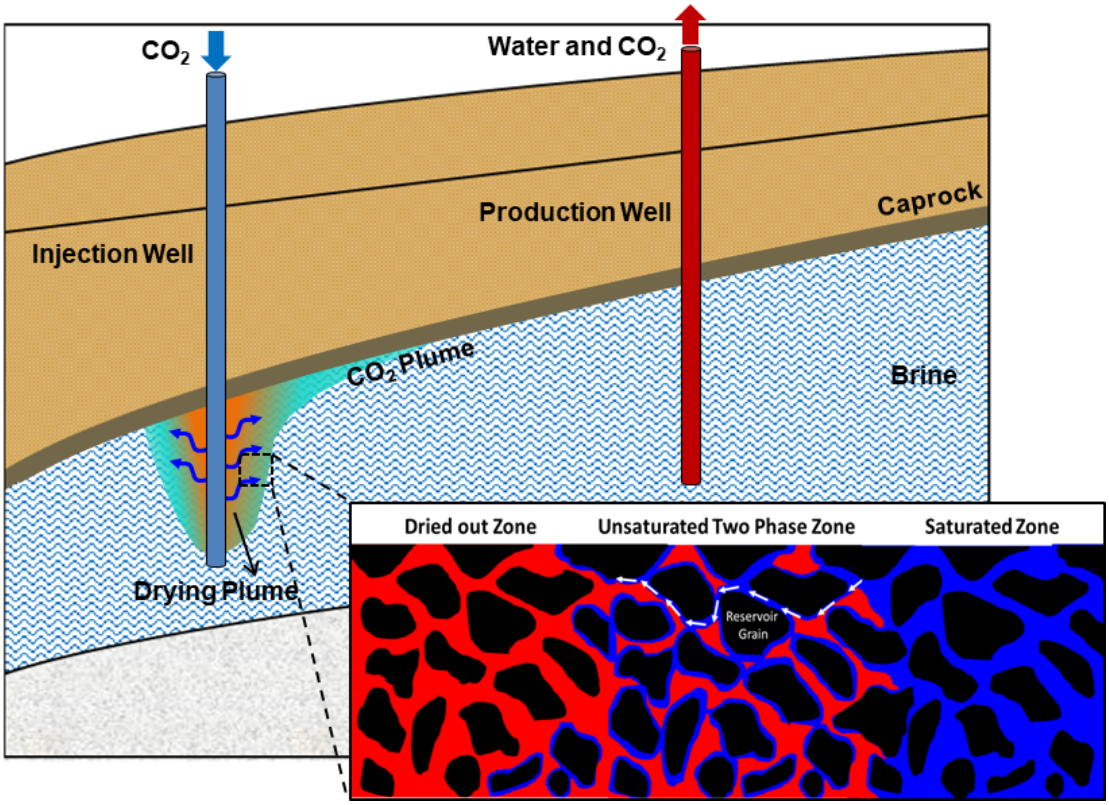

Figure 2.1: CPG system with injection and production wells (main figure), and capillary backflow inside the aquifer (inset figure). Water moves backwards as a result of the water saturation gradient between the dry-out and the saturated zones. Here, the two-phase zone plays an important role in moving water backwards through the water films and to the dry-out region, and consequently the salt precipitation near the injection well.

Capillarity affects the spreading of the liquid saturation profile across the drying fronts. Previously the evolution of water saturation with time was calculated using a fitting procedure [75] to relate the decrease in water saturation after two-phase immiscible displacement due to evaporation to gas flow rate. In another study, Cui et al. [76] used the CMG-GEM simulator to include geochemical reactions in a CO_2 injection process and observed the capillary-driven brine backflow at the edge of the two-phase zone near the injection well, which resulted in localized salt precipitation. Similarly, Pruess and Müller [77] included brine backflow in their numerical solution for the CO_2-brine system. They reported that precipitation only happened in the dry-out region (the region affected by capillary-driven backflow). Also, the inclusion of the capillary effect in the solution increased the amount of precipitation by a factor of 1.1 compared to the case without applying capillary pressure.

The fact that capillary backflow and the resulting salt precipitation mainly happen in the dry-out region is also supported by some experimental works such as [78]. They found local salt precipitation mainly inside the capillary-dominated region, and as a consequence, the absolute permeability was reduced by a factor of 4. Ott et al. [79] studied salt precipitation due to capillary-dominated flow in a sandstone reservoir and proposed a length scale for the dry-out zone, as well as a permeability-porosity correlation considering the effect of salt precipitation. Showing the importance of the capillary-driven backflow, Miri et al. [80] investigated the physics of salt precipitation in a micromodel experiment and observed two phenomena contributing to localized salt precipitation (*i.e.*, salt self-enhancing and water film salt transport). Based on their results, trapped water films inside the two-phase and dry-out region could transport brine from the saturated zone to the dry-out zone, resulting in a continuous salt precipitation in this region. Also, at high flow rate conditions, the effects of capillary-driven backflow were negligible and as a result, very limited precipitation happened. Roels et al. [81] conducted a core-flooding experiment on a Bentheimer sandstone core, and a considerable reduction in the injectivity due to salt accumulation through capillary pressure was reported.

2.2.3 This study

According to the above-mentioned papers, and to the authors' knowledge, there is almost no consistent work focusing on capillary-driven backflow and its relation to salt precipitation. In this regard, the present study provides a comprehensive sensitivity analysis of governing parameters, including relative permeability and capillary pressure curves, injection temperature and flow rate; reservoir's salinity, temperature, and porosity; and the production well

bottomhole pressure, and their effects both on brine backflow and salt precipitation. The range of the governing parameters was chosen in a way to cover all ranges studied in previous studies. In addition, a backflow extent parameter (BEP) is defined, which relates all governing parameters to water backflow and salt precipitation, and it is shown that changes in other governing parameters, which result in an increase in BEP, would contribute to salt precipitation.

2.3 Problem description and backflow and energy metrics

The model includes different processes and mechanisms –namely heat and mass transport, geochemical reactions, minerals dissolution/precipitation and their effects on porosity and the permeability, water vaporization, and capillary backflow– fully coupled with a geochemical compositional equation of state (EoS) simulator (CMG-GEM)[62]. The EoS parameters and the equations used in this simulator are described in Appendix A. Also, the results of the solution validation, as well as the grid resolution sensitivity analysis, are reported in Appendix B.

2.3.1 Reservoir properties

A 600 m $\times$ 500 m $\times$ 100 m reservoir (as shown in Fig. 2.2) is considered to investigate the relationship between water capillary-driven backflow and the subsequent salt precipitation, as well as the resulted increase in the required pumping power. Heat and mass transport, aqueous and mineral reactions, water vaporization, capillary backflow, minerals dissolution/precipitation and their effects on the porosity and the permeability of the field are considered during these simulations. The size of the domain is the same as the model by Cui et al. [76], with which the simulations are validated.

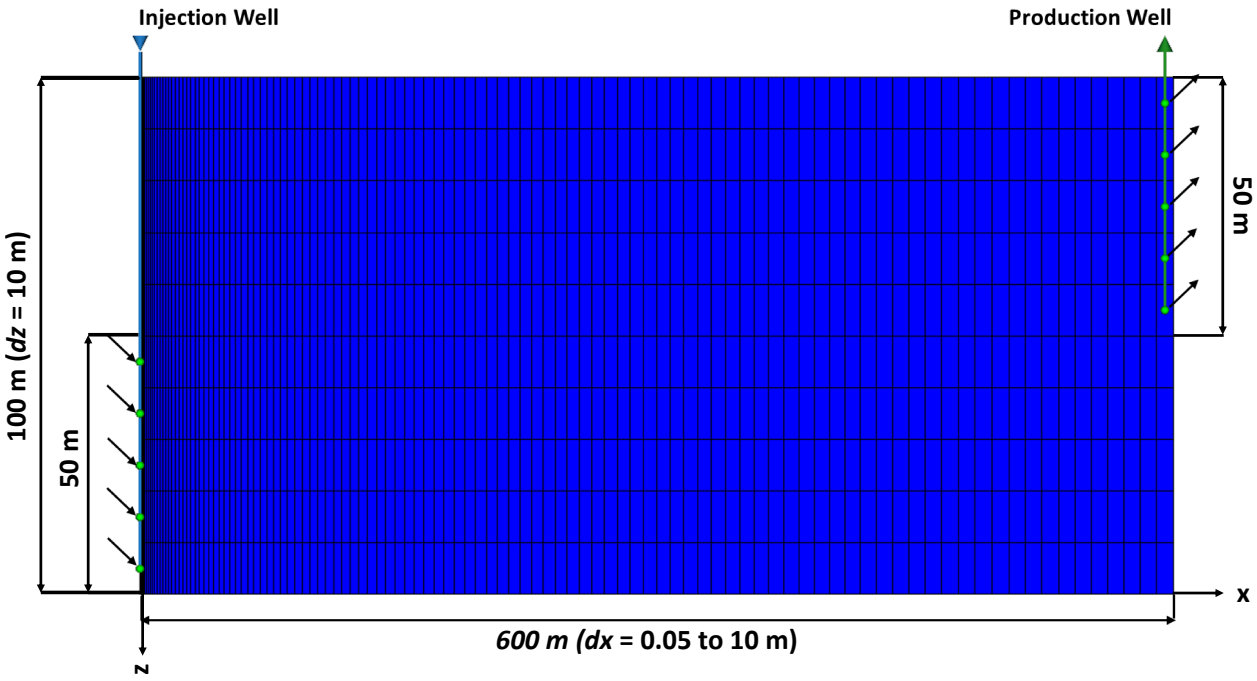

Figure 2.2: 2D grid and geometry of the studied aquifer. This is a $111 \times 1 \times 10$ structured grid with near-injection dx=0.05 which then increases to 10 m. The injection well is perforated at the lower half (lower 50 m) of the reservoir, and the production well is perforated at the upper half (upper 50 m).

The aquifer is studied both through a 1D and a 2D grid. Since the 1D case required less simulation time, it is used to provide multiple simulations covering a wide range of governing parameters. The 2D grid is used to analyse the main cases, *i.e.*, the salinity sensitivity analysis, in more detail. Since most of the salt precipitation occurs near the injection well, a finer mesh is used in this region. Although a coarser grid would reduce the simulation time, it may result in a noticeable over- or underestimation of salt precipitation [82]. Therefore, for the 1D case, a $111 \times 1 \times 1$ structured grid (with near-injection dx=0.05 and then increasing to 10 m) is used. Similarly, for the 2D case, a $111 \times 1 \times 10$ grid with the same dx as the 1D case and dz=10 m is utilised. It should be mentioned that the size of dz, which represents the vertical resolution, can have an impact on the vertical distribution of CO_2 and the upward density-driven flow. Consequently, it may also affect the extent of salt precipitation near the injection well, as this region experiences the most CO_2 vertical flow. Therefore, altering the vertical resolution has the potential to change the locations of localised salt precipitation near the injection area.

Some considerations are taken into account for the design of the simulations. The designed reservoir is considered to be representative of a sandstone reservoir in terms of min-

eralogy and petrophysical properties; and the reservoir's boundaries maintain heat transfer with the surrounding rock, however, a no-flow condition is applied at the boundaries. In addition, CO_2 is injected at the supercritical condition through an injection well that is perforated at the lower half (lower 50 m) of the reservoir, and at the production well, perforated at the upper half (upper 50 m), hot fluid is extracted. Additionally, it should be mentioned that the permeability, porosity, and temperature gradient of the reservoir (42.5 °C/km) considered in this study are selected for a reservoir with an ideal condition for CPG exploitation. However, these values over-represent the characteristics of most actual reservoirs available for CPG. Also, It is important to note that these parameters have been selected in such a manner as to facilitate comparisons with other similar works in this field. The general properties of the reservoir are summarised in Table 2.1.

Table 2.1: Reservoir and model initial properties for the main simulation case.

Parameter	**Value**	**Parameter**	**Value**
Top depth _ D, [m]	3500	Thermal conductivity _ K, [W.m^{-1}.°C^{-1}]	2
Length _ L, [m]	600	Initial water saturation _ S_w^0	1
Width _ W, [m]	500	Solubility of CO_2 in water [83], %	2.7
Height _ H, [m]	100	Solubility of water in CO_2 [83], %	10.45
Pressure _ P, [MPa]	35	CO_2-Water diffusion coefficient, [m^2.s^{-1}]	11E-09
Temperature _ T, [°C]	150	Brine salinity _ $\hat{S}$, [ppm]	58440
Horizontal permeability _ $k_{x,y}$, [md]	100	CO_2 injection rate _ $\dot{m}$, [kg.s^{-1}]	15
Vertical permeability _ k_z, [md]	50	CO_2 injection temperature _ T_{inj}, [°C]	40
Initial porosity _ ϕ^0	0.1	Displace pressure, [MPa]	2
Density _ ρ, [kg.m^{-3}]	2650	Simulation time _ t, [year]	30
Heat capacity _ c, [J.kg^{-1}.°C^{-1}]	840		

As mentioned, the reservoir is considered to be sandstone, where calcite, anorthite, and kaolinite represent carbonate, silicate, and clay mineral components, respectively. Based on the literature in this field [61, 62, 84, 85], the following chemical reactions for a sandstone reservoir including aqueous and mineral reactions are considered. These reactions are applicable for all geological structures that include interactions between the aforementioned minerals, CO_2, and brine. The reactions' equilibrium coefficients and minerals' rate law parameters are provided in Tables A2 and A3, respectively.

$$H^+ + OH^- \rightleftharpoons H_2O \tag{2.1a}$$

$$CO_2 + H_2O \rightleftharpoons HCO_3^- + H^+ \tag{2.1b}$$

$$HCO_3^- \rightleftharpoons CO_3^{2-} + H^+ \tag{2.1c}$$

$$\text{Calcite} + H^+ \rightleftharpoons Ca^{2+} + HCO_3^- \tag{2.1d}$$

$$\text{Anorthite} + 8H^+ \rightleftharpoons 4H_2O + Ca^{2+} + 2Al^{3+} + 2SiO_{2,aq} \tag{2.1e}$$

$$\text{Kaolinite} + 6H^+ \rightleftharpoons 5H_2O + 2Al^{3+} + 2SiO_{2,aq} \tag{2.1f}$$

$$\text{Halite} \rightleftharpoons Na^+ + Cl^- \tag{2.1g}$$

The initial composition of the brine and the reservoir are set based on Cui et al. [76] and are presented in Table 2.2.

Table 2.2: Reservoir and brine initial compositions.

Brine	**Ion**	H^+	Ca^{2+}	Al^{3+}	$SiO_{2,aq}$	Na^+	Cl^-
	mol.L^{-1}	1×10^{-7}	9.12×10^{-5}	2.32×10^{-11}	2.35×10^{-8}	1	1
	Ion	HCO_3^-	CO_3^{2-}	OH^-			
	mol.L^{-1}	2.5×10^{-2}	1.2×10^{-5}	5.45×10^{-7}			
Mineral	**Component**		Anorthite	Calcite	Kaolinite	Halite	
	Volume fraction		0.036	0.153	0.00135	0.00	

Corey model [86, 87] is used to calculate relative permeabilities as shown in Eq. 2.2a. For the main case, the irreducible water saturation (S_{wir}) is set to be 0.3 and the gas critical saturation (S_{gc}) is 0.05. In addition, to generate various relative permeability curves, five different S_{wir} values are considered, *i.e.*, S_{wir} = 0.1, 0.2, 0.3, 0.4, and 0.5 [88, 89].

$$k_{rw} = S_{wn}^4, \quad k_{rg} = (1 - S_{wn})^2(1 - S_{wn}^2) \tag{2.2a}$$

$$S_{wn} = \frac{S_w - S_{wir}}{1 - S_{wir} - S_{gc}} \tag{2.2b}$$

For the capillary pressure, the van Genuchten model [90] is used as Eq. 2.3. Again, for the main case, P_{cap}^0 is equal to 0.004 MPa, and the capillary force parameter (γ) is set to be 0.412. Same as the relative permeability, various capillary curves are generated by changing the P_{cap}^0 (0.002, 0.004, and 0.008 MPa) and the force parameter (0.412 and 0.5) [73, 74, 89]. These curves are illustrated in Fig. 2.3. It should be noted that changes in porosity caused by precipitation and dissolution can influence the relative permeability and capillary pressure curves. However, for the sake of simplicity, these curves are assumed to remain constant

throughout the simulations, and the impact of porosity changes on them is neglected.

$$P_{cap} = P^0_{cap}(S^{-1/\gamma}_{wn} - 1)^{1-\gamma} \tag{2.3}$$

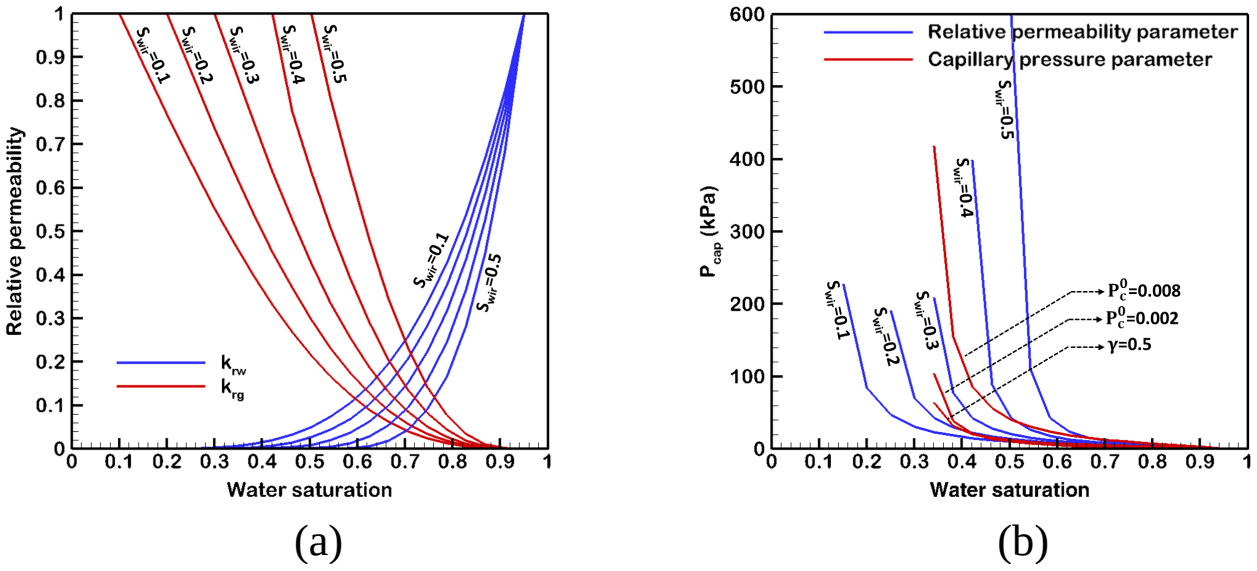

Figure 2.3: (a) Relative permeability [88, 89], and (b) capillary pressure curves [73, 74, 89] considered in this work. These curves are chosen in a way to cover a wide range of relative permeability and capillary properties that are used in other relevant works. However, it should be noticed that these curves are considered to remain constant during the simulations and the effect of porosity change on them is neglected.

2.3.2 Simulation cases and governing parameters

A total of 140 simulations were performed, covering wide ranges of parameters considered by numerical and simulation works such as [40, 73]. A complete description of the properties of the simulation cases is provided in Table 2.3. It should be mentioned that for each of the five salinity cases, variations of all governing parameters are studied, *i.e.*, 27 simulations for each salinity case. In addition, a case with no capillary pressure effect is considered for each of these salinity cases. The general conservation equations, such as the mass conservation equation, CO_2 and water solubility, and geochemical equations utilised in the simulations, are thoroughly described in Appendix A. In order to conduct these 140 simulations, certain simplifying assumptions are made, as explained in the previous section. One potential source of error in this study is the 1D geometry used in the simulations, which overlooks the effects of vertical density-driven flow. However, to address this concern, some 2D cases are also

defined and studied in the present work to provide additional insights and justification.

Table 2.3: 1D and 2D simulation cases and studied parameters.

Parameter		Simulation case
S_{wir}	0.1, 0.2, 0.3*, 0.4, and 0.5	Cases 1 to 5
P^0_{cap}, [MPa]	0.002, 0.004*, and 0.008	Cases 6 and 7
γ	0.412* and 0.5	Case 8
T_{inj}, [°C]	40*, 60, 80, 100, 120, and 140	Cases 9 to 13
T_{res}, [°C]	50, 70, 90, 110, 130, and 150*	Cases 14 to 18
$\dot{m}$, [kg.s^{-1}]	10, 15*, 20, and 25	Cases 19 to 21
P_{prod}, [MPa]	10, 20, 30, 33*, and 40	Cases 22 to 25
ϕ	0.05, 0.1*, and 0.15	Cases 26 and 27
$\hat{S}$, [mg.L^{-1}]	29220, 58440*, 116880, 175320, and 233760	Cases 28 to 140

* indicates parameters used for the main simulation case.

2.3.3 Backflow and energy parameters

To better study the effects of minerals and especially salt (dissolution and precipitation) on reservoir damage and pressure drop of the system, a resistance factor parameter is defined as:

$$R_f = \frac{k^n}{k} \tag{2.4}$$

where, k^n represents the permeability of the previous time-step, and k stands for the current permeability. Utilising Eq. A13, the resistance factor can be written as below:

$$R_f = \left(\frac{\phi^n}{\phi}\right)^{R_{f,exp}} \left(\frac{1-\phi}{1-\phi^n}\right)^2 \tag{2.5}$$

To correlate the minerals' precipitation effect to the energy consumption of the system and the required pumping power, Eq. 2.4 is implemented into Darcy's law. In Eq. 2.6, Q is constant and is equal to the injection rate and ΔP is calculated for every time step using the calculated value of R_f. Also, it is important to note that this equation is used only for the 1D cases.

$$\Delta P = \frac{-Q\mu L R_f}{A k^n} \tag{2.6}$$

Using the equation for the pumping power, the relation between the required pumping

power and the resistance factor (resulted from minerals precipitation) can be illustrated.

$$w_{\text{pump}} = \left(\frac{\dot{m}}{\rho}\right)\Delta P = \frac{-\dot{m}Q\mu LR_f}{\rho A k^n} \tag{2.7}$$

In the above equation, w_{pump} represents the pumping power (W) as a function of resistance factor.

Capillary backflow of water is experimentally shown to be the main mechanism causing salt precipitation near the injection well [69]. Based on its profiles, it is found that both the strength of the capillary backflow (maximum amount of the water backflow velocity) and its time span reflect the magnitude of salt precipitation at any location. Therefore, to account for both of these parameters, a backflow extent parameter (BEP) is defined and used to illustrate the results.

$$\text{BEP} = \int_0^{t_B} V_B.dt \tag{2.8}$$

In which, t_B is the time at which water backflow disappears and V_B is the water backflow velocity.

2.4 Results and discussion

Based on the literature, mineral precipitation has damaging effects on the reservoir's porosity, permeability, and CO_2 injectivity. Accordingly, in this section, 1D and 2D results of the simulations are presented, and as described earlier, various parameters are considered for the sensitivity analysis.

2.4.1 Main case

A main case as a benchmark is considered, and its results are used for the study of the parameters' effects. Properties of this benchmark case are provided in Table 2.3. 1D results are shown in Fig. 2.4 and the 2D profiles of the main case are illustrated (with a 1:3 scale) in Fig. 2.5.

As illustrated in Fig. 2.1, beginning with the CO_2 injection process, three zones form inside the aquifer, including a two-phase zone. This zone plays a significant role in the salt precipitation process and has a leading front with its propagation speed mainly controlled by the injection rate. By the movement of the flooding front toward the aquifer, the formation water evaporates, and the concentration of the dissolved salt increases. When the salt

concentration surpasses its solubility value, the excess salt begins to precipitate. During this process, some residual brine also becomes trapped in the two-phase zone. This trapped water eventually evaporates as well, resulting in more salt precipitation. The capillary-driven backflow plays as a brine supplier for this region. That is, when the capillary pressure becomes higher than the pressure gradient resulted from the injection fluid, water moves backwards to this two-phase zone. As a consequence, vaporization happens and solid salt builds up. Moreover, it is worth mentioning that despite the existence of various mechanisms that could potentially lead to water backflow, it was observed that there was minimal water backflow in cases without the capillary effect. As a result, the main conclusion drawn from the observations is that water backflow primarily occurs due to capillary pressure. The amount of time that the two-phase zone exists in a certain place, plays an important role in the amount of salt that precipitates in that location. The lifetime and the extent of this two-phase zone are mainly determined by the capillary pressure and the resulted capillary backflow. Therefore –as will be shown in the following sections by considering a case with no capillary effect, it can be concluded that salt precipitation mainly happens due to the evaporation of water and capillary backflow. Moreover, complementary cases are defined in Appendix C, where it is shown that even if the water phase pressure in a no-capillary case is equal to water phase pressure in a capillary-enabled case, the salt precipitation pattern is significantly different due to capillary pressure and capillary back-driven flow.

Fig. 2.4(a) shows the amount of minerals precipitation and dissolution throughout the reservoir after 30 years of CO_2 injection. As can be seen, the main mineral that precipitated is salt and it mainly occurred near the injection well, where the strongest capillary backflow happened in the two-phase zone. Although other minerals, such as kaolinite and calcite precipitated near the production well, it is seen that the porosity reduction that happened by their build-up is much less than that of solid salt. In other words, kaolinite and calcite precipitation about 110 $mol.m^{-3}$ caused the porosity to become 0.108 from its maximum amount of 0.112 (about 3.57% reduction), while the salt precipitation about 1861 $mol.m^{-3}$ caused the porosity to reduce to 0.066 (about 41% reduction). Therefore, based on this fact, in future sections, only salt precipitation is reported as the preponderant component that affects the reservoir's porosity.

Fig. 2.4(b) shows the variations of water velocity inside the reservoir at three different times. As time goes on, within the first year of injection, water saturation in the vicinity of the injection well reduces and so is its velocity. Therefore, by the increase of the CO_2 plume, water velocity moves toward zero. However, near the boundary of the CO_2 plume, in which

the two-phase zone is present (for these three cases 15, 20, and 25 m from the injection well), the water velocity is negative, indicating that capillary backflow is happening. As the simulation time evolves, the backflow region moves forward, but its magnitude reduces to such an extent that almost no salt precipitation happens far from the injection well. The magnitude of backflow and its time span, as well as the magnitudes of the resistance factor, porosity, and salt precipitation at the injection well, are presented in Fig. 2.4(c) and (d). First, it is seen that the water backflow time span is exactly the same as the time at which resistance factor, porosity, and salt precipitation become constant (about 396 days). This could also mean that these phenomena are triggered by the capillary-driven backflow. Additionally, it is also observed that salt precipitation and porosity linearly change as time increases, but the resistance factor follows an exponential pattern. Therefore, the capillary backflow and the resulted salt build-up exponentially increase the amount of resistance factor, which based on Eq. 2.7 represents the required pumping power in this study.

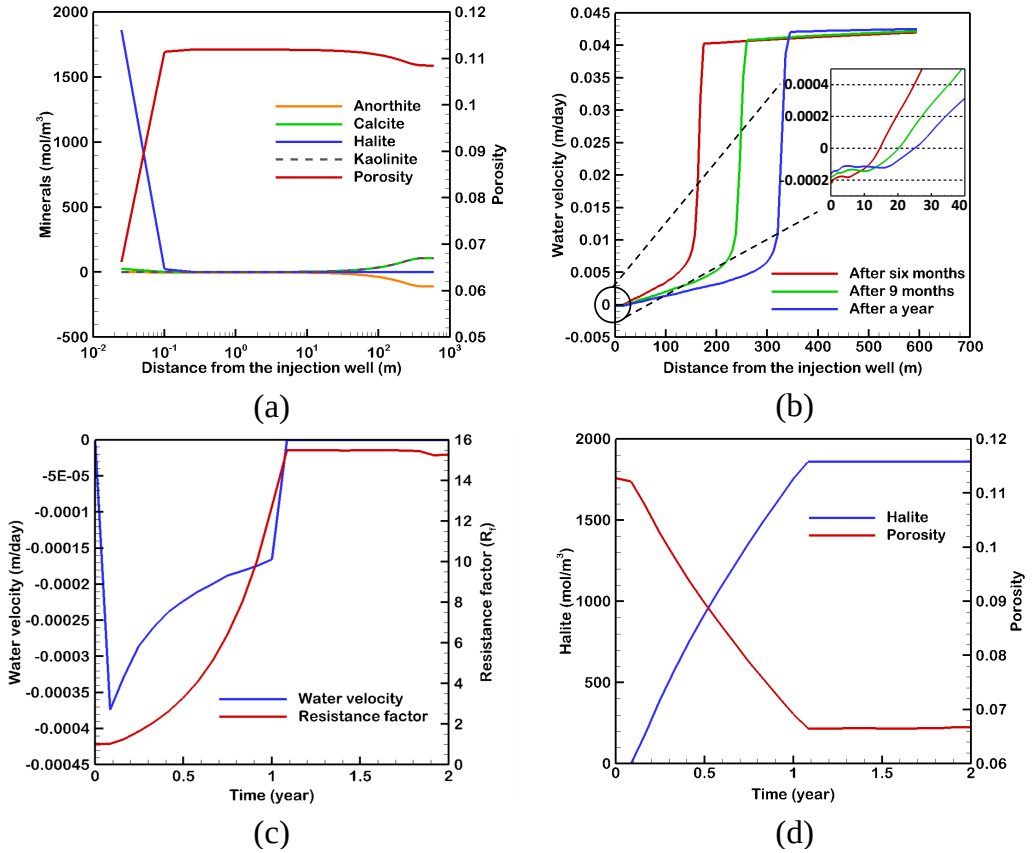

Figure 2.4: Main case 1D results: (a) minerals (anorthite, calcite, halite, and kaolinite) precipitation/dissolution and porosity after 30 years, (b) water velocity and water backflow velocity (the inset figure) after 30 years of injection, (c) water backflow velocity and the resistance factor at the injection well block at different times, and (d) salt precipitation and porosity at the injection well for different time steps from the onset of injection.

The 2D results of the main case are illustrated in Fig. 2.5. The interpretations deduced from 1D results are also valid here. Fig. 2.5(a) shows that anorthite most intensely dissolves near the production well, where the aqueous phase region is present. In addition, from Fig. 2.5(b), it can be seen that except in the vicinity of the injection well, calcite is precipitated in the reservoir, which can also mean that a portion of CO_2 is sequestrated through this mechanism inside the reservoir. Fig. 2.5(c) shows that kaolinite precipitation has inverse behaviour compared to anorthite. In other words, at places that anorthite is dissolved, kaolinite is precipitated. Based on Fig. 2.5(d), salt precipitation is limited to the vicinity of the injection well (about 10 m from the injection well). However, it will be shown in the following sections that for a brine with higher initial salinity the precipitation spread would be much higher. Fig. 2.5(e) shows that CO_2 plume tends to move upward because of its lower density. As a result, below the production well, a region with low gas saturation and high water saturation forms, in which brine is trapped. This can be the reason that almost no precipitation/dissolution or changes in the porosity happen below the production well. According to Fig. 2.5(f), two phenomena can be observed. First is that the initial porosity of the reservoir is slightly increased (about 0.015) due to the fluid pressure and the rock compressibility factor (4E-06 kPa^{-1} at the reference pressure of 3550 kPa for the present study). The second phenomenon is that porosity is greatly reduced (about 35 to 40%) at the injection well. Fig. 2.5(g) shows the temperature distribution inside the reservoir. It is seen that after 30 years of injection, there is still geothermal heat available to be used. However, since CO_2 saturation near the production well is increasing, CO_2 thermal plume will eventually reach the production well, and it would not be feasible to exploit that amount of remaining heat. Fig. 2.5(h) displays the capillary-driven backflow and the CO_2 saturation for three different times. As it is seen in this figure, the backflow mainly happens at the boundary of CO_2 saturation, which is exactly where the two-phase region exists. As the CO_2 plume extends, the intensity of the water backflow reduces, which could be a key factor that salt precipitation did not happen far from the injection well (see Appendix C for further analyses).

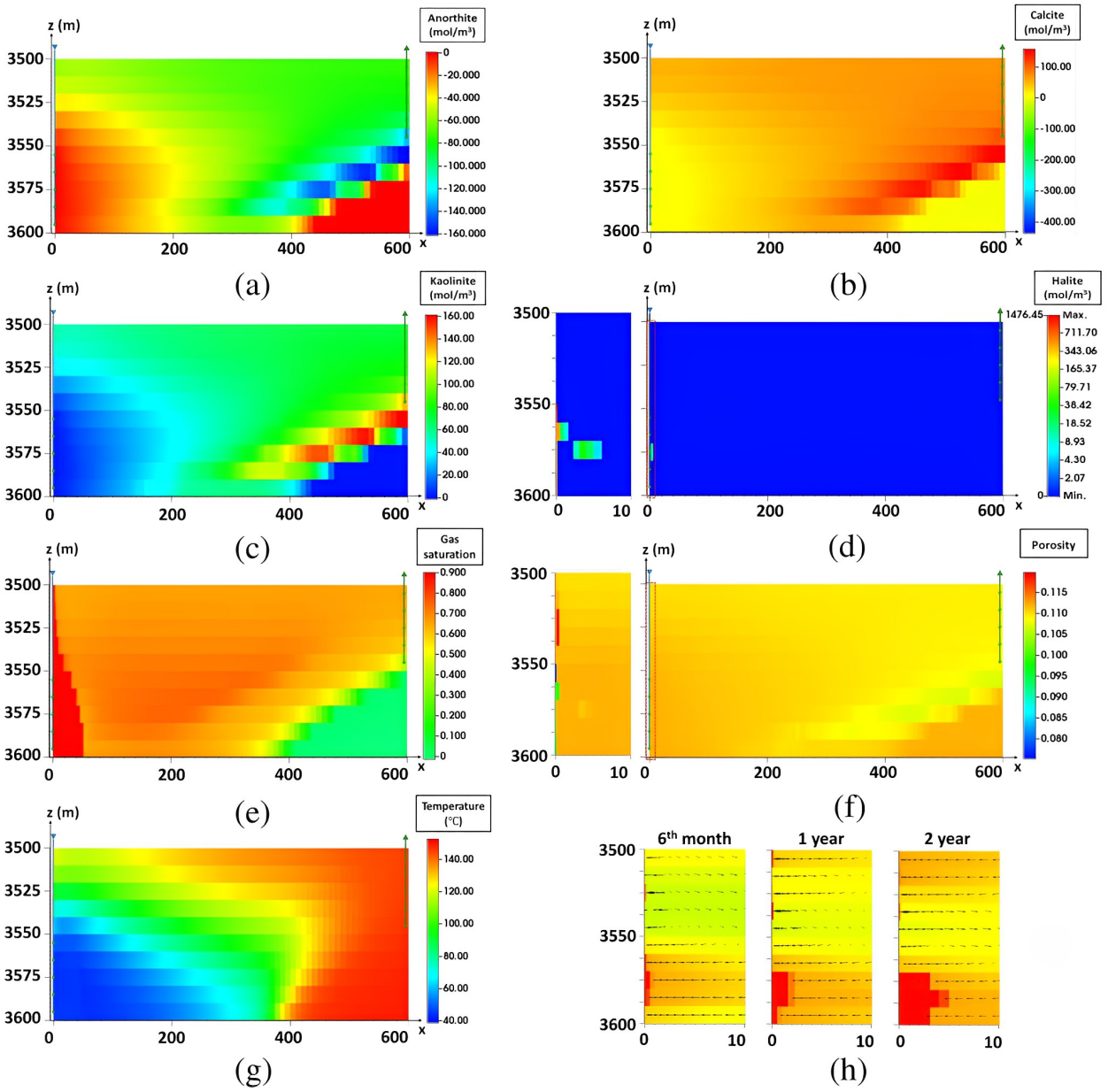

Figure 2.5: 2D results of the main case: (a), (b), (c), and (d) represent anorthite, calcite, kaolinite, and halite precipitation/dissolution throughout the reservoir and after 30 years of injection, respectively, (e), (f), and (g) show the CO_2 saturation, porosity, and the reservoir temperature distribution after 30 years of cold (40 °C) CO_2 injection, respectively, and (h) shows the capillary-driven backflow, happening near the dry-out region boundary, and gas saturation for three different times.

2.4.2 Effects of different parameters on backflow and salt precipitation

Based on the results of the previous section, since it was salt that had the most preponderant effect on porosity and resistance factor, in the following sections only the precipitation/dissolution of this component is illustrated.

Relative permeability and capillary pressure

The main reason for the salt precipitation is the vaporization of the water that is driven back toward the injection well due to the capillary force. Therefore, it is expected that the capillary and relative permeability curves play important roles in the precipitation process. In this regard, two sets of parameters are studied; first, is a relative permeability-related parameter (S_{wir}), and the second set includes capillary-related parameters (P^0_{cap} and γ). The corresponding relative permeability and capillary pressure curves are illustrated in Fig. 2.3.

Fig. 2.6 shows the results for these parameters. For the capillary-related parameters, any changes that result in increasing the capillary pressure will intensify the capillary-driven backflow and as a result, the salt precipitation will be strengthened. However, it should be noted that the intensified capillary only affects the duration of the backflow that happens in a certain area and not its magnitude. For instance, by increasing P^0_{cap} from 0.002 to 0.008 MPa, first, the capillary pressure almost becomes five times higher, second, as shown in Fig. 2.6(a), the backflow time span also increases from 180 days to 699 days. By this increase in the time span of the backflow that happens at the injection well, salt precipitation increases from 1090 to 2787 mol/m^3 (almost 155.7% increase in salt amount), and the porosity reduces from 0.085 to 0.043 at the injection well (about 49% reduction) which is a considerable amount.

For the case of the relative permeability parameter, *i.e.*, the irreducible water saturation, the physical interpretation is more complicated. By increasing S_{wir} two phenomena happen. First, the water relative permeability reduces at a constant saturation, which means that water has become more immobile. Second, the gas relative permeability increases, meaning that the mobility of the gas phase is increased. As a result, the dry-out front velocity increases as well. The combined effect of these two phenomena will be an increase in the extent of the two-phase mixing zone by an increase in the amount of the irreducible water saturation –as is seen in Fig. 2.6(b), which shows that the water backflow has an extent about 18 m for the case with $S_{wir} = 0.5$ and 10 m for the case of $S_{wir} = 0.1$. Nonetheless, the increased velocity of the dry-out front results in a shorter time span of backflow near

the injection well, which is evident in Fig. 2.6(a); and as discussed, the shorter the backflow time, the less the amounts of the salt precipitation and porosity reduction will be. The general conclusion from this analysis is that an increase in any parameter that strengthens the capillary pressure and makes the capillary-driven backflow prolong will increase the salt precipitation.

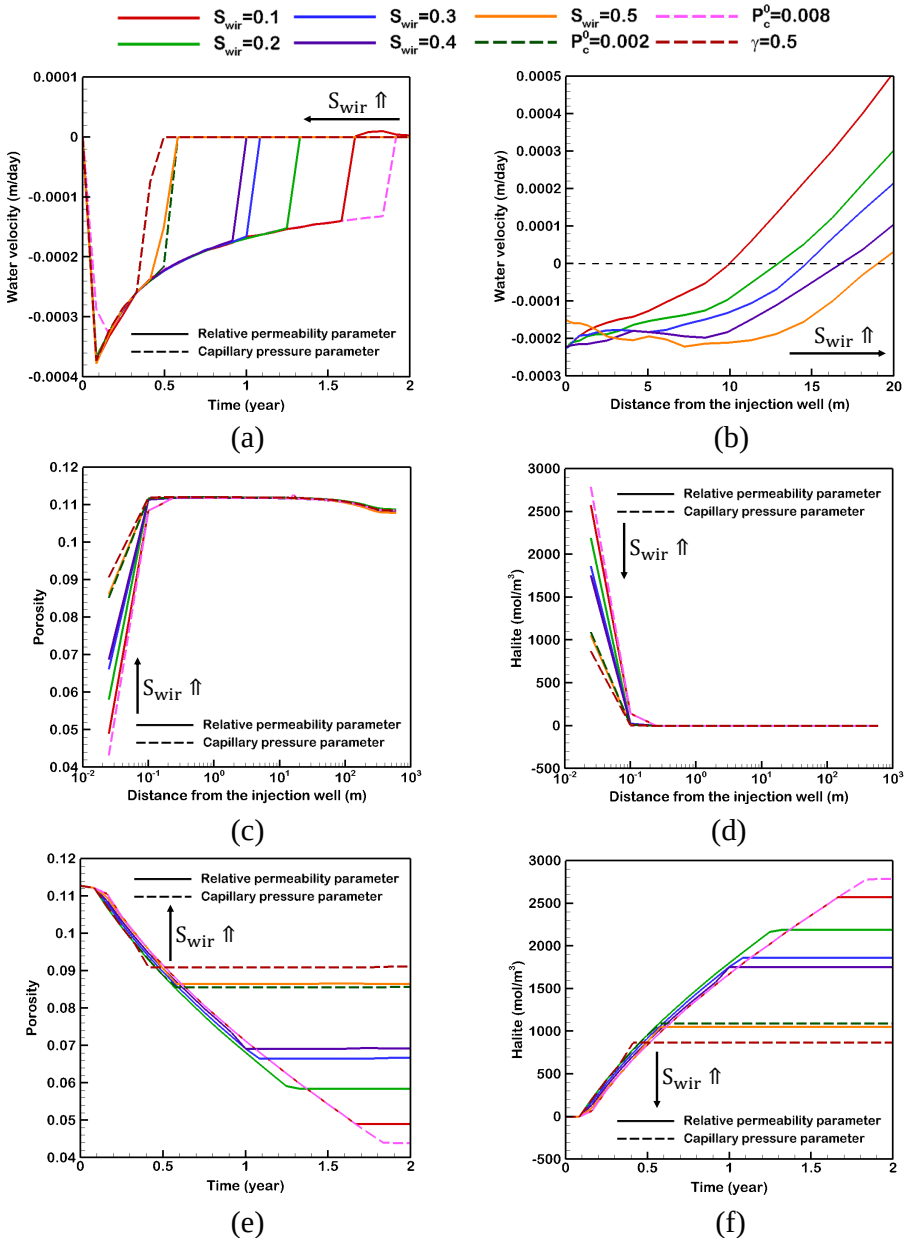

Figure 2.6: 1D results of the relative permeability and capillary pressure effects on: (a) backflow at the injection well, (b) water velocity throughout the reservoir after 6 months, (c) porosity after 30 years, (d) salt precipitation after 30 years, (e) porosity at the injection well, and (f) salt precipitation at the injection well for different times from the onset of the injection.

To further study the effects of different relative permeability curves and values of S_{wir} on water backflow velocity at the injection well, Fig. 2.7 is presented here. Fig. 2.7(a) shows the water backflow velocity at the injection well block for 4 different time steps. Based on this figure, it is observed that the backflow velocity profile moves and changes faster for higher S_{wir} values. For instance, the backflow velocity at the injection well for the case with $S_{wir} = 0.5$ becomes zero at 9 months, while for the case with $S_{wir} = 0.4$ it becomes zero at 12 months. Also, some fluctuations are observed in the curves in Fig. 2.7(a). The reason for these fluctuations could be the non-uniformity and the variations in grid sizes in the x direction (dx) from 0.05 m at the injection well to 10 m at the production well. Fig. 2.7(b) shows the water saturation at the injection well versus time and its relation to the water backflow velocity. In the curves of this figure, two sudden drops in water saturation are observed. The first drop represents the viscous displacement of water by supercritical CO_2. Then there is a gradual reduction of water saturation by a combined effect of vaporization and water backflow until the time that backflow velocity becomes zero. At this point, the second saturation drop happens. In all of the S_{wir} cases, except for $S_{wir} = 0.1$, the water saturation after the end of the backflow has a value lower than the S_{wir}. Therefore, for the case with $S_{wir} = 0.1$, after backflow stops, CO_2 still can push small amounts of water forward and this can be the reason for the small positive values of water velocity in Fig. 2.6(a) for the case with $S_{wir} = 0.1$ at times above 1.5 years.

Injection and reservoir temperature

The injection temperature of sc-CO_2 affects the amounts of CO_2 dissolution in brine and water vaporization, and since water vaporization is a key mechanism, the amounts and the time of the salt precipitation vary due to changes in injection temperature [91, 92]. Therefore, various injection temperatures, ranging from 40 to 140 °C, are considered (Fig. 2.8). By an increase in the injection temperature, the intensity of the backflow increases, but at the same time, its time span reduces (Fig. 2.8(a)). This is because, the increased temperature will increase the water solubility in CO_2, capillary backflow, and vaporization. However, since the drying-out process takes place at a higher pace –due to higher temperature, the time span of the backflow region is notably reduced. For the case with the injection temperature of 40 °C the maximum amount of backflow and the time span are 0.00037 m.day^{-1} and 396 days, respectively, while for the injection temperature of 140 °C these amounts are 0.00059 m.day^{-1} and 243 days. Also, based on Fig. 2.8(b), it is observed that the extent of the water backflow slightly decreases for the higher injection temperatures.

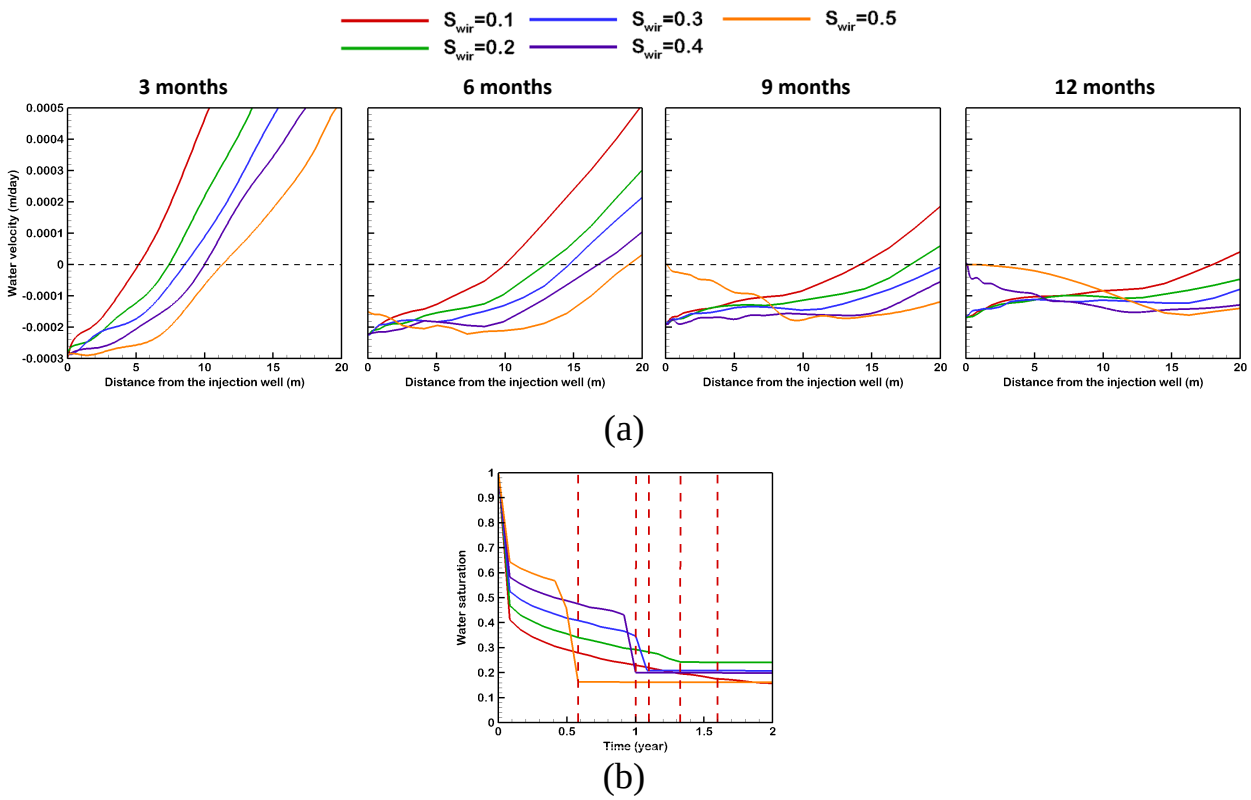

Figure 2.7: 1D results of the effects of different relative permeability curves and values of S_{wir} on: (a) water backflow velocity at the injection well at four different time steps, and (b) water saturation versus time and its relation to the water backflow velocity. The red dashes in Fig. (b) show the times that water backflow velocity becomes zero at the injection well.

As discussed earlier, both the intensity and the time span of the capillary-driven backflow affect the amount of salt precipitation and porosity reduction. Therefore, BEP parameter is described as Eq. 2.8, which is the surface integral of the backflow diagrams. In the cases of different injection temperatures, this parameter,*i.e.*, the water velocity profile integral, is slightly higher for higher injection temperatures, such as 140 °C. As a result, since the difference in BEP is negligible for various injection temperatures, the difference in salt precipitation and porosity is very little compared to other parameters, *i.e.*, 370 mol.m^{-3} and 0.008, respectively (Fig. 2.8(c) and (d)). In Fig. 2.8(e) and (f), it is observed that the backflow intensity affects the slope of the linear profile of the porosity and salt versus time. In addition, it is seen that the increase in the injection temperature will also increase the amount of precipitation and porosity reduction.

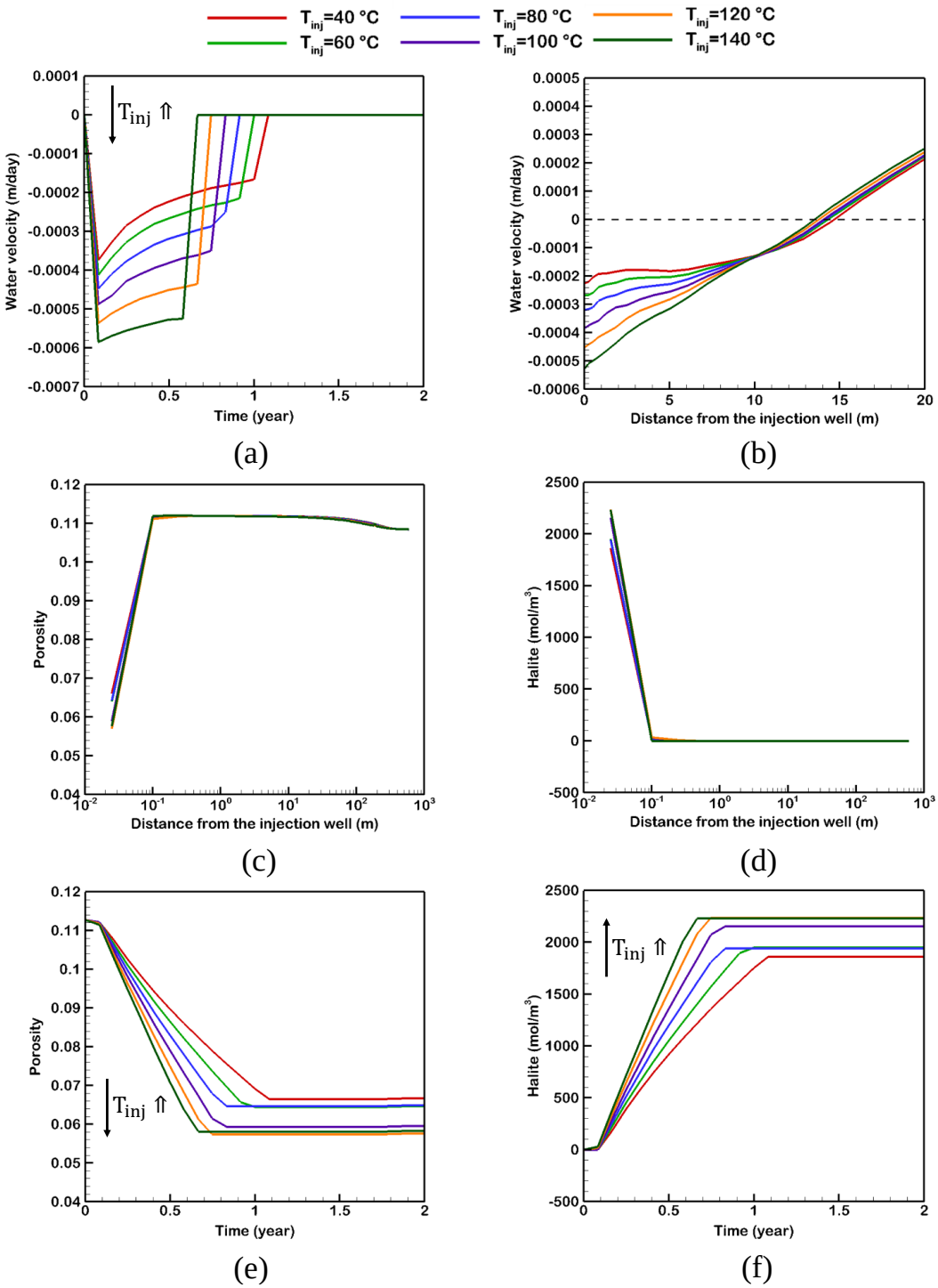

Figure 2.8: 1D results of the CO_2 injection temperature effects on: (a) backflow at the injection well, (b) water velocity throughout the reservoir after 6 months, (c) porosity after 30 years, (d) salt precipitation after 30 years, (e) porosity at the injection well, and (f) salt precipitation at the injection well for different times from the onset of the injection.

Effects of the initial reservoir temperature, ranging from 50 to 150 °C are illustrated in

Fig. 2.9. In Fig. 2.9(a), as the reservoir initial temperature increases, the maximum value of the water backflow increases as well, however, simultaneously the time span that the backflow region exists in a certain place reduces. The difference between Fig. 2.9(a) and Fig. 2.8(a) is that the time span variation is more noticeable in Fig. 2.9(a), meaning that BEP does not remain the same and affects the trend in salt and porosity diagrams. In addition, the lower reservoir temperature cases, such as 50 °C, have higher surface integrals and therefore, higher salt precipitation and porosity reduction, which is shown in Fig. 2.9(b) and (c). In conclusion, the reservoir initial temperature has a more considerable effect than CO_2 injection temperature, and as it increases less salt precipitation occurs.

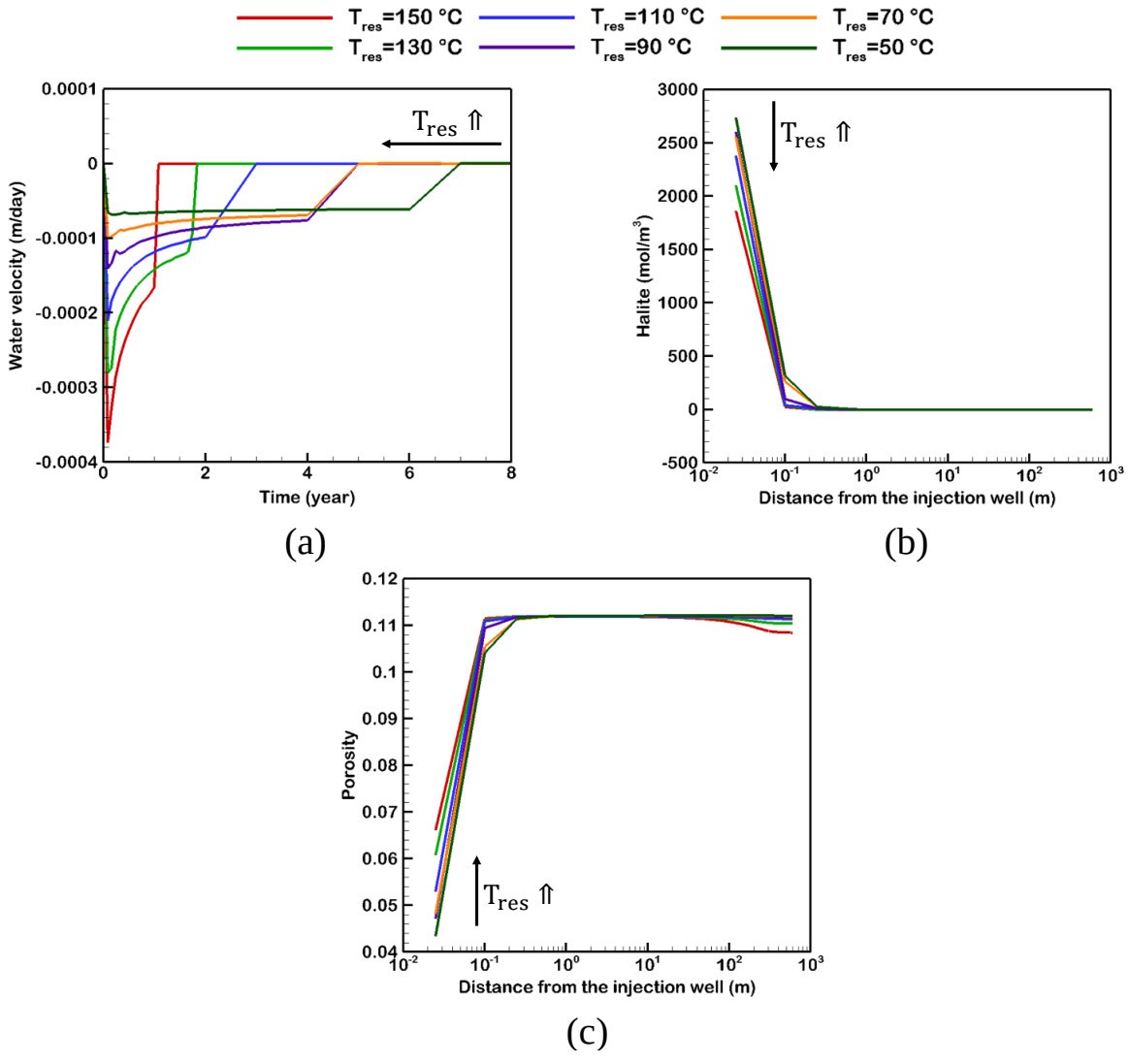

Figure 2.9: 1D results of the reservoir temperature effects on: (a) backflow at the injection well at different times, (b) salt precipitation throughout the reservoir after 30 years, and (c) porosity throughout the reservoir after 30 years of injecting CO_2.

Injection flow rate and production well BHP

Effects of injection flow rate and production well BHP are illustrated in Fig. 2.10. Four different injection flow rates (10, 15, 20, and 25 kg.s^{-1}) and five production well BHPs (10, 20, 30, 33, and 40 MPa) are considered. When the injection flow rate increases, the dry-out zone evolves more rapidly; also, a higher pressure gradient is induced near the injection well, suppressing the capillary-driven backflow. Based on these interpretations, as in Fig. 2.10(a) and (b), when the flow rate increases, the backflow region time span reduces considerably (from 730 days for 10 kg.s^{-1} to 181 days for the 25 kg,s^{-1} case). However, the influence of increment in injection rate becomes smaller in higher injection rates. As a result, as the flow rate increases the reservoir damage due to salt precipitation reduces about 33.7% (Fig. 2.10(b)).

Fig. 2.10(c) and (d) show the same results for the production well BHP. This parameter influences both the mass flow rate in the reservoir and its pressure. An increment in the production well BHP is somehow like reducing the injection flow rate. Therefore, it is expected that the time span of the two-phase backflow zone increases. This fact is clearly shown in Fig. 2.10(c). However, for the porosity, the situation is a bit more complex. The BHP of the production well can alter the reservoir's pressure, therefore it has a direct effect on porosity through the rock compressibility factor, *i.e.*, higher BHP results in higher reservoir pressure and higher initial porosity. Nonetheless, the amount of reservoir damage due to salt precipitation follows the same trend as the injection rate diagram. In other words, higher BHP (representing a lower mass flow rate) results in higher salt precipitation. For instance, for the cases of 10, 20, 30, 33, and 40 MPa BHP at the production well the amounts of porosity reduction are 0.025, 0.035, 0.0425, 0.045, and 0.049, respectively; which represent about 24.31, 33.1, 38.5, 40.69, and 43.07% porosity reduction accordingly.

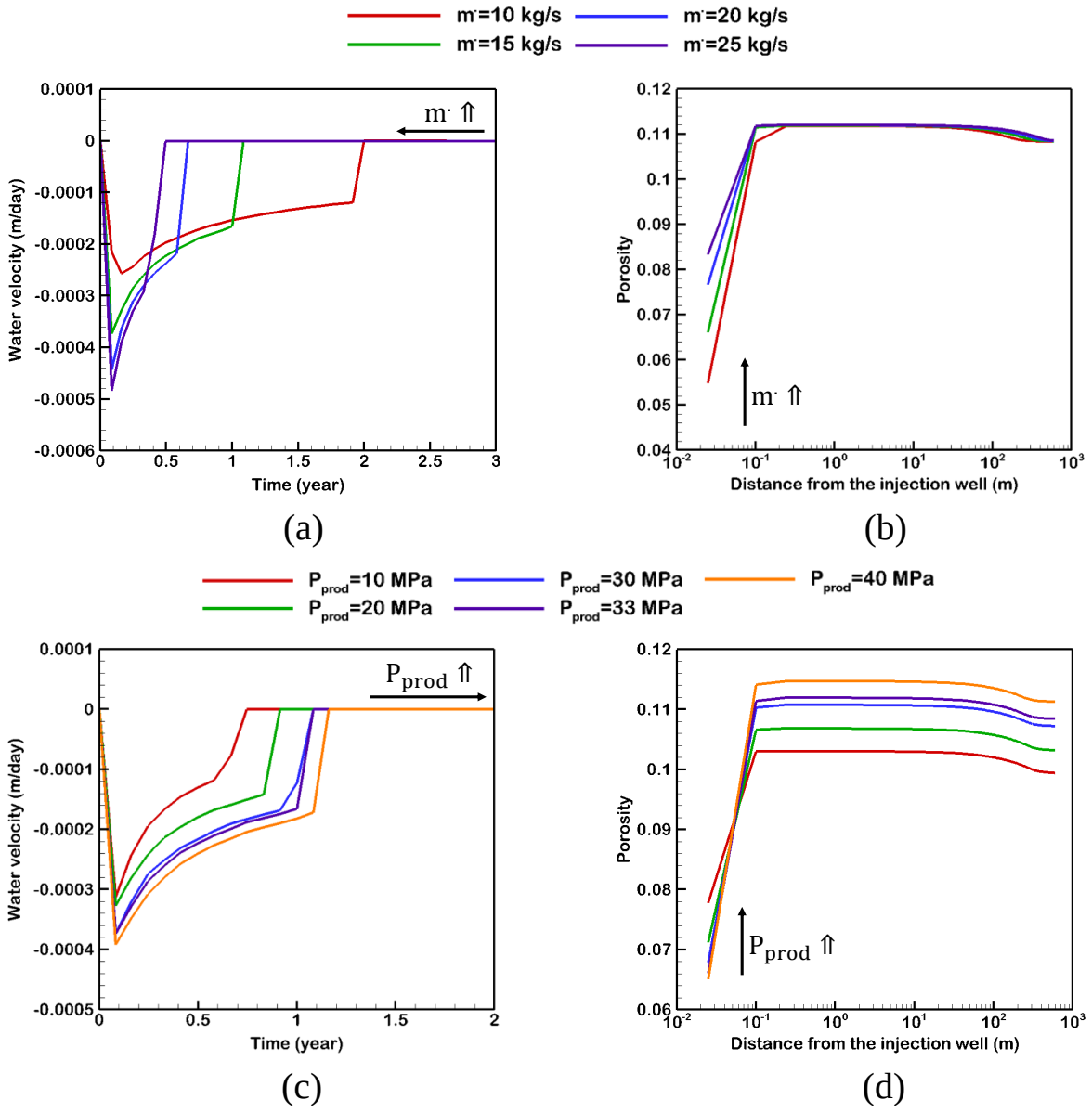

Figure 2.10: 1D results of the (a) effects of injection flow rate on backflow at the injection well at different times from the onset of injection, (b) effects of injection flow rate on porosity inside the reservoir after 30 years, (c) effects of production well bottomhole pressure on backflow at the injection well at different times from the onset of injection, and (d) effects of production well bottomhole pressure on porosity inside the reservoir after 30 years.

Initial reservoir porosity

Effects of the reservoir initial porosity are studied with three values, *i.e.*, $\phi = 0.05$, 0.1, and 0.15, in Fig. 2.11. When the reservoir porosity increases, the mobility of both the gaseous and the aqueous phases increase, therefore, as discussed in Section 2.4.2, higher

salt precipitation occurs. Fig. 2.11(a) shows that the backflow time span increases with an increase in the reservoir initial porosity; and based on Fig. 2.11(b) higher porosity results in more salt build-up. Despite higher salt precipitation in higher porosity cases, Fig. 2.11(c) illustrates that the per cent of porosity reduction is the same for all these cases. Here, porosity reduces about 0.023 for the case with $\phi = 0.05$, which is a 40.89% reduction; about 0.045 for the case with $\phi = 0.1$, which is a 40.69% reduction; and about 0.069, which is about 41% reduction. Therefore, despite the increased salt precipitation for the cases with higher porosity, the percentage of reservoir damage remains the same. This fact is also observed in the resistance factor diagrams in Fig. 2.17(f), which shows that the resistance factor remained almost the same for all porosities. However, Kim et al. [93] claimed that this interpretation is only applicable for high CO_2 injection rates and at lower rates the trend alters.

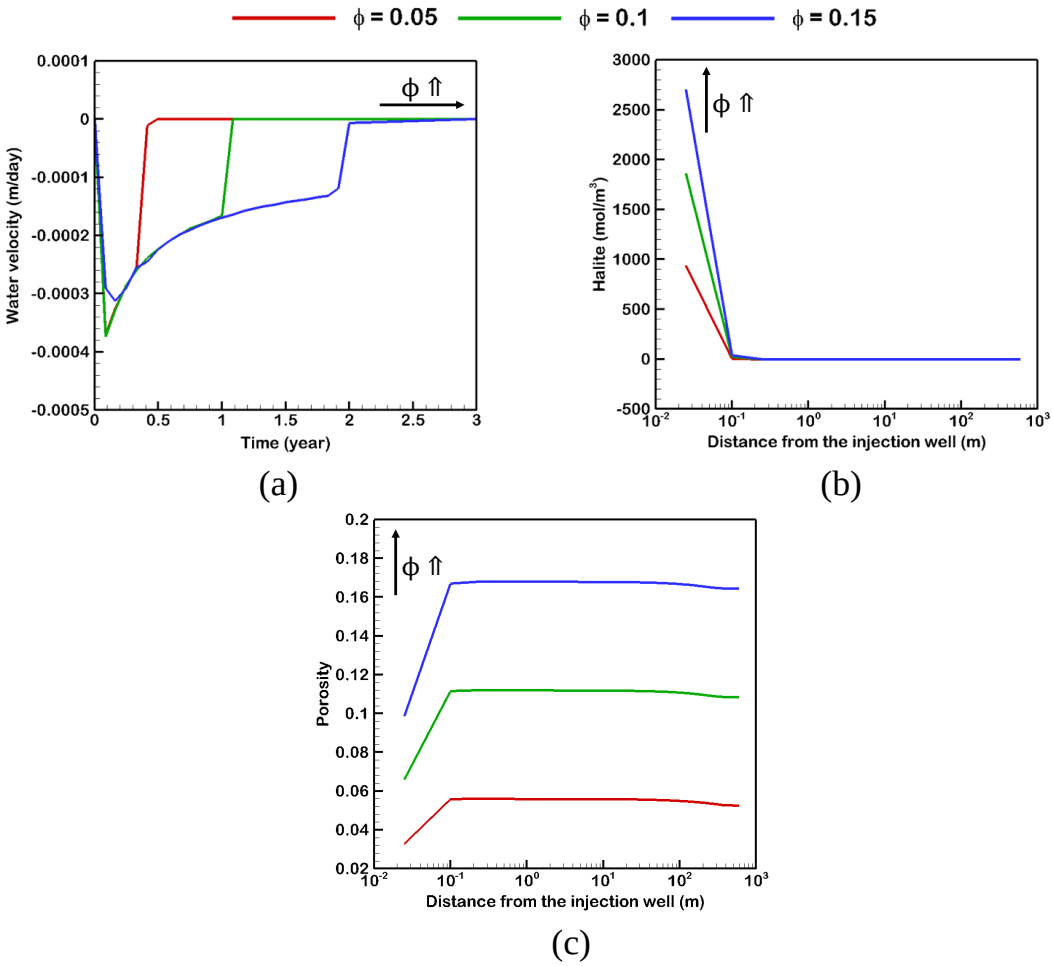

Figure 2.11: 1D results of the reservoir initial porosity effects on: (a) backflow at the injection well at different times from the onset of the injection, (b) salt precipitation inside the reservoir after 30 years, and (c) porosity inside the reservoir after 30 years.

Initial brine salinity

Among the governing parameters, brine salinity is the most influential one, which can significantly alter the amount and the extent of the salt precipitation and the subsequent reservoir damage. Five initial brine salinity values including 29220, 58440, 116880, 175320, and 233760 ppm are considered, which respectively represent 0.5, 1, 2, 3, and 4 mol.L^{-1} of NaCl. Fig. 2.12 shows the contours of salt distribution for these five cases. Since the difference between the amount of the precipitated salt near the injection well and the rest of the reservoir is huge, a logarithmic scale is used to show the results. It is observed that, should the salinity be less than 100000 ppm, the salt precipitation will be limited only to the close vicinity of the injection well (Fig. 2.12(a) and (b)). However, if the brine has an initial salinity above the above-mentioned value, salt will precipitate inside the whole dry-out region, although, again the difference between the amount of precipitation at the injection well and the field is considerable.

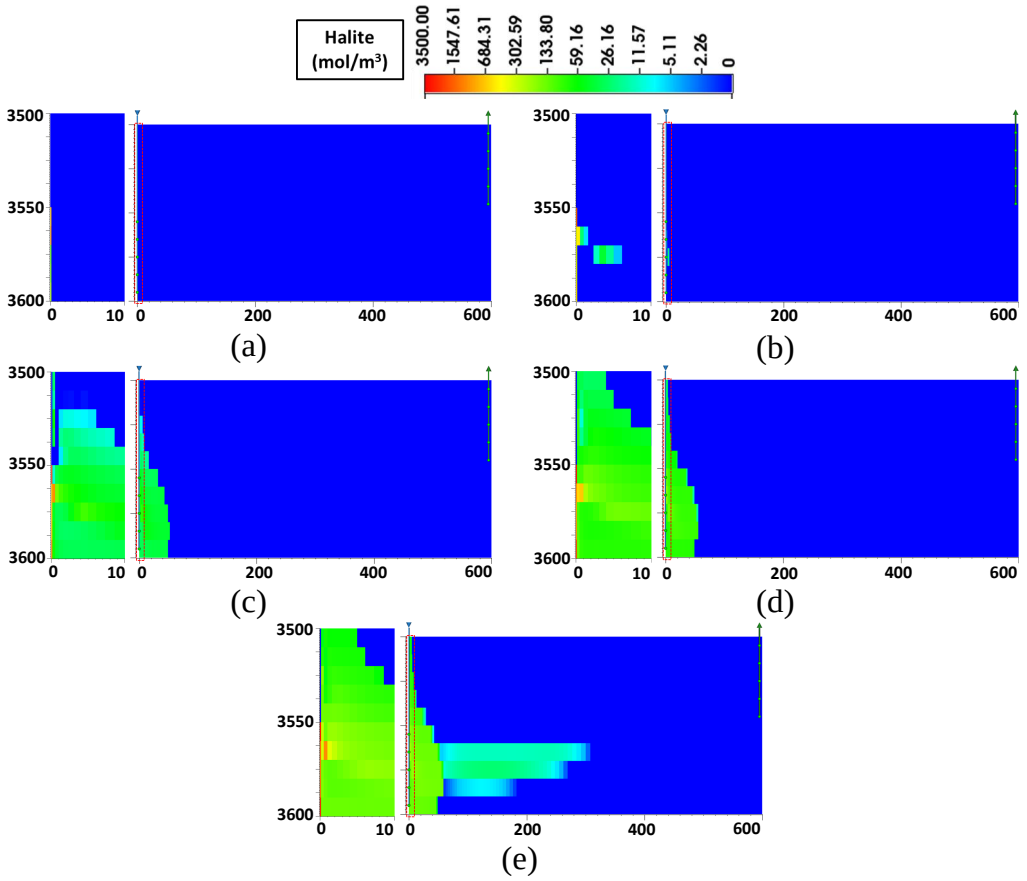

Figure 2.12: 2D results of the effects of initial brine salinity on salt precipitation: (a) salinity 29220 ppm, (b) 58440 ppm, (c) 116880 ppm, (d) 175329 ppm, and (e) 233760 ppm. The inset figures show the area close to the injection well (0 to 10 m), which is mainly affected by the salt precipitation resulting from water backflow to the dry-out area.

To further study the development of salt precipitation and variations in water backflow at the area close to the injection rate, Fig. 2.13 and Fig. 2.14 are presented here. Fig. 2.13 shows the amount of the precipitated salt for different initial brine salinity cases at different time steps. It is observed that the overall precipitation in the reservoir does not reach stability, however, the precipitation at the injection well becomes almost constant after about 2 years, coinciding with the presence of backflow in this area. A combined observation from Fig. 2.13 and Fig. 2.14 is that salt precipitation only happens inside the dry-out region where gas saturation is above 0.8-0.9.

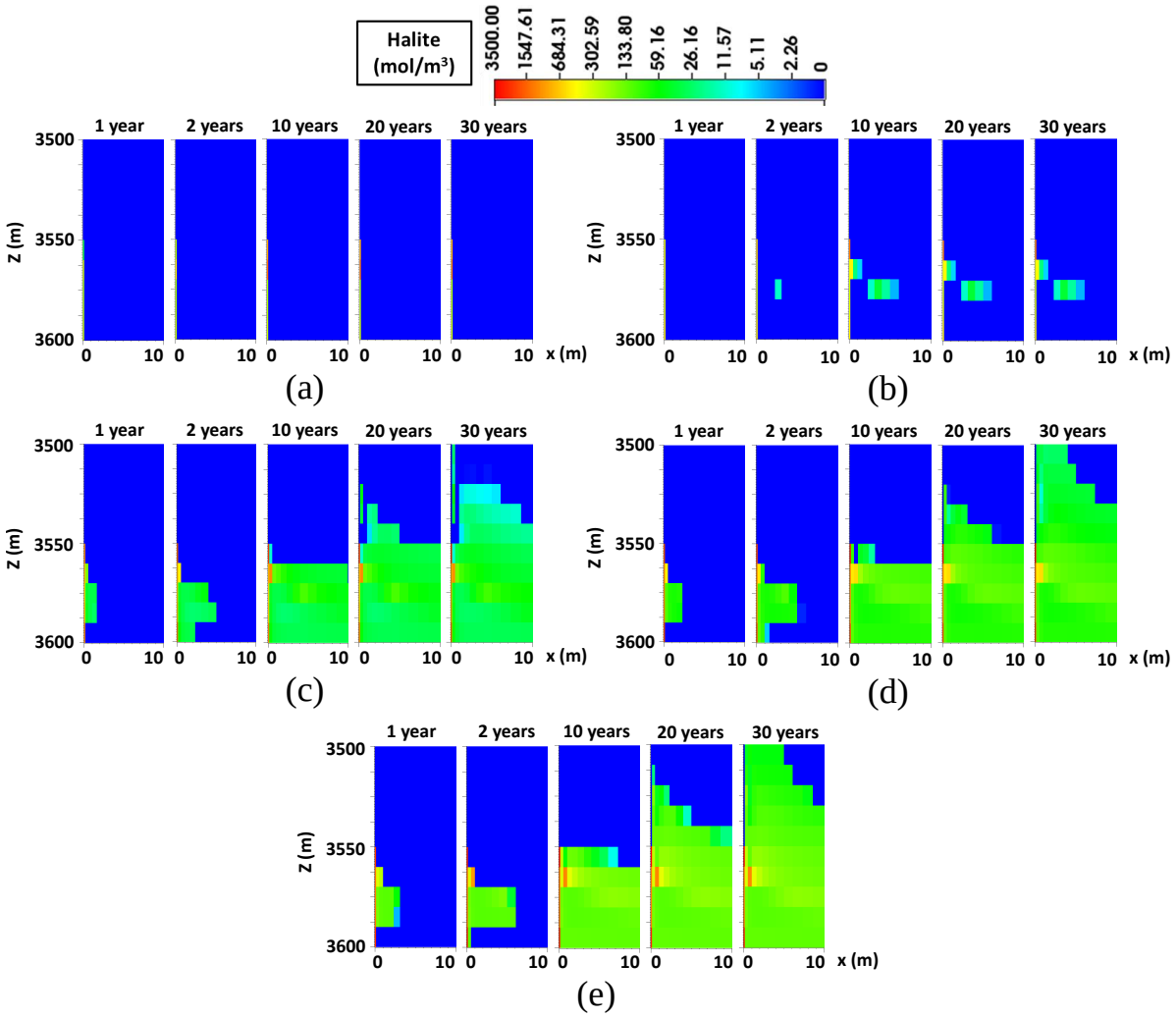

Figure 2.13: 2D results of salt saturation distribution inside the area near the injection well (0 to 10 m) for different initial brine salinity cases at five different time steps (1, 2, 10, 20, and 30 years) after the onset of injection. The area close to the injection well is the area that is mainly affected by salt precipitation. However, even in this small area itself, it is seen that the main salt precipitation happens at the injection well, in which the amount of the precipitated salt stabilises after a certain time.

Fig. 2.14 illustrates gas saturation and water backflow over time. These figures help to better understand the pattern of salt precipitation inside the reservoir. As shown in Fig. 2.14(a) and (b), in the 2D case, there is more than one backflow stream towards the injection well and this is mainly because of the upward density-driven flow of CO_2. The interactions between these backflow streams and the development of the drying plume are the main parameters defining the salt precipitation pattern. As a result, as shown in Fig. 2.13(b) and (c), there is some non-uniformity in the distribution of the precipitated salt. This non-uniformity arises from the fact that certain locations near the injection well are affected by more than one backflow stream, leading to increased precipitation in those areas.

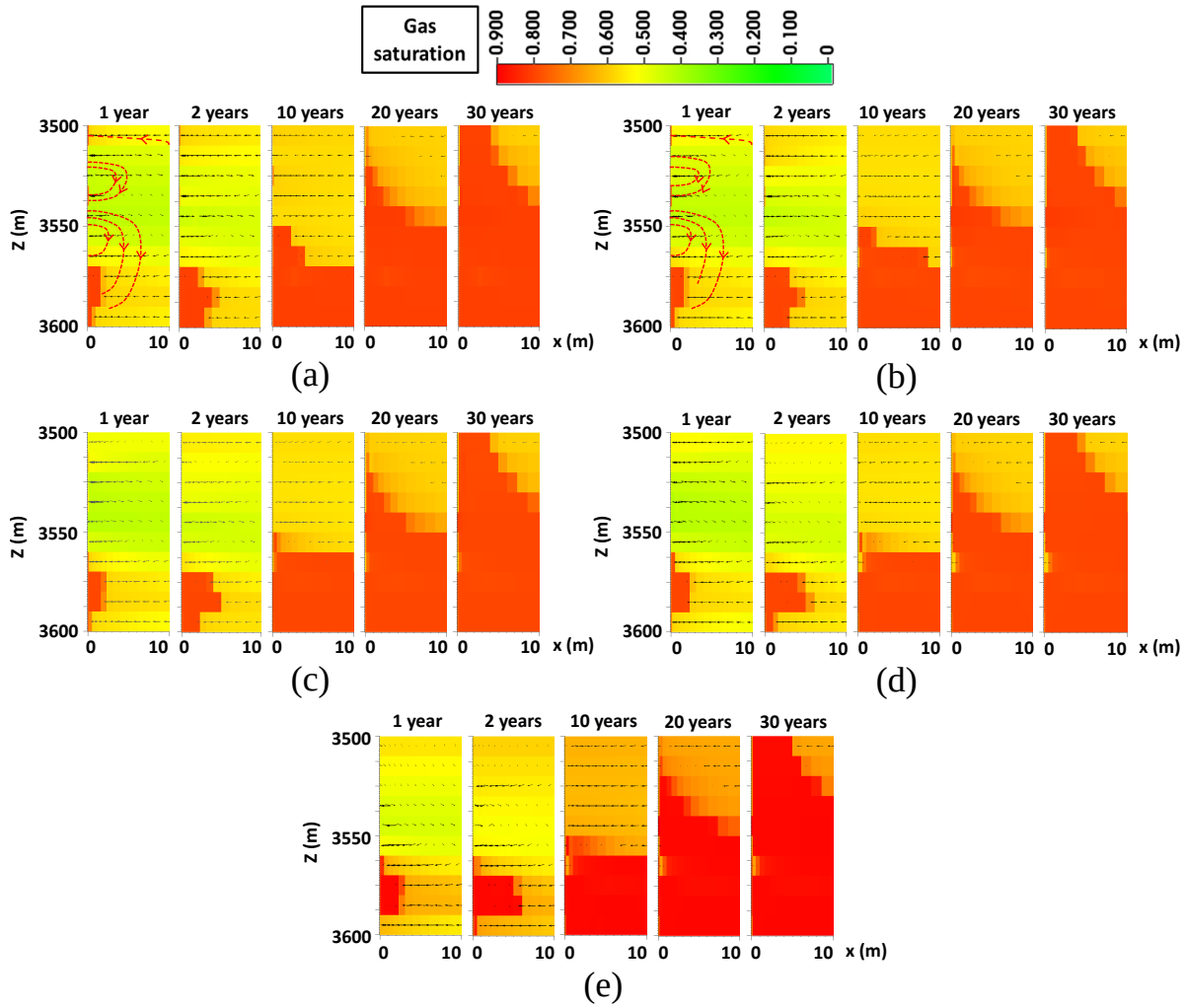

Figure 2.14: 2D results of gas saturation distribution and water velocity vectors inside the area near the injection well (0 to 10 m) for different initial brine salinity cases at five different time steps (1, 2, 10, 20, and 30 years) after the onset of injection. The red dashed arrows in Figures (a) and (b) show the two main backflow streams that happen inside a 2D reservoir.

Fig. 2.15 shows the relation between the brine salinity and the capillary-driven backflow and its effects on salt build-up and reservoir damage. Based on Fig. 2.15(a), as the initial salinity increases, the time span of the backflow reduces, which is because at higher salinities brine has less mobility and the capillary backflow is suppressed (confirming the conclusions of Andre et al. [94]). The interesting phenomenon observed here is that as the BEP reduced the amount of precipitation increased significantly (Fig. 2.15(b)), which is in conflict with the results in previous sections. For example, for the case with the salinity of 29220 ppm, the backflow region has a time span of 396 days and the salt precipitated about 907 mol.m^{-3}, while for the case with the initial salinity of 233760 ppm, these amounts are 151 days and 3369 mol.m^{-3}, respectively. This phenomenon defined the salinity constant lines in Fig. 2.16. In addition, as the salinity increases, its effect on salt precipitation and porosity becomes less, which could mean that there is a critical salinity, at which the maximum salt precipitation and the most reservoir damage occur, and beyond that salinity, no considerable changes happen in the salt build-up or porosity reduction. Fig. 2.15(c) shows how seriously this parameter can damage a reservoir. It is seen that salinity can increase the amount of porosity reduction at the injection well from 0.02 (about 19.14%) to 0.085 (about 72.03%). Also, the average porosity of the reservoir can be reduced by about 2.26% for the lowest and about 2.6% for the highest salinity cases.

In addition to the above-mentioned effects, it is important to see how salt precipitation affects the amount of the stored CO_2, as well as the heat extraction in integrated carbon sequestration-geothermal systems. Therefore, since the highest increase in salt precipitation happened by increasing the brine salinity, these two parameters are studied here. The heat extraction rate from the reservoir depends on both the extracted fluid temperature and its flow rate. As a result, a heat extraction parameter is defined by multiplying the production fluid volumetric flow rate ($\dot{Q}$) by its temperature. This parameter, as well as the CO_2 mass inside the reservoir, is illustrated in Fig. 2.15(d). It is observed that the effect of salt precipitation on the mass of the stored CO_2 and the heat extraction parameter is negligible –there is about a 3% difference between the highest and the lowest brine salinity cases. Zhang et al. [83] also observed that the effect of salt precipitation on heat extraction becomes considerable only when the precipitation reaches the vicinity of the production well and impairs the porosity near it. Therefore, it can be concluded that salt precipitation mainly affects the reservoir's injectivity and the required pumping power.

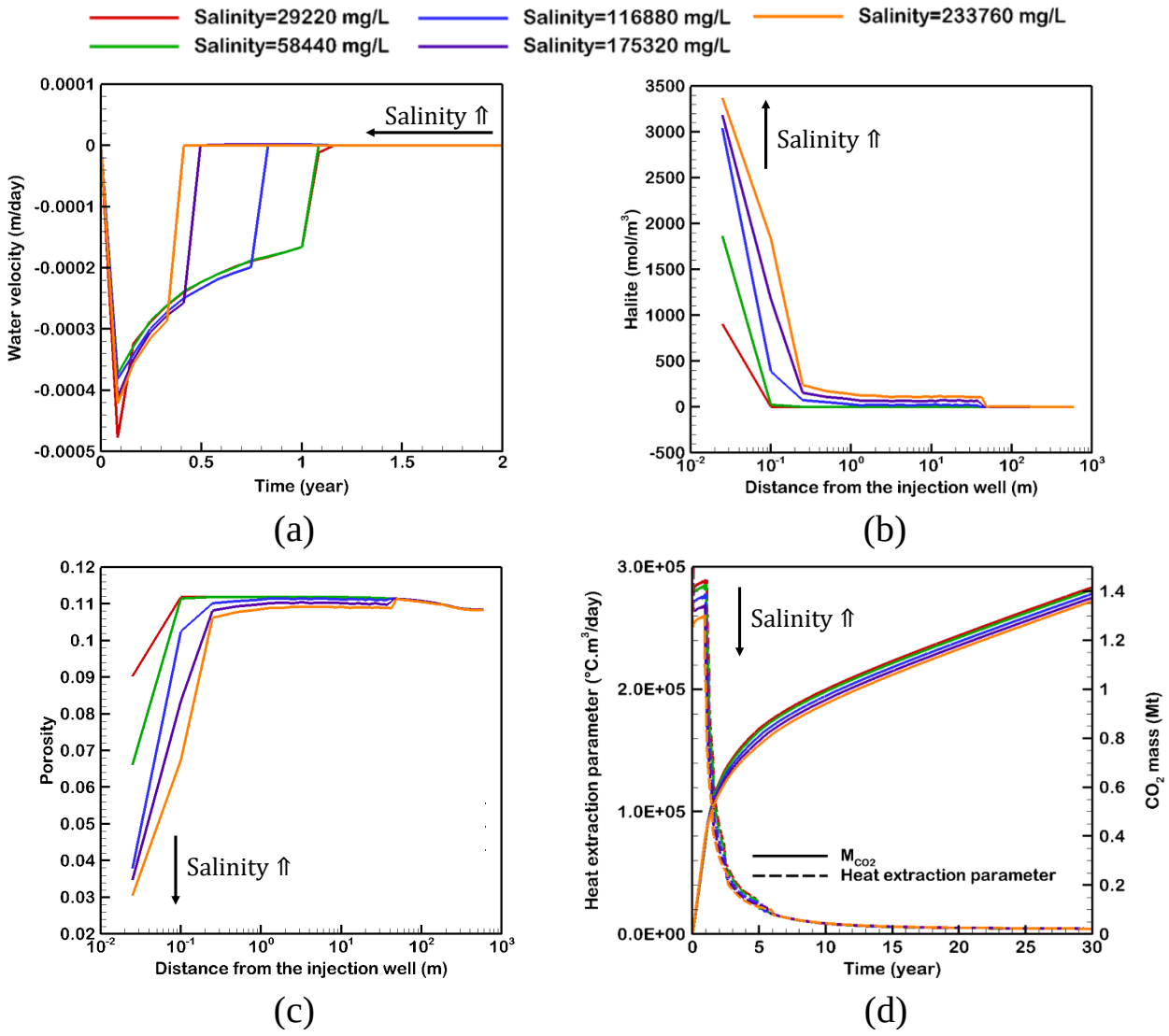

Figure 2.15: 1D results of the brine salinity effects on: (a) backflow at the injection well at different time steps from the onset of injection, (b) salt precipitation inside the reservoir after 30 years, (c) porosity inside the reservoir after 30 years, and (d) heat extraction parameter and CO_2 mass inside the reservoir in million tonnes at different times.

Correlations between backflow integrals and salt precipitations at the injection well are shown in Fig. 2.16. For each initial salinity, the BEP and the precipitated salt follow a semi-linear correlation. This means that regardless of the varying parameters, it is the capillary-driven backflow that causes the salt precipitation. In other words, any changes in parameters, such as the injection or the reservoir temperature, injection rate, or reservoir porosity, affect the amount of salt precipitation because they affect the backflow profile at the injection well. Therefore, it is concluded that salt precipitation is self-enhanced by the

capillary effect. It is obvious that there are other precipitation mechanisms that play a role in salt build-up. To further support that the capillary backflow is the preponderant factor, 5 simulations without the effect of the capillary were carried out. No capillary means that no backflow occurs at the injection well, *i.e.*, BEP equals zero, therefore these no-capillary simulations are represented as intercepts in Fig. 2.16. As seen for the no-capillary cases (five cases with BEP=0), precipitation only happens –with a very little amount compared to other cases– for the high salinity reservoirs. In other words, in reservoirs with low to moderate salinity values, should there be no effect of the capillary, almost no salt precipitation will happen.

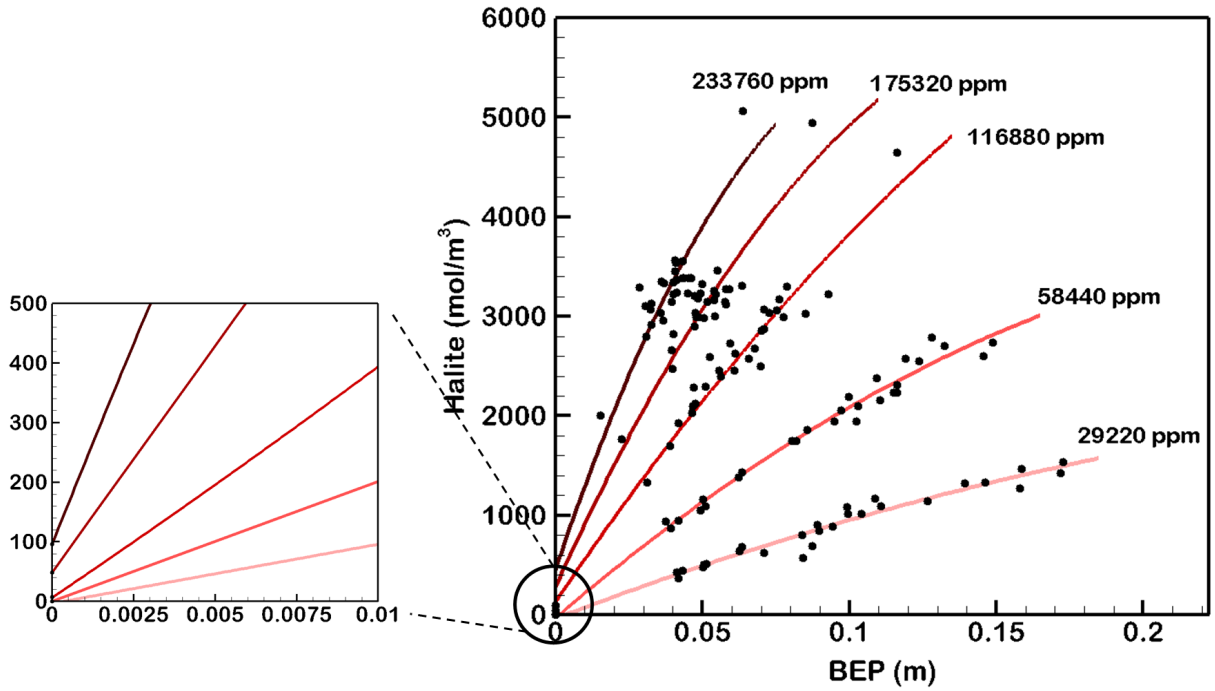

Figure 2.16: Salt precipitation at the injection well and BEP correlation for all of the 1D simulations in five different brine salinities at the injection well after 30 years of injection. The aquifer's initial salinity defines the salinity constant lines (red lines) in this figure. Also, from the onset figure, salt precipitation of the cases with very small/zero BEP can be observed, which shows that the cases with no capillary backflow (BEP= 0) experience very little/zero salt precipitation.

2.4.3 System energy and the required pumping power study

The main effect of salt precipitation is on the porosity and permeability of the reservoir. The changes in these parameters and the damage to the reservoir can be expressed as the

resistance factor parameter as Eqs. 2.4 and 2.5. Fig. 2.17 shows the effects of the governing parameters on the resistance factor. Trends of the diagrams are the same as previous results and the same interpretations are applicable here as well. However, it is seen that the resistance factor varies exponentially versus time, and is more sensitive to changes in governing parameters. Although it is seen that the resistance factor can be increased significantly due to salt precipitation, it should be noted that these amounts are only for the injection well grid cell –which had the highest salt build-up. Since the injection well grid cell has a small length, its effect on the total pressure drop of the reservoir is not significant.

To provide a more general conclusion about the imposed pressure drop resulted from salt precipitation and the required pumping power, the field-average values of the resistance factor are considered for the 1D cases (Fig. 2.18). As is seen in this figure, the average resistance factor of the reservoir is increased up to 1.26, 1.22, 1.20, 1.18, and 1.17 for the reservoirs with the salinity values of 233760, 175320, 116880, 58440, 29220 ppm, respectively. In other words, based on Eqs. 2.6 and 2.7, the pressure drop of the system is increased about 17-26% and therefore, to keep the injection flow rate constant, an average amount of 20% more pumping power is required. This means additional costs that are imposed to the CO_2 sequestration process. In addition, from the result reported in Fig. 2.18, it can be decided when it is the suitable time to do mitigating solutions against the salt precipitation, such as water flushing. For instance, if the maximum allowed amount of the increase in pressure drop and the pumping power is 15%, then the appropriate time for the water flushing would be 8 years, 13 years, 16 years, 22 years, and 23 years after the onset of the injection for the reservoirs with the salinity values of 233760, 175320, 116880, 58440, 29220 ppm, respectively.

The same as the previous section, a general diagram is provided for the resistance factor of the injection well in all simulations versus BEP (Fig. 2.19). According to this figure, the above-mentioned interpretations are applicable here as well, and the only difference is that the correlation between the BEP and the injection well resistance factor is exponential instead of semi-linear, meaning that it is more sensitive to BEP variations than the salt precipitation. In other words, a slight increase in BEP can result in a considerable increase in the required pumping power. Also, again it is observed that the effect of the increase in salinity becomes weaker in higher brine initial salinity values.

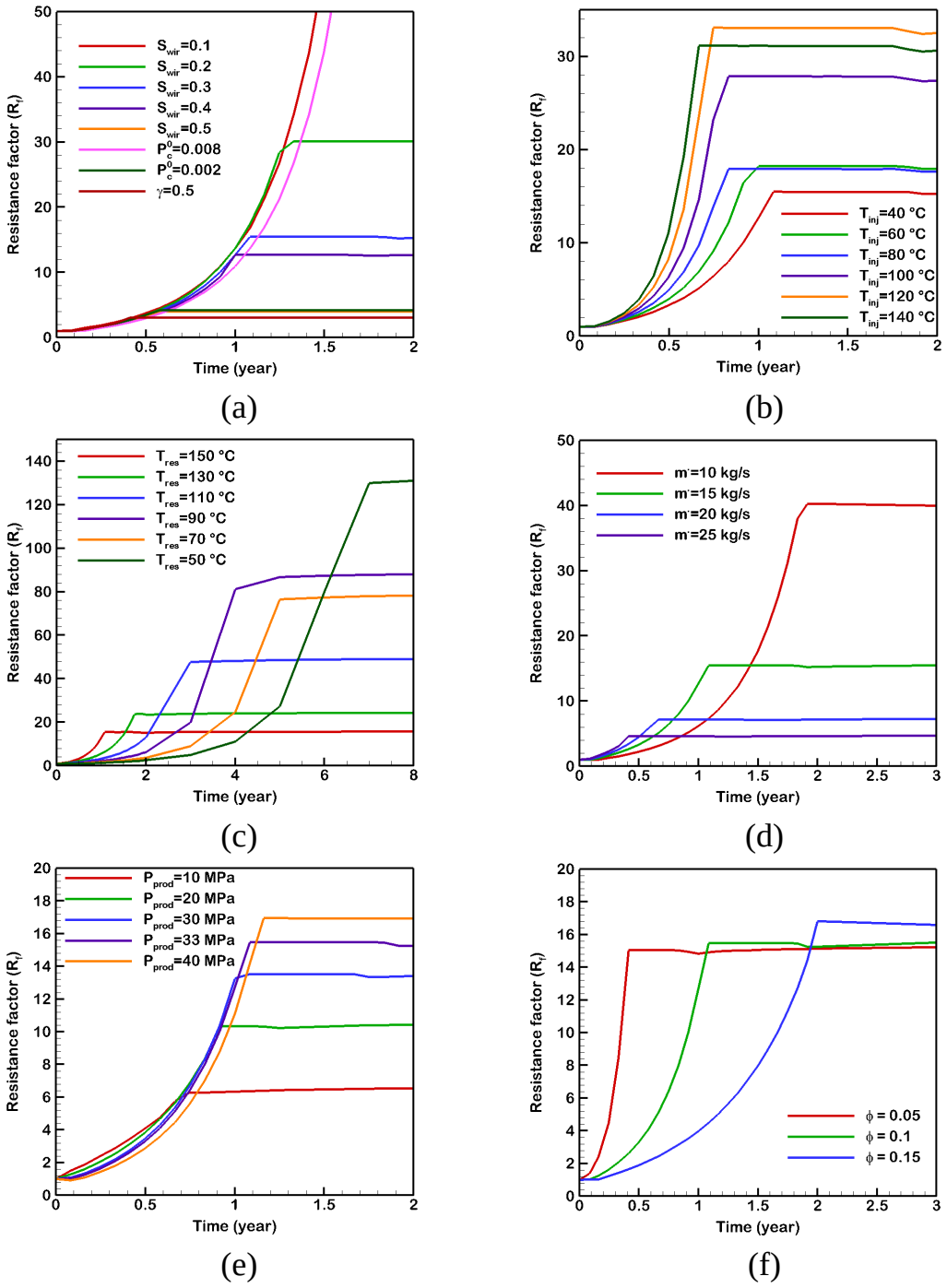

Figure 2.17: 1D results of the effects of different parameters on the injection well resistance factor at different times from the onset of injection: (a) relative permeability and capillary pressure parameters, (b) CO_2 injection temperature, (c) reservoir initial temperature, (d) injection flow rate, (e) production well BHP, and (f) reservoir initial porosity.

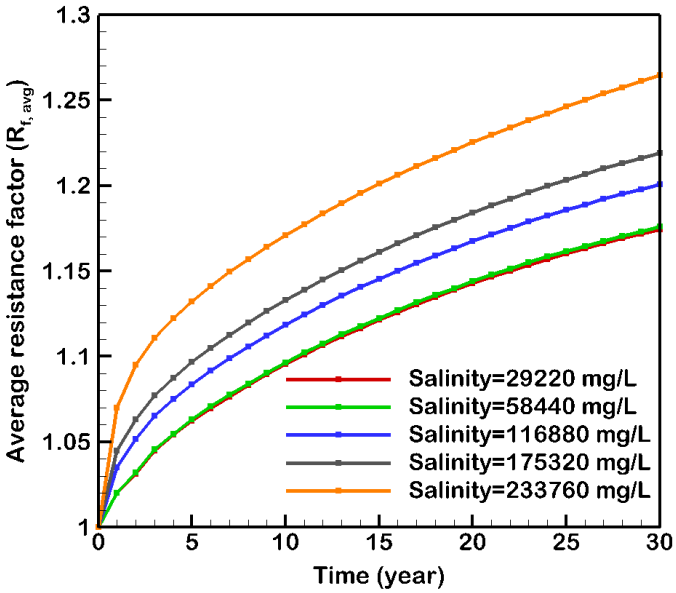

Figure 2.18: 1D results of the field-average resistance factor for various brine salinities during the simulation time.

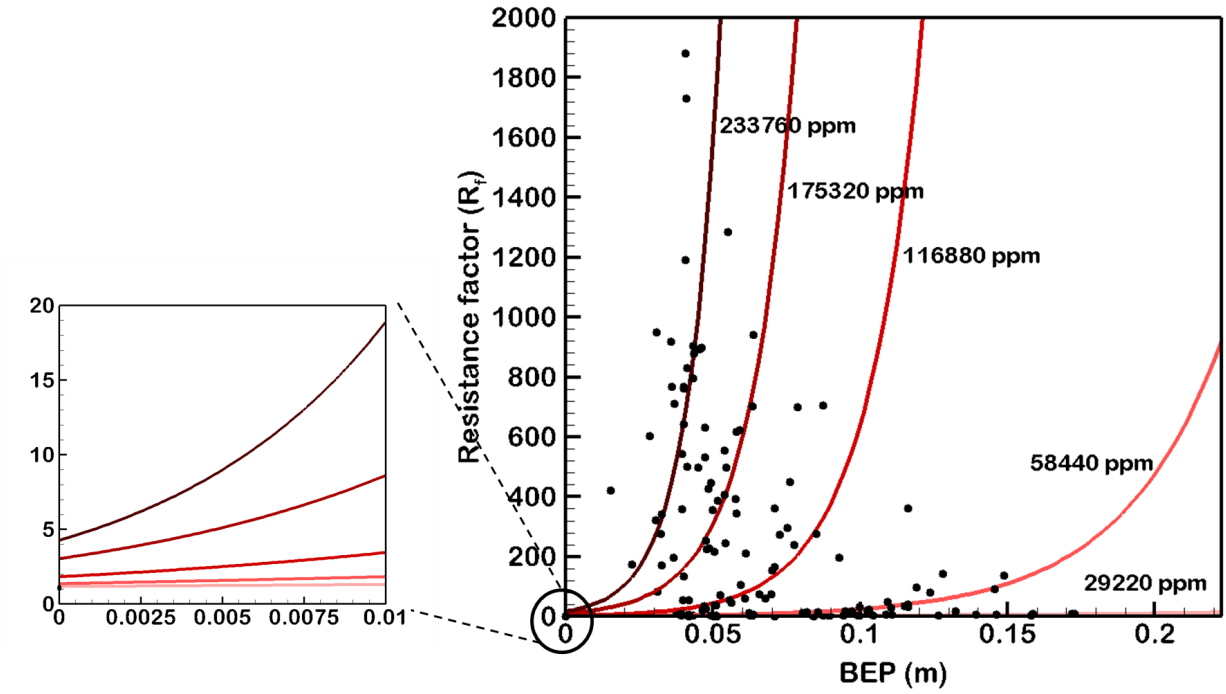

Figure 2.19: Injection well resistance factor and BEP correlation for all of the 1D simulations in five different brine salinity values. The aquifer's initial salinity defines the salinity constant lines (red lines) in this figure. Also, from the onset figure, salt precipitation in cases with very small/zero BEP is observed.

2.5 Conclusions

Minerals precipitation and dissolution, especially salt, can significantly affect the reservoir properties, such as porosity and permeability, and cause reservoir damage. This imposes additional costs regarding the required pumping power. Among the various mechanisms leading to salt precipitation, it is observed that the effect of the capillary-driven backflow is dominant. Capillary pressure affects the liquid phase saturation inside the dry-out zone and the subsequent water vaporization and the salt precipitation rate. To study the relationship between the precipitated salt, reservoir damage, and the imposed additional costs with the capillary-driven backflow, a comprehensive sensitivity analysis, covering a wide range of governing parameters, was conducted. In addition, a new backflow extent parameter (BEP) was introduced, which allowed studying the relationship between the governing parameters and the water backflow more meticulously. Finally, the total effects of the salt precipitation on the amount of the induced pressure drop and the imposed additional required pumping power were investigated. The key results of the present study can be summarised as follows:

- Among all the minerals and components that take part in the geochemical reactions, salt has the most influence on the reservoir damage and porosity reduction (about 41% reduction in the porosity of the injection well).

- Initial brine salinity has the highest influence on salt precipitation, while it was observed that it has negligible effects on the mass of the stored CO_2 and the heat extraction parameter. As the brine salinity increased from 58440 to 233760 ppm, the amount of porosity reduction at the injection well, increased from 19.14% to 72.03%. Also, the field-average reservoir porosity was reduced about 2.26% and 2.6% in these two cases, respectively. In addition, at higher values of salinity, the effect of the increase in this parameter reduces, meaning that there could be a critical salinity ($\sim$ 170000 ppm for our simulations), at which the maximum salt is precipitated and no further precipitation can happen.

- Based on the results of the cases with no capillary effect, it is concluded that the main mechanism contributing to salt precipitation is the capillary-driven backflow. It is observed that various governing parameters can affect salt precipitation because they affect the water backflow profile and its extent and magnitude. Therefore, a backflow extent parameter (BEP) is defined and it is observed that it has a semi-linear and an exponential correlation with the amounts of the precipitated salt and the resistance factor at the injection well, respectively.

- Due to salt precipitation, porosity and permeability of the reservoir change. As a result, the pressure drop is affected inside the reservoir. Based on the results, the field-average resistance factor increased up to 1.26, 1.22, 1.20, 1.18, and 1.17 for the reservoirs with salinity values of 233760, 175320, 116880, 58440, and 29220 ppm, respectively. Therefore, to keep the injection rate constant, an average of 20% more pumping power is required.

Acknowledgement

The authors acknowledge the University of Manchester President's Doctoral Scholar (PDS) award to Amir Mohammad Norouzi that made this research possible. In addition, Kue-Young Kim was supported by the Basic Research Project of the Korea Institute of Geoscience and Mineral Resources (KIGAM).

Nomenclature

A	Cross-sectional area, [m^2]
A_k	Symbol of the k-th species, [-]
$\hat{A}_\beta$	Reactive surface area, [$m^2.m^{-3}$]
a_k	Activity of component k, [$mol.kg^{-1}$]
BEP	Backflow extent parameter, [m]
c	Heat capacity, [$J.kg^{-1}.°C^{-1}$]
c_i	Mass fraction of component i, [-]
c_ϕ	Rock compressibility, [kPa^{-1}]
D	Depth from the base level, [m]
F_{iw}	Changes of component i by diffusion, [$kg.m^{-3}.s^{-1}$)]
f_i	Fugacity of component i, [MPa]
g	Gravitational acceleration, [$m.s^{-2}$]
h	Enthalpy, [$J.kg^{-1}$]
H	Henry's constant, [MPa]
K	Rock thermal conductivity, [$W.m^{-1}.°C^{-1}$]
k	Permeability, [md]
k_r	Relative permeability, [-]
K_{eq}	Reaction chemical equilibrium constant, [-]
k_β	Reaction rate constant, [$mol.m^{-2}.s^{-1}$)]
L	Length, [m]
$\dot{m}$	Mass flow rate, [$kg.s^{-1}$]
n	Number of components, [-]

N_β	Moles of mineral β, [mol.m^{-3}]
P	Pressure, [Pa]
P_{cap}	Capillary pressure, [Pa]
Q	Volume flux, [m^3.s^{-1}]
q	Phase flux, [m.s^{-1}]
Q_{E}	Energy source, [J.m^{-3}.s^{-1}]
Q_α	Reaction active product, [-]
Q_{M}	Mass source, [kg.m^{-3}.s^{-1})]
q_{i}	Injection and production of component i, [kg.m^{-3}.s^{-1}]
R	Number of reactions, [-]
R_{iw}	Changes of component i by chemical reactions, [kg.m^{-3}.s^{-1}]
R_{f}	Resistance factor, [-]
$R_{\text{f,exp}}$	Resistance factor exponent, [-]
S	Saturation, [-]
$\hat{S}$	Brine salinity, [mg.L^{-1}, ppm]
T	Temperature, [°C]
t	Time, [year, s]
U	Internal energy, [J.kg^{-1}]
w_{pump}	Pumping power, [W]
y	Mole fraction, [-]

Greek letters

γ	Capillary force parameter, [-]
μ	Dynamic viscosity, [Pa s]
ν	Stoichiometric coefficient, [-]
ϕ	Porosity, [-]
ρ	Density, [kg.m^{-3}]
ζ	Chemical equilibrium constant, [°C^{-i}, $i = 0, \dots 4$]

Subscripts

aq	Aqueous
g	Gas
inj	Injection
m	Solid matrix
mn	Mineral
prod	Production
res	Reservoir
w	Water

Chapter 3

Analytical solution for predicting salt precipitation during CO_2 injection into saline aquifers in presence of capillary pressure

This chapter is a modified version of the paper published in '*Water Resources Research*'.

Authors: **A. M. Norouzi**, V. Niasar, J. Gluyas, M. Babaei. Analytical solution for predicting salt precipitation during CO_2 injection into saline aquifers in presence of capillary pressure. *Water Resources Research*, vol.58, no.6, p.e2022WR032612, 2022.

3.1 Abstract

Salt precipitation within the pores of the reservoir is an important phenomenon occurring during CO_2 injection into saline aquifers. The phenomenon results in permeability reduction and injectivity impairment. Salt precipitation mainly happens because of water vaporization inside the CO_2-saturated (dry-out) region. For water-wet systems, the capillary pressure acts towards the lower water saturation regions in the reservoir, thereby displacing a film of brine backwards to the dry-out region. This results in more precipitation. Overlooking this phenomenon, referred to as capillary-driven backflow, results in over-estimations of injectivity in the dried region. Here, I have developed an analytical solution based on fractional flow theory and shock waves for CO_2-brine systems considering the effect of capillary pressure. The validity of the solution is verified by comparing the outputs of our model with those of numerical results from a commercial numerical simulator for a hypothetical reservoir. An equation is derived to calculate the distance at which capillary pressure is most influential, and also the injectivity impairment at the injection well due to salt precipitation was reasonably accurately estimated. The results emphasise that the effects of capillary pressure should not be ignored.

3.2 Introduction

Reducing CO_2 emissions into the atmosphere has become a focal point to reduce future temperature rises in our planet. As a mitigating measure, developing subsurface CO_2 injection into saline aquifers can be a partial solution for the reduction of net greenhouse gas emissions worldwide. However, when injecting supercritical CO_2 ($scCO_2$), salt precipitates because of water vaporization. The outcome is impairment of the reservoir's permeability and injectivity. This should be considered in the simulation of systems containing CO_2-brine displacement [40, 84].

Various studies, based on both simulation and field data, observed salt precipitation and its destructive effects on the reservoir. For instance, Baumann et al. [63] reported a salt saturation of about 1.4% within the dry-out region with the maximum saturation up to 14.1%, Muller et al. [66] observed solid salt precipitation of about 16% with a subsequent permeability reduction of about 40%, Bacci et al. [68] detected a 3-5% porosity reduction and 13-75% permeability reduction, Kim et al. [72] reported 20% porosity reduction due to salt precipitation, Tang et al. [95] mentioned a 14.6% and 83.3% reduction in porosity and permeability of their model, respectively, and Lima et al. [96] reported 21.98% permeability

reduction, in their studies.

When CO_2 displaces brine in water-wet systems, a capillary pressure is formed because of the water saturation gradient away from the injection. Capillary pressure acts against the flow and moves brine backwards to the CO_2-saturated region (dry-out region) through water films. Here, because of small water vapour pressure, water evaporates and solid salt precipitates. Since capillary-driven backflow is a continuous phenomenon, it constantly adds to the amount of the precipitated salt inside the dry-out region. Therefore, I hypothesise that overlooking the effect of capillary pressure will result in a considerable underestimation of the amount of the precipitated salt. However, implementing capillary pressure is complicated because of the various contact angles and surface tensions that different minerals have, leading to different irreducible water saturation. Therefore, for the sake of simplicity, these effects are not usually considered in models.

Miri and Hellevang [40] described capillary-driven backflow as one of the main salt precipitation mechanisms in their study. In another work, Parvin et al. [74] provided a formulation accounting for capillary backflow and salt self-enhancing, showing that capillary pressure can massively increase the amount of the precipitated salt. Similarly, Pruess and Müller [77] observed the effect of capillary backflow and noted that the inclusion of capillary pressure increased the amount of the precipitation by a factor of 1.1. Roels et al. [81] also observed that the reservoir's injectivity was greatly reduced because of salt precipitation through capillary pressure in their core-flooding model. In another work that included capillary pressure, Kim et al. [93] also observed a region of localised salt precipitation inside the dry-out region with considerably high salt saturation, deteriorating well injectivity. In a more recent study, Norouzi et al. [38] performed a sensitivity analysis on parameters that affect capillary-driven backflow and its subsequent salt precipitation. They also observed a considerable increase in the amount of the precipitated salt at the near injection area for the case with capillary effect.

Accordingly, most studies that considered the effect of capillary pressure are numerical ones. Nonetheless, numerical results are highly case dependant and costly both in terms of time and computational costs; while analytical solutions can efficiently model CO_2-brine systems and salt precipitation without computational costs. Most analytical works in this field only considered simple CO_2-water displacement systems and gravity currents with no mass transfer and salt precipitation. For instance, Hesse et al. [97] developed the Method of Characteristics to study the migration of CO_2 plume after the end of CO_2 injection, or using Darcy's equation as well as a modified Buckley–Leverett theory, McMillan et al. [98] de-

veloped a model to determine CO_2 injectivity inside a homogeneous reservoir with constant pressure at the boundaries based on phase mobilities and the saturation fronts propagation speed. There are few analytical studies available trying to mathematically formulate the saturation distribution inside the reservoir considering mass transfer and minerals/salt precipitation. A review of these analytical works is in Table 3.1.

Table 3.1: Analytical investigations of CO_2-brine systems considering mass transfer and salt precipitation.

Study	Methodology
Nordbotten and Celia [99]	Developed a similarity solution to find the locations of the interfaces between different saturation regions. Their solution is also able to capture CO_2 density-driven flow.
Noh et al. [100]	Investigated minerals precipitation inside the reservoir through fractional flow theory and shock waves definition for cases that CO_2 displaced water and water displaced CO_2. Based on a graphical solution (drawing tangent lines), they provided equations to calculate the retardation factors and the I and J coordinates of the tangent lines.
Zuluaga and Lake [101]	Using a constant capillary diffusion coefficient and numerical integration, they proposed a travelling-wave solution to analytically solve water vaporization for dry gas (methane) injection into immobile water.
Pruess [102]	Used mass balance for the dissolved water into the CO_2 stream and the saturation profiles from the Buckley-Leverett fractional flow theory and proposed an equation that related the average gas saturation ($\bar{S}_g$) inside the dry-out region to the amount of the precipitated salt, which they considered to be constant in the dry-out region.
Zeidouni et al. [103]	The similar fractional flow approach is used to formulate gas saturation inside a cylindrical reservoir. They also provided equations to estimate salt precipitation inside the dry-out region. However, they suggested a uniform and constant precipitation inside the drying region.
Mathias et al. [104]	Extended an analytical solution to estimate the pressure buildup within the injection well area, considering water evaporation, CO_2 dissolution into the brine, and salt precipitation. However, they considered negligible capillary pressure in their work.
Kelly and Mathias [105]	Presented a similarity solution relating capillary pressure and salt precipitation around the injection well. Their results revealed that the amount of the precipitated salt is highly controlled by the capillary strength and that the presence of capillary pressure led to a higher amount of precipitation near the injection area.

Based on the provided literature review, it is concluded that there is no analytical solution that accounts for the "capillary effects on the propagation speed of saturation shocks and on the salt precipitation" in the dry-out region. Moreover, as observed from numerical and experimental investigations, capillary-driven backflow significantly increases the amount of the precipitated salt at near injection well area [84, 63, 66, 68, 72, 95, 96, 38, 106]. Pruess [102] considered no capillary pressure, and based on the similarity solution (defined later in this work) derived values for constant solid salt saturation in the dry-out region. Nonetheless, in Figure 7 of another work by Pruess and Spycher [107], it is observed that salt saturation increases by getting closer to the injection well, and therefore it is not constant. As a result, the maximum amount of precipitated salt in the dry-out region happens close to the injection area and requires a model to be estimated. In the present study, I have used fractional flow theory and provided equations to calculate gas saturation distribution and shock waves' locations in the presence of capillary pressure effect. In addition, two methods are proposed to calculate salt precipitation inside the drying region accounting for capillary-driven backflow effects. Finally, the validity of the results is confirmed by a comparison provided with a numerical compositional reservoir simulator CMG-GEM.

3.3 Reservoir model interpretation

The reservoir considered for the analytical and numerical investigations in the present study is based on [103, 107]. It is a sector of a cylindrical reservoir at the depth of 1200 m, with a thickness of 100 m, and an infinite length (Fig. 3.1). For the numerical simulations, a structured grid with 100 blocks along the reservoir radius with a grid spacing of dx=0.3 to 115 m is generated. To implement the infinite reservoir length in the numerical case, the pore volume modification method is used, through which the volume of the last grid block is enlarged representing an infinite cell. The reservoir is considered infinite to keep its initial conditions (*i.e.*, T_0=45 °C and P_0=12 MPa) constant during the scCO$_2$ injection period. CO$_2$ is injected uniformly in the supercritical phase over a period of 10 years (3.15×10^8 s) with the rate of 100 kg/s (≈ 0.15 m^3/s considering the scCO$_2$ density of about 643.1 kg/m^3 based on [103]) and the temperature of T_{inj}=45 °C. In addition, the reservoir is representative of a high-salinity sandstone reservoir with a permeability of 100 mD, porosity of 12%, and salinity of 15% by weight ($\approx$ 150000 ppm).

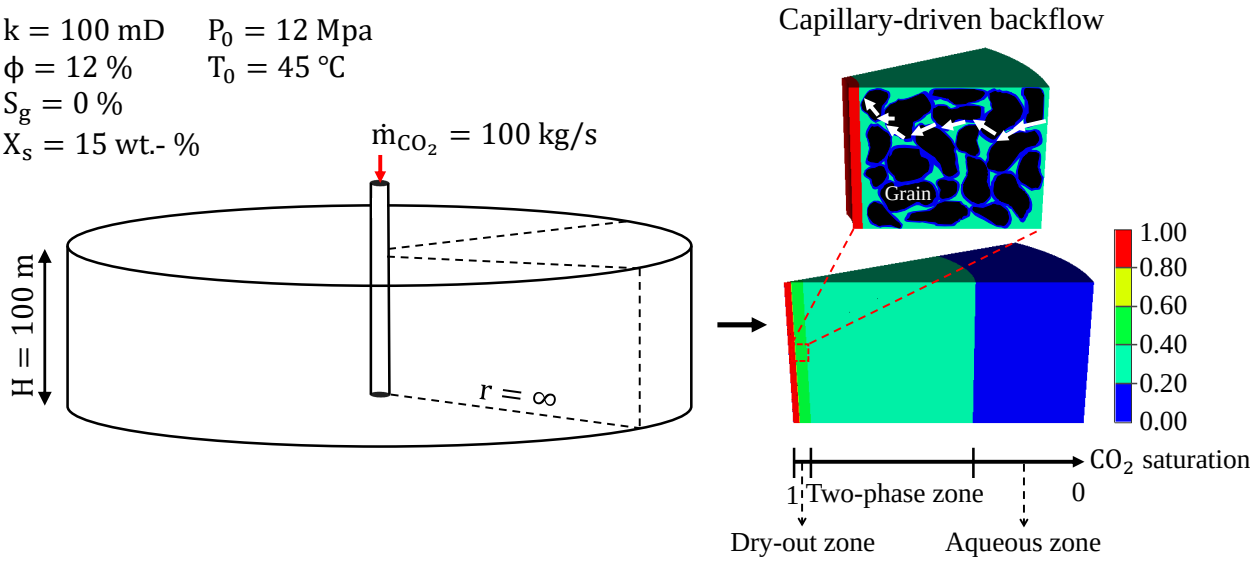

Figure 3.1: Schematic of the problem and reservoir specifications. A 1D radial reservoir with an infinite radius and a thickness of 100 m is considered for this study. At the bottom right, a sector of the reservoir on the left is shown with dry-out, two-phase and single aqueous phase zones. A microscopic domain of this sector is zoomed out in the top right to highlight the capillary-driven backflow process through the water films.

The reservoir is initially filled by brine, representing a case where CO_2 is displacing water (Fig. 3.1). Here, water is the wetting phase ($P_{\text{cap}} = P_{CO_2} - P_{\text{water}}$) and is pushed toward the two-phase region, consequently, there will be a gradient in water saturation between the dry-out and two-phase zones. Therefore a capillary force acting against the pressure gradient, resulted from the injection pressure, will form. This results in brine backflow toward the dry-out zone. Inside the dry-out zone, because of low water vapour pressure, brine evaporates and subsequent salt precipitation occurs. The fact that brine backflow contributes to salt precipitation will be elaborated in the next sections. For gas/liquid relative permeabilities and the capillary pressure between CO_2 and brine, Corey [86] and modified van Genuchten [90] models are used, respectively. Porosity is directly influenced by fluid-rock properties, and any variations in porosity due to precipitation or dissolution can impact the relative permeability and capillary pressure curves. However, in the current analytical work, the effects of porosity change on these curves are disregarded to keep the analysis simple. Taking the porosity change into account would lead to a solution that is not fully analytical, necessitating the resolution of equations at each time step.

$$k_{\text{ra}} = \sqrt{S^*}(1-(1-[S^*]^{1/\gamma})^{\gamma})^2, \text{ where: } \gamma = 0.457 \text{ and } S^* = \frac{S_{\text{a}} - S_{\text{wir}}}{1 - S_{\text{wir}}} \tag{3.1a}$$

$$k_{\text{rg}} = (1-\hat{S})^2(1-\hat{S}^2), \text{ where: } \hat{S} = \frac{S_{\text{a}} - S_{\text{wir}}}{1 - S_{\text{wir}} - S_{\text{gc}}} \tag{3.1b}$$

$$P_{\text{cap}} = P^0_{\text{cap}}(\hat{S}^{-1/\gamma} - 1)^{1-\gamma}, \text{ where: } P^0_{\text{cap}} = 0.004 \text{ MPa} \tag{3.1c}$$

Further details of the problem and the reservoir are provided in Table 3.2, which are based on a previous work by Zeidouni et al. [103].

Table 3.2: Reservoir model and rock-fluid properties [103].

Property	**Symbol**	**Value**
Salinity [mole fraction, ppm]	X_{s}	0.0516, 150000
Reservoir temperature [°C]	T_0	45
Reservoir pressure [MPa]	P_0	12
Porosity [%]	ϕ	12
Injection rate [kg/s]	$\dot{m}$	100
Reservoir thickness [m]	H	100
Gaseous phase viscosity [Pa.s]	μ_{g}	0.0496×10^{-3}
Aqueous phase viscosity [Pa.s]	μ_{a}	0.8260×10^{-3}
Irreducible water saturation	S_{wir}	0.3
Critical gaseous phase saturation	S_{gc}	0.05
Equilibrium mole fraction of CO_2 in gaseous phase	$\omega_{CO_2,\text{g}}$	0.9953
Equilibrium mole fraction of CO_2 in aqueous phase	$\omega_{CO_2,\text{a}}$	0.0110
Initial brine saturation	$S_{\text{a},0}$	1
Brine density [kmol/m^3]	$\rho_{\text{a},0}$	54.8527
CO_2 density [kmol/m^3]	ρ_{inj}	14.6126
Equilibrium aqueous phase density [kmol/m^3]	ρ_{a}	54.3046
Equilibrium gaseous phase density [kmol/m^3]	ρ_{g}	14.6846
NaCl molecular weight [kg/kmol]	-	58.43
NaCl density [kmol/m^3]	ρ_{s}	37.05
Injection well radius [m]	r_{w}	0
Capillary force parameter	γ	0.457

3.4 Analytical solution

3.4.1 Shock waves specifications

In the case where $scCO_2$ is displacing water, if salt is considered in the solution, there exist three phases (solid, gas, and liquid) and three components (salt, CO_2, and water). In the present study, the effects of geochemical reactions are neglected, but it is still possible to capture and calculate the amount of the precipitated salt. This is because salt precipitation mainly happens because of the vaporization of water from the connate brine and its behaviour is closely linked with gas and liquid saturations inside the domain. Finding a general analytical solution for a three-phase mixture is complex, however, since salt is an immobile phase and its precipitation is correlated to brine saturation, it is possible to consider salt as a dependant phase and reduce the problem to a semi-two-phase case.

To determine the flow behaviour and phase saturations, the initial equation to be solved is the conservation equation inside the reservoir:

$$\phi A \frac{\partial S_{\mathrm{g}}}{\partial t} + \frac{\partial q_{\mathrm{g}}}{\partial x} = 0 \tag{3.2}$$

Based on the fractional flow theory, Buckley and Leverett [108], reformed Eq. 3.2 as a function of gas fractional flow as below, in which $\frac{\partial f_{\mathrm{g}}}{\partial x} = \frac{df_{\mathrm{g}}}{dS_{\mathrm{g}}}\frac{\partial S_{\mathrm{g}}}{\partial x}$:

$$\frac{\partial S_{\mathrm{g}}}{\partial t} + \frac{q_{\mathrm{inj}}}{\phi A}\frac{\partial f_{\mathrm{g}}}{\partial x} = 0 \tag{3.3}$$

The intermediate values of brine saturation that have the maximum velocity will overtake the lower saturation values, resulting in the formation of saturation discontinuity and shock waves that propagate with a specified velocity.

As CO_2 is injected into the aquifer, two shock waves appear including a leading (flooding) wave and a trailing (drying) wave. These shock waves divide the whole domain into three distinct regions, *i.e.*, a dried region, a two-phase region, and a wet (water-saturated) region.

The solution to Eq. 3.3 was previously reported by Buckley and Leverett [108] as follows:

$$\left(\frac{x}{t}\right)_{S_{\mathrm{g}}} = \frac{q_{\mathrm{inj}}}{\phi A}\left(\frac{df_{\mathrm{g}}}{dS_{\mathrm{g}}}\right)_{S_{\mathrm{g}}} \tag{3.4}$$

According to Eq. 3.4, at any given time from the onset of $scCO_2$ injection, positions of different water saturation lines can be plotted only by knowing the slope of the f_{g}-S_{g} curve for a specific gas saturation. When plotting f_{g} versus S_{g} (Fig. 3.2a), two points exist that

represent the leading and the trailing shocks. Therefore, it will be possible to determine the gas saturation at the shocks as well as their propagation speed by locating these points. To do so, through a graphical approach, two tangent lines are drawn from two certain points (I for the initial point and J for the injection point) to the curve. The tangent point, $(S_{\mathrm{g}}^{\mathrm{b}}, f_{\mathrm{g}}^{\mathrm{b}})$ and $(S_{\mathrm{g}}^{\mathrm{c}}, f_{\mathrm{g}}^{\mathrm{c}})$, specify the leading and the trailing shocks, respectively.

For a radial case, Zeidouni et al. [103] reported the wave similarity variable for no capillary case by using the Buckley-Leverett method and Darcy equation to solve the 1D radial continuity equation accounting for the vaporization of water and dissolution of CO_2 as below:

$$\eta_{\text{no cap}} = \left(\frac{r^2 - r_{\mathrm{w}}^2}{t}\right)_{\mathrm{G_{CO_2}}} = \frac{q_{\mathrm{inj}}}{\pi H \phi}\left(q_{\mathrm{D}}\frac{df_{\mathrm{g}}}{dS_{\mathrm{g}}}\right)_{\mathrm{G_{CO_2}}} \tag{3.5}$$

where r_{w} is the injection well radius, $q_{\mathrm{D}} = q_{\mathrm{t}}/q_{\mathrm{inj}}$, q_{t} is the total local flow rate, and $G_{\mathrm{CO_2}}$ is the normalised CO_2 global concentration that is a function of S_{g} ($G_{\mathrm{CO_2}} = \rho_{\mathrm{aD}}\omega_{\mathrm{CO_2},a}S_a + \rho_{\mathrm{gD}}\omega_{\mathrm{CO_2},g}S_g$, where as temperature and pressure are constant and fluids are at equilibrium everywhere, $\omega_{\mathrm{CO_2},g}$ and $\omega_{\mathrm{CO_2},a}$ are constant, and $\rho_{\mathrm{aD}} = \rho_{\mathrm{a}}/\rho_{\mathrm{inj}}$, $\rho_{\mathrm{gD}} = \rho_{\mathrm{g}}/\rho_{\mathrm{inj}}$). In Eq.3.5, q_{D} at points b (location of leading shock) and c (location of trailing shock) in Fig. 3.2a is the same [109, 103]. Therefore, only one q_{D} needs to be calculated to determine shocks' similarity variables, in which $\Delta\rho_{\mathrm{D}} = \rho_{\mathrm{aD}} - \rho_{\mathrm{gD}}$, and $\Delta\omega_{\mathrm{CO_2}} = \omega_{\mathrm{CO_2,a}} - \omega_{\mathrm{CO_2,g}}$.

$$q_{\mathrm{D}} = \frac{(\rho_{\mathrm{aD}}\omega_{\mathrm{CO_2,a}} - \rho_{\mathrm{gD}}\omega_{\mathrm{CO_2,g}})S_{\mathrm{g}} - \Delta\rho_{\mathrm{D}}S_{\mathrm{g}} + \omega_{\mathrm{Brine,a}}\rho_{\mathrm{aD}}}{(\rho_{\mathrm{aD}}\omega_{\mathrm{CO_2,a}} - \rho_{\mathrm{gD}}\omega_{\mathrm{CO_2,g}})f_{\mathrm{g}} - \Delta\rho_{\mathrm{D}}f_{\mathrm{g}} + \omega_{\mathrm{Brine,a}}\rho_{\mathrm{aD}} + \rho_{\mathrm{aD}}\rho_{\mathrm{gD}}\Delta\omega_{\mathrm{CO_2}}(S_{\mathrm{g}} - f_{\mathrm{g}})} \tag{3.6}$$

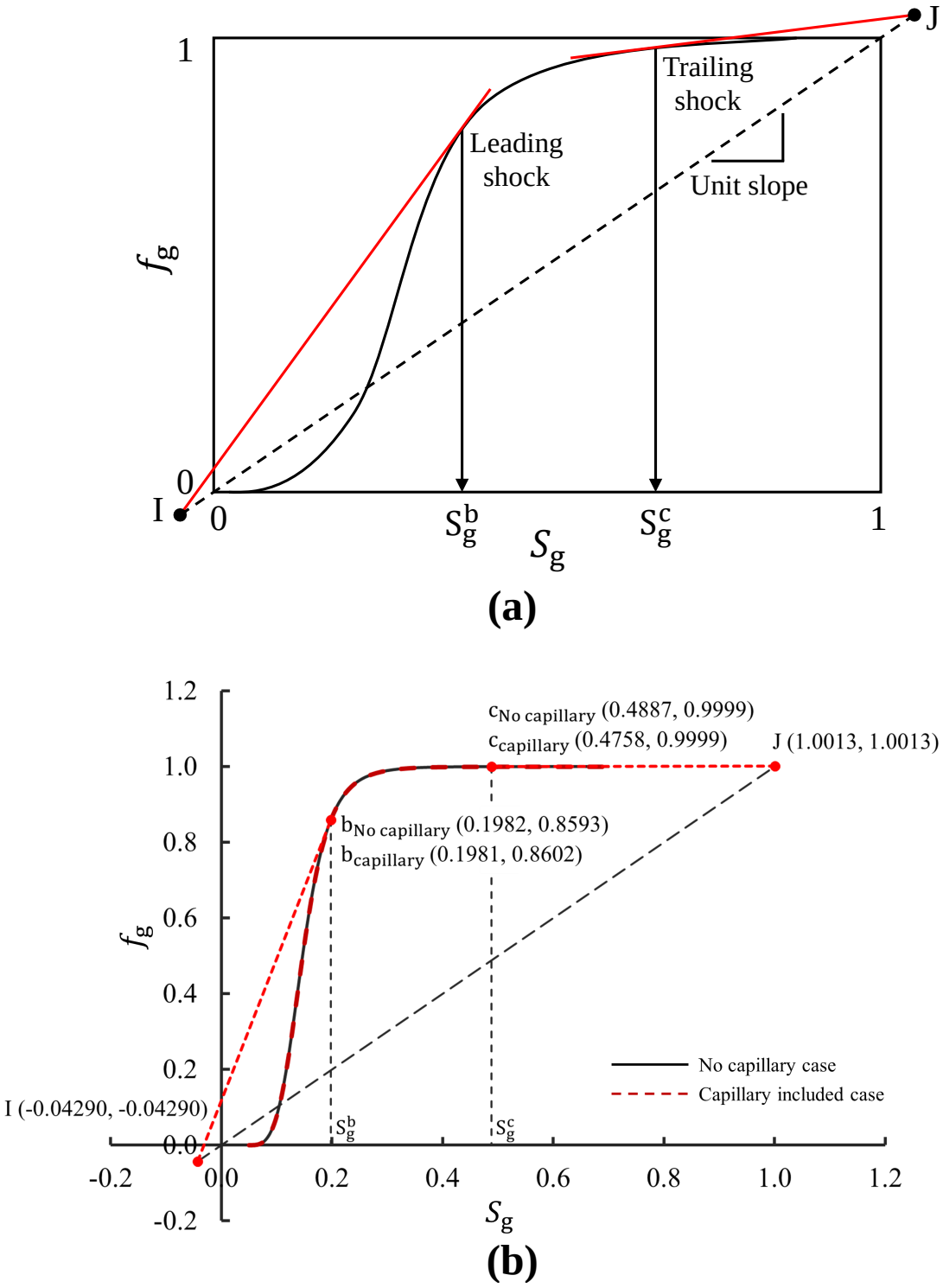

Figure 3.2: (a) Schematic of the graphical method for determination of saturation shock waves, and (b) trailing and leading shocks specifications for capillary ($t = 10$ years) and no capillary cases based on Buckley–Leverett method. S_g^b shows the saturation upstream of the leading shock and S_g^c shows the saturation downstream of the drying shock. Also, I and J represent the initial aquifer condition and the injection condition, respectively.

To locate points b and c for the shock waves in a radial case, points I and J based on components mole fraction (ω) are defined as below and shown in Fig. 3.2b.

$$(S_{\mathrm{g}}^{\mathrm{I}}, f_{\mathrm{g}}^{\mathrm{I}}) = \left(\frac{\rho_{\mathrm{aD}}\omega_{\mathrm{CO_2,a}}}{\rho_{\mathrm{aD}}\omega_{\mathrm{CO_2,a}} - \rho_{\mathrm{gD}}\omega_{\mathrm{CO_2,g}}}, \frac{\rho_{\mathrm{aD}}\omega_{\mathrm{CO_2,a}}}{\rho_{\mathrm{aD}}\omega_{\mathrm{CO_2,a}} - \rho_{\mathrm{gD}}\omega_{\mathrm{CO_2,g}}} \right) \tag{3.7a}$$

$$(S_{\mathrm{g}}^{\mathrm{J}}, f_{\mathrm{g}}^{\mathrm{J}}) = \left(\frac{\rho_{\mathrm{aD}}\omega_{\mathrm{Brine,a}}}{\rho_{\mathrm{aD}}\omega_{\mathrm{Brine,a}} - \rho_{\mathrm{gD}}\omega_{\mathrm{Water,g}}}, \frac{\rho_{\mathrm{aD}}\omega_{\mathrm{Brine,a}}}{\rho_{\mathrm{aD}}\omega_{\mathrm{Brine,a}} - \rho_{\mathrm{gD}}\omega_{\mathrm{Water,g}}} \right) \tag{3.7b}$$

In Eqs 3.4 and 3.5, capillary pressure is ignored in the definition of the gas phase fractional flow ($f_{\mathrm{g}} = q_{\mathrm{g}}/q_{\mathrm{t}}$). Based on Darcy's law, for incompressible fluids, this parameter is defined as:

$$f_{\mathrm{g}} = \frac{1}{1 + (k_{\mathrm{ra}}/k_{\mathrm{rg}})(\mu_{\mathrm{g}}/\mu_{\mathrm{a}})} \tag{3.8}$$

However, based on previous studies such as [105, 38] capillary pressure is important to be considered as it affects salt precipitation. Since capillary moves brine backwards, it is anticipated that adding a capillary term to Eq. 3.8 will add a negative term on the right side of this equation, which was previously overlooked. The gas fractional flow equation can be written as the following equation, (the derivation procedure - using a similar approach as [110, 111] - is fully described in Appendix D1):

$$f_{\mathrm{g}} = \frac{q_{\mathrm{g}}}{q_{\mathrm{t}}} = \frac{\lambda_{\mathrm{g}}}{\lambda_{\mathrm{t}}} - \frac{kA\lambda_{\mathrm{g}}\lambda_{\mathrm{w}}}{q_{\mathrm{t}}\lambda_{\mathrm{t}}} \frac{\partial P_{\mathrm{cap}}}{\partial r} \tag{3.9}$$

In the above equation, $\lambda_{\mathrm{t}} = \lambda_{\mathrm{g}} + \lambda_{\mathrm{a}}$, $\lambda_{\mathrm{g}} = k_{\mathrm{rg}}/\mu_{\mathrm{g}}$, $\lambda_{\mathrm{a}} = k_{\mathrm{ra}}/\mu_{\mathrm{a}}$, and permeability ($k$) has a unit of m^2. Inserting Eq. 3.9 into Eq. 3.5 and also, considering $\frac{\partial P_{\mathrm{cap}}}{\partial r} = \frac{dP_{\mathrm{cap}}}{dS_{\mathrm{g}}} \frac{\partial S_{\mathrm{g}}}{\partial r}$, $q_{\mathrm{D}} = q_{\mathrm{t}}/q_{\mathrm{inj}}$, $A = 2\pi r H$, and $r_{\mathrm{w}} = 0$ m, the solution for the shocks similarity variable in presence of capillary pressure (η_{cap}) is reached.

The (capillary-driven) backflow similarity variable is defined as the difference between the similarity variables of the shocks for no-capillary and capillary cases ($\Delta\eta = \eta_{\text{no cap}} - \eta_{\mathrm{cap}}$). This value at the trailing shock can be calculated from Eq. 3.10, which results in a positive value. The complete procedure of deriving this equation, which is one of the key achievements of the present work, is described in Appendix D2.

$$\Delta\eta = \frac{2r_{\mathrm{c}}kP_{\mathrm{cap}}^{0}}{\phi} \left(\frac{\partial S_{\mathrm{g}}}{\partial r} \right)_{\mathrm{r=r_{c,t}}} \frac{d}{dS_{\mathrm{g}}} \left(\frac{\lambda_{\mathrm{a}}\lambda_{\mathrm{g}}}{\lambda_{\mathrm{a}} + \lambda_{\mathrm{g}}} \frac{d}{dS_{\mathrm{g}}} (\hat{S}^{-1/\gamma} - 1)^{1-\gamma} \right) \tag{3.10}$$

To calculate $\Delta\eta$, some considerations are required. Firstly, the term r_{c} in the equation can be calculated from the trailing shock similarity variable of the no-capillary case as:

$r_c = \sqrt{\eta t}$. Secondly, q_D is almost equal both in the capillary and no-capillary cases (based on Eq. 3.6) and is defined as $q_D = q_t/q_{inj}$. Thirdly, based on both analytical and numerical results for gas saturation versus distance for the cases with and without capillary effect, it is observed that in these two cases, the slope of the S_g-r diagram is the same. The only difference is that the whole curve is slightly moved to the left (because of the negative effect of capillary on shocks' speed). As a result, the term $(\frac{\partial S_g}{\partial r})_{r=r_c,t}$ can be estimated from the analytical results of the no-capillary case. However, the analytical results report an infinite slope for the S_g-r diagram in places where shocks are located, resulting in an infinite capillary force. To overcome this issue, an estimation has been done by considering saturation values of neighbouring locations ($r_c \pm dr$) with a dr (transition length scale) similar to the numerical simulation grid size to calculate $(\frac{\partial S_g}{\partial r})_{r=r_c,t}$ instead of the trailing shock location itself.

3.4.2 Salt precipitation estimation in presence of capillary pressure

Small amounts of brine remain in the dry-out region, and because of low water vapour pressure in this area, they evaporate, resulting in salt precipitation. The velocity of the drying shock is the same as the velocity of the brine in front of it, which has the saturation of $1-S_g^c$. Also, it is assumed that all the brine in the drying zone evaporates and the gaseous phase entering the two-phase area is water saturated, as a result, for the case with constant T and P, vaporization and precipitation mainly occur in the drying region.

In this section, equations are derived to calculate salt precipitation resulted from water vaporization. For a no-capillary case, Pruess [102] and Zeidouni et al. [103] proposed similar equations to estimate solid salt saturation inside the drying region, in which X_s is the brine initial salinity in mass fraction (0.15 in the present study), $\bar{S}_g$ is the average gas saturation behind the drying front, and densities are in kg.m^{-3}.

$$S_s = (1 - \bar{S}_g)\frac{\rho_a}{\rho_s}X_s \tag{3.11}$$

In this equation, it is assumed that all the water inside the dry-out region, which has the average saturation of $1 - \bar{S}_g$, is vaporized and consequently, salt precipitation happens. Furthermore, the average gas saturation behind the drying front is defined as below and has a value of about 0.526 in the current case:

$$\bar{S}_g = S_g^c + \frac{1 - f_g^c}{(df/dS_g)_{S_g^c}} \tag{3.12}$$

Capillary pressure acts against the natural pressure gradient inside the reservoir and results in a constant backflow of brine to the drying region. This amount of brine that is moved backward results in a reduction in the drying wave propagation speed. Therefore, r'_c (the drying shock location in the capillary included case) becomes smaller than r_c (shock's location in the no-capillary case). The brine addition to the drying region will obviously increase the brine saturation inside the drying region (the $1 - \bar{S}_g$ term in Eq. 3.11), and salt precipitation in this area increases. A schematic of capillary effect on drying shock's location is illustrated in Fig. 3.3.

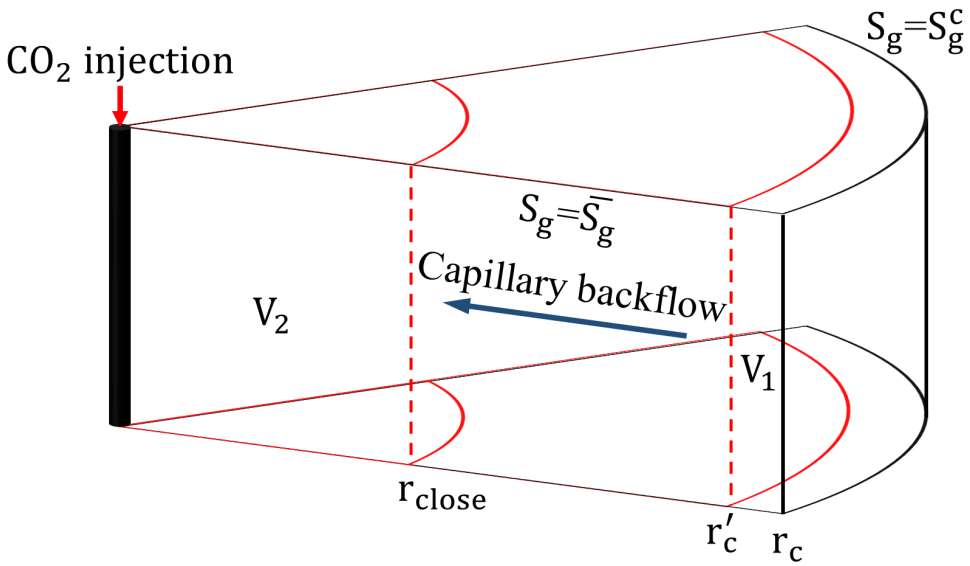

Figure 3.3: Schematic of the drying front shock wave variations in presence of capillary effect. Here, v_1 is the volume of water added to the drying region (the volume difference of the drying region between capillary included and no-capillary cases), and V_2 is a volume equal to V_1 adjacent to the injection well.

The amount of brine addition to the dry-out region through backflow can be calculated from $\Delta\eta$ in Eq. 3.10. To do so, it is assumed that all of the brine from a section with the pore volume of V_1 is moved back to the drying zone. V_1 is the same as the volume difference of the drying region in capillary included and no-capillary cases (volume V_1 in Fig. 3.3), and is calculated as follows:

$$V_1 = \pi H \phi (r_c^2 - r_c'^2) \tag{3.13}$$

Knowing $r_c^2 - r_c'^2 = \Delta\eta t$ (from Eq. D9), the above equation can be written as a function of backflow similarity variable as follows:

$$V_1 = \pi H \phi \Delta\eta t \tag{3.14}$$

Considering that the region V_1 has the same brine saturation as the rest of the drying zone $(1-\bar{S}_g)$, the volume of the brine backflow can be calculated from the definition of phase saturation as:

$$S_a = 1 - \bar{S}_g = \frac{V_{brine}}{V_1} \tag{3.15}$$

Therefore, the volume of brine that is moved backwards will be as follows.

$$V_{brine} = (1 - \bar{S}_g)\pi H \phi \Delta \eta t \tag{3.16}$$

Having the volume of the brine added to the drying region because of the capillary-driven backflow, the amount of solid salt saturation can be estimated, assuming that all this water is vaporized. Previously, by omitting the capillary pressure effect, a term was overlooked in Eq. 3.11, but here, through Eq. 3.10, that term is considered in Eq. 3.11. The term represents the brine addition to the dry-out region through backflow. To do so, two approaches are considered in the present paper. In the first approach, the whole dry-out region is in equilibrium, and it is assumed that the backflow brine results in a uniform increase in the amount of precipitated salt inside the whole dry-out region. Therefore, the added saturation to the initial brine saturation inside the dry-out region is calculated as follows:

$$S_{brine} = \frac{\text{added brine volume}}{\text{total pore volume}} = \frac{(1 - \bar{S}_g)\pi H \phi \Delta \eta t}{\pi H \phi r_c^2} \tag{3.17}$$

Having $r_c^2 = \eta_{\text{no cap}} t$, S_{brine} is derived as below:

$$S_{brine} = (1 - \bar{S}_g)\frac{\Delta \eta}{\eta_{\text{no cap}}} \tag{3.18}$$

Adding this to the saturation term in Eq. 3.11, solid salt saturation is calculated from the following equation for the first approach proposed in the present study.

$$S_s = (1 - \bar{S}_g)\left(1 + \frac{\Delta \eta}{\eta_{\text{no cap}}}\right)\frac{\rho_a}{\rho_s} X_s \tag{3.19}$$

In the second approach, it is assumed that capillary-driven backflow continues happening inside the dry-out region, or in other words brine constantly moves towards the injection well; therefore, even inside the dry-out region, salt precipitation is not constant and higher precipitation happens closer to the injection well. As a result, based on material balance in the system, capillary-driven backflow will only affect a region near to the injection well, which has the same volume as the volume of the backflow brine ($V_1 = V_2$). Using this concept

and Eq. 3.14, r_{close} that defines the close injection well area will be defined as below, which is about 22.81 m in the present case study. This parameter is one of the main achievements of the present study that defines the distance from the injection well that is mainly affected by salt precipitation.

$$\pi H \phi \Delta \eta t = \pi H \phi r_{\text{close}}^2 \tag{3.20a}$$

$$\Delta \eta t = r_{\text{close}}^2 = r_{\text{c}}^2 - r_{\text{c}}'^2 \tag{3.20b}$$

Using the above equation to calculate the additional brine saturation inside the close injection area, the following equation is achieved.

$$S_{\text{brine,close}} = \frac{(1-\bar{S}_{\text{g}})\pi H \phi \Delta \eta t}{\pi H \phi r_{\text{close}}^2} = \frac{(1-\bar{S}_{\text{g}})\pi H \phi \Delta \eta t}{\pi H \phi \Delta \eta t} \tag{3.21}$$

Therefore, the added brine saturation to the near injection well area will be as below:

$$S_{\text{brine,close}} = 1 - \bar{S}_{\text{g}} \tag{3.22}$$

As a result, the amount of brine saturation at the near injection well area is doubled and so does the solid salt saturation:

$$S_{\text{s}} = \begin{cases} 2(1-\bar{S}_{\text{g}})\frac{\rho_{\text{a}}}{\rho_{\text{s}}} X_{\text{s}} & \text{for } r < r_{\text{close}} \\ (1-\bar{S}_{\text{g}})\frac{\rho_{\text{a}}}{\rho_{\text{s}}} X_{\text{s}} & \text{for } r_{\text{c}}' > r > r_{\text{close}} \end{cases} \tag{3.23}$$

This second approach suggested in the present study causes a discontinuity (solid salt saturation shock) in the salt saturation curve in the drying region. Through the second approach, it is possible to define the area in which capillary pressure has its major effect. Finally, it will be possible to reasonably accurately estimate salt precipitation at the injection point.

3.4.3 Porosity and permeability variations due to salt precipitation

The reduced porosity because of salt precipitation is calculated as below:

$$\phi = \phi_0 (1 - S_{\text{s}}) \tag{3.24}$$

There are many models available to relate porosity to permeability [112]. In the present study, I use the simple Kozeny-Carman grain model that is based on spheres [113, 114]. Accordingly, the resistance factor (ratio of the reduced permeability to the initial permeability) is calculated as follows.

$$\frac{k}{k_0} = \left(\frac{\phi}{\phi_0}\right)^3 \left(\frac{1-\phi_0}{1-\phi}\right)^2, \tag{3.25a}$$

or

$$\frac{k}{k_0} = \frac{(1-S_s)^3}{(1+(\phi_0/(1-\phi_0))S_s)^2} \tag{3.25b}$$

Since permeability is directly related to S_s, similar to the salt saturation curve, a discontinuity is expected in the permeability ratio.

3.5 Results and discussion

In this section, results of the proposed analytical solution for a CO_2-brine system with capillary effect are reported. In each section, results are presented for both capillary included and no-capillary cases and all of them are validated with numerical results derived from a geochemical compositional equation of state (EoS) simulator (CMG-GEM). In the first section, the model validity is studied by comparing its result to the ones reported from the numerical solution. Then, in a separate section, effects of capillary pressure and capillary-driven backflow on shocks propagation, salt precipitation, and permeability reduction are studied.

3.5.1 Model validation

Fig. 3.4 shows the result of the case with no capillary pressure. Based on Fig. 3.4a, shock waves are also observed in the numerical results, with a flooding front's propagation speed and similarity variable much larger than the drying shock. In Fig. 3.4b, results of the no-capillary analytical solution are compared with numerical ones. It is observed that the analytical solution is in a good agreement with the numerical results. The similarity variables for the drying and the leading fronts are 1.12×10^{-5} and 0.0154 m^2/s, with $S_g^c = 0.4887$ and $S_g^b = 0.1982$, respectively. However, there is an important difference between the results of the analytical and numerical solutions. In the analytical $S_g - r$ curve, unlike the numerical one, the slopes at shocks locations' are infinity ($\frac{dS}{dr} = \infty$), whereas for numerical solutions the shocks are inclined. This results in a slight curvature in the numerical curves in figure Fig. 3.4b, This means that, unlike the analytical solution, the capillary pressure will have

a finite value, but it has higher intensity at the drying front since the slope of saturation variations is higher at this location (about 50 times higher) compared to the flooding front. Therefore, capillary pressure and the resulting capillary backflow mainly affect the drying front.

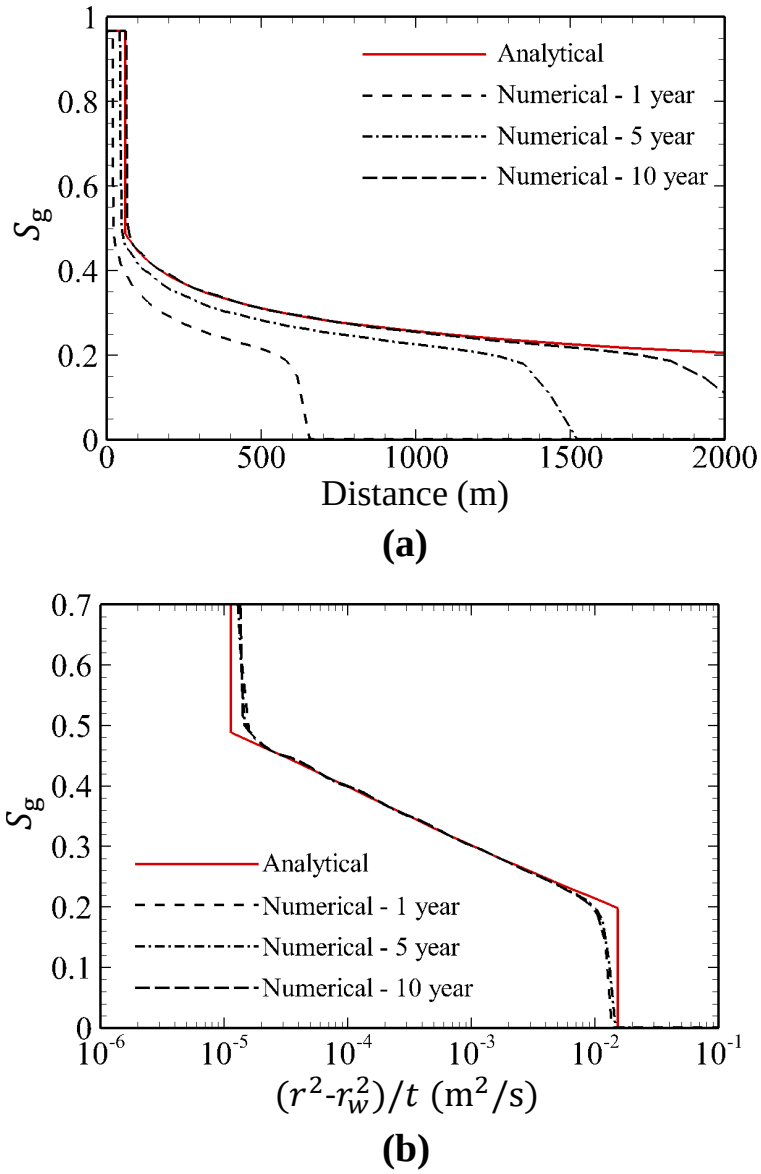

Figure 3.4: No-capillary pressure case analytical and numerical results, (a) gas saturation vs. distance from the injection well at three times, and (b) gas saturation vs. the similarity variable for analytical and numerical methods.

Fig. 3.5 shows the results of the analytical solution for the capillary included case (at $t =$ 10 years) and its comparison to the capillary included numerical ones. Firstly, it is observed that the capillary pressure included analytical solution also demonstrates an acceptable

agreement with the numerical results. Here, the drying front has the similarity variable of 9.55×10^{-6} m^2/s with $S_g^c = 0.4758$ and the flooding front has the similarity variable and S_g^b equal to the no-capillary case. This acknowledges the fact that capillary mainly, if not only, affects the drying region (about 15% reduction in the drying front's similarity variable). Also, it is observed that the slope of saturation variations is almost the same as the no-capillary case, making the assumption considered for $\frac{dS}{dr}$ in Section 3.4.1 valid.

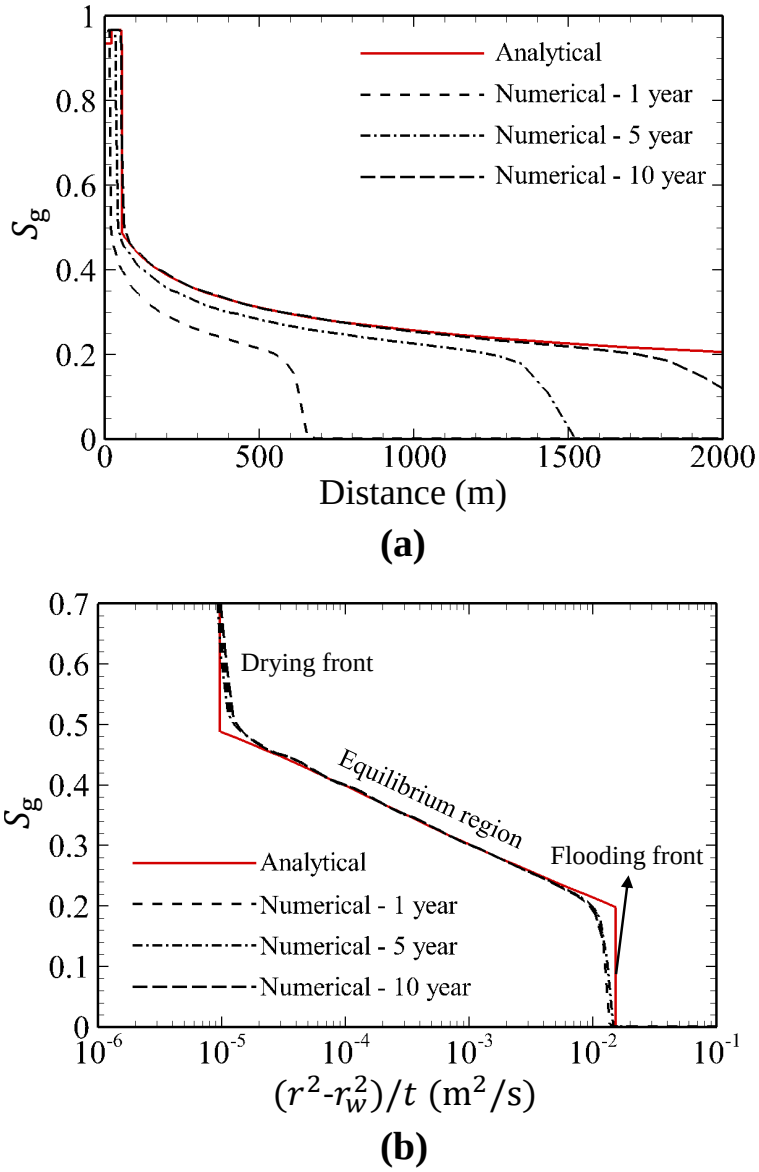

Figure 3.5: Capillary included case analytical and numerical results, (a) gas saturation vs. distance from the injection well at three times, and (b) gas saturation vs. the similarity variable for analytical and numerical methods.

3.5.2 Effects of capillary pressure on dry-out front propagation speed

Based on both the analytical and the numerical solutions in Figs 3.6(a & b), the capillary included case has a lower drying front similarity variable. $\Delta\eta$ is about 1.65×10^{-6} m^2/s and 3.22×10^{-6} m^2/s for the analytical (Fig. 3.6a) and numerical (Fig. 3.6b) solutions (at $t = 10$ years), respectively. Subsequently, based on these results, the drying front will be at 54.88 m after 10 years of injection (about 4.55 m less than the no-capillary case) for the analytical case, and will be at 50.17 m for the numerical one. Therefore, overlooking the effect of capillary pressure and capillary-driven backflow will result in about 8.3% overestimation in extent of the drying region.

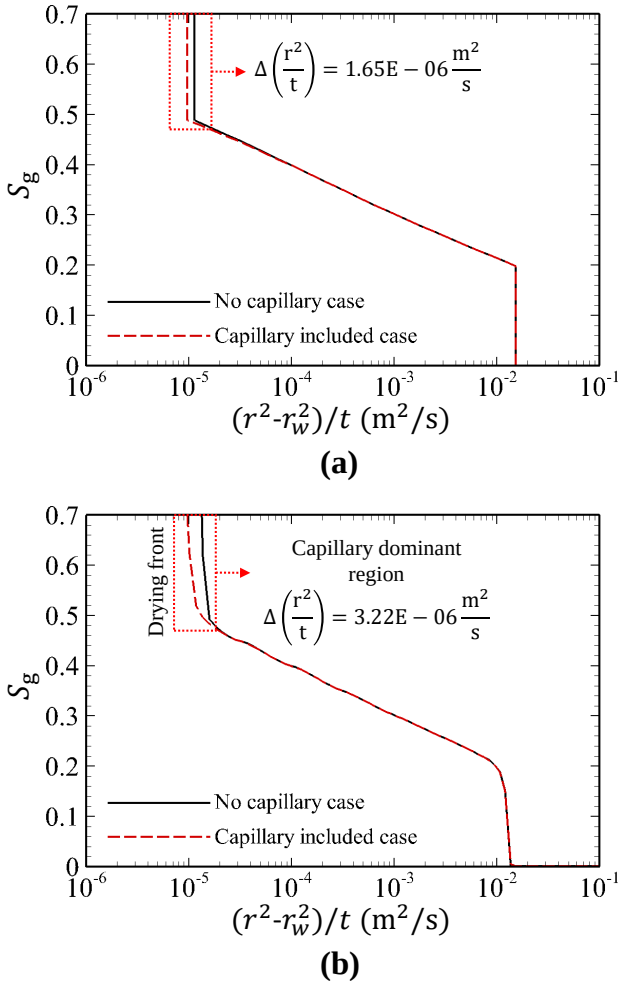

Figure 3.6: Results of the effect of the capillary pressure on drying front propagation speed, (a) analytical results, and (b) numerical results at $t = 10$ years. The difference in similarity variable between the capillary included and no-capillary cases are about 1.65×10^{-6} and 3.22×10^{-6} $\frac{m^2}{S}$, respectively.

3.5.3 Effects of capillary pressure on salt precipitation and permeability variation

In this section, the results of salt precipitation and permeability reduction in the dry-out region (due to water vaporization) for both capillary included and no-capillary pressure cases are reported and compared. Here and for the upcoming figures, the red shading in the figures shows the dry-out region extent, and the green shading shows the near injection area mainly affected by salt precipitation.

Fig. 3.7a shows the salt saturation profile for the no capillary pressure case. The analytical method has a good agreement with the numerical results (about 0.61% error). However, neglecting capillary pressure leads to an extreme underestimation of the amount of the precipitated salt especially near the injection point (the green region). Fig. 3.7b shows the amounts of the precipitated salt, calculated based on the first approach as in Eq. 3.19. Due to the brine addition to the dry-out zone, more brine is vaporized and as a result, more salt will precipitate in this area. Accordingly, capillary-driven backflow leads to about 14.71% (for analytical method) and 1.41% (for numerical method) more average precipitation in the drying region as reported in Fig. 3.7b. The analytical results from the proposed method in Eq. 3.19 have about 12.46% error compared to the numerical ones. The reason for the increase of error between analytical and numerical results is that the calculated amount of brine moving backwards is over-represented by the analytical method. In the analytical approach it is assumed that brine moves backwards –with the backflow velocity– and fills the pores. However, brine moves backwards through small water films attached to the pores, leading to a much smaller cross-sectional area than what is assumed in the solution. As a suggestion in this regard, pore-scale study and definition of a dimensionless parameter as $t_{\mathrm{D}} = \frac{t_{\mathrm{film}}}{D_{\mathrm{pore}}}$, which is the ratio between the water films thickness and pores diameter, will be helpful.

In all of the figures of this section, there is a near injection area in the dry-out region that salt precipitation starts to grow exponentially (the green area), showing that the highest reservoir damage occurs at the injection well. In comparison to the increment in the average salt precipitation in the drying region of the capillary included case (by a factor of about 1.1), salt precipitation at near injection well area is much more noticeable with $S_{\mathrm{s}} = 0.078$ (about 58.73% increase) in presence of capillary pressure. Therefore, it is critical to develop a model able to capture and define this near-injection area.

According to the discussion in Section 3.4.2, the second approach is defined as Eq. 3.23, in which the near injection area is defined and it is assumed that the additional salt precipitation

due to capillary-driven backflow only affects this area. Therefore, through this method, a salt precipitation shock is also observed in Fig. 3.7c, which has the similarity variable almost the same as the green area's right side boundary. This method has the same error (13.01%) as the first approach. However, it features two main advantages compared to the previous one. Firstly, it is possible to define the near injection area (r_{close}) at which capillary is most influential and the precipitation is maximum (here, it is about 22.81 m from the injection well); and secondly, it is possible to estimate the salt precipitation and reservoir damage at the injection well vicinity, which is about 2-2.5 times higher than the rest of the reservoir. Compared to the first approach, the error of estimating the saturation of salt at the injection point has decreased from 50.54% to 13.79% by using the second approach.

The ratio of the reservoir's permeability, after salt is precipitated, to its initial value is calculated through Eq. 3.25b. Fig. 3.8a shows the permeability reduction results for the case with no capillary effect. It is observed that the average permeability ratio for the analytical solution is about 0.897, while it is about 0.896 for the numerical one.

Fig. 3.8b shows permeability reduction in presence of capillary pressure for salt precipitation calculated from Eq. 3.23. Permeability ratio is reduced by an average of 1.6%, but again it is observed that the reduction value at near injection area is much higher (about 9.27%), with the k/k_0 ratio of about 0.77. Fig. 3.8c shows the same results versus distance from the injection well. From this figure, it is clearly seen that capillary pressure affects the reservoir mainly at the near injection area (the green area in the figure), whose extent is calculated as $r_{\text{close}} = \sqrt{\Delta\eta}$ and is about 22.81 m in this study.

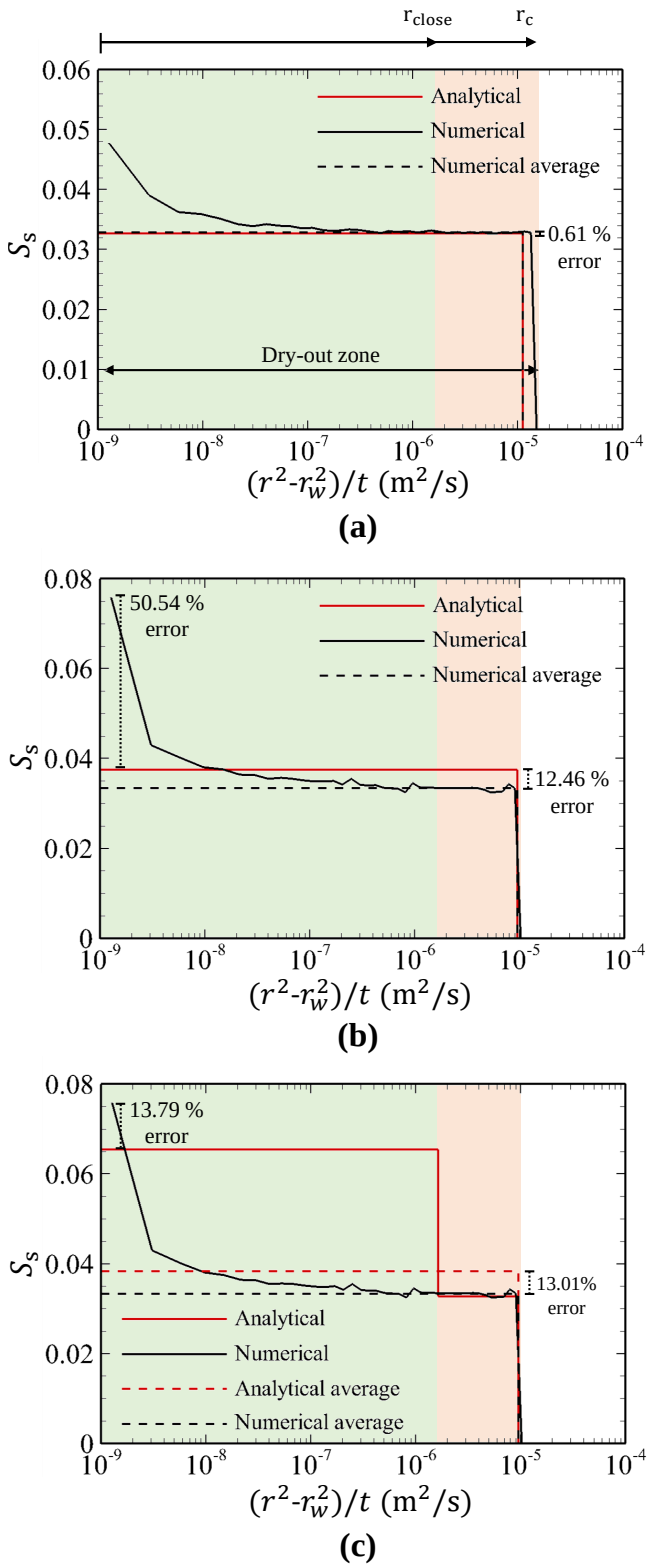

Figure 3.7: Salt saturation profiles at $t = 10$ years for (a) the case with no capillary pressure, (b) the first approach for the case with capillary effect (uniform precipitation), and (c) the second approach for the case with capillary effect (localised salt saturation).

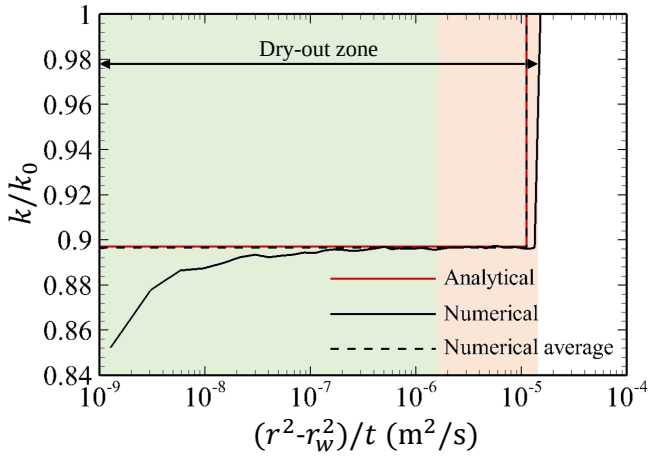

(a)

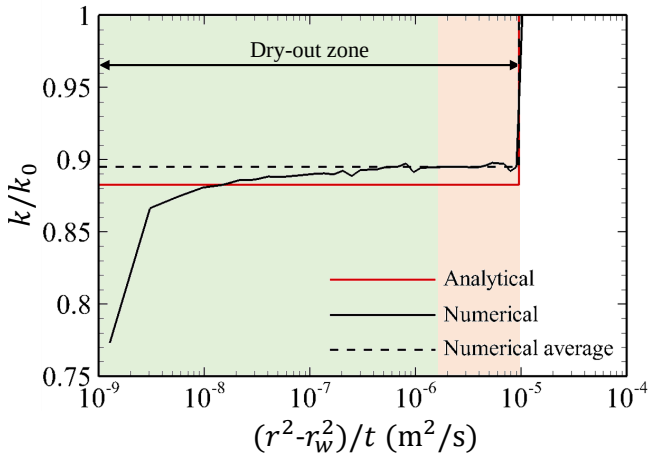

(b)

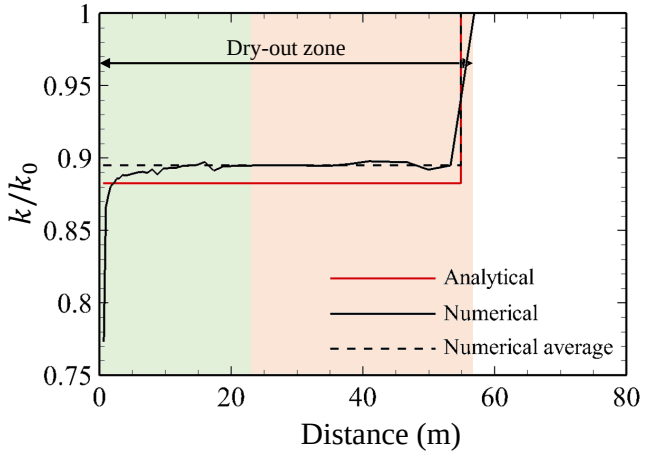

(c)

Figure 3.8: Permeability variation results, (a) for the case with no capillary effect, (b) with capillary effect, and (c) permeability variation results vs. distance from the injection well for the case with capillary effect (t=10 years).

3.5.4 Analytical solutions for different salinities

To compare the accuracy of the three analytical solutions (*i.e.*, Eq. 3.11 for no capillary case, Eq. 3.19 for the first approach in presence of capillary pressure, and 3.23 for the second approach in presence of capillary pressure) in predicting salt precipitation at the injection well, 4 cases with different initial brine salinities (X_s ≈100000, 150000, 200000, and 250000 ppm) are considered. By changing the initial salinity, brine density and equilibrium mole fractions of CO_2 and water vary as well. Fig. 3.9a shows the calculated equilibrium mole fractions of aqueous CO_2 ($\omega_{CO_2,a}$) and gaseous water ($\omega_{Water,g}$) for each salinity case. The values reported in Fig. 3.9a are comparable with those reported by Spycher and Pruess [115].

Fig.3.9b shows the calculated salt saturation (S_s) at the injection well through different methods for 10 years of injection. Amongst the analytical solutions, the second approach (Eq. 3.23) that used mass balance to calculate the precipitated salt at near injection area inside the dry-out region (r_{close}), has the closest results to the numerical ones with an average error of about 8%.

Comparing the results of the analytical solution to those available from experiments and field studies, as reported in Table 1 of the work by Miri and Hellevang [40], it is observed that the results of the proposed analytical solution fall within the range reported by experiments and field observations (permeability reduction of about 13-80%). However, it is acknowledged that both numerical and analytical solutions underestimate the amount of permeability reduction. This can be because of several reasons, such as homogeneity of the reservoir for analytical/numerical cases, or the fact that our model does not have z direction. The latter removes the phenomenon in which salt accumulates at the bottom of the reservoir and exacerbates the permeability reduction. Another reason for the underestimation is the relatively high injection rate considered in the present study; and according to Norouzi et al. [38], as the injection rate increases, the amount of the precipitated salt and permeability impairment decrease considerably.

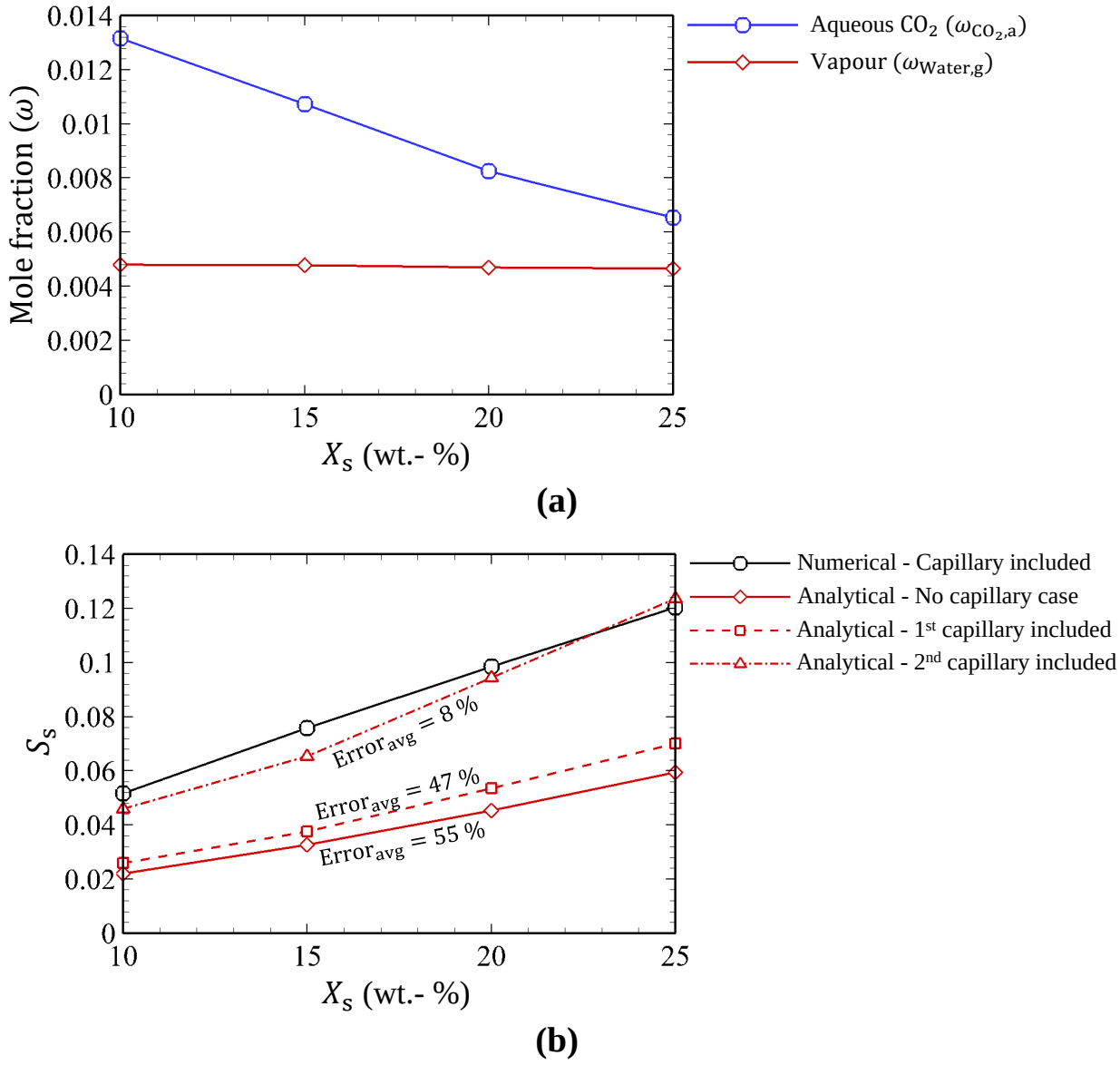

Figure 3.9: (a) CO_2 and water mole fractions for different initial brine salinities, and (b) solutions comparison based on the average error of the precipitated salt at the injection well after 10 years.

3.6 Conclusions

An analytical solution to calculate salt precipitation was previously proposed by Pruess [102]. However, capillary pressure was omitted in that work. This paper provided an analytical solution based on fractional flow theory and definition of shocks in presence of capillary

pressure. The key findings of the current paper can be summarised as below:

- Capillary pressure acts against the pressure gradient caused by the saturation difference and injection pressure. It reduces the saturation shocks' propagation speeds. Therefore, a backflow similarity variable ($\Delta\eta$) is defined. It is calculated that the drying shock travels less distance compared to the no capillary pressure case (4.55 m in the case studied).

- Capillary-driven backflow acts as a water supplier to the dry-out region, making the vaporization and precipitation processes continuous versus time. This results in an increase in the average amount of precipitated salt (14.71% here) and an increase in the salt precipitation at the near injection well area (58.73% here) based on the first proposed analytical approach.

- Through the second approach suggested in this paper, it is possible to estimate the area that is mostly affected by precipitation near injection. Through mass balance, the radius of this area is calculated as $r_{\text{close}} = \sqrt{\Delta\eta t}$, (22.81 m in the present case study).

- It is also possible to reasonably estimate the amount of the precipitated salt at the injection well ($S_{\text{s}} \approx 0.65$ for $X_{\text{s}} \approx 150000$ ppm) with an average error of about 13.79% compared to the computationally intensive numerical solution.

- Finally, salt precipitation by capillary-driven backflow can increase permeability reduction (by 1.61% for this study) and the near-injection well damage (by 9.27% for this study).

The analytical solutions developed in this paper can provide guidelines for possible future works to investigate the effects of capillary pressure and capillary-driven backflow in saline reservoirs. Also, through the proposed equations, it is possible to avoid under-predictions in reservoir damage due to salt precipitation and accurately estimate the main areas affected by this phenomenon.

Open research

Availability statement: The Excel file for the CMG simulations data for Figs 3.4a, 3.5a, and 3.7 is available to download at https://doi.org/10.6084/m9.figshare.19115018. Also, The programming code used to generate Fig. 3.2(b) is available upon request made to the corresponding author.

Acknowledgement

The authors thank Prof Larry Lake, at the University of Texas at Austin, for his constructive comments on the initial draft of the paper. Also, the authors acknowledge the University of Manchester's President's Doctoral Scholar Award to Amir Mohammad Norouzi. Masoud Babaei and Vahid Niasar thank EPSRC for funding the project EP/W008718/1 that supported their research on salt precipitation in CCS.

Nomenclature

A	Cross-sectional area, [m^2]
C	Molar concentration, [$mol.L^{-1}$]
f	Fractional flow, [-]
G	Normalised global concentration, [-]
H	Aquifer thickness, [m]
k	Permeability, [mD, m^2]
M	Mass, [kg]
$\dot{m}$	Mass flow rate, [$kg.s^{-1}$]
P	Pressure, [MPa]
q	Volumetric flow rate, [$m^3.s^{-1}$]
r	radius, [m]
S	Saturation, [-]
T	Temperature, [°C]
t	Time, [s]
V	Volume, [m^3]
X_s	Salinity, [Mole/mass fraction, ppm]
x	Distance, [m]
Greek letters	
η	Similarity variable, [$m^2.s^{-1}$]
γ	Capillary force parameter, [-]
λ	Mobility, [$Pa^{-1}.s^{-1}$]
μ	Viscosity, [Pa.s]
ω	Mole fraction, [-]
ϕ	Porosity, [-]
ρ	Density, [$kmol.m^{-3}$, $kg.m^{-3}$]
Subscripts	
a	Aqueous
avg	Average
brine	Brine backflow
c/cap	Capillary
g	Gaseous

inj	Injection
r	Relative
s	Trailing shock/solid salt
t	Total
w	Well
0	Initial
Superscripts	
b	Upstream of the leading shock
c	Downstream of the trailing shock
dry	Dry-out region

Chapter 4

CO_2-plume geothermal in fluvial formations: A 2D numerical performance study using subsurface metrics and upscaling

This chapter is a modified version of the paper published in '*Geothermics*'.

Authors: **A. M. Norouzi**, J. Gluyas, M. Babaei. CO_2-plume geothermal in fluvial formations: A 2D numerical performance study using subsurface metrics and upscaling. *Geothermics*, Vol.99, p.102287, 2022.

4.1 Abstract

CO_2-plume geothermal (CPG) operations are considered for sufficiently permeable formations due to their superiority compared to conventional water-based geothermal systems. The fluvial heterogeneity in sedimentary reservoirs can significantly affect the pumping energy losses and heat extraction from hot sedimentary aquifers. In the present study, I have implemented the braided type of fluvial channels to account for the geological uncertainty and investigated the subsurface performance metrics of a CPG system with a checkers-board pattern. An optimisation of doublet/well spacing is performed based on the coefficient of performance (CoP), energy sweep parameter, and an objective function (f) defined specifically for the optimisation of the process. In addition, a sensitivity analysis on the grid resolution, braided channel thickness and orientation, and the injection flow rate and span of the supercritical (sc)-CO_2 is performed. The upscaled grid resolution mainly affects the pressure-related parameters, including CoP and f, resulting in an average error of 80 and 60% between the fine- (120×120) and the coarse-scale (15×15), respectively. As a result, the grid resolution of 60×60 with $dx \approx$16.5 m is found to have both acceptable average error and optimum runtime. The optimum doublet/well spacing for the present case is about $L = 450$ m, in which the CPG system provides about 9 to 13 times higher values of f compared to cases with doublet/well spacing higher or lower than the optimum value. Moreover, injection wells with I_1-I_2 line parallel to channels' orientation, provide about 30% higher f compared to the perpendicular case. However, the channels' orientation does not change the optimum doublet/well spacing ($L = 450$ m).

Keywords: CO_2-plume geothermal, Heterogeneity, Braided channels, Doublet/well spacing, Upscaling.

4.2 Introduction

4.2.1 CO_2-plume geothermal systems, fluvial heterogeneity, and doublet/well spacing optimisation

The importance of reducing CO_2 emissions into the atmosphere and shifting toward renewable sources of energy has become evident in the past few decades [116, 46]. An efficient method of reducing CO_2 emissions is by storing CO_2 in underground geological reservoirs, such as oil and gas reservoirs - for enhanced oil [49, 50, 51] and gas [52, 117] recovery - and saline aquifers [118, 119, 120], or for heat extraction through CO_2-based enhanced geothermal

systems (EGS) [29, 35, 121] and CO_2-plume geothermal (CPG) systems [122].

Previously, water was mainly used in geothermal systems as the heat transmission fluid, namely in conventional hydrothermal and EGS systems [123, 124], however, CO_2 also was proposed as the working fluid. At the reservoir condition, CO_2 is at its supercritical (sc) state, and according to Adams et al. [56] and Ezekiel et al. [117] utilisation of $scCO_2$ has many advantages compared to water. $scCO_2$ has lower viscosity (higher mobility) compared to water. Putting this asset besides the buoyancy-driven thermosiphon effect [125, 56, 126] that occurs during CO_2 injection inside the reservoir, results in a reduction in the amounts of the required pumping power. Based on these advantages of $scCO_2$ utilisation, Randolph and Saar [122] and Adams et al. [127] provided a comparison between the heat extraction rates and electric power output of a water-based and a CO_2-based system and reported that not only CO_2 results in less pressure drop inside the reservoir but also provides more geothermal heat and net power by a factor of 2.9 and 4.1, respectively, compared to a water-based system.

The concept of CPG was first proposed by Randolph and Saar [122]. Unlike water-based systems, in CPG systems both brine (with very small mass-fractions) and $scCO_2$ are produced from the production wells, contributing to heat extraction from the reservoir. However, it is CO_2 that is mainly used as the heat transmission fluid. These systems have two main objectives, *i.e.*, heat extraction from the reservoir and CO_2 storage. Compared to EGS and water-based systems, CPG systems typically target shallower reservoirs (1000 to 4000 m) with lower temperatures. Based on Bonté et al. [128], there are many low-enthalpy geothermal sites at depths of 2-2.5 km with temperatures of 70-90 °C. Due to the high applicability of these systems, and that they can both produce renewable heat and store CO_2 simultaneously, they gained much attention from researchers. There are many pieces of research regarding the study of the performance of CPG systems, the most recent of which are [117, 53, 59, 84, 106, 129, 130, 38]. A brief review of these works is provided in Table 4.1.

Table 4.1: Review of the most recent works in the field of CPG systems.

Study	Objective and key findings
Ezekiel et al. [117] (2020)	$scCO_2$ was used in a dual-purpose system, first to enhance gas production (EGR) and then working as a CPG system for electric power generation of about 2 MW_e. Also, at the end of the process, all the external injected CO_2 (about 16 Mt) was stored inside the reservoir.
Babaei [53] (2019)	A comparison between open and closed flow boundary of CPG systems for a 3D, homogeneous, and isotropic reservoir was provided. It was observed that, although boundary type has a great effect on the performance metrics of the system, its effects on salt precipitation are negligible.
Pan et al. [59] (2018)	Pressure variations of the reservoir in a CPG system were studied through sensitivity analysis of various parameters, including wells spacing. However, only 3 values were considered for spacing in a 3D-homogeneous case.
Cui et al. [84], [106] (2017 and 2018)	Effects of complicated geochemical reactions on heat extraction from a CPG system were studied and experimental tests were performed to quantify the kinetics of the reactions. Initial injection of low salinity water was proposed to reduce salt precipitation.
Adams et al. [129] (2021)	The optimum well spacing for a 5 well pattern (1 injection in middle and 4 productions around it) CPG system was investigated, and it was found that a 707 m spacing provides the most consistent electricity production over 50 years.
Fleming et al. [130] (2020)	Heat was extracted from the mixture of water and CO_2 produced from a CPG system, rather only considering CO_2. It was shown that the turbine power increased on average by 15-25%.
Norouzi et al. [38] (2021)	Capillary backflow and its effects on salt precipitation in a 2D and homogeneous CPG system were studied. It was concluded that the main mechanism contributing to salt precipitation was the capillary-driven backflow; however, this effect was confined to the close vicinity of the injection wells.

All reservoirs are heterogeneous in nature. In saline aquifer reservoirs, the heterogeneity of the field can be of fluvial type, *i.e.*, braided (Bunter sandstone reservoir, UK; Tarim basin, China; the Triassic St Bees Sandstone Formation, Cumbria, UK [131]; and Sherwood Sandstone Group of the Wessex Basin, UK [132]), meandering (Cretaceous Nieuwerkerk Formation, West Netherlands Basin [133]), or anabranching. The existence of fluvial channels can affect the pressure and temperature distributions inside the reservoir, which in turn alters the performance parameters of a geothermal system including the energy sweep and the coefficient of performance (CoP). Therefore, it is crucial to consider these types of hetero-

geneity to perform an accurate simulation resembling actual fields. Despite the importance of fluvial geological heterogeneity, few works considered this type of heterogeneity in their geothermal models, such as, [134, 135, 136, 137]. However, even among these works, no study focused on heterogeneity in a CPG system and they mostly investigated brine geothermal systems and CO_2 geological sequestration in heterogeneous reservoirs.

Willems et al. [134] studied the effects of doublet well spacing on the performance metrics and the lifetime of a hot sedimentary aquifer with fluvial (meandering) heterogeneity for a water-based system. It was claimed that the optimum spacing is highly related to the geological uncertainty of the field. Therefore, a detailed meandering fluvial model was generated in their work. The main objective parameters were the Net Present Value (NPV) and the lifetime of the system. According to the results, which were reported for the West Netherlands Basin, if the spacing is reduced from 1400 m to 1000 m, the NPV would improve by 15%. In another paper, Gershenzon et al. [135] investigated the potential of fluvial reservoirs in CO_2 trapping. The key objective of their work was to analyse the CO_2 capillary trapping and dissolution in highly heterogeneous fluvial-type reservoirs. A similar work in the field of CO_2 sequestration was done by Issautier et al. [136], in which a semi-braided reservoir was modelled and its CO_2 storage capacity was compared with a reservoir with a fluvial belt with a 100% sand content. In a recent work by Soltanian et al. [137], multi-phase transport of brine and CO_2 in braided fluvial channels with geochemical reactions was studied for CO_2 sequestration applications. It was concluded that the properties of fluvial channels and slight changes in field properties (porosity and permeability) through the geochemical reactions, significantly affect CO_2 transport and storage inside the reservoir.

The location of injection and production wells controls the performance efficiency of a geothermal system. In the case of high-enthalpy deep brine geothermal systems, there are numerous works regarding the optimisation of doublet systems and well spacing. However, for the low-enthalpy and shallower reservoirs, as mentioned by Babaei et al. [138], the number of works regarding the optimised well locations is considerably low and this issue is overlooked in the literature. Although the lower viscosity of the $scCO_2$ and its higher mobility can significantly affect the optimised doublet pairs spacing, no optimisation has been performed in this regard. Adams et al. [129] and Pan et al. [59] considered the effects of well spacing on heat extraction rate and pressure buildup, which were described in Table 4.1. Although these works considered the effects of well spacing, their models were homogeneous with limited performance metrics and doublet pairs distances.

4.2.2 This study

Based on the provided literature review, to the authors' knowledge, there is no work that provides the doublet well spacing optimisation in a reservoir with braided fluvial channels for CPG applications. In this regard, in the present work, an in-house code is developed to generate braided geometries. The optimum doublet spacing (spacing between two doublets) and well spacing (spacing between two wells in one doublet) is reported for them. The spacing will be referred to as *doublet/well spacing* throughout the paper. The optimisation is done based on the subsurface performance metrics only, as will be defined later. In addition, since adding geological uncertainty and heterogeneity to the reservoir will add the computational costs and the simulations runtime, a grid resolution sensitivity analysis through upscaling is provided. Also, the effects of channels' thickness and orientation with respect to the wells, $scCO_2$ injection rate, and the open/closed flow boundary condition on the performance and the optimum doublet/well spacing are studied.

4.3 Geothermal model characteristics

4.3.1 Reservoir properties

In the present study a 2D reservoir with the main domain of 1000 m $\times$ 1000 m $\times$ 10 m is modelled for the supercritical CO_2 injection period of 20 years. The reservoir is representative of a high-salinity North Sea sandstone reservoir, designed based on the data provided by Warren et al. [139] and previous available works in the literature, especially [53, 138, 38]. For the benchmark case, the reservoir is uniformly discretized into a 120 $\times$ 120 mesh with only 1 layer in the vertical direction. The reservoir has a depth of 2000 m and the initial conditions of T_{initial}=100 °C and P_{initial}=20 MPa. The reservoir's rock density, heat capacity, and thermal conductivity are set to 2650 kg/m^3, 750 J/kg/K, and 2.1 W/m/K, respectively. Also, the rock compressibility at 20 MPa is 7.0×10^{-7} 1/kPa. A schematic of the reservoir is displayed in Fig. 4.1.

Boundaries of the reservoir (horizontal/vertical) are open to heat transfer but closed to fluid flow. However, to study the effects of open vs. closed boundary conditions, a series of simulations with the open boundary to flow are also performed. To implement open flow boundary conditions in the cases, pore volume modification (PVM) is used. To this end, a layer of grid blocks is added to the initial mesh from each side of the reservoir, and then through the PVM method, the gross volume of these cells is multiplied by a

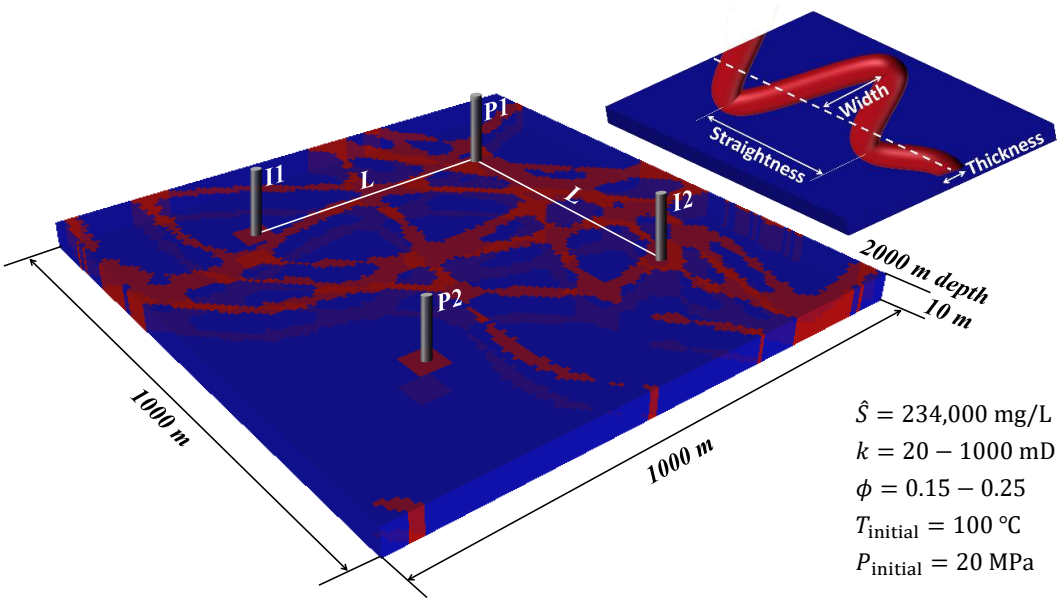

Figure 4.1: The 1000 m × 1000 m × 10 m fluvial reservoir, at the depth of 2000 m, with braided channels considered for the CPG system (main figure), and the fluvial channels' defining parameters [140] (inset figure). The pattern of doublets and wells is a "checkers-board layout" [141].

constant coefficient to represent cells with large pore volumes. In the present study, the PVM coefficient is set in a way that as if 1000 m is added to the reservoir from each side in the horizontal direction. Through this method inlet and outlet of flow from the boundaries are considered in simulations.

Two injection (I_1 and I_2) and two production (P_1 and P_2) wells are placed in a symmetrical manner at the centre of the reservoir. The main parameter that is optimised in the present study, is the doublet/well spacing (L) as shown in Fig. 4.1. For all wells, a well-surrounding modification is performed, meaning that an area of 50 m × 50 m around each well is assumed to have high permeability and porosity, which mimics the actual field practice of well stimulation through acidizing [142]. The injection wells have the injection temperature of T_{inj}=40 °C and the injection rate of 1.5×10^5 sm^3/day (with the assumption of the CO_2 density at standard condition, 1.98 kg/m^3). Also, the constraint for the production wells is the minimum bottomhole pressure (BHP) of 20 MPa.

Braided fluvial channels specifications

Among various types of fluvial channels that exist in subsurface reservoirs, *i.e.*, straight, meandering, braided, and anabranching [42], braided channels are chosen for the present study due to their complexity. It was previously observed that the orientation of braided

channels affects the performance metrics of the geothermal system. For a water-based system, the case with injection wells parallel to channels (similar to the 45° case in the present study) provided the best performance [138]. As a result, in the present study, braided channels with 45°, 0°, and -45° orientation with respect to the injection wells are considered. Braided channels consist of a network of channels that are of relatively low sinuosity and are separated by small and scattered islands [143]. The main parameters that are used to create fluvial braided channels are shown in Fig 4.1. Fluvial channels can be defined by the aspect ratio between channels' thickness and depth, and a channels' mean depth of about 9 m is acceptable (based on Gibling and Martin [140]). Therefore, in our model, which represents a 2D case with 1 layer of fluvial heterogeneity, a depth of 10 m is chosen for the channels. To study channels' thickness, a dimensionless thickness parameter is defined as below:

$$T_N = \frac{\text{Channels average thickness } (m)}{\text{Reservoir width } (m)} \tag{4.1}$$

To generate reservoirs that replicate realistic fluvial reservoirs with randomly scattered braided channels, an in-house code is developed. Through this code, which is based on Piece-wise Cubic Hermite Interpolating Polynomial (PCHIP) fitting method [144], a binary matrix with the number of rows and columns equal to the intended final mesh (120×120 in the present work) is created. The first step of creating braided channels is that some points are randomly selected within the domain, then a curve is fitted to them based on the PCHIP method, and after that, the channel's edges are smoothened, and thickness (T_N) is added to the channel. By defining the number of channels (n) and repeating the same procedure, more channels are added to the reservoir. Finally, the generated matrix is rotated to generate the final mesh for different channels' orientations. After the binary matrix is created, the porosity and permeability values of the fluvial reservoir are assigned to them. For the present work, a porosity ϕ of 0.15 for the inter-channel areas and 0.25 for the channelled areas are designated. Also, for the permeability ($k_x = k_y$), values of 20 and 1000 mD are assigned for the inter-channels and channelled areas, respectively.

Overall, 50 different realisations are used in the present study, 10 of them are for doublet/well spacing optimisation, 25 realisations to study different channel thicknesses (T_N = 0.035, 0.062, 0.097, 0.137, and 0.171), and 15 realisations to study the effects of channels orientations (θ = 45°, 0°, and -45°). These realisations are illustrated in Fig. 4.2.

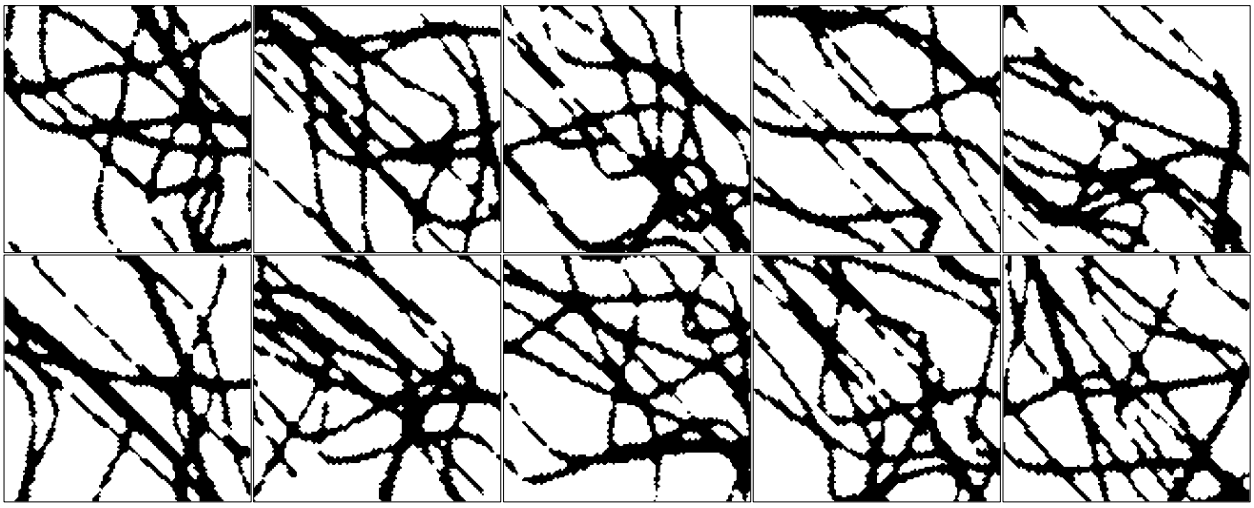

(a)

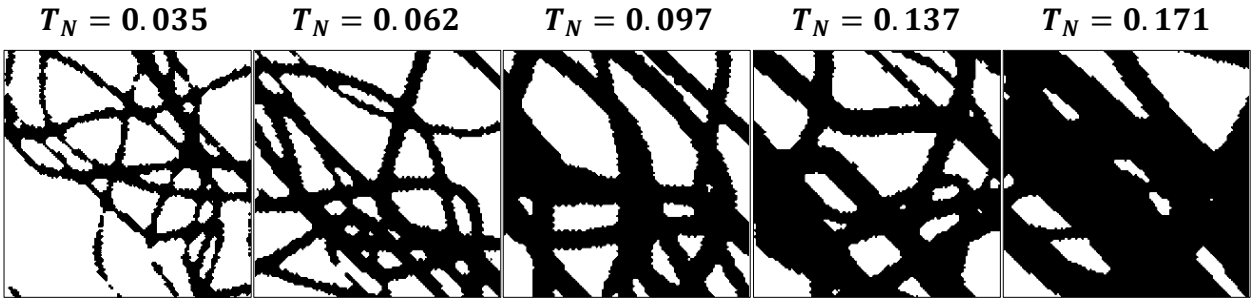

(b)

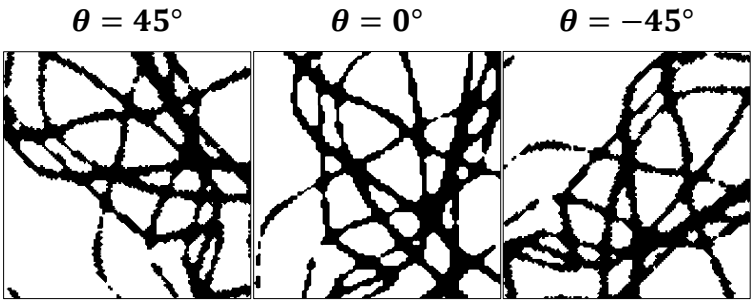

(c)

Figure 4.2: (a) The 10 braided realisations used for doublet/well spacing optimisation, (b) first 5 (out of 25) realisations used to study the effects of channels' average thickness (T_N = 0.035, 0.062, 0.097, 0.137, and 0.171), and (c) first 3 (out of 15) realisations used to study the effects of channels orientation ($\theta = 45°, 0°, and -45°$) on the performance metrics of a CPG system.

4.3.2 Brine and CO_2 properties

Brine is comprised of different components. The salinity of brine ($\hat{S}$) is set to 234,000 mg/L compatible with the salinity data for high-saline aquifers [139]. To calculate brine density and viscosity as functions of temperature and pressure, respectively, the Rowe and Chou [145] and the Kestin et al. [146] correlations are used, both of which are applicable for saline solutions with the pressure range of $P \leq 35$ MPa, temperature range of 20-150 °C, and salinity of $\hat{S} \leq 330000$ mg/L [147].

The density of the $scCO_2$ is calculated from the Peng-Robinson equation of state (EoS) [148], and the viscosity from the Jossi, Stiel, and Thodos correlation [149]. Further information regarding other equations that are used in the solver for other physics and parameters such as brine vaporization, CO_2-brine diffusion, and solubility calculations are available in previous works done by Norouzi et al. [38] and Nghiem et al. [62].

Corey [86] and van Genuchten [90] models are used to calculate relative permeabilities and capillary pressure, respectively, with the irreducible water saturation (S_{wir}) of 0.3, CO_2 residual saturation (S_{gr}) of 0.05, initial capillary pressure (P^0_{cap}) of 0.004 MPa, and capillary force parameter (γ) of 0.412.

4.4 Methodology

4.4.1 Upscaling

Upscaling is an efficient method to reduce and optimise the computational costs and the required time for performing simulations. One of the main objectives of the present paper is to study the effects of different grid resolutions on the subsurface performance metrics of the CPG system and the error caused by this procedure. In this regard, four different resolutions - with the upscaling factor of 4 - (120×120, 60×60, 30×30, and 15×15) are considered.

To upscale the fine-scale model, grid cells are divided into groups of 2×2 blocks, as shown in Fig. 4.3(a). Then through an equation, a new parameter (k^* and ϕ^*) is calculated, which represents a single value for that block of 2×2 in the coarse-scale model. By repeating this procedure it is possible to produce upscaling models with different resolutions.

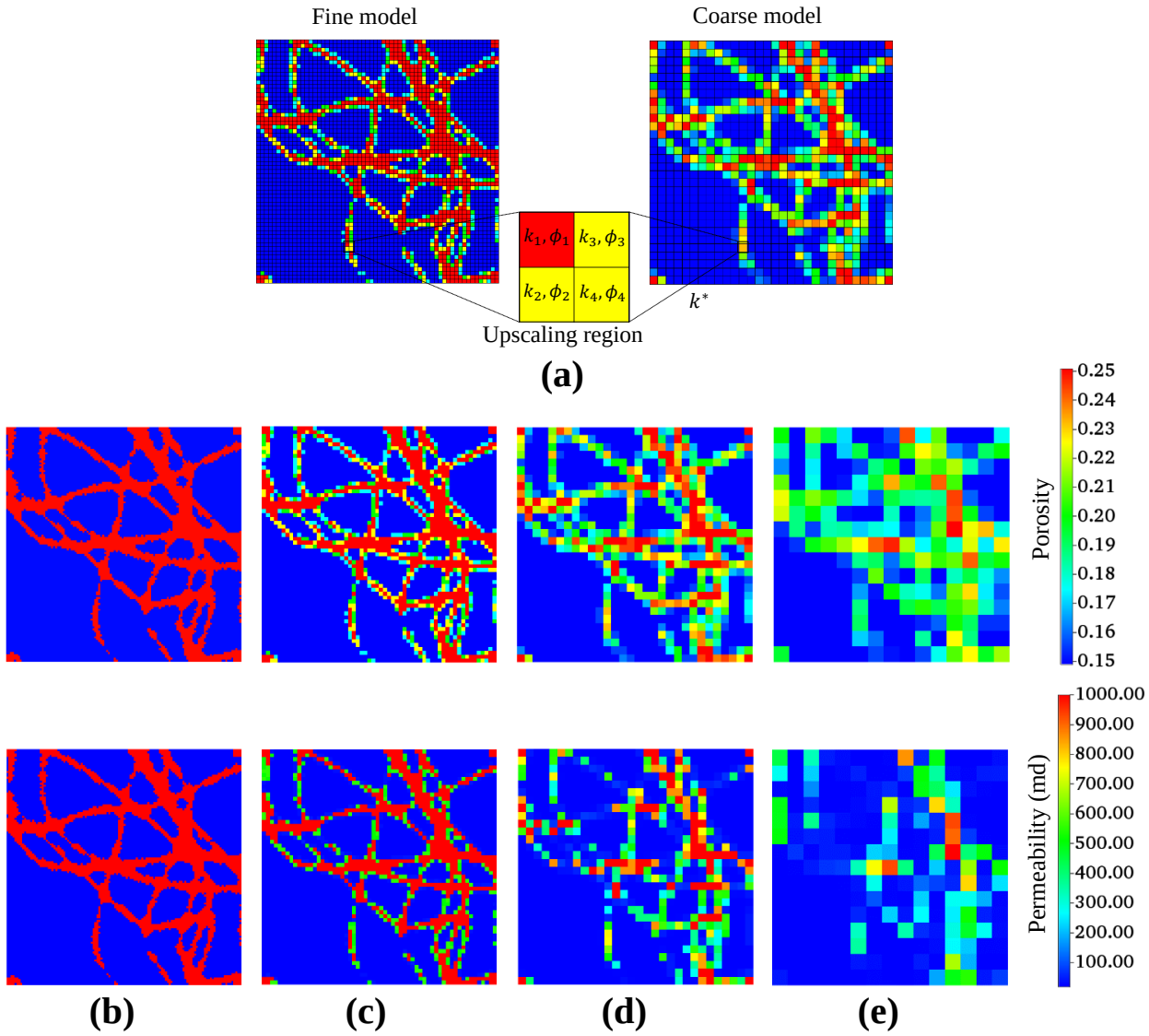

Figure 4.3: Top: Schematic of the upscaling process, and bottom: porosity and permeability maps at different grid resolutions used in the present study, from the fine-scale case (left) to the coarse-scale case (right) for the first realisation: (b) 120×120, (c) 60×60, (d) 30×30, and (e) 15×15.

Porosity is upscaled through weighted averaging as it is not a flow dependant property. On the other hand, permeability is flow-related and depends on flow direction. Therefore, to calculate upscaled permeability, the following equation is used [150, 151]:

$$k_i^* = \frac{A}{B + C} \tag{4.2a}$$

$$A = 4(k_1 + k_3)(k_2 + k_4)(k_2 k_4(k_1 + k_3) + k_1 k_3(k_2 + k_4)) \tag{4.2b}$$

$$B = (k_2k_4(k_1 + k_3) + k_1k_3(k_2 + k_4))(k_1 + k_2 + k_3 + k_4) \tag{4.2c}$$

$$C = 3(k_1 + k_2)(k_3 + k_4)(k_1 + k_3)(k_2 + k_4) \tag{4.2d}$$

As seen from Fig. 4.3(b) to 4.3(e), through the upscaling process, some channels and inter-channel sections are smeared. More severely, in the 15×15 case, some channels that were thinner (had low T_N) are disconnected from each other. It is anticipated that these variations considerably affect the results of different resolution cases. Also, this is why the channels' thickness is studied in the present work.

According to the permeability and the porosity distribution diagrams that are provided in Fig. 4.4, the porosity upscaling makes both the channel and the inter-channel areas smoother and the porosity distribution more normal, which is why even in the coarse case, the porosity of the field still maintains its original shape and channels are visible. However, for the permeability, the upscaling mainly affects the channel areas (permeability 800-1000) compared to the inter-channel ones (permeability 20-200). Therefore, at the coarse scale (low resolutions) connections between some channels are lost and some channels are smeared.

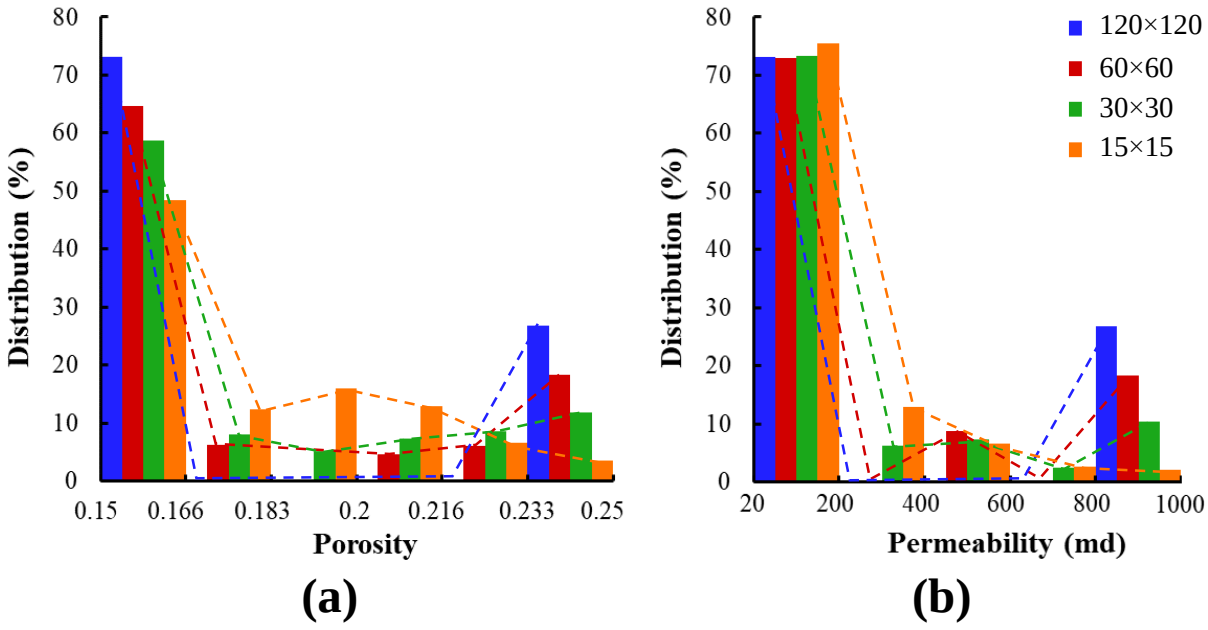

Figure 4.4: Porosity and permeability distribution throughout the reservoir in different grid resolutions. Upscaling makes the distribution more uniform, but for permeability, channel areas are smeared more compared to inter-channel ones.

4.4.2 Objective functions

The objective functions that are studied in the present work are divided into four groups: (1) pressure-related parameters including coefficient of performance (CoP), pumping energy loss, and the optimisation function that will be described later in this section; (2) temperature-related parameters such as production wells' average temperature drop, energy sweep, and thermal plume dispersion; (3) CO_2-related parameters, including stored CO_2 and the CO_2 storage efficiency; and (4) computational cost parameter including the simulations' runtime. According to the focus of the present study, all the performance metrics are calculated based on subsurface metrics. These objective functions are calculated based on the following equations.

The production wells' average temperature drop is calculated from Eq. 4.3, in which $T_{\text{res}}^{\text{initial}}$, T_{P1}^{t}, and T_{P2}^{t} are the reservoir initial temperature and production wells bottomhole temperatures at time t, respectively. This parameter can also be used to determine the lifetime of a CPG system by defining it as the time (years) when this parameter (dT) passes 1 °C, *i.e.*, dT >1 °C.

$$dT = T_{\text{res}}^{\text{initial}} - \frac{T_{P1}^{t} + T_{P2}^{t}}{2} \tag{4.3}$$

The total amount of the stored CO_2 at time t ($CO_{2_{\text{stored}}}^{t}$) in (million tonnes, Mt) is calculated through Eq. 4.4. $CO_{2_{\text{sc}}}^{t}$ is the amount of the $scCO_2$ inside the reservoir due to structural storage, $CO_{2_{\text{Mineral}}}^{t}$ is the amount of the CO_2 in the form of precipitated minerals, and $CO_{2_{\text{Dissolved}}}^{t}$ is the amount of the CO_2 dissolved into the brine. It is acknowledged that the amounts of the stored CO_2 in the present study do not represent the actual values of a CPG reservoir. However, since the present work is a comparative study, these values can be used for comparison purposes regarding CO_2 storage metrics.

$$CO_{2_{\text{stored}}}^{t} = (CO_{2_{\text{sc}}}^{t} + CO_{2_{\text{Mineral}}}^{t} + CO_{2_{\text{Dissolved}}}^{t}) \times 10^{-9} \tag{4.4}$$

Also, the CO_2 storage efficiency is defined as:

$$\eta_{CO_2}^{t} = \frac{CO_{2_{\text{inj,total}}}^{t} - CO_{2_{\text{prod,total}}}^{t}}{CO_{2_{\text{inj,total}}}^{t}} \times 100 \tag{4.5}$$

The dimensionless parameter that shows the heat extraction quality and the remaining potential heat inside the reservoir is the energy sweep (S):

$$S = \frac{E_{\text{prod}}}{E_{\text{r}}} \tag{4.6a}$$

$$E_{\text{prod}} = E_{\text{prod,brine}} + E_{\text{prod,CO}_2} \tag{4.6b}$$

$$E_{\text{prod,brine}} = \int_0^t (\rho c)_w Q^t_{w,P1}(T^t_{P1} - T_{\text{inj}})dt + \int_0^t (\rho c)_w Q^t_{w,P2}(T^t_{P2} - T_{\text{inj}})dt \tag{4.6c}$$

$$E_{\text{prod,CO}_2} = \int_0^t (\rho c)_{CO_2} Q^t_{CO_2,P1}(T^t_{P1} - T_{\text{inj}})dt + \int_0^t (\rho c)_{CO_2} Q^t_{CO_2,P2}(T^t_{P2} - T_{\text{inj}})dt \tag{4.6d}$$

$$E_{\text{r}} = \int_{i=1}^{N_b} ((\rho c)_w \phi^0_i + (\rho c)_r (1 - \phi^0_i))(T^{\text{initial}}_{\text{res}} - T_{\text{inj}})dV_{bi} \tag{4.6e}$$

In the above equations, E_{prod} is the amount of the extracted heat from the reservoir after t years, and E_r is the total amount of the energy available in the reservoir at the initial state. ρ and c represent the fluids (CO_2/brine) density and specific heat capacity, respectively. Also, Q^t_P represents the fluids volumetric production rate at time t, T^t_P shows the production wells bottomhole temperature at time t, T_{inj} is the scCO$_2$ injection temperature, N_b is the number of grid blocks, ϕ^0_i shows the initial porosity of cell i, and dV_{bi} shows the volume of block i.

Another dimensionless parameter that is used to optimise doublet/well spacing is CoP, which also takes into account the amount of the pumping energy loss (E_{pump}) inside the reservoir.

$$\text{CoP} = \frac{E_{\text{prod}}}{E_{\text{pump}}} \tag{4.7a}$$

$$E_{\text{pump}} = \frac{Q^t_{\text{CO}_2,\text{avg}}}{\varepsilon} \int_{t=0}^{t} \frac{P_{I1} + P_{I2} - P_{P1} - P_{P2}}{2} dt \tag{4.7b}$$

In the above equations, ε is the pump efficiency of 0.6, $Q^t_{\text{CO}_2,\text{avg}}$ is the total injection rate of scCO$_2$, calculated by integral averaging in the case of varying injection rates, and P_I and P_P are the bottomhole pressures of the injection and production wells respectively. Therefore, the injection rate provided in Section 4.3.1 should be converted to the scCO$_2$ rate by considering its density.

A main objective function is defined as Eq. 4.8 to include both CoP and S in a single dimensionless parameter and to optimise doublet/well spacing.

$$f^t = S^t \times \text{CoP}^t \tag{4.8}$$

Another parameter that is considered in this study is CO_2 thermal plume dispersion (%), which is directly related to flow patterns inside the reservoir and the optimum doublet/well

spacing. This parameter is defined as the percentage of the grid blocks, whose temperatures are dropped more than 5 °C from the initial reservoir temperature ($T_{\text{res}}^{\text{initial}}$).

4.4.3 Simulations and runs

The main objective of the present study is to investigate the upscaling effects and to optimise the doublet/well spacing (L) based on the subsurface objective functions defined in Section 4.4.2. In addition, parameters such as different injection flow rates and duration; open/closed boundary; and channels' presence, thickness, and orientation are also considered as variables. To this end, various simulations are designed as described in Table 4.2.

To perform these simulations, a finite volume-based fully coupled geochemical compositional EoS simulator (CMG-GEM) is utilised. A simulation validation was provided in the previous work done by the authors [38]. Also, as described in Section 4.3.2, a full description of the equations and solvers methodology are provided in [62] and [38].

Table 4.2: Different simulation scenarios considered at the present study and their description.

Studied variable	**Varying parameters**	**Number of simulations**	
		New	**Total**
Upscaling resolution	10 doublet/well spacing: 100, 200, 300, 400, 500*, 600, 700, 800, 900, 1000 (m) 4 resolutions (120 × 120, 60 × 60*, 30 × 30, 15 × 15)	40	40
Channel thickness (T_N)	5 T_N (0.035*, 0.062, 0.097, 0.137, 0.171) 4 resolutions 25 realisation (Fig. 4.2(b))	80	100
Doublet/well spacing (m)	10 doublet/well spacing as above 3 resolutions (60 × 60, 30 × 30, 15 × 15) 10 realisations (Fig. 4.2(a))	270	300
Channels orientation	4 cases (45°*, 0°, -45°, and 3 no-channel cases) 10 doublet/well spacing 15 realisations (Fig. 4.2(c))	130	180
Flow rate (m^3/day)	8 flow rates (1.5×10^3, 1.5×10^4, 0.5×10^5, 1×10^5, 1.5×10^5*, 2×10^5, 2.5×10^5, 1.5×10^6) 10 doublet/well spacing	70	80
Boundary condition	2 boundary conditions (open and close*) 8 flow rates 10 doublet/well spacing	80	160

* indicates parameters that are used as constant parameters for other simulations.

4.5 Results and discussion

In this section, first, the results of the upscaling effects on the performance metrics of the CPG are analysed. Then, the results of the doublet/well spacing optimisation, as well as the effects of the channels' thickness and orientation, and injection rate and span are reported.

4.5.1 Effects of upscaling and doublet/well spacing on the objective functions

Main case

A benchmark case is considered for the future comparisons. This benchmark case is a 120×120-grid block fine-scale model with channel thickness (T_N) of 0.035 and 45° orientation, doublet/well spacing (L) of 500 m, and the injection rate of CO_2 1.5×10^5 m^3/day. The boundary conditions are closed for flow, and capillary pressure is considered for this case. The model is simulated for 20 years of CO_2 injection and its results are reported in Fig. 4.5.

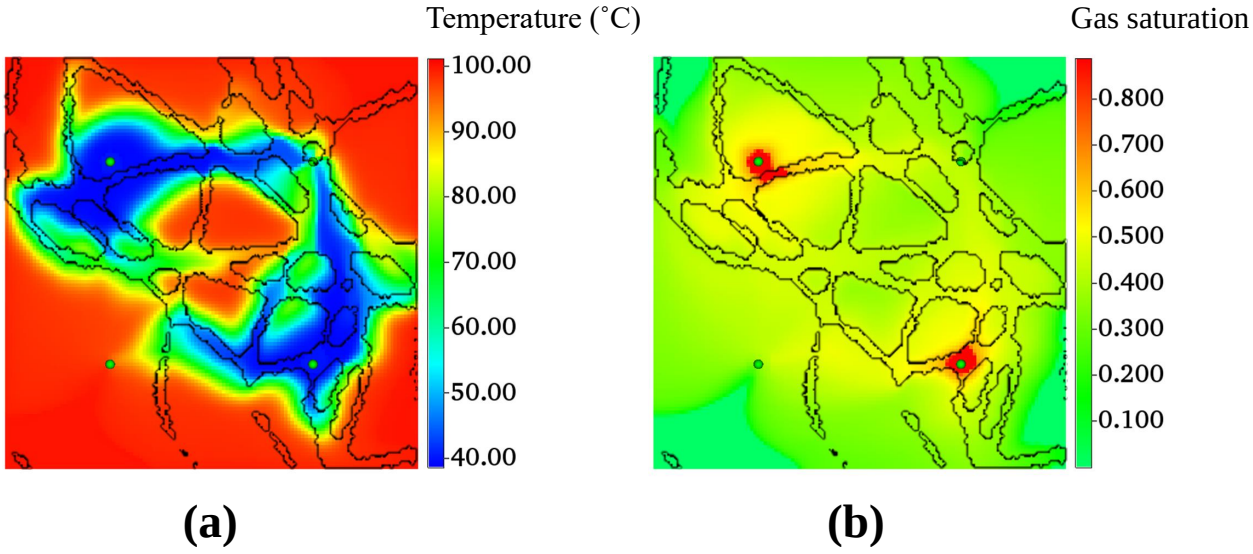

Figure 4.5: Results of the main case (L =500 m) after 20 years of injecting CO_2 with T_{inj}=40 inside a heterogeneous fluvial reservoir: (a) temperature distribution, and (b) CO_2 saturation distribution.

Based on the temperature plume distributions in Fig. 4.5(a), thermal plume is expanded in the channels' direction and optimistically only half of the reservoir's thermal potential is used, which is mainly because of the channelised nature of the reservoir. Therefore, it is expected that the CPG system lifetime and energy sweep parameter (S) to be less than those of the homogeneous reservoirs. Same observation is deduced from the saturation profile in Fig. 4.5(b). However, compared to thermal plume, it is seen that CO_2 has reached places far from the channels' route, showing that the areas close to the two-phase region outer boundary (low CO_2 saturation) do not have a noticeable impact on the reservoir's temperature drop.

Upscaling and doublet/well spacing effects on the performance metrics

To study the effects of upscaling on the performance metrics of the system and the error resulted from this process, 40 simulations were carried out. The behaviour of each parameter is studied versus doublet/well spacing as well as the grid resolution. The average errors, reported in this section, are calculated by comparing the results to those of the fine-scale model (120×120).

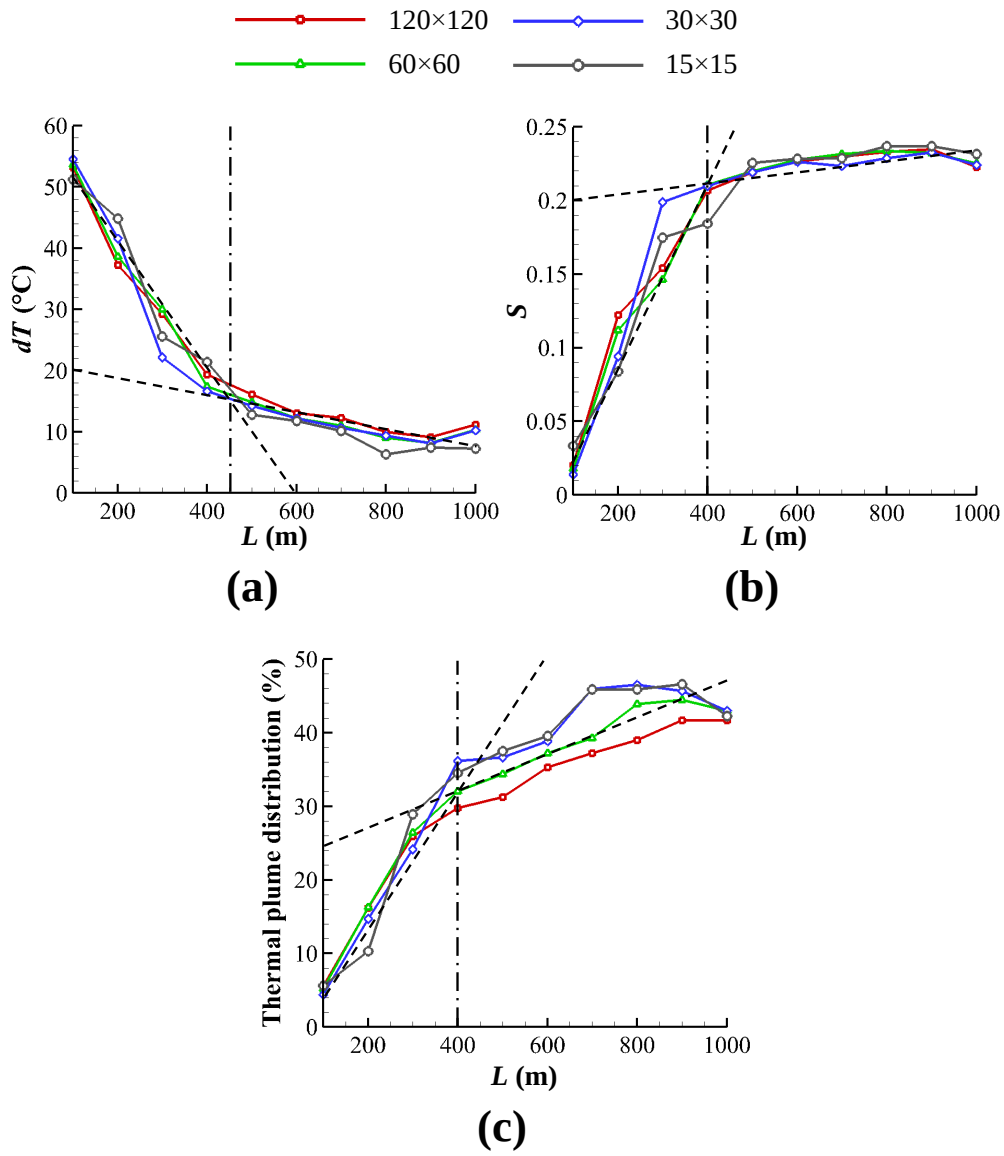

Figure 4.6: Effects of upscaling and doublet/well spacing on temperature-dependant metrics: (a) production wells' temperature drop; (b) energy sweep parameter; and (c) CO_2 thermal plume distribution, after 20 years. The vertical dashed lines show the doublet/well spacing at which the slope of variations in temperature-dependant parameters reduces, and the optimum performance happens.

Fig. 4.6(a, b, & c) show the results of the first group of performance parameters, which are related to temperature distribution inside the reservoir, and temperature is the dominant factor affecting them. The performance metric dT, which is the average temperature drop of the production wells, is shown in Fig. 4.6(a) as a function of doublet/well spacing (L). As the doublet/well spacing increases, less cold CO_2 reaches the vicinity of the production wells. As a result, the temperature reduction in production wells decreases (from about 50 °C for L = 100 m to 8.97 °C for L = 1000 m). As shown in this figure, at a doublet/well spacing between 400 and 500 m, the slope of dT variations is greatly reduced and after that distance, the increase of L has a negligible effect on the reduction of dT. The reason for this phenomenon is that the number of the cells affected by CO_2 thermal plume and the ones not affected, reaches a balance at this point. This will be more discussed in Section 4.5.2. The errors resulted from the upscaling process for this parameter are about 6.9, 10.74, and 18.44% for 60×60, 30×30, and 15×15 cases, respectively.

Fig. 4.6(b) shows the energy sweep parameter. As the doublet/well spacing increases, more areas of the reservoir are covered by the injected CO_2 and S is increased by a factor of 10 from L=100 m to L=1000 m. Again, the same change of variations in slope is observed at a distance of about 400 m. Also, it is seen that the error caused by the upscaling is high for very low doublet/well spacing ($L < 300$ m). Fig. 4.6(c) illustrates the variations of thermal plume dispersion. Upscaling affects this parameter more than the previous ones, and the deviation of the 30×30 and 15×15 cases from the fine-scale model is more noticeable. Also, it is observed that because of fluvial channels inside the reservoir, only about 45-59% of the reservoir is affected by the CO_2 thermal plume. Therefore, the definition of the licence area in heterogeneous fields, especially with braided channels, should be modified compared to conventional homogeneous models.

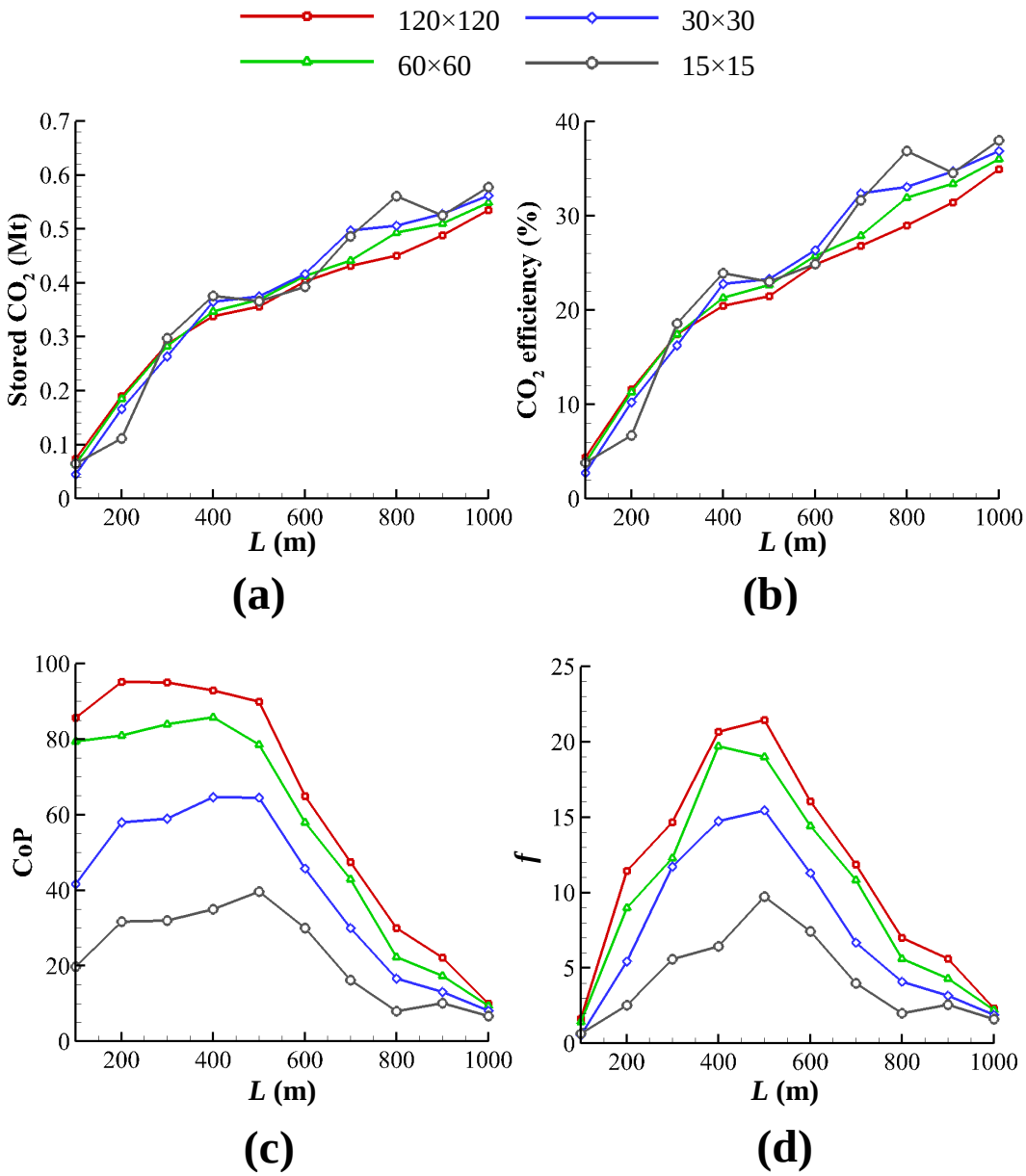

Figure 4.7: Effects of upscaling and doublet/well spacing on the subsurface performance metrics: (a) stored CO_2 inside the reservoir; (b) CO_2 storage efficiency; (c) CoP; and (d) the optimisation function, after 20 years. The system's maximum performance happens at doublet/well spacing of about 400-500 m.

Fig. 4.7(a & b) show the CO_2-related metrics, including storage and efficiency. As the doublet/well spacing (L) increases, CO_2 has a greater portion of the reservoir to be stored in, therefore, stored CO_2 will increase. As in Fig. 4.7(a), by increasing L from 100 to 1000 m, stored CO_2 increases by about 0.46 Mt. Nevertheless, similar to the temperature-dependant parameters, a change in the slope of the diagram (around L=400 m) is observed. Also, It is seen that the upscaling error for low and high values of L are high, and for the

average doublet/well spacing around 500 m, errors are lower than those for the temperature dependant parameters. Same observations are applicable for the results of CO_2 efficiency shown in Fig. 4.6(b). By increasing L, CO_2 will reach the production wells at a later time, therefore CO_2 storage efficiency will increase (about 30.5% when L increases from 100 to 1000 m). However, CO_2 storage is not the only decisive parameter in the efficiency of a system, and parameters such as CoP, which are not always ascending by increasing L, also affect the economical feasibility of the system.

The third group of the objective functions are the dimensionless parameters of CoP and f, which are highly affected by the pressure drop between the injection and the production wells. CoP of the system is defined as the proportion of the extracted heat to the pumping energy loss inside the reservoir. As illustrated in Fig. 4.7(c), when L is too small or too high, CoP reduces. The former is because at low doublet/well spacing, the injected CO_2 rapidly reaches the production wells. Having little time to exchange heat with the reservoir, less heat is extracted. However, when the injection and the production wells are close to each other, the pressure drop is smaller and less pumping energy loss happens. The reduced pumping loss will partly compensate for the deficiency in heat extraction (both the nominator and the denominator of the Eq. 4.7a will decrease). Therefore, the CoP drops less at low doublet/well spacing compared to high doublet/well spacing. On the other hand, when doublet/well spacing increases above 500 m (L >500 m), the heat extraction does not change considerably, however, the pressure drop between the injection and the production wells considerably increases. As a result, the denominator of the CoP equation grows, which results in a noticeable CoP reduction (from 89.87 for L=500 m to 9.97 for L=1000 m).

According to Fig. 4.7(d), since the effect of produced energy from the reservoir is more pronounced in the definition of f, this parameter decreases more sharply at low doublet/well spacing (L < 400 m) compared to CoP. This results in the appearance of a peak in the diagram at L=500 m. It is observed that in this doublet/well spacing, the objective function is about 9.26 and 13.02 times higher than its values for L=1000 and 100 m, respectively.

Regarding the upscaling error, it is seen that upscaling has the highest impact on pressure-related parameters. As mentioned in Section 4.4.1, while reducing the resolution of the generated model, some channels will fade and some originally connected channels will be disconnected from each other, especially in permeability fields that upscaling mainly affects channel areas rather than inter-channel areas. This significantly affects and increases the pressure drop. Therefore, by reducing the resolutions of the model, CoP and f will greatly decrease, resulting in a significant deviation and error from the fine-scale model. For the

objective function, the maximum amounts are 21.44, 19.72, 15.45, and 9.74 for the 120×120, 60×60, 30×30, and 15×15 resolutions, resulting in errors of 4.63, 27.94, and 54.57% compared to the fine-scale model, respectively.

Finally, simulations runtimes are presented in Fig. 4.8. This figure shows the average required time to perform simulations in each grid resolution. By decreasing the resolution, the required time decreases with a logarithmic trend. The required runtime for simulations are 13621, 1326.4, 159.89, and 28.82 s for 120×120, 60×60, 30×30, and 15×15, respectively. In this figure, also the average error resulted from upscaling is reported for all the objective functions. As described in the previous sections, the order of largest errors is as the following: first are the pressure-related parameters, second are the temperature-related parameters, and third are the CO_2 storage parameters, with average values of 11, 5, and 4% for the optimum resolution, respectively. The optimum region (the green area in Fig. 4.8) is defined such that the errors be at an acceptable range (less or about 10%) and the required computational costs are minimised at the same time.

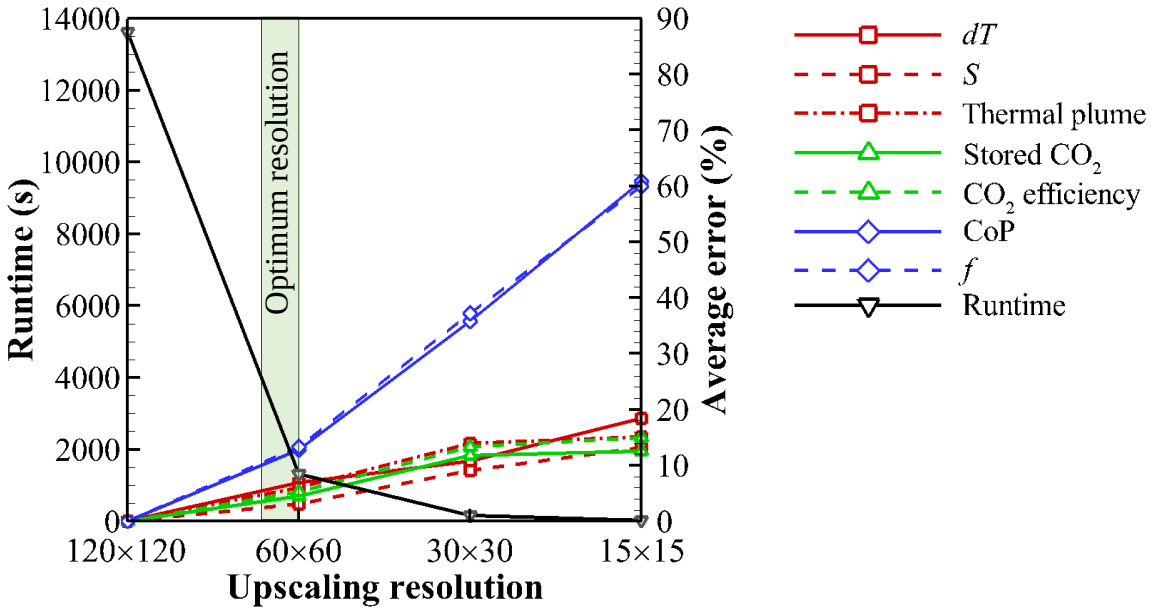

Figure 4.8: Average upscaling error for all objective parameters and the simulations average runtime. The green area represents the upscaling resolution that provides an error of less than about 10% and a runtime of about half an hour for each case.

Effects of channels' thickness on the upscaling error and performance metrics

To study the effects of channels' thickness, 25 braided realisations, as shown in Fig. 4.2(b), are considered. Based on Fig. 4.9(a & b), a fluvial reservoir with thicker channels ($T_N = 0.137$) provides higher performance metrics of CoP and f by a factor of about 4.5 compared to $T_N = 0.035$, which is because increasing channels thickness greatly reduces the pressure loss inside the reservoir and at the same time slightly increases heat extraction.

As observed in Section 4.4.1, through upscaling some of the channel areas are smeared and some channels become disconnected. As in Fig. 4.9(c), when the channel thickness (T_N) is low, smearing happens more intensely, and as a result, more channel areas are smeared due to the decrease in the resolution. As a result, the upscaling error increases. The same happens when the channel thickness is high (geologically happens when flow had passed through channels for many years). In this situation, inter-channel areas are more affected compared to the channel ones. Therefore, again, at high values of T_N the amount of error increases. The minimum upscaling error happens at $T_N \approx 0.14$.

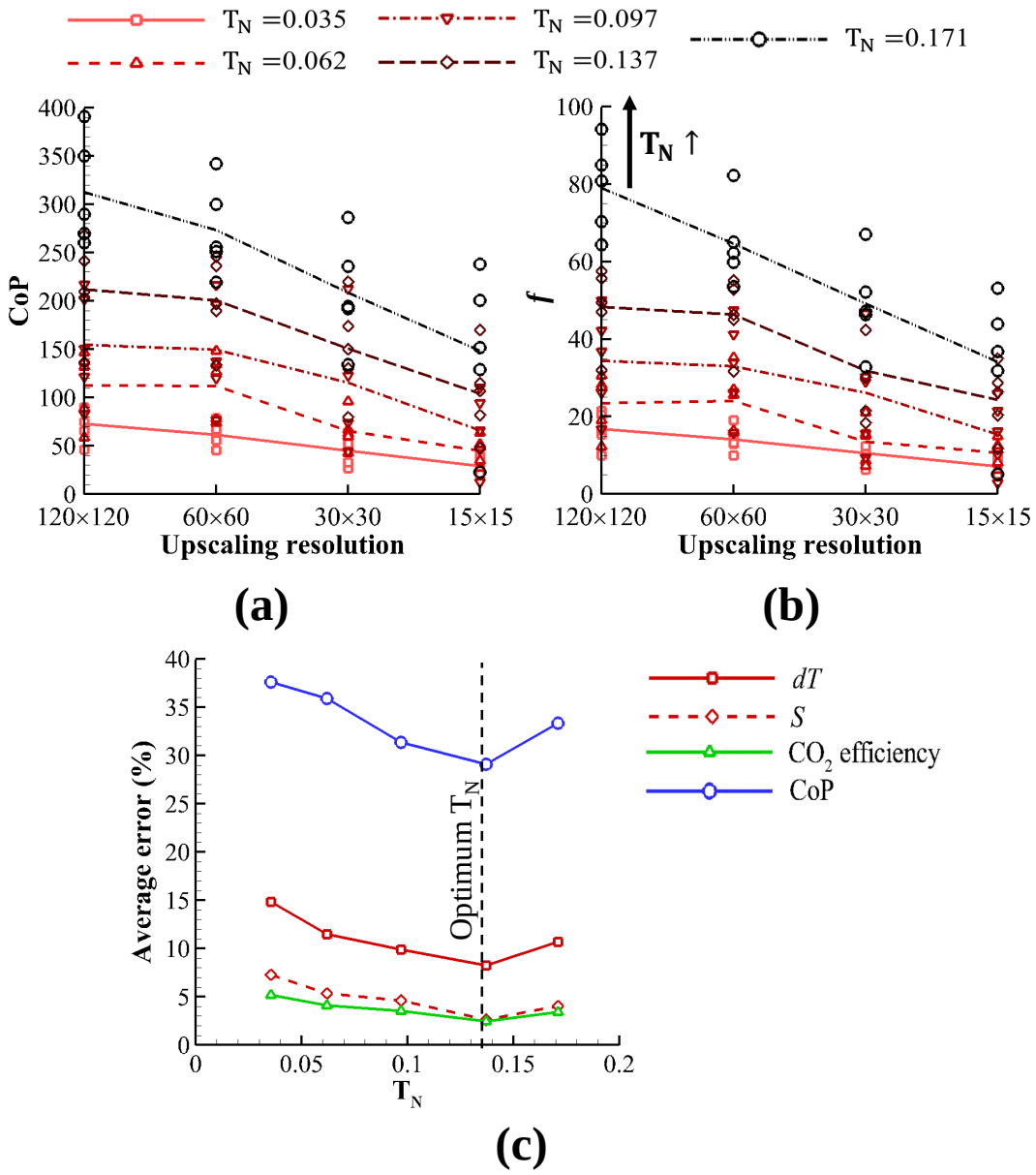

Figure 4.9: Effects of braided fluvial channel thickness (T_N) on: (a) CoP, (b) f, and (c) the average error of upscaling (between the finest and the 30 × 30 resolution) for different objective parameters after 20 years (L =500 m). The vertical dashed line in Fig. (c) shows the channel thickness that experiences the least upscaling error.

4.5.2 doublet/well spacing optimisation

Doublet/well spacing significantly affects the performance metrics of a CPG system, therefore it is crucial to find an optimised L that provides the system with the highest overall efficiency. To do so, 10 channelised realisations as shown in Fig. 4.2(a) are used. Based on the results

provided in Fig. 4.10(a), all these realisations have an optimum doublet/well spacing around L =450 m (exactly the distance at which the slope of the temperature related diagrams changed). This value is confirmed by the average f diagram reported in Fig. 4.10(b). As seen in this figure, the optimum doublet/well spacing has a value between 400 to 500 m.

The flow pattern of CO_2 inside the reservoir leads to this optimum value. Generally, in a homogeneous reservoir, flow patterns follow a simple source and sink pattern as shown in Fig. 4.10(c). In the heterogeneous case, although fluvial channels affect this pattern, the overall trend remains the same. As seen in profiles in Fig. 4.10(d), after L = 500 m, the thermal plume variations (which is also a representative of scCO_2 distribution inside the reservoir) becomes subtle, and the area inside the CO_2 plume (A_2) reaches a balance with the area outside the plume (A_1). This is why in Section 4.5.1, it was observed that after 500 m the variations of the slope of the temperature-related parameters dropped. In conclusion, by increasing doublet/well spacing above 500 m, the extracted energy from the reservoir does not increase considerably and cannot compensate for the pressure drop between the wells. Therefore, the pumping energy loss dominates the objective function (f) and results in its decrease for high values of (L).

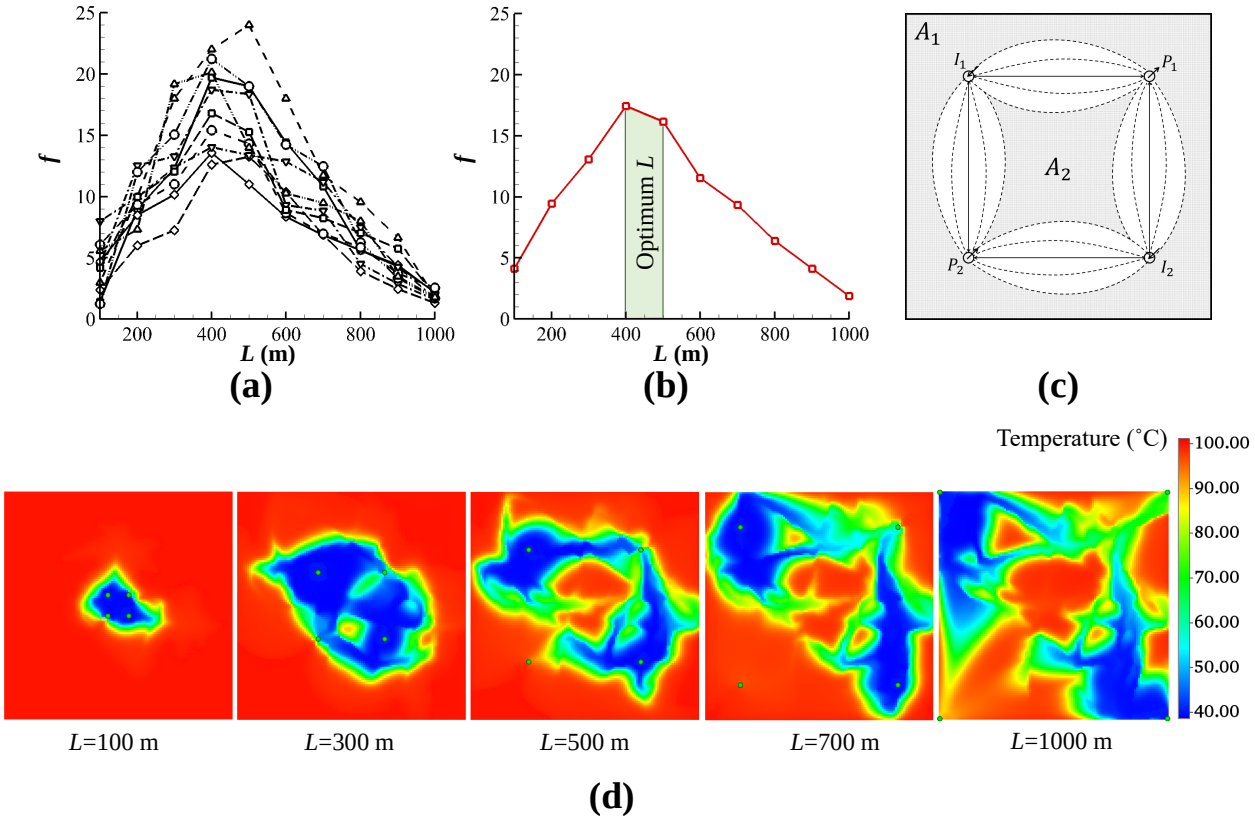

Figure 4.10: doublet/well spacing optimisation: (a) objective function results for 10 different realisations, (b) average objective function for all the cases vs. doublet/well spacing, (c) general CO_2 distribution pattern that follows a source and sink model, and (d) temperature profiles for different doublet/well spacing after 20 years.

Effects of channels' orientation on the optimised doublet/well spacing and performance of the system

Fluvial channels' orientation with respect to injection wells (I_1 and I_2) is another parameter that affects the performance of a CPG system. In this regard, 6 different cases, including 3 homogeneous ones, are considered. First, is the case that the I_1-I_2 line (as in Fig. 4.11(a)) is parallel to the channels' direction, which is referred to as the $\theta = 45°$ case. Second, is the case that the I_1-P_2 and I_2-P_1 lines are aligned with channels, rather than I_1-I_2. Third, is the case that the I_1-I_2 line is perpendicular to the channels direction ($\theta = -45°$); and finally, 3 cases with no fluvial channels are also considered to generally study the effect of fluvial channels on the performance of the system. These homogeneous cases comprise a low permeability/porosity field with $k = 20$ mD and ϕ =0.15 as the inter-channel areas

(case 1), a case with average permeability/porosity equal to those of the fluvial cases (case 2), and a case with high permeability/porosity with k = 1000 mD and ϕ =0.25 similar to channels (case 3). For each orientation scenario, 5 realisations are designed (Fig. 4.11(a)). Fig. 4.11(b) represents the results of the channels' presence and orientation effect on f versus doublet/well spacing. Firstly, it is observed that the system performance is highly affected by the presence of fluvial channels. Compared to the low permeability/porosity case (case 1), a CPG system with a braided reservoir highly outperforms the homogeneous reservoir (by about 3 to 4 times higher f). However, compared to the cases with similar average permeability/porosity (case 2) and the high permeability/porosity case (case 3), the braided reservoir has a lower system performance by about 3 and 5 times, respectively.

Secondly, similar to the water-based geothermal systems [138], a CPG system, with the I_1-I_2 line parallel to the heterogeneities' general direction, provides the highest performance compared to other orientation cases. This is because, as discussed in 4.5.2, unlike the heat extraction parameter, the pumping loss variation for these cases is considerably high. Therefore, the case with the lowest pumping loss ($\theta = 45^\circ$) provides the highest performance. Moreover, although there are different system performances in these cases, all of them have an optimum doublet/well spacing between 400 to 500 m, which shows that this value is independent of the channels' presence and direction.

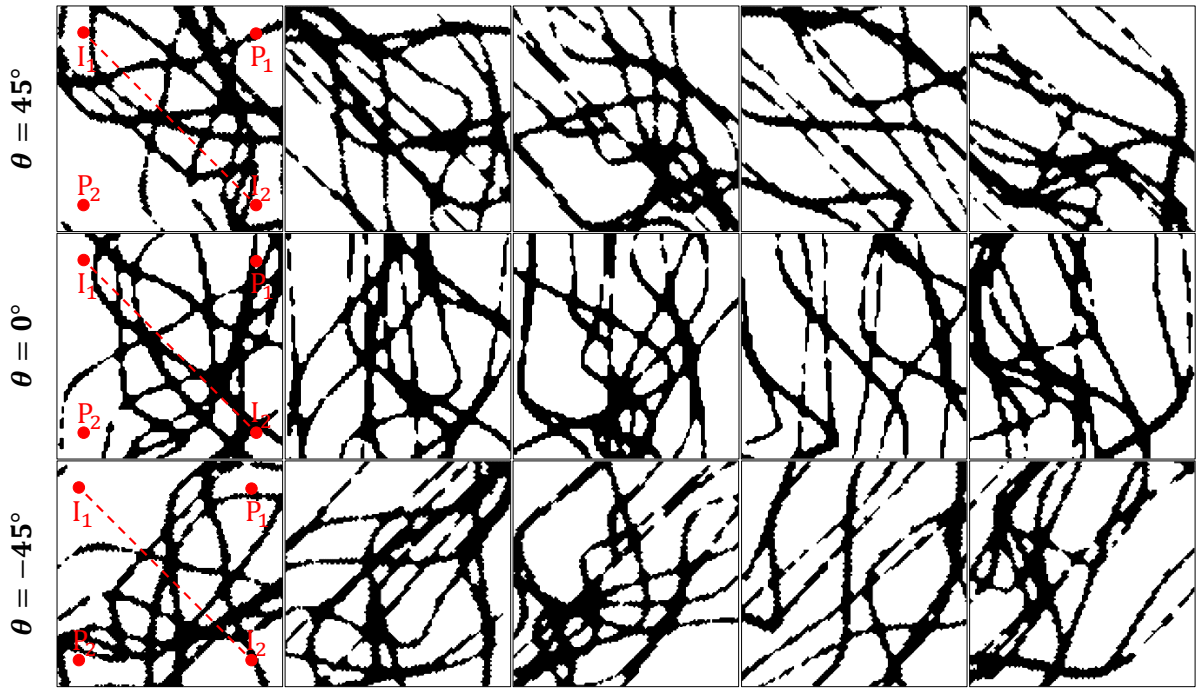

(a)

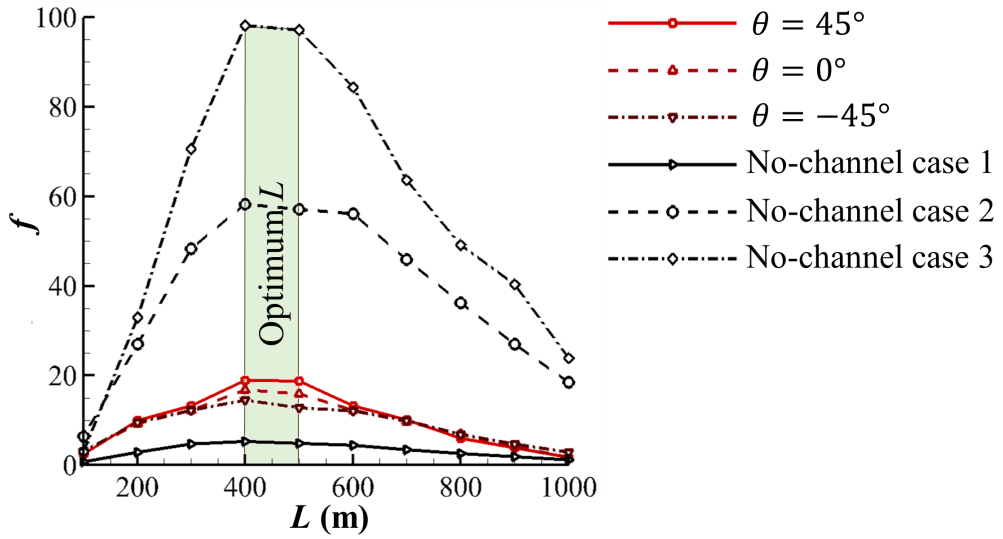

(b)

Figure 4.11: Effects of channels orientation on the optimisation functions f and the optimum doublet/well spacing. (a) 15 different realisations with channels orientation of $\theta = 45°, 0°$, and $-45°$ with respect to the I_1-I_2 line. (b) Objective function versus doublet/well spacing for different orientations and homogeneous cases, in which, case 1 has a $k = 20$ mD and ϕ =0.15 as the inter-channel areas, case 2 has an average permeability/porosity equal to those of the fluvial cases, and case 3 has a $k = 1000$ mD and ϕ =0.25 similar to the channels.

Effects of injection and boundary conditions on optimised doublet/well spacing and performance of the system

Here, 8 flow rates, including both low and high flow rates are considered. Fig. 4.12(a) shows the variations of the objective function for different flow rates for both open and closed boundary conditions. As the flow rate increases, the optimum L moves toward higher values. For instance, by increasing the flow rate from 1.5×10^3 to 1.5×10^4 and 1.5×10^5, the optimum L moves from 100 m to 400 m and then to 600 m, respectively. According to Fig. 4.12(a), the optimum L (green line) follows a logarithmic behaviour versus the injection rate. Also, a considerable change in the injection flow rate (multiplying by a factor of order 10) is required to make the optimum spacing vary noticeably, *i.e.*, low flow rate variation will not affect the optimum L. This is the reason why in low flow rate variations (0.5×10^5), the value of optimum L is the same for all injection rates. In addition to the flow rate, the injection time span can also alter the optimum doublet/well spacing. For CPG systems with higher CO_2 injection periods, the optimum L moves toward higher values (as shown in Fig. 4.12(b)). However, similar to the injection flow rate, considerable variations in the injection span are required to change the optimum spacing. In conclusion, for a typical CPG system with a conventional injection rate and lifetime, the optimum doublet/well spacing (L) has a value of around 500 m.

Finally, to study the effects of open flow boundary type, 80 cases with open flow boundaries using the PVM method (described in Section 4.3.1) are considered. A comparison between the results of the open and the closed flow boundary cases is also provided in Fig. 4.12(a & b). As the injection rate and the injection span increase, the boundary condition effect increases as well. However, it is observed that except for high doublet/well spacing that wells are close to reservoir boundaries, the boundary type does not affect the results, and therefore the trend of the f diagram and the optimum doublet/well spacing remains the same.

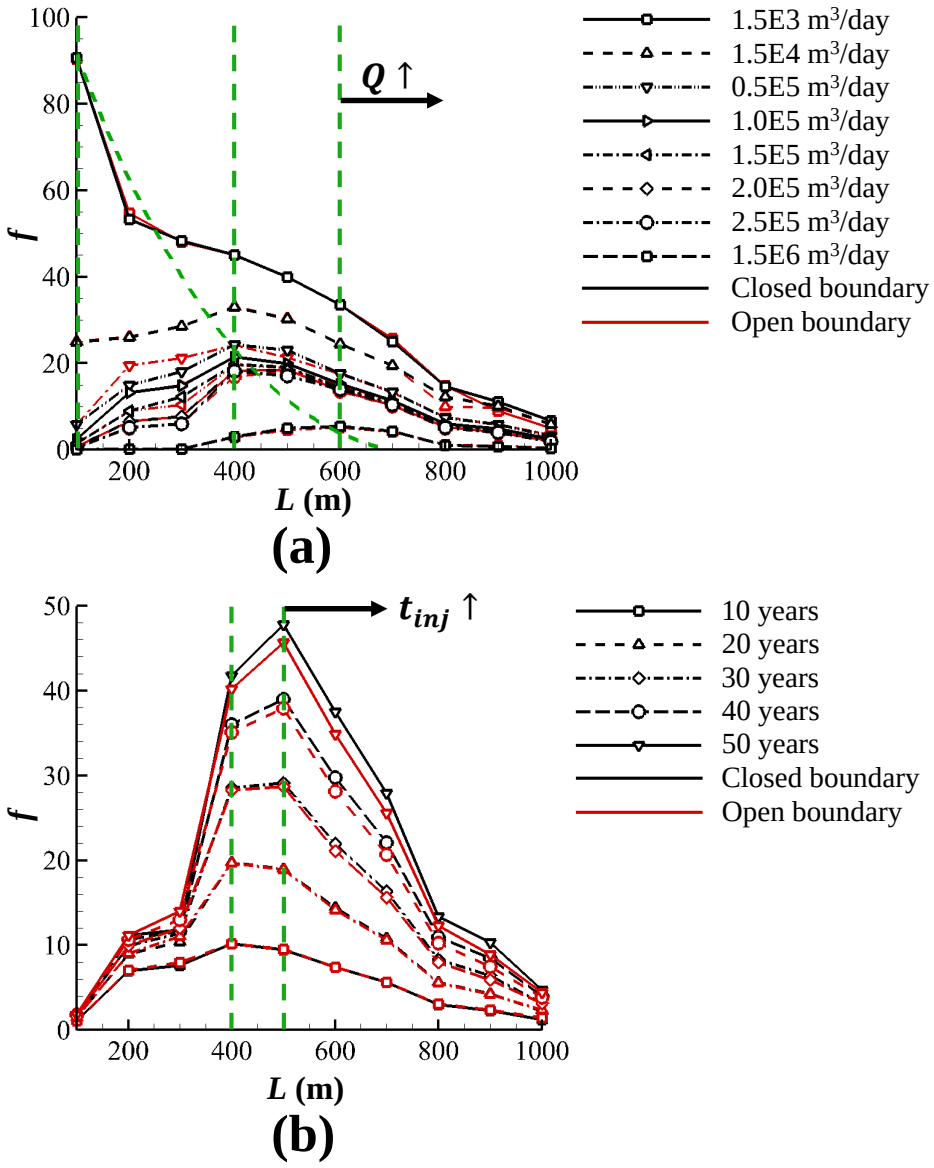

Figure 4.12: Effects of (a) injection flow rate, and (b) injection span on the optimised doublet/well spacing for both open and closed boundary conditions. Green lines show the optimum L for each case.

4.6 Conclusions

This study optimised the doublet wells spacing, as well as the required grid resolution for capturing heterogeneities, through a series of simulations (with 50 different braided fluvial realisations) and subsurface performance metrics. The key findings of the present study are:

- The upscaling error from the highest to lowest values occurred for pressure-related

parameters, temperature-related parameters, and CO_2 parameters. In addition, simulation runtime is reduced with a logarithmic trend as the grid resolution decreased.

- The CPG system has a better performance in reservoirs with higher channels' thickness. Also, if the channel thickness is either low or high, the upscaling error will increase, and that is because in each case some areas (whether channel or inter-channel) are smeared, mainly affecting the pressure-related parameters.

- The optimised doublet/well spacing was found to be between $400 < L < 500$ m ($L \approx 450$ m) for both homogeneous and fluvial heterogeneous cases. Both the injection rate and the injection duration of the $scCO_2$ affect the optimum L. However, the effects of the injection rate are more noticeable compared to injection span. The injection rate can change the optimum L only when it is either enlarged 10 times or lowered by 1 tenth. In other words, high variations in injection rate are required to change the optimised L. As a result, our key finding is that for a typical CPG system with conventional injection rates and lifetime, the value of the optimum L is about 500 m, for a "checkers-board layout" of doublet/well pattern.

- Presence of fluvial channels in a reservoir highly affects the performance of the CPG system (by a factor between 3 to 5). A homogeneous reservoir, with an average permeability and porosity similar to the channelised case, outperforms the fluvial reservoir by a factor of 3 in terms of net power. Also, the case with I_1-I_2 line (injection wells) parallel to channels' direction ($\theta = 45°$) provides the highest optimisation function (f). However, for all orientation cases, the optimum doublet/well spacing is the same and about 450 m.

Our future studies will include a fully heterogeneous 3D reservoir CPG model as well as wellbore and power cycle modelling to analyse the effects of field heterogeneity replicating an actual field case. The results obtained in the present study, particularly the determination of the optimal grid resolution for both homogeneous and heterogeneous cases, as well as the optimal doublet/well spacing, offer valuable guidelines for conducting future numerical simulations with high accuracy and low computational costs.

Acknowledgement

The authors acknowledge the University of Manchester President's Doctoral Scholar (PDS) award to Amir Mohammad Norouzi that made this research possible.

Nomenclature

c_{p}	Specific heat capacity, [kJ.kg^{-1} K^{-1}]
c_{ϕ}	Rock compressibility, [kPa^{-1}]
dT	Temperature drop, [°C]
f	Objective function, [-]
k	Permeability, [mD]
k^{*}	Upscaled permeability, [mD]
L	Doublet/well spacing, [m]
$\dot{m}$	Mass flow rate, [kg.s^{-1}]
n	Number of channels, [-]
P	Pressure, [MPa]
P_{cap}^{0}	Initial capillary pressure, [MPa]
Q	Volume flow rate, [m^3.day^{-1}]
S	Energy sweep parameter/saturation, [-/-]
$\hat{S}$	Salinity, [mg.L^{-1}]
T	Temperature, [°C]
T_N	Dimensionless channel thickness, [-]
t	Time, [year, s]
V	Cell volume, [m^3]
Greek letters	
γ	Capillary force parameter, [-]
ε	Pump efficiency, [-]
$\eta_{\mathrm{CO_2}}$	CO_2 storage efficiency, [%]
θ	Channels' orientation, [°]
μ	Dynamic viscosity, [Pa s]
ρ	Density, [kg.m^{-3}]
ϕ	Porosity, [-]
ϕ^{*}	Upscaled porosity, [-]
Subscripts	
avg	Average
I	Injection well
initial	Initial condition
inj	Injection
P	Production well
prod	Production well
res	Reservoir
sc	Supercritical
w	Water

Chapter 5

CO_2-plume geothermal: Power net generation from 3D fluvial aquifers

This chapter is a modified version of the paper published in '*Applied Energy*'.

Authors: **A. M. Norouzi**, F. Pouranian, A. Rabbani, N. Fowler, J. Gluyas, V. Niasar, J. Ezekiel, M. Babaei. CO_2-plume geothermal: Power net generation from 3D fluvial aquifers. *Applied Energy*, Vol.332, p.120546, 2023.

5.1 Abstract

Previously CO_2, as a heat-extraction fluid, has been proposed as a superior substitute for brine in geothermal energy extraction. Hence, the new concept of CO_2-plume geothermal (CPG) is suggested to generate heat from geothermal aquifers using CO_2 as the working fluid. In January 2015, a CPG-thermosiphon system commenced at the SECARB Cranfield Site, Mississippi. By utilising CO_2, the demand for the pumping power is greatly reduced due to the thermosiphon effect at the production well. However, there are still parameters such as aquifer thermal depletion, required high injection rates, and CO_2-plume establishment time, that hinder CPG from becoming viable. Moreover, the fluvial nature of sedimentary aquifers significantly affects the heat and mass transfer inside the aquifer, as well as the system performance. In the present study, a direct-CO_2 thermosiphon system is considered that produces electricity from a 3D braided-fluvial sedimentary aquifer by providing an excess pressure at the surface that is used in the turbine. The system performance and net power output are analysed in 15 3D fluvial heterogeneous - with channels' widths of 50, 100, and 150 m - and three homogeneous aquifer realisations with different CO_2 injection rates. It is observed that the presence of fluvial channels significantly increases the aquifer thermal depletion pace (22-120%) and therefore, reduces the system's performance up to about 75%. Additionally, it is found that the CPG system with the CO_2 injection rate of 50 kg/s and the I-P line parallel to the channels provides the maximum cycle operation time (44 years), as well as the optimum performance for the heterogeneous cases of the present study by providing about 0.06-0.12 TWh energy during the simulation time of 50 years. Also, to prevent rapid drops in excess pressure, a system with a yearly adjustable injection rate is implemented, which prevents the production well bottomhole temperature to fall below 80 °C.

Keywords: CO_2-plume geothermal, Thermosiphon, Heterogeneity, Fluvial channels, Geothermal power.

5.2 Introduction

About 41% of global (25% of the UK) carbon dioxide (CO_2) emissions from fossil fuel combustion in 2017 are due to electricity and heat production activities [152]. Now, more than ever, the importance of reducing global CO_2 emissions has become evident. Several measures have been taken to tackle this problem, among which, CO_2 capture and storage (CCS) is the most considered and noted one [116, 46, 153]. Instead of only storing CO_2 in underground

formations, CO_2 can be circulated to the surface and used in carbon capture utilisation and storage (CCUS) systems, such as enhanced oil recovery (EOR) [49, 50, 51], enhanced gas recovery (EGR) [52, 117], and heat extraction in enhanced geothermal systems (EGS) [29, 35, 121].

Recently, CO_2 is suggested as a substitute for water for geothermal power generation in naturally permeable sedimentary formations, known as CO_2-plume geothermal (CPG) process [122], and in 2015, a CPG-thermosiphon system started at the SECARB Cranfield Site, Mississippi [154]. However, this project was not completely successful and the thermal breakthrough was not significant even after several years of injection, and one reason was that the thermosiphon was not sustainable [154]. In CPG power generation, CO_2 is injected and produced in the supercritical (sc) phase. During this cycle of geothermal power generation, all of the produced CO_2 is re-injected into the aquifer, and eventually, all of the initially injected CO_2 will be kept in the underground aquifer.

Using CO_2 features three main advantages, *i.e.*, (i) self-sustaining thermosiphon effect, (ii) lower frictional losses, and (iii) grid-scale electricity storage [129, 155]. Unlike water, CO_2's density is highly temperature-dependent. This results in a considerable drop in its density while it is heated inside the aquifer, resulting in an upward flow from the density-driven thermosiphon effect [56]. Additionally, CO_2's lower viscosity results in lower frictional losses and pressure drop inside the aquifer. Therefore, higher flowrates (with the same amount of pressure drop) compared to water-based systems are possible. Moreover, because of the CO_2's higher compressibility, it is possible to provide grid-scale electricity storage [156].

Since the introduction of CPG, there have been some studies on the performance and thermal potential assessment of CPG sites, as well as studies on different aspects of the CPG systems. The most recent of these studies are about minerals precipitation [84, 106, 38], wells' spacing [129, 157], well pattern and reservoir boundary condition [53], surface power plant cycle [155, 158, 159], water and $scCO_2$ saturation and mass-fraction at the production well [160, 130], CPG combination with natural gas recovery [117], and CPG economic feasibility [158].

CPG typically is recommended for relatively shallower sedimentary aquifers with depths of about 0.5 km to 3 km [56] compared to deep EGS systems. Compared to fractured formations, sedimentary aquifers are naturally porous and permeable and are abundant worldwide [161, 162, 163]. As noted by Bonte et al. [128], there are many low-enthalpy geothermal aquifers available with depths of 2-2.5 km and an average temperature of 70-90

°C. Heterogeneity is the nature of all geological aquifers, and in sedimentary brine aquifers (that are used for CPG), these heterogeneities can be of the fluvial type, *i.e.*, braided, meandering, and anabranching [42]. Fluvial sandstones are common as reservoirs for both water and hydrocarbon. Examples include the Triassic strata and significant parts of the Permian section in Europe including the Triassic Sherwood Sandstone of the Worcester Graben, Wessex, Cheshire and East Irish Sea Basins, UK [164, 132], the Triassic Bunter Sandstone of the UK and Dutch Southern North Sea, North German Basin [165, 166], Permo-Triassic sandstone reservoirs of the Junggar Basin China [167], Devonian sandstones at Battery Point Quebec [168], and more [169].

It has been demonstrated in previous studies [84, 106, 38, 170] that salt precipitation near the injection well can have a significant impact on reservoir injectivity in that area. This phenomenon can lead to a reduction of up to 70% in reservoir porosity. The mechanism primarily responsible for salt precipitation near the injection well is capillary-driven backflow [38]. A recent study by Norouzi et al. [170] proposed an analytical solution to calculate the amount of precipitated salt at the injection well in the presence of the capillary effect. Despite the importance of salt precipitation in CPG systems, there has been no research conducted on the effects of backflow on salt precipitation in a 3D fluvial heterogeneous aquifer.

Our previous study showed that the presence of fluvial channels in the aquifer affects the heat and mass dispersion inside the aquifer and therefore, significantly affects the performance and the energy output of CPG [157]. However, despite the importance of geological uncertainty in modelling such systems, there are few studies that considered realistic three-dimensional (3D) models of heterogeneity [135, 136, 137, 134, 171]. Most of these works focused on CCS and water-based systems, rather than CPG. In our previous study [157], the performance of a CPG system in a two-dimensional (2D) braided fluvial aquifer was investigated through subsurface performance metrics. It was observed that the injection wells parallel to fluvial channels direction and with a spacing of about 450 m provide the best system performance. Moreover, the presence of fluvial heterogeneity reduced the system's net power by a factor of 3. The study had some limitations. The model was 2D and could not capture the density-driven upstream flow of $scCO_2$ inside the aquifer. Additionally, the performance of the system was analysed based on subsurface metrics only and thermosiphon was not considered.

In addition to heterogeneity and salt precipitation, the aquifer thermal depletion and variations of aquifer temperature during the CPG lifetime is also mostly overlooked in studies in this field. Among the works that considered the reservoir heat depletion [117], [172], [122],

and [173] can be mentioned. Most recently, Adams et al. [129] considered the reservoir thermal depletion and suggested a system working with the optimal flowrate at each time step. However, the issue with this approach is that, in practice, it is not possible to instantly adjust the injection rate every time step. Also, due to the large volume of the reservoir, the system has a response time regarding the variations in flowrate.

Despite the importance of geological uncertainty and aquifer heat depletion, there is no study on 3D heterogeneous aquifers, with a direct-CO_2 thermosiphon power generation cycle. Against this backdrop, I have focused on the realistic 3D heterogeneity of aquifers and how they affect the efficiency and performance of CPG, thermosiphon, and power generation. A fully heterogeneous braided fluvial 3D aquifer is considered for a direct-CO_2 thermosiphon system. Various fluvial realisations are created and the results are compared with their representative homogeneous cases. In addition to the aquifer and well modelling, a direct-CO_2 expansion turbine is considered at the surface power plant for power generation. Also, the effects of various parameters such as fluvial channels' width and orientation and CO_2 injection rate are studied and an optimum injection rate for heterogeneous and homogeneous cases is suggested. Finally, a CPG system with an annually adjusting injection rate is suggested to keep the produced excess pressure at the surface (associated with thermosiphon) constant during the cycle lifetime.

5.3 Methods

To model the CPG system as realistically as possible, several aspects of the CPG cycle should be considered, including modelling fluid flow and heat transfer in the aquifer, fluid transfer from bottomhole condition to the surface, and energy production at the surface power plant. Each of these is described in the following sections.

5.3.1 Aquifer and well modelling

A 3D rectangular Cartesian aquifer with the domain of 1000 m $\times$ 1000 m $\times$ 100 m at the depth of 2000 m is modelled for 50 years of heat extraction. The aquifer is initially uniformly discretized into $400 \times 400 \times 25$ grid blocks and then upscaled to a model of $50 \times 50 \times 25$ grid blocks to reduce the simulations' time [157]. Grid resolution sensitivity results are provided in Section 5.3.3. Based on the optimised results provided in previous studies [157, 174], a pair of vertical injection (I) and production (P) wells with the spacing of $L = 500$ m and the I-P line parallel to the channels' orientation is considered to provide the highest performance.

However, to further study the effect of the I-P line and channels' orientation, the performance of CPG systems with the I-P line parallel to channels is compared with cases with the I-P line perpendicular to channels in Section 5.4.1. The injection and the production wells are perforated at the lower and the upper halves of the aquifer, respectively.

The aquifer is designed based on the data from Warren et al. [139] and previous publications, particularly [53, 138, 38, 157], to represent a high-salinity North Sea sandstone aquifer. Although salt precipitation, due to water vaporization in the dry-out region, and geochemical reactions take place in the reservoir, it was previously shown that the main reaction is salt precipitation, with effects limited to the close vicinity of the injection well. Despite the increase in the pressure drop inside the reservoir due to salt precipitation, its effects on the system's thermal performance are small [38, 157, 53, 175]. However, to further investigate this matter, a sensitivity analysis on the effects of geochemical reactions, specifically salt, is provided in Appendix E. Additionally, the effects of the fluvial channels' permeability and porosity, as well as the injection well bottomhole temperature are studied in this section.

The aquifer is initially filled with brine with a salinity of 20% by weight. The initial pressure equates to the hydrostatic elevation potential at the aquifer depth which will be about 20 MPa at the aquifer's top. Also, the aquifer's initial temperature is the product of the temperature gradient (42.5 °C km^{-1}) and the aquifer depth plus the ambient temperature (15 °C), which will be about 100 °C. Because of the caprock and bedrock at the top and bottom of the aquifer, the vertical boundaries of the aquifer are closed to flow. However, conductive heat exchange happens at the boundaries. Pore volume modification is used at the side boundaries to represent an aquifer with side boundaries open to flow and heat transfer. The aquifer is modelled using two-phase flow simulations of CO_2 and brine with varying temperature and pressure, and the Peng-Robinson [148] Equation of State is used to calculate the thermodynamic properties of each phase. Detailed aquifer properties are provided in Table 5.1.

The pressure drop for a steady and laminar flow inside the aquifer can be calculated using Darcy's equation [176]. The term inside the bracket in Eq. 5.1 is the average specific inverse mobility (M) that is the product of the kinematic viscosity (μ/ρ) and the aquifer-dependent properties ($L/k/A$) and shows the aquifer's resistance to flow. Since the aquifer permeability is not constant, and $scCO_2$'s density and viscosity are temperature dependent, it is not possible to directly calculate M, however, knowing the injection rate and the pressure drop from the aquifer simulations, M can be calculated. It is assumed that the fluvial channels and heterogeneity reduce the aquifer mobility and therefore, increase the required pumping

power. This parameter will be used in future sections to optimise the CO_2 injection rate at each time step.

$$\Delta P = \left[\frac{\mu L}{\rho k A}\right]\dot{m} \quad \text{(cartesian)} \tag{5.1a}$$

$$\Delta P = P_{\mathrm{e}} - P_{\mathrm{w}} = \left[\frac{\mu \ln \frac{r_{\mathrm{e}}}{r_{\mathrm{w}}}}{\rho 2\pi k h}\right]\dot{m} \quad \text{(radial)} \tag{5.1b}$$

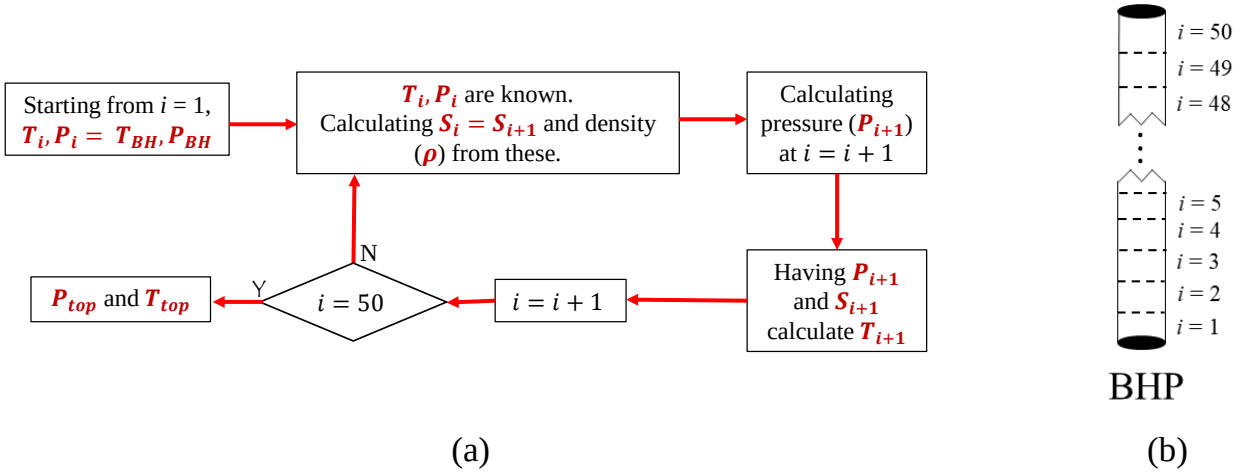

Figure 5.1: (a) Flowchart of well modelling procedure and calculating fluid surface properties from the bottomhole data, and (b) schematic of the well and its discretization to the surface.

A schematic of the well model and the flowchart of the well modelling procedure are shown in Fig. 5.1. It is assumed that CO_2 goes through isentropic (adiabatic and reversible) compression and expansion processes in the injection and production wells, respectively [129]. To model the injection and the production wells and to calculate CO_2's temperature and pressure at the surface and bottomhole conditions, wells are divided into segments of 50 m (from the surface to the bottom of the well) to reach an accuracy within 1% of the values found through a fine-scale model. The injection temperature of CO_2 ($T_{\mathrm{inj}} = 40$ °C) is calculated by isentropically compressing the injected saturated liquid CO_2 at $T = 22$ °C and $P = 6$ MPa at the surface to the supercritical phase at the aquifer pressure. Similarly, at the production well, knowing the bottomhole temperature and pressure, the fluid temperature and pressure are calculated through numerical well modelling, considering an isentropic expansion. A schematic of the modelled CPG aquifer is illustrated in Fig. 5.2.

Table 5.1: Aquifer and model properties.

Property	**Value**
Aquifer properties: constant	
Aquifer domain	1000 m × 1000 m × 100 m
Depth	2000 m
Salinity	20 wt.-%
Initial temperature	100 °C
Initial top pressure	20 MPa
Channels' width to thickness ratio (w/T)	10
Channels' porosity	0.25
Inter-channels' porosity	0.15
Channels' horizontal permeability	1000 mD
Inter-channel's horizontal permeability	20 mD
Vertical to horizontal permeability ratio	0.1
Rock density	2650 kg/m^3
Rock heat capacity	1987.5 kJ/m^3/K
Rock thermal conductivity	2.1 W/m/K
Bottomhole injection temperature	40 °C
Wellbore diameter	0.31 m
Well pipe surface roughness	55 μm
Aquifer properties: varied	
Injection rate ($\dot{m}_{\text{inj}}$)	5, 10, 25, 50*, 100, and 200 kg/s
Fluvial channels' width (w)	50*, 100, and 150 m
Homogeneous average porosity (ϕ)	0.17*, 0.185, and 0.208
Homogeneous average permeability (k_{avg})	225.5*, 336.5, and 568.4 mD
I-P wells' orientation with respect to channels	parallel* and perpendicular

* indicates the base case parameters.

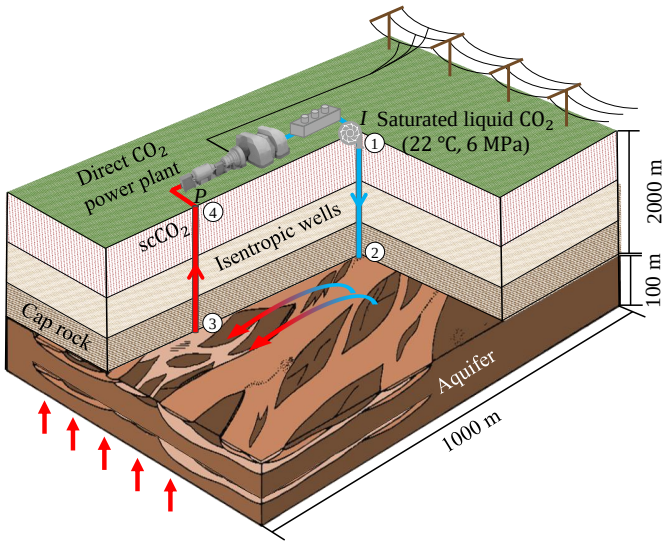

Figure 5.2: Schematic of the direct-CPG cycle and surface power plant. CO_2 is injected as a saturated liquid at stage 1, then it self-compresses to stage 2, then it is heated inside the reservoir to stage 3 at which CO_2 density is reduced, then it self-expands to the surface at stage 4, and then the produced supercritical CO_2 is used in a direct power plant. The turbine's isentropic efficiency (η_T) is considered to be 78%.

5.3.2 Sequestration stage vs. CPG lifetime

When CO_2 is injected into the aquifer, it initially displaces brine, a stage known as the CO_2-Plume Establishment (PE) stage. Having a sufficient amount of CO_2 in the aquifer is crucial; otherwise, once the production begins, water will emerge at the production well. At this stage, the CO_2 mass-fraction is too low and cannot be used in a turbine for energy production. It is argued that the turbine requires a minimum CO_2 mass-fraction of about 94% [172], however, Adams et al. [129] suggested that based on the discussions with turbine manufacturers much lower values are acceptable. Ezekiel et al. [160] suggested that in light of the CO_2's lower viscosity compared to brine, only when CO_2 saturation around the production well is higher than about 0.3, the influx of CO_2 into the well is much higher than the water. Hence, to sustain a desirable *annular* production flow regime, a minimum CO_2 mass-fraction of 80% is considered for the onset of energy production and the CPG cycle [129, 160, 172]. In the present work, the required time interval for this stage is called the *sequestration stage*.

Furthermore, it is essential that the produced CO_2 at the surface (stage 4 in Fig. 5.2) is still at its supercritical condition; thus, a shutdown trigger is considered at the production well that stops power production when either the temperature or the pressure of the

produced CO_2 fall below its critical point of 30.3 °C and 7.38 MPa, which defines the *CPG lifetime*. The span between the sequestration stage and CPG lifetime is the cycle *operation time*. Finally, one of the major concerns in CPG is the production temperature drop, which weakens thermosiphon, reduces power production, and shortens the CPG lifetime. To non-dimensionalize the production temperature and temperature decay, a temperature fraction parameter (Γ) is defined:

$$\Gamma_t = \frac{T_t - T_{inj}}{T_0 - T_{inj}} \tag{5.2}$$

where T_t is the production bottomhole temperature at time t, T_0 is the aquifer initial temperature (100 °C), and T_{inj} is the $scCO_2$ injection temperature (40 °C).

5.3.3 Fluvial channels

There are different types of fluvial channels, including straight, meandering (e.g., Cretaceous Nieuwerkerk Formation, West Netherlands Basin [133]), and braided (e.g., Bunter sandstone reservoir, UK; Tarim basin, China; the Triassic St Bees Sandstone Formation, Cumbria, UK [131]; and Sherwood Sandstone Group of the Wessex Basin, UK [132]). Generally, a single thread channel with a low degree of sinuosity (< 1.5) is called straight and with a higher degree of sinuosity (> 1.5) is called meandering [42]. Sinuosity is the ratio between the curvilinear length and the straight line connecting the curve's endpoints. The aquifer modelled in the present study has the subsurface fluvial channels of braided type. Braided channels have low sinuosity and consist of a network of channels with high porosity and permeability that are mostly ($> 50\%$) separated by scattered low porosity and permeability matrices [177, 143]. The braided channels' degree of heterogeneity is defined by their channels' width and width-to-thickness ratio (w/T). Based on the review and the geological data provided by Gibling [140], channels' widths of 50, 100, and 150 m with the w/T ratio of 10 are considered to generate the fluvial realisations in this study (Fig. 5.3a).

In total, 15 randomly-created 3D braided aquifers are generated for this study (Fig. 5.3b). To generate these realisations, an in-house code that works based on the Piece-wise Cubic Hermite Interpolating Polynomials [144] and generates 2D braided realisations is further developed to make 3D heterogeneous models. To generate each 3D realisation, at first, five layers of randomly generated 2D braided channels with a considered width, *i.e.*, w=50, 100, and 150 m, are created. The process of creating 2D channels is described in our previous studies [157, 174]. Then, using the w/T ratio of 10, a thickness is assigned to all the channels. Next, these five braided realisations that now have a thickness, are put on top of

each other to form a 3D braided aquifer. Finally, the initial fine-scale cases are upscaled to reach the final cases with $50 \times 50 \times 25$ grid blocks, as shown in Fig. 5.3(b). To compare the homogeneous versus heterogeneous aquifers, a homogeneous case is created representing each channel width. For each homogeneous case, the average porosity and permeability are calculated by averaging the values of the volumetric-averaged porosity and permeability of the related heterogeneous cases.

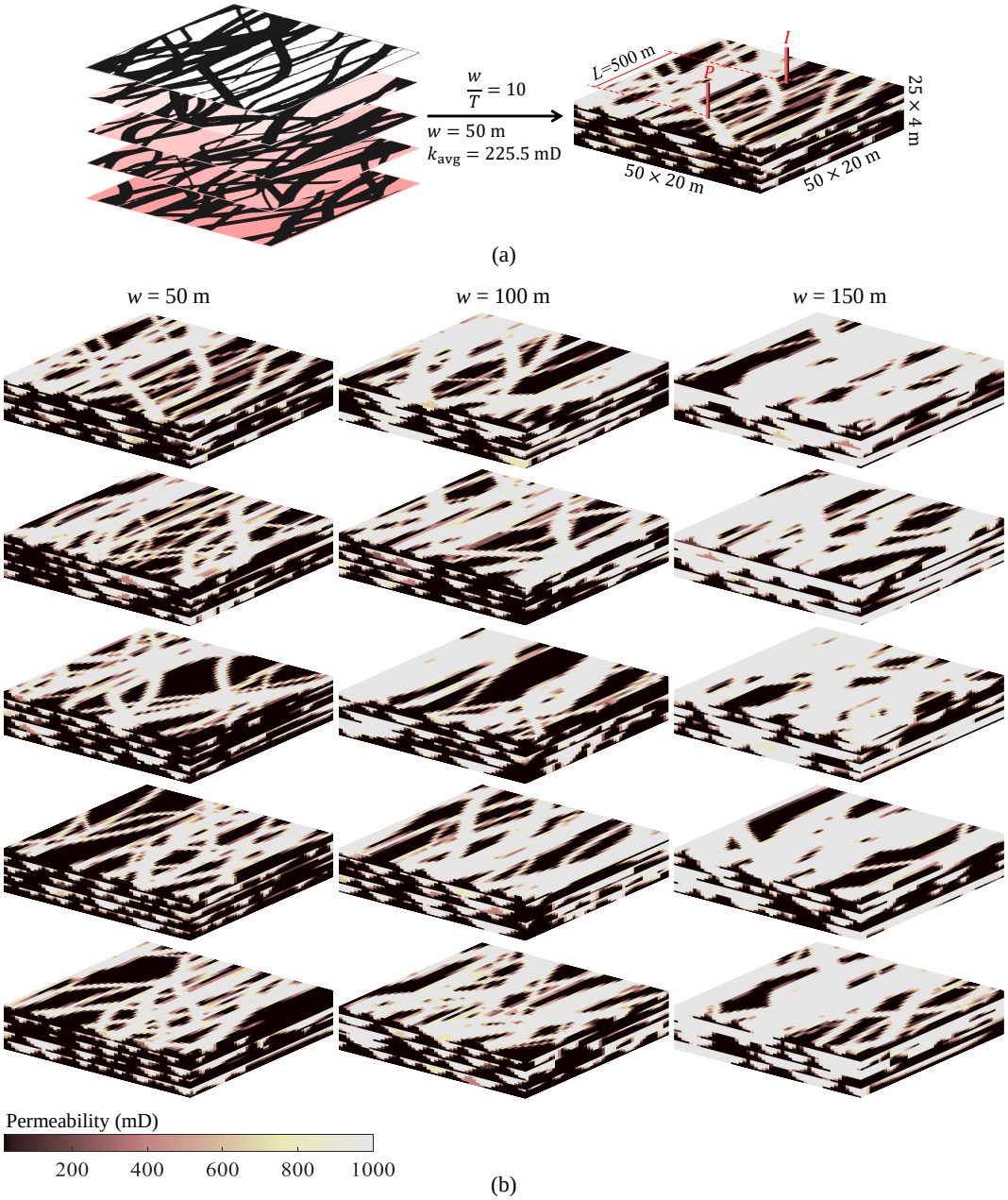

Figure 5.3: (a) Schematic of the problem and the aquifer ($w = 50$ m); and (b) heterogeneous cases with 15 different realisations, (left): $w = 50$ m and $k_{\text{avg}} = 225.5$ mD, middle: $w = 100$ m and $k_{\text{avg}} = 336.5$ mD, and right: $w = 150$ m and $k_{\text{avg}} = 568.5$ mD.

To study the effects of mesh resolution on the subsurface results and find the optimum resolution both in terms of simulation runtime and results error, four resolutions, including $200 \times 200 \times 25$, $100 \times 100 \times 25$, $50 \times 50 \times 25$, and $25 \times 25 \times 25$ are considered, as in Fig. 5.4. The overall simulation CPU time, as well as the production well bottomhole temperature and the injection well bottomhole pressure, after 50 years of injection, are used to study the resolution effect.

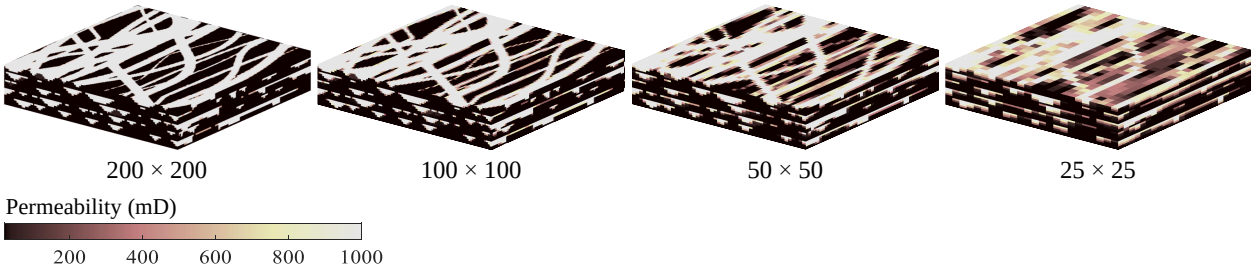

Figure 5.4: Permeability distribution for the aquifer resolutions considered for the grid sensitivity analysis.

Fig. 5.5 illustrates the grid resolution sensitivity analysis results. The simulations are performed on an HP ProLiant High-Performance Server with two E5-2690v3 processors. The simulation runtime is increased with a logarithmic trend as the aquifer resolution is increased, while the variations in bottomhole temperature and pressure are negligible (less than 1 °C and 50 kPa). Therefore, considering both the runtime and the upscaling error, the optimised grid resolution for the present study is $50 \times 50 \times 25$, which is similar to the results of the 2D model in our previous study [157].

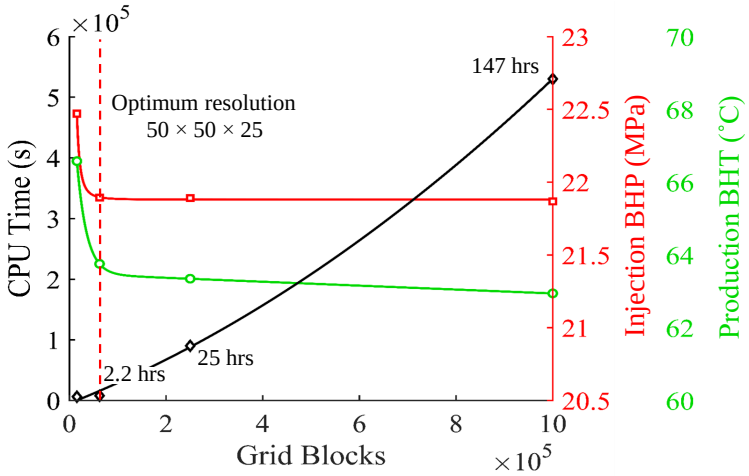

Figure 5.5: Grid resolution sensitivity analysis: CPU time, production bottomhole temperature, and injection bottomhole pressure versus aquifer resolution. The vertical red line shows the optimum number of grid blocks.

5.3.4 Surface power plant modelling and flowrate optimisation

In the present study, CO_2 is directly used as the working fluid of the power cycle and is expanded through a turbine to produce power. Therefore, a direct-CO_2 thermosiphon CPG system, comprised of an expansion turbine, a cooler/condenser heat exchanger, and a pump is used to generate electricity from the medium-temperature aquifer of the present study [117, 56, 127]. A schematic of this direct-CO_2 power cycle is shown in Fig. 5.6.

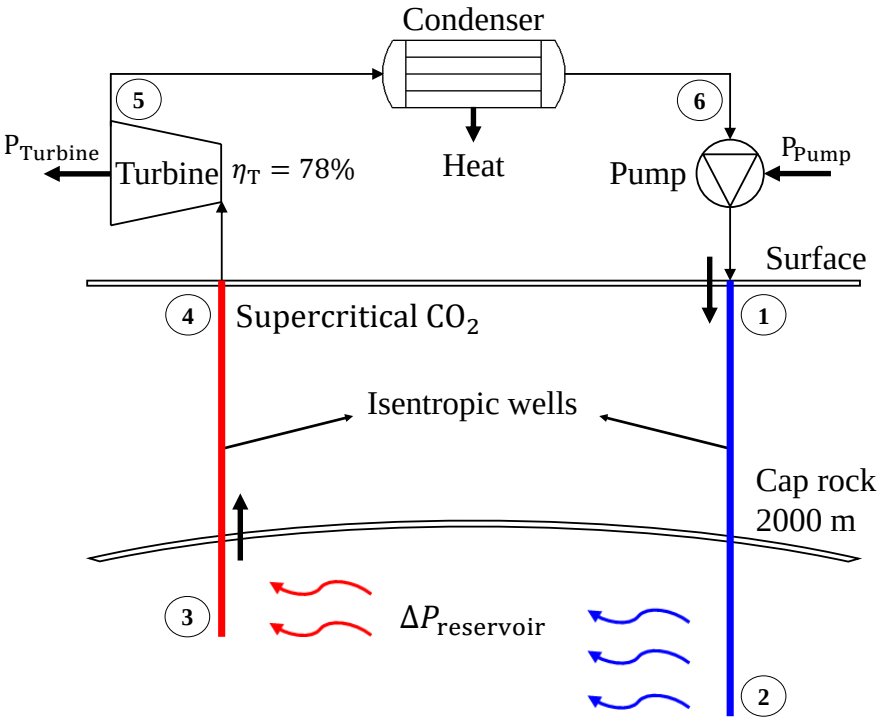

Figure 5.6: Direct-CO_2 thermosiphon system. In this system, CO_2 is injected as a saturated liquid at stage 1, and then it self-compresses in an isentropic process to stage 2. Subsequently, it is heated inside the reservoir to stage 3, where the CO_2 density is reduced. After that, it self-expands in an isentropic process to the surface at stage 4, and the produced supercritical CO_2 is used in a direct power plant. During the initial stages of CPG, small amounts of water may be produced, leading to an excess pressure drop at these initial steps, which may require a pump to compensate for it.

Saturated liquid CO_2 with a temperature and pressure within the ranges of 22–27 °C and 6.0–6.7 MPa, respectively, is injected into the reservoir (Fig. 5.6, stage 1). Then the injected CO_2, in an isentropic process, self-compresses inside the injection well and becomes supercritical as it reaches the aquifer condition at stage 2. As the $scCO_2$ is heated inside the aquifer from stage 2 to 3, its density considerably decreases. For instance, CO_2 density decreases from about 850 kg/m^3 at 40 °C (bottomhole injection temperature) to about

450 kg/m^3 at 100 °C (aquifer temperature). The compression and the expansion inside the wells are considered to be isentropic. As a result of the density gradient, the pressure difference between the bottom and top of the production well will be less than that of the injection well, *i.e.*, $|\Delta P_{3,4}| < |\Delta P_{1,2}|$. Hence, the aquifer bottomhole pressure itself is sufficient to produce the scCO$_2$ from the production well to the surface and no additional pump is required, resulting in an excess pressure ($P_{\text{excess}} = P_4 - P_1$) at the surface. P_{excess}, which is the difference between the production and injection wells' head pressure, shows that the produced fluid has higher exergy. The high-pressure sc/gaseous CO$_2$ that is produced from the aquifer is expanded in the turbine and using a generator, electric power (MW$_e$) is generated.

The gross turbine power (P_T) is calculated by multiplying the scCO$_2$ mass flowrate by the fluid enthalpy difference between the inlet (stage 4) and the outlet (stage 5) of the turbine (Δh). Eq. 5.3 is used to calculate P_T. Ideally, the expansion process inside the turbine is isentropic, however, because of irreversibilities, an isentropic turbine efficiency (η_T) of 78% is used to calculate the enthalpy at the turbine's exit as in Eq. 5.4. This value for the turbine efficiency is taken from the previous works by Adams et al. [56, 127]. However, it is important to note that in typical turbines, the efficiency usually is lower than this value, and consequently, in real-world scenarios, the power output may be less than the values calculated in this study.

$$P_T = X_{CO_2} \dot{m} (h_{in} - h_{out}) \tag{5.3}$$

$$h_{out} = h_{in} - [\eta_T (h_{in} - h_{out,s})] \tag{5.4}$$

In the above equations, X_{CO_2} is the produced CO$_2$ mass-fraction in the gas phase and $\dot{m}$ is the produced CO$_2$ mass flowrate in kg/s. h_{in} is the inlet enthalpy of the turbine (stage 4), which is a function of the scCO$_2$ temperature ($T_{\text{prod,head}}$) and pressure ($P_{\text{prod,head}}$) at the production wellhead, and h_{out} represents the exit enthalpy of the turbine. $h_{out,s}$ is the enthalpy of the outlet CO$_2$ considering an ideal turbine (η_T=100%) and is a function of the entropy of the inlet CO$_2$ (s_{in}) and the condenser pressure (P_{cond}). P_{cond} itself is a function of the condenser outlet temperature ($T_{\text{out,cond}}$), which is considered to be 7 °C above the ambient temperature (T_{ambient}=15 °C) [117, 127]. Also, it is considered that the mass vapour quality of the fluid leaving the condenser is equal to zero (Q=0), *i.e.*, CO$_2$ is in the liquid phase.

$$h_{in}, s_{in} = f(P_{\text{prod,head}}, T_{\text{prod,head}}) \tag{5.5a}$$

$$h_{\text{out,s}} = f(P_{\text{cond}}, s_{\text{in}}) \tag{5.5b}$$

$$P_{\text{cond}} = f(T_{\text{out,cond}}, Q) \tag{5.5c}$$

To calculate the net power (P_{net}) of the direct-CO_2 cycle, we should subtract the parasitic condenser power (P_{cond}) and pump power (P_{pump}) from the gross turbine power (P_{T}), as in Eq. 5.6.

$$P_{\text{net}} = P_{\text{turbine}} - P_{\text{cond}} - P_{\text{pump}} \tag{5.6}$$

In light of the thermosiphon effect, the required pumping power for a direct CPG cycle is equal to zero ($P_{\text{pump}} = 0$) [117, 127], which is the main advantage of CPG compared to water-based systems. Electrical submersible pumps in wells are very expensive, and also, are the most common equipment to fail, increasing maintenance costs [178].

To calculate the parasitic condenser power (P_{cond}), Eq. 5.7 is used, in which, $h_{\text{in,cond}}$ and $h_{\text{out,cond}}$ represent the fluid enthalpy at the condenser inlet (stage 5) and exit (stage 6), respectively, and λ is the parasitic load fraction, which is the ratio of parasitic energy load to heat-rejection energy and is considered to be 0.03 [117].

$$P_{\text{cond}} = X_{CO_2}\dot{m}(h_{\text{in,cond}} - h_{\text{out,cond}})\lambda \tag{5.7}$$

The related thermodynamic changes in the state of CO_2 through the cycle are shown in the T-s diagram in Fig. 5.7. In this figure, step 1-2 illustrates the CO_2 isentropic compression inside the injection well, followed by step 2-3 which indicates the heating and the pressure drop within the aquifer. Step 3-4 shows the CO_2 isentropic expansion inside the production well, step 4-5 shows the power production through the turbine (for both ideal and non-ideal cases), and step 5-1 represents the CO_2 phase change inside the condenser. It is worth noting that point 5, which represents the outlet condition of the turbine, is highly uncertain as it can fall into either the supercritical or the unsaturated two-phase regions. This uncertainty can lead to issues with the turbine and potentially reduce its efficiency. Consequently, to ensure the viability of using the produced fluid in a direct turbine, a pump or compressor may be required.

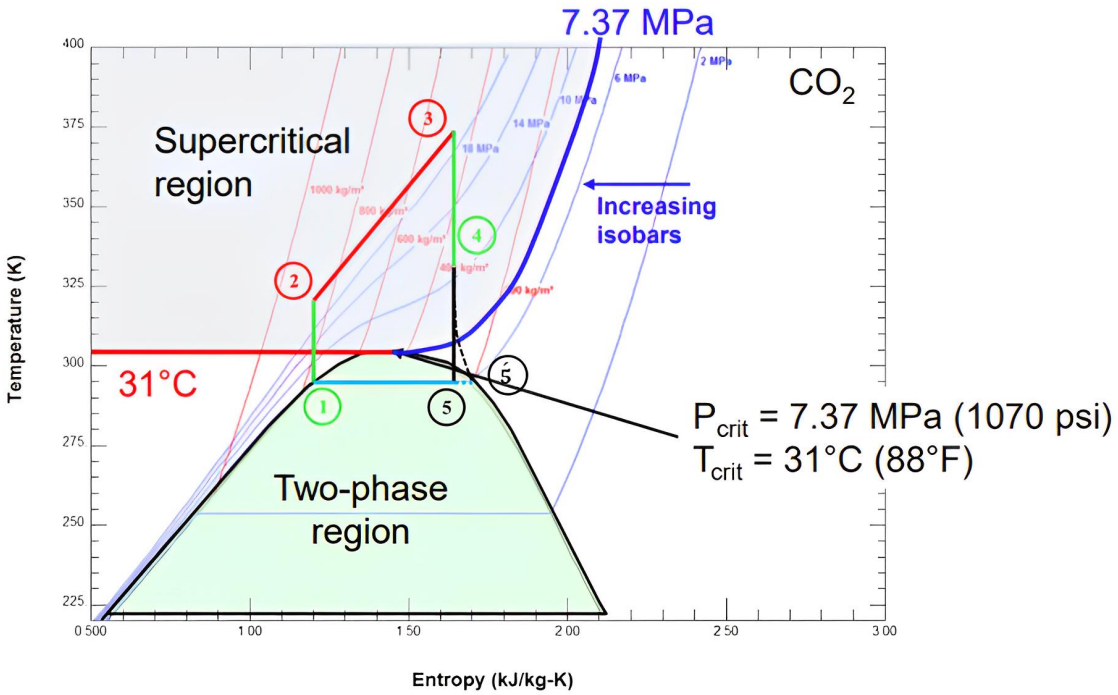

Figure 5.7: Temperature-entropy (T-s) diagram of the power cycle that represents fluid properties at each step of the cycle. Step 1-2 represents the CO_2 isentropic compression inside the injection well, step 2-3 shows CO_2 heating inside the aquifer and the pressure drop, step 3-4 shows the CO_2 isentropic expansion inside the production well, step 4-5 shows the power production through the turbine (both ideal and non-ideal cases), and step 5-1 represents the CO_2 phase change inside the condenser.

One of the main issues in CPG systems is the temperature drop at the production well. When the injected $scCO_2$ thermal plume reaches the production well, its temperature greatly decreases, and therefore, weakens the thermosiphon at the production well. In addition, it is important to limit the pressure drop at the turbine's inlet during the CPG lifetime. In this regard, a set of simulations are designed where the aquifer parameters (*i.e.*, the aquifer pressure drop and inverse mobility M), are recalculated every year and the CO_2 injection rate is adjusted in a way to keep the production temperature and the excess pressure (P_{excess}) above certain levels at all times (80 °C and 3.5 MPa). To do so, first, a lower limit for the excess pressure is assumed, then at time step i, we have the injection rate from time step $i-1$, so from Eq. 5.1a we can calculate the inverse mobility M. For time step $i+1$, the pressure drop is calculated by having the value of M, and knowing the updated pressure drop, the injection rate is adjusted. This process repeats every year to adjust the injection rate and prevent the bottomhole production temperature and the P_{excess} fall below the defined values

of 80 °C and 3.5 MPa, respectively.

5.3.5 Simulations and the employed simulators

In total, 156 cases that include 18 different 3D aquifer realisations (5 heterogeneous and 1 homogeneous realisation for each channel width) are simulated. For each realisation, 6 different injection mass flowrates (5, 10, 25, 50, 100, and 200 kg/s) and a case with a time step-adjusted injection rate are considered. Additionally, 5 heterogeneous cases with the I-P line perpendicular to the channels' orientation are considered to study the effect of channels' orientation. All the simulations are carried out using the ECLIPSE E300 simulator [179], and the governing equations are detailed in [179, 138]. The simulator's capability of modelling geothermal processes has been validated previously against the benchmark geothermal examples from Stanford University [180]. The authors proved that the simulator is suitable for use in complex geothermal modelling problems. Simpler adaptations of CPG have been implemented by other authors employing industry-standard simulators such as CMG [127, 160]. Additionally, the well and the direct-CO_2 power plant models are developed in MATLAB, and the CoolProp-MATLAB wrapper [181] is used for the iterative calculation of the fluid thermodynamic properties at each stage.

5.4 Results and discussion

Results are presented in two sections. First, a detailed comparison of the performance and the net power of the CPG system between the homogeneous and the heterogeneous fluvial cases is provided. To do the comparison, parameters including the temperature fraction, production wellhead temperature, the aquifer inverse mobility and production rate, cycle excess pressure, and instantaneous and cumulative net power, are studied in Section 5.4.1. Last, in Section 5.4.2, results of the cases with constant target excess pressure are presented and the CPG system potential is analysed and compared between the cases.

5.4.1 Effects of heterogeneity, injection rate, and channels' orientation on system performance

Fig. 5.8a and b show the temperature fraction and the wellhead temperature, as well as the cycle sequestration stage, versus time for the constant channels' width of 50 m. One of the main problems of CPG is the aquifer thermal depletion that weakens thermosiphon.

Fig. 5.8a shows the sequestration stage (the length of the PE stage, at which the CO_2 pore-space saturation reaches about 0.3 or mass-fraction of about 80% around the production well). The $scCO_2$ injection rate significantly affects the required sequestration stage - from about 2 years to 37 years. Based on these results, CPG with a single pair of wells and low injection rates (such as 5 and 10 kg/s in this study) is not practical if used in brine-filled aquifers, because although the temperature drop is very low, the required sequestration stage will be more than 20 years, which is about 0.4 of the cycle's expected operation time (50 years). A solution to this issue can be using multiple injection and production wells in a pattern that they supplement each other's CO_2-plume to provide the minimum required mass-fraction at the production well. For higher injection rates, the sequestration stage is about 9, 5.5, 3, and 2 years for injection rates of 25, 50, 100, and 200 kg/s, respectively.

In Fig. 5.8b, the values of the production wellhead temperature are reported. It is observed that the temperature achieved at the surface - for the power plant use - has much lower values compared to the downhole ones. This is because CO_2 goes through an isentropic expansion in the production well that can reduce its temperature from about 100 °C to about 63 °C. The time at which either the temperature or the pressure of the produced CO_2 at the surface falls below the critical values of 30.3 °C and 7.38 MPa is the CPG lifetime. In contrast with the sequestration stage, as the injection rate increases, the aquifer thermal depletion occurs at a faster pace, and therefore, the CPG lifetime decreases on average about 17 and 38 years for the 100 kg/s and 200 kg/s injection rate cases, respectively (Fig. 5.8b). As a result, finding an injection rate that observes the balance between the sequestration stage and CPG lifetime is vital.

The presence of fluvial channels increases the slope of the curve for aquifer thermal depletion compared to homogeneous cases since the $scCO_2$ thermal plume reaches the production well faster (Fig. 5.8a and b). For instance, from Fig. 5.8c and d, for $\dot{m}_{\text{inj}} = 50$ kg/s and $w = 50$ m, the amount of reduction in Γ ($\Delta\Gamma$) versus time increases from about 0.3 to 0.6. However, heterogeneity slightly affects the sequestration stage by about 1 to 6 years, depending on the injection rate. There are two observations when the channels' width increases from 50 m to 150 m. Firstly, the higher the channels' width, the lower the difference between homogeneous and heterogeneous cases. In other words, the heterogeneous case becomes similar to its representative homogeneous case. Secondly, the temperature drop is less in aquifers with higher channels' width (higher average porosity and permeability) compared to lower w cases. For instance, for the injection rate of 50 kg/s, the temperature drop over 50 years for the cases with $w = 100$ m and $w = 150$ m is about 18% and 53% lower

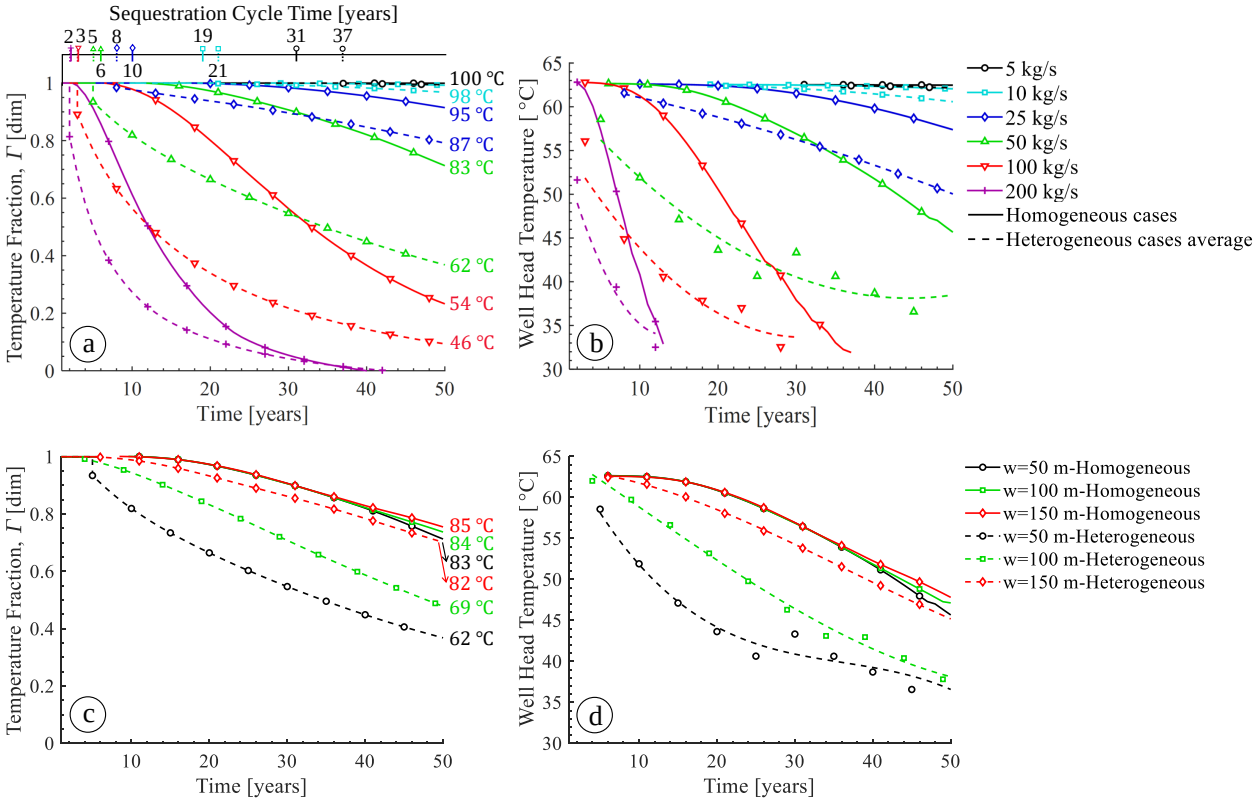

Figure 5.8: Production well temperature fraction (Γ) and production wellhead temperature versus flowrate for constant channels' width $w = 50$ m (a & b), and versus channels' width for constant injection rate $\dot{m}_{\text{inj}} = 50$ kg/s (c & d). These plots also indicate the sequestration time and CPG lifetime, as well as the aquifer thermal depletion for different cases.

compared to the $w = 50$ m case, respectively. This is because as w increases, not only does the average pore volume (flow cross-section area) increase but also channels' vertical connection increases, and the permeability in the $y-$direction (k_{y}) is improved. Therefore, for a constant mass flowrate, the CO_2 flooding front moves slower horizontally, and the upward movement of $scCO_2$ due to the buoyancy effect becomes easier and the CO_2 travel in upper levels of the aquifer intensifies. As a result, $scCO_2$ vertical flow increases despite the uniform and piston-like movement in lower channels' widths (Fig. 5.9), and the $scCO_2$ *thermal plume* reaches the production well at a later time compared to lower w cases; subsequently, thermal depletion decreases.

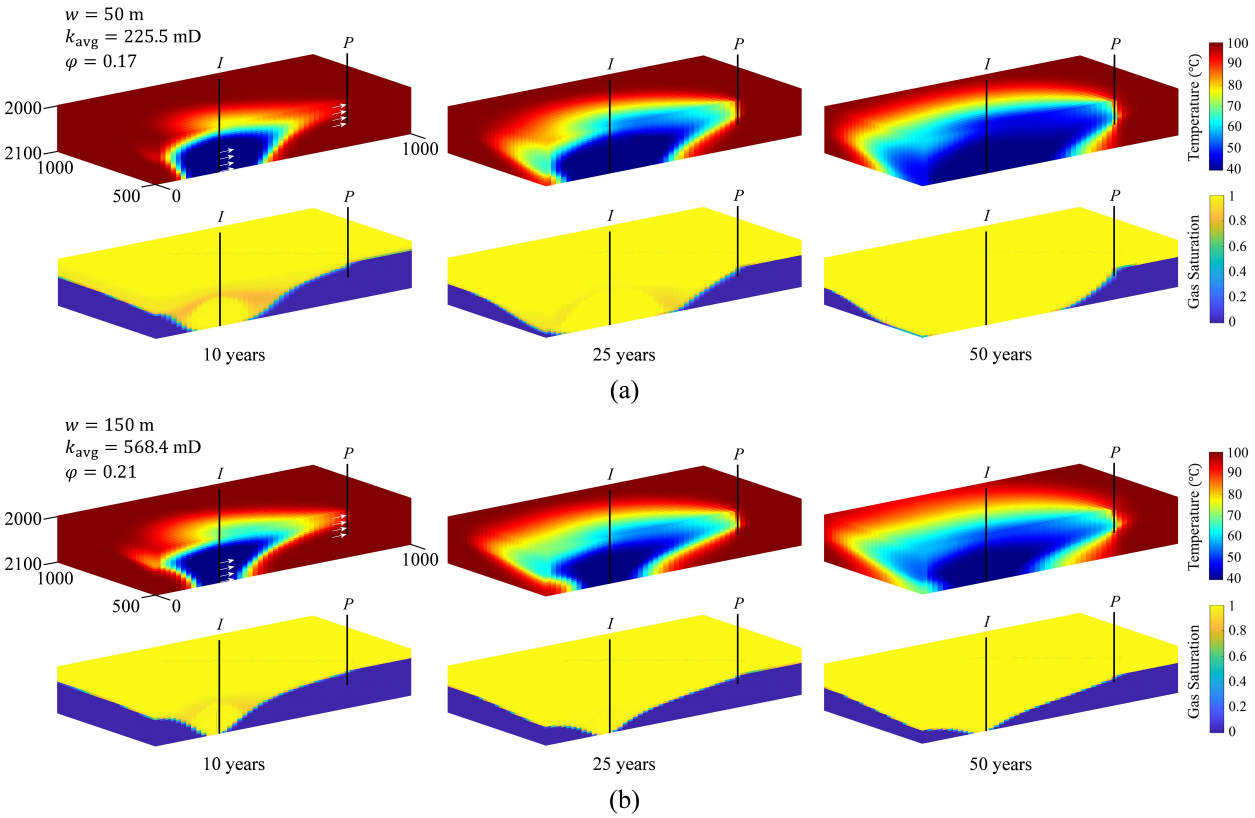

Figure 5.9: Temperature and gas saturation distribution at different time-steps for homogeneous cases, representing (a) $w = 50$ m and (b) $w = 150$ m, and injection rate of $\dot{m}_{\text{inj}} = 50$ kg/s. As k_{avg} increases, k_{y} increases as well; and CO_2 disperses more vertically and reaches the production well at a later time.

Fig. 5.10 shows the values of $scCO_2$ production rate and inverse mobility (M), calculated every time step. From Fig. 5.10a and c, it is observed that heterogeneity has a negligible effect on the CO_2 production rate. Also, the CO_2 production rates are slightly lower than their injection rates. This indicates there is some CO_2 loss in the reservoir, and that not all the injected CO_2 reaches the production well. This loss is more sensible for lower injection rates and impairs the CPG performance by reducing the production mass flowrate. While the effect of heterogeneity on the production rate is negligible, heterogeneity increases the aquifer pressure drop in heterogeneous cases. It results in higher inverse mobility (M) values compared to their homogeneous cases by about 1.2, 1.5, and 1.7 times for cases with $w = 150$, 100, and 50 m, respectively (Fig. 5.10d). The value of M (which is essentially the aquifer impedance), becomes relatively constant after about 5 years for high injection rates (100 and 200 kg/s) and after about 10 years for lower injection rates (Fig. 5.10b). Also, M is considerably higher for a brine-geothermal system, and therefore, the thermosiphon

performance of CO_2 is significantly higher than that of brine, especially in shallow aquifers [56].

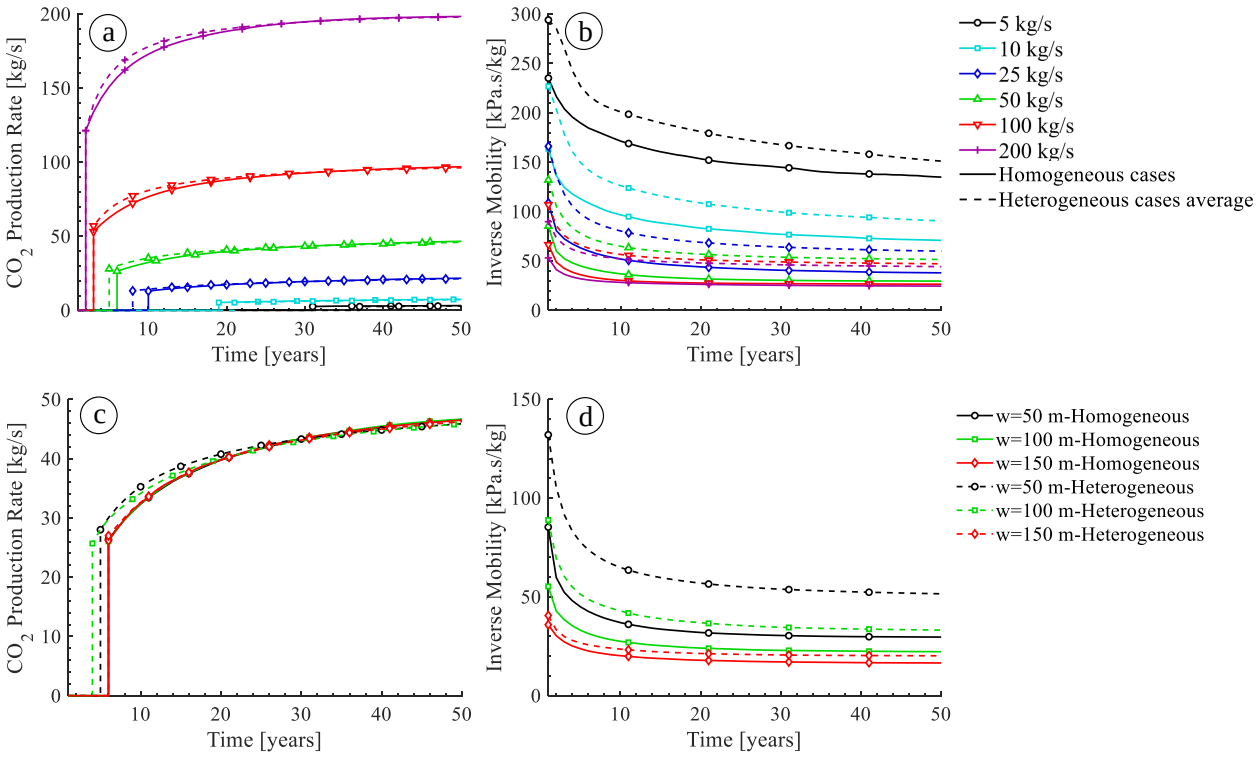

Figure 5.10: CO_2 production rate and the aquifer impedance (inverse mobility) versus flowrate for constant channels' width $w = 50$ m (a & b), and versus channels' width for constant injection rate $\dot{m}_{\text{inj}} = 50$ kg/s (c & d).

Fig. 5.11a shows the values of the CPG cycle excess pressure (P_{excess}) for different injection rates. Ideally, when thermal depletion happens at a very slow pace, such as in the cases with 5 kg/s and 10 kg/s flowrates, the maximum P_{excess} (about 5.4 MPa) is achieved at the surface power plant. However, as observed from the results of the temperature fraction (Fig. 5.8a), the aquifer gradually thermally depletes as CO_2 is injected. By decrease in the downhole temperature of the production well, the CO_2 density gradient between the two wells decreases and consequently, the thermosiphon is weakened. For high injection rates, P_{excess} decreases faster and therefore, the CPG lifetime will be shorter. For the homogeneous cases that represent the aquifer with $w = 50$ m ($k_{\text{avg}} = 225.5$ mD), the CPG power plant operation time (the span between the sequestration stage and CPG lifetime) is about 19, 31, 40, 44, 34, and 11 years for the injection rates of 5, 10, 25, 50, 100, and 200 kg/s, respectively. Therefore, it is observed that the case with an injection rate of 50 kg/s provides the highest CPG operation time.

Although heterogeneity slightly affects the CPG lifetime, it has a significant impact on P_{excess} (Fig. 5.11b). In an aquifer with the presence of fluvial channels, the average value of P_{excess} that thermosiphon provides is about 34%, 20%, and 5% lower for cases with $w = 50$ m, 100 m, and 150 m, respectively, compared with their representative homogeneous cases.

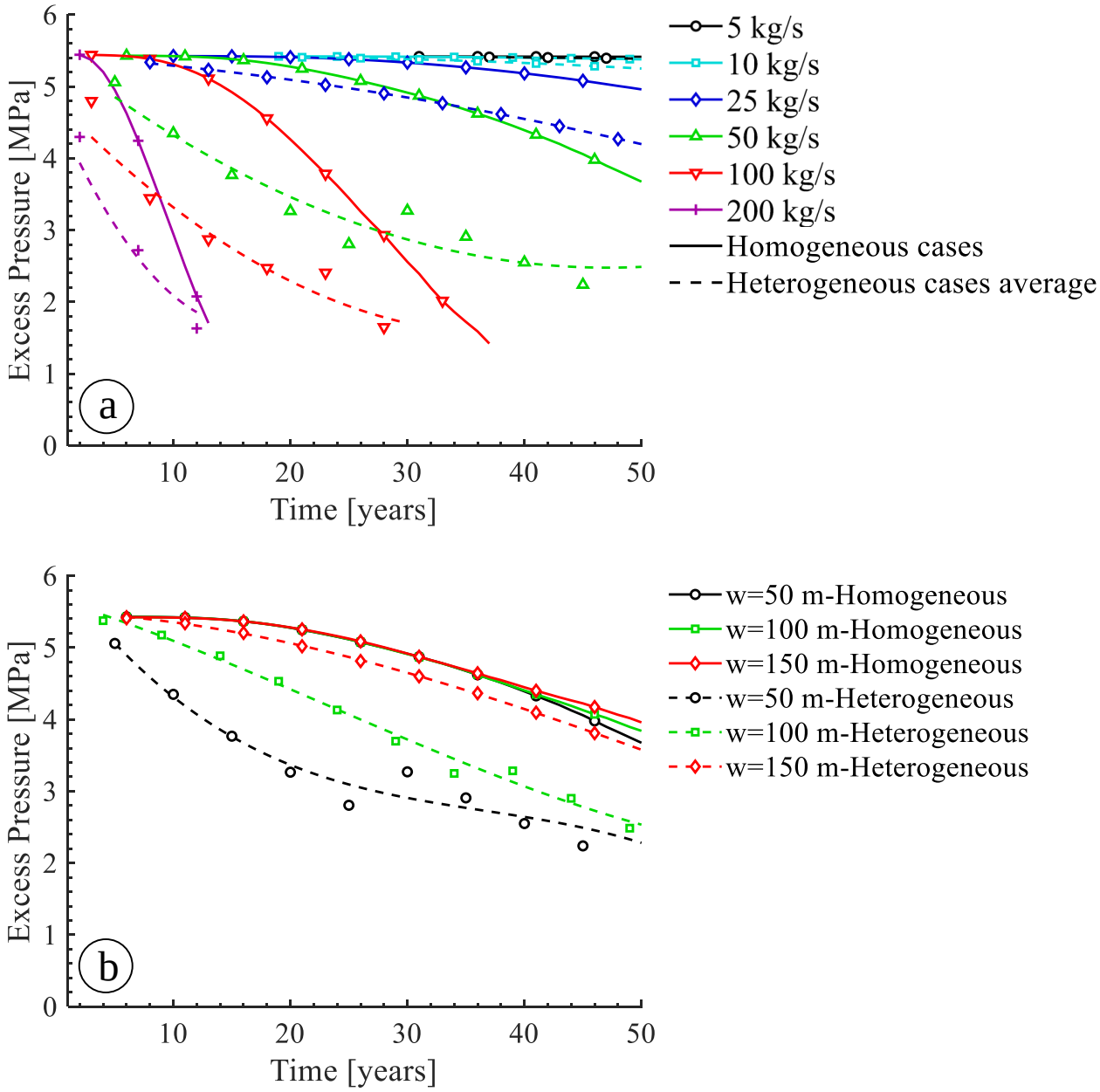

Figure 5.11: CPG cycle excess pressure (the pressure difference between the surface injection and production conditions) for (a) different flowrates and constant channels' width $w = 50$ m, and (b) for different channels' width and constant injection rate $\dot{m}_{\text{inj}} = 50$ kg/s.

The instantaneous net electric power generation values, from the sequestration stage

to the CPG lifetime, are found for each aquifer realisation (Fig. 4.2) and are displayed in Fig. 5.12(a) with fixed channels' width ($w = 50$ m), and in Fig. 5.12(b) with fixed injection rate ($\dot{m}_{\text{inj}} = 50$ kg/s). During the initial years of injection, the net power is ascending. This is because, at the initial stage, the $scCO_2$ production rate is increasing, the inverse mobility M is decreasing, and the thermal plume has not yet reached production well. Therefore, a maximum point happens after the PE stage, resulted from the interactions between the aquifer mobility and temperature drop at the production well. After this point, when the CO_2 thermal plume reaches the production well, aquifer thermal depletion occurs and the temperature fraction (Γ) decreases, resulting in a decrease in net power. As the injection rate is increased, contrary to the CPG cycle lifetime, the maximum value of net power increases. For the homogeneous case with $\dot{m}_{\text{inj}} = 200$ kg/s, the maximum net power is about 1.34 MW_e. Nevertheless, this value decreases to about 0.82 MW_e for the representative heterogeneous case. Again, it is observed that fluvial heterogeneity, especially with lower channels' width (50 m), significantly decreases the instantaneous net power. Therefore, considering a homogeneous aquifer for CPG representation can overestimate the net power output to about 3 times the actual heterogeneous reservoir.

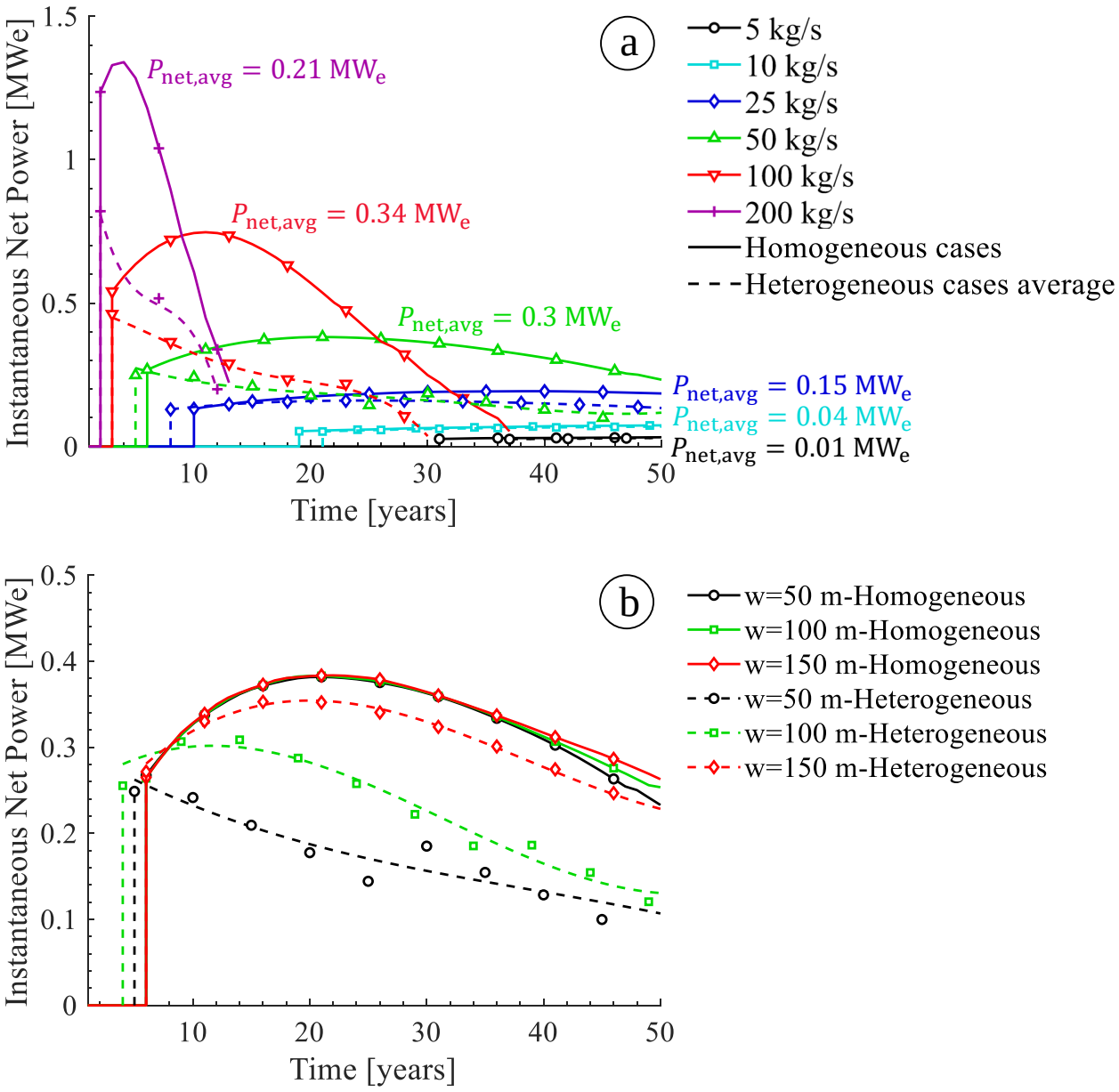

Figure 5.12: Instantaneous net power for (a) different flowrates and constant channels' width $w = 50$ m, and (b) for different channels' width and constant injection rate $\dot{m}_{inj} = 50$ kg/s. $P_{net,avg}$ shows the average produced net power over 50 years.

The CPG system's cumulative net power over 50 years, from the sequestration stage to the CPG lifetime, is illustrated in Fig. 5.13(a). Since it was observed that the injection rate has a significant effect on both the sequestration stage and the CPG lifetime, it is vital to find an optimum injection rate that observes a balance between these two periods and provides the highest output power. It was concluded in the previous sections that the injection rate of 50 kg/s provides the longest CPG cycle operation time (44 years), over the 50 years of injection.

From Fig. 5.13(a), the optimum injection rate for the homogeneous cases of the present paper is about 100 kg/s and for the heterogeneous cases is about 50 kg/s. Heterogeneous cases have a lower optimum injection rate because thermal depletion and temperature drop happen faster in these cases. Additionally, heterogeneity has reduced the CPG system cumulative power over 50 years by about 75%, 61%, and 41% for $w = 50$, 100, and 150 m, respectively, for the 100 kg/s cases. Meanwhile, for lower injection rates ($\dot{m}_{\text{inj}} < 10$ kg/s) heterogeneity has a negligible effect on the cumulative net power and therefore, can be overlooked. The grey area in Fig. 5.13, shows the region where the optimum injection rate happens.

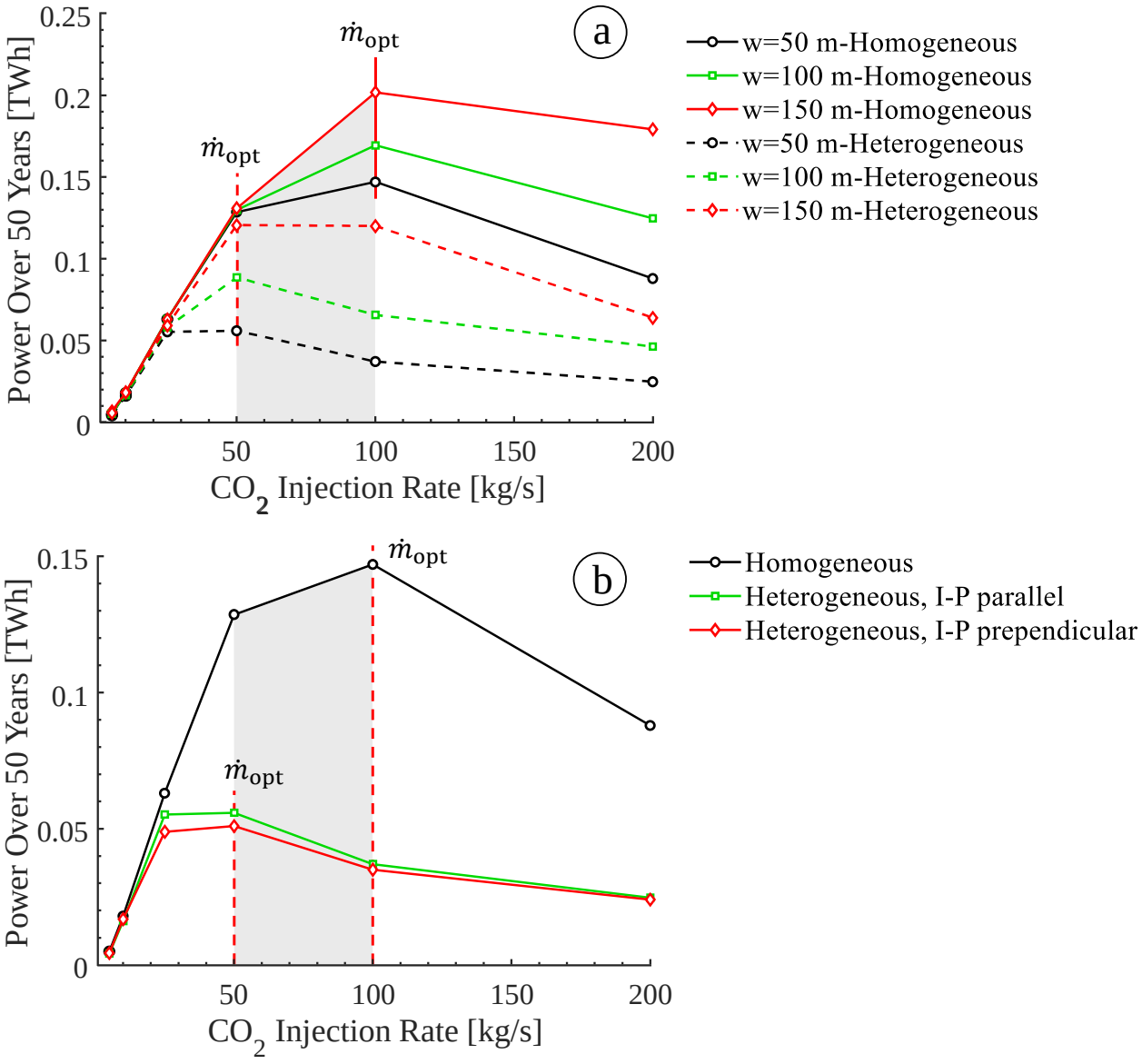

Figure 5.13: Cumulative power over 50 years for (a) different channels' width, and (b) heterogeneity cases. The vertical lines show the optimum injection rate for each of the cases.

It is expected that the I-P line orientation with respect to the channels' orientation affects the pressure drop, and CO_2 and temperature distribution in the aquifer. Therefore the overall CPG performance is affected. I previously studied doublet well patterns and it was observed that the I_1-I_2 line parallel to channels provides the highest performance [157, 174]. In the present study, effects of I-P line orientation in heterogeneous cases with a single injection-production well pair are analysed. Fig. 5.13(b) shows the overall CPG performance for aquifers without channels, with I-P line parallel to channels, and with I-P line perpendicular to channels' orientation. In cases with parallel I-P line, the thermal plume extension toward the production well is almost the same as the perpendicular cases. However, the CO_2 thermal plume mostly expands in the direction of channels and therefore, it sooner reaches the production well. Thus, thermal depletion happens faster in parallel cases (Fig. 5.14). Similarly for the CO_2 saturation in parallel cases – in a similar time-frame with the perpendicular ones – the CO_2 saturation near the production well is much higher. In contrast, in the perpendicular cases, channels misdirect CO_2 propagation and prevent it from reaching the production well. This results in considerably shorter sequestration times and more importantly, higher CO_2 production rates for parallel cases. Resulting from a combination of factors such as faster thermal depletion, lower sequestration time, higher CO_2 saturations and flowrates, and lower pressure drop, it is observed that the cases with I-P line parallel to the channels' orientation provide a higher cumulative power generation by about 10% compared to the perpendicular cases (Fig. 5.13(b)).

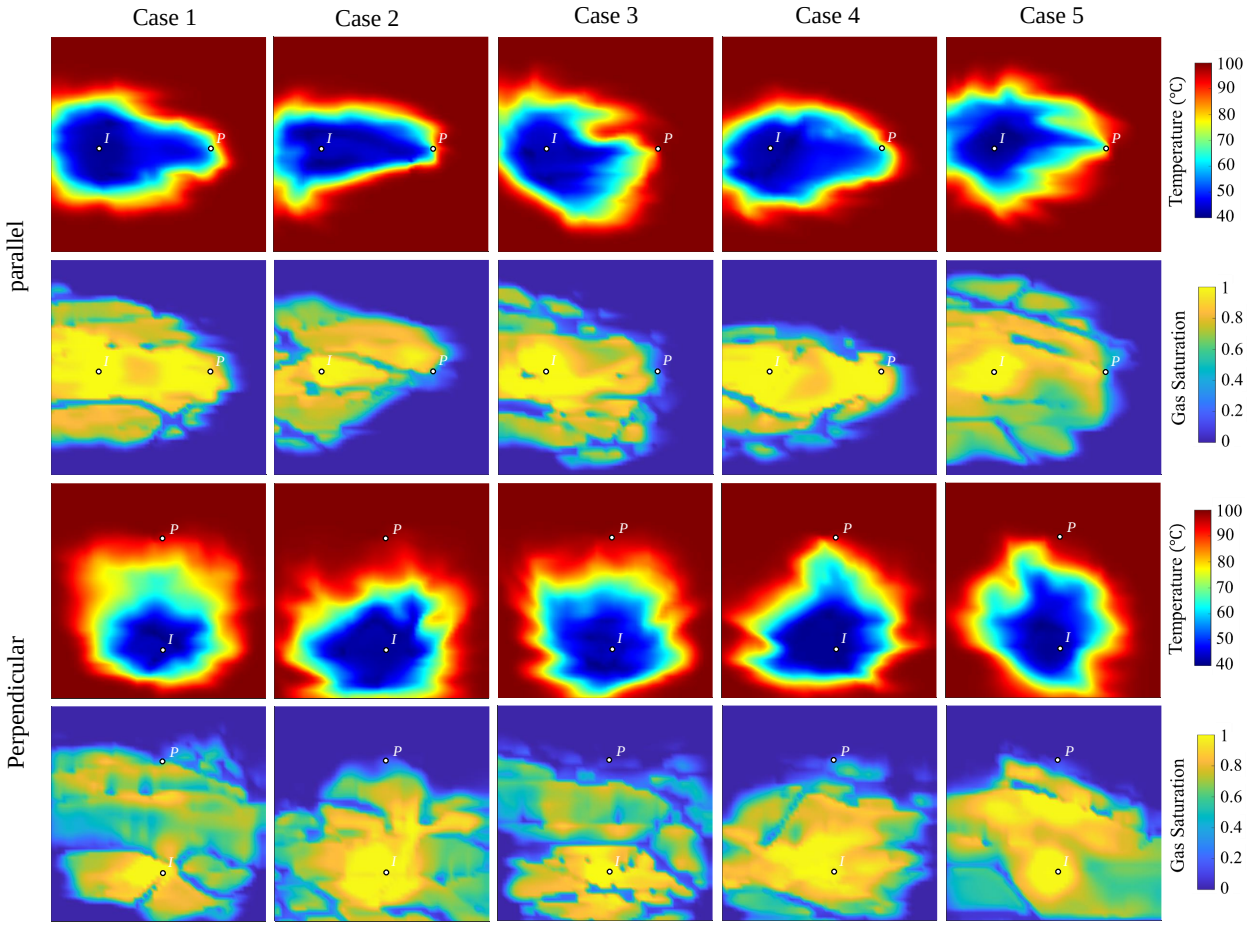

Figure 5.14: Temperature and CO_2 saturation distribution at the mid-surface of the reservoir (2050 m) for the parallel and perpendicular heterogeneous cases with channels' width of $w = 50$ m after 25 years of injection.

5.4.2 Adjusting flowrate and constant excess pressure

As observed in Section 5.4.1, due to the aquifer thermal depletion, the CPG performance is dropped and at some point (when either the CO_2 temperature or pressure falls below the critical values) the system is stopped to prevent possible damage to the turbine. Therefore, it is important to constantly have a supercritical fluid at the turbine's inlet. As a result, a lower bound for P_{excess} (3.5 MPa) is defined, and by adjusting the system flowrate, I keep the system above the operational limit. Initially, CO_2 is injected at the rate of 50 kg/s, and when the PE stage has passed, the flowrate is updated on a yearly basis. The optimum flowrate is a result of the balance between the P_{excess}, aquifer pressure loss, and temperature drop. The injection and the production rates for the homogeneous cases are shown in Fig. 5.15.

At some point, to observe the $P_{\text{excess}} \geq 3.5$ MPa condition, the injection rate moves toward zero, which defines the power cycle lifetime. The CPG operation time is about 45, 34, and 23 years for the homogeneous cases of $k_{\text{avg}} = 225.5$, 336.5, and 568.5 mD, respectively.

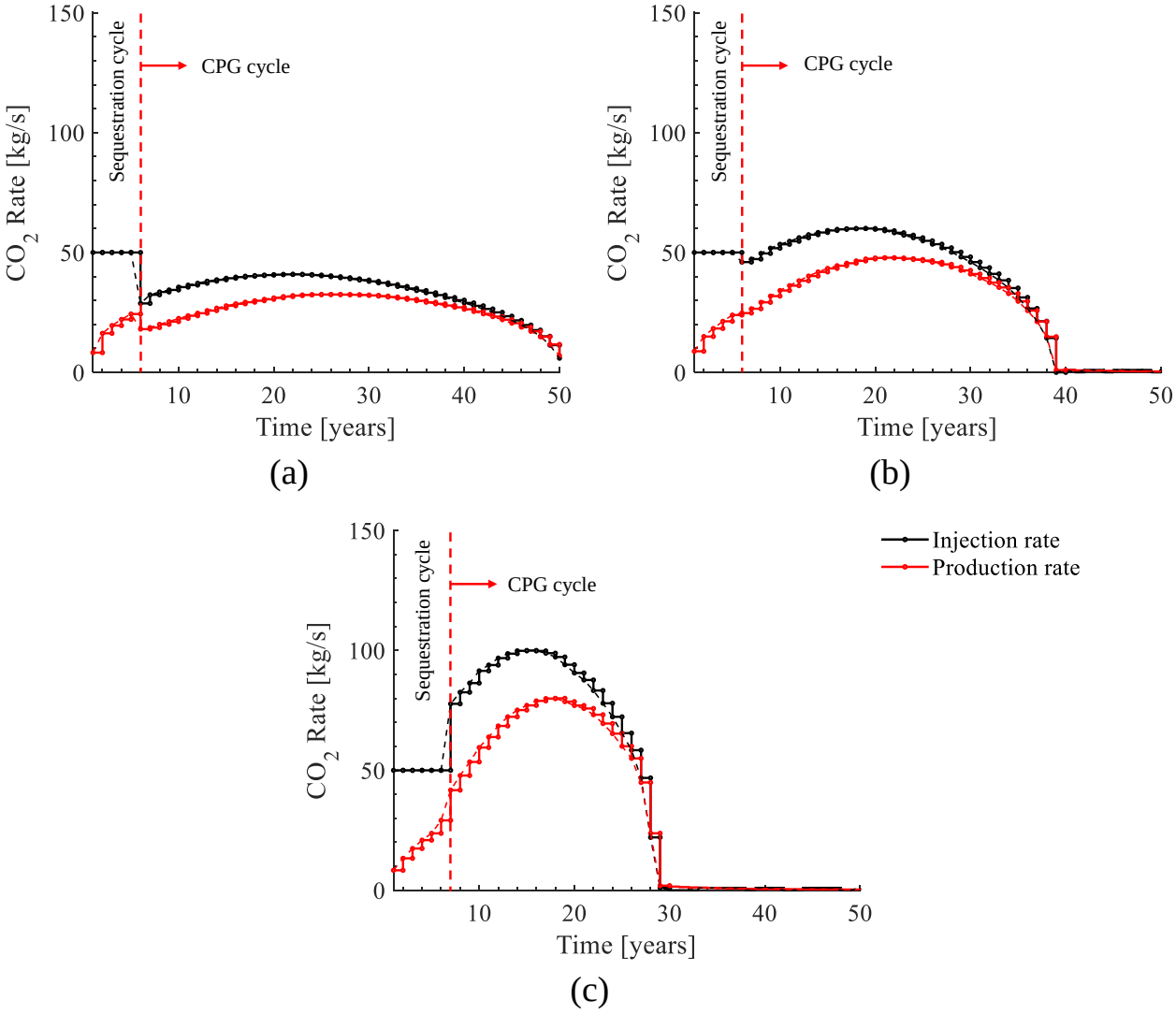

Figure 5.15: Optimised CO_2 injection rate and the resulted production rate for the homogeneous cases of (a) $k_{\text{avg}} = 225.5$ mD or $w = 50$ m, (b) $k_{\text{avg}} = 336.5$ mD or $w = 100$ m, and (c) $k_{\text{avg}} = 568.5$ mD or $w = 150$ m.

Fig. 5.16 shows the production well bottomhole temperature, wellhead temperature, excess pressure, and the cumulative power over 50 years, for the cases with adjusting CO_2 injection rate. The adjusting injection rate almost obeys the lower bound that is considered for P_{excess} (3.5 MPa), and it is observed that for only a few time steps, P_{excess} falls below the limit. This is because the injection rate is updated yearly and that the system has a

response time, meaning that it takes some time for the updated injection rate to have its impact on the production well temperature. The considered bound for P_{excess} also results in lower bounds for the well bottomhole temperature (80 °C) and for the wellhead temperature (42.5 °C) as well. This means that we can rely on the CPG system to produce $scCO_2$ with the minimum surface temperature of 42.5 °C and the pressure of at least 9.5 MPa ($P_1 + P_{\text{excess}}$ from Fig. 5.6) during the CPG lifetime.

From Fig. 5.16a, b, and c, the CPG system in a heterogeneous aquifer has a shorter response time and is controlled better. However, from Fig. 5.16d, it is seen that the cumulative electric power is about 70%, 50%, and 18% lower for the heterogeneous cases of $w = 50$, 100, and 150 m, compared to their representative homogeneous cases.

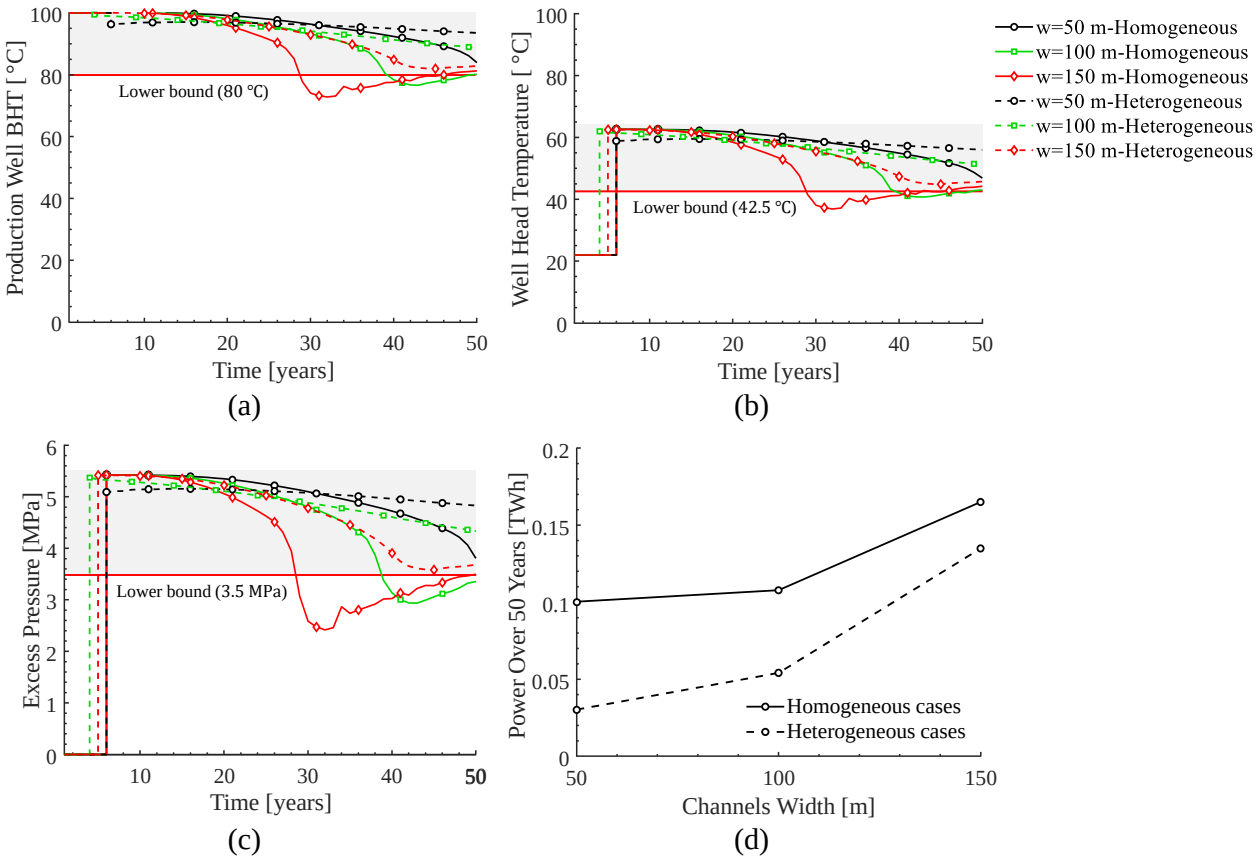

Figure 5.16: Optimised CO_2 injection rate results: (a) production well bottomhole temperature, (b) production wellhead temperature, (c) CPG cycle excess pressure, and (d) cumulative power over 50 years for different channels' width and heterogeneity cases. Here, the lower limits for the production well bottomhole temperature, well head temperature, and excess pressure are set as 80 °C, 42.5 °C, and 3.5 MPa, respectively.

5.5 Conclusions and remarks

Performance and electric power generation and limits of a direct-CO_2 thermosiphon system combined with a CO_2 expansion turbine cycle in both homogeneous and 3D fluvial braided heterogeneous aquifers, with different channels' widths, are studied in this paper.

The key findings can be summarised as below:

- The CO_2 injection rate considerably affects the required sequestration stage for CO_2 to reach a minimum pore-space saturation of about 0.3 to 0.4. As a result, flowrates such as 5 and 10 kg/s that have a very long CO_2-plume establishment stage (about 20 to 35 years) are not applicable for a single pair of wells.

- The aquifer thermal depletion and the production temperature drop are two of the main problems affecting the thermosiphon. Additionally, fluvial heterogeneity deteriorates thermal depletion by a value between 22% and 120%, depending on the channels' width.

- Since the produced CO_2 is directly used in an expansion turbine, it is important that CO_2 is produced at its supercritical phase in the production well. The time that CO_2 falls below the supercritical condition defines the cycle lifetime. Higher injection rates have a shorter cycle lifetime due to their faster aquifer thermal depletion (as expected).

- The I-P line orientation with respect to channels affects both CO_2 and thermal plume distributions inside the aquifer. Cases with the I-P line parallel to the channels' orientation provide higher cumulative power by 10% compared to the cases with I-P perpendicular to channels.

- Among the considered injection rates, $\dot{m}_{\text{inj}} = 50$ kg/s provided the highest CPG cycle operation time by about 44 years (the span between the sequestration stage and the CPG lifetime).

- CO_2 injection rate of 100 kg/s provides the highest performance in homogeneous cases, considered in the present study, with cumulative power generation of about 0.15, 0.17, and 0.20 TWh for $k_{\text{avg}} = 225.5$, 336.5, and 568.5 mD, respectively. On the other hand, the injection rate of 50 kg/s is the optimum rate in heterogeneous cases of the present study and provides about 0.06, 0.09, and 0.12 TWh for $w = 50$, 100, and 150 m, respectively. To put this in perspective, according to [182], a typical domestic household in the UK consumes about 242 kWh per month. Therefore, should the CPG

described in the present study work in its optimal performance ($\dot{m}_{\text{inj}} = 100$ and 50 kg/s for homogeneous and heterogeneous aquifers, respectively), it can provide the required electricity for about 1600 households[1] over 43 years lifetime and 920 households over 45 years lifetime for the CPG working in homogeneous and heterogeneous aquifers with $w = 150$ m, respectively.

- Neglecting the heterogeneous nature of aquifers can result in an overestimation both in cycle electric power output and lifetime. The presence of fluvial heterogeneity in the aquifer decreases the CPG performance up to about 75%, depending on the channels' width and CO_2 injection rate.

Results suggest that for a CPG system, to provide acceptable electric power and to become commercial, high mass flowrates are required (50 to 100 kg/s). However, these values for injection rate are relatively high to be practical for a single injection/production well pair. For example in Sleipner, the injection rate of the single injection well is 1 million tonnes per year of CO_2 which is around 32 kg/s [183]. Or in Cranfield Geological Carbon Sequestration Project, the maximum injection rate per well is only 500 kg/min or 8.33 kg/s [184, 185]. Or in the North Sea, median UK oil and gas production rate corresponds to around 0.35 Mt/yr/well or 11.1 kg/s/well of CO_2 [186]. Therefore, to inject 50 kg/s, several injection and production wells are required. In this scenario, well patterns [53] and perforation cost are two major issues. In addition, by dividing the injection rate into smaller values, the sequestration stage increases, which is not desirable. To tackle these issues, two alternative scenarios are proposed. The first is to use CPG in depleted oil reservoirs, or the reservoirs that currently include CO_2 from sequestration processes, such as the SECARB Cranfield Site that a brine-saturated sand has been under CO_2 flood [154]. The second is to use CPG in shallower depths and smaller scales for peak shaving purposes, such as [187] and [188]. In the latter approach, when the cost of energy is low, CO_2 is injected into the reservoir but the production well is shut down, letting the CO_2 to warm-up and reach the required mass-fraction at the production well; and when the cost of energy is high, scCO_2 production starts and cheap renewable geothermal electricity substitutes the expensive fossil fuel-based one. In the peak shaving approach, the reservoir is used as on-site energy storage, and since energy is produced in discrete periods, time is given to the reservoir to recover its temperature and compensate for the thermal depletion.

Another remark is about the electricity output of CPG that I found to be in order of a tenth of TWh. This value is small, however, we need to consider expanding CPG across

[1] (0.2 TWh/43 years)/(242 kWh/month)

multiple wells and deeper, hotter systems. Additionally, one must consider the value of CCS and CCUS, that is, both sequestering CO_2 at the end of the operation, and utilising CO_2 for the operation. The calculation of revenue from CCS and CCUS is not straightforward. However, an analysis by the Committee on Climate Change [189] in 2018 indicates that CCUS will be the only way to decarbonise certain key industrial sectors before 2050. They recommend that 10 MtCO2 should be stored annually by 2030, 3 MtCO2 of which are from industry, to maintain the option of high levels of deployment by 2050, potentially over 100 MtCO2/year. CPG will be an attractive CCUS option to practice the engineering of large volumes of CO_2 storage needed beyond 2050. Assuming 50 kg/s of CO_2 injection, a CPG operation can utilise 1.58 MtCO2/year that will be stored at the end of the operation.

The results and the discussion about the merits and demerits of CPG in this paper can provide guidelines for possible future works to enhance and optimise the CPG technology. Also, this paper proposed a method to prevent possible power over-predictions that are resulted from field uncertainties.

Acknowledgement

The authors acknowledge the University of Manchester President's Doctoral Scholar (PDS) award to Amir Mohammad Norouzi that made this research possible.

Nomenclature

A	Cross-sectional area, [m^2]
h	Specific enthalpy, [J kg^{-1}]
k	Permeability, [mD, m^2]
L	Length, [m]
$\dot{m}$	Mass flowrate, [kg s^{-1}]
P	Pressure, [Pa, MPa]
P_{net}	Net power, [MW_e, TWh]
Q	Mass vapour quality, [-]
s	Specific entropy, [J kg^{-1} $°C^{-1}$]
T	Temperature/channels' thickness, [°C, m]
t	Time, [year]
w	Channels' width, [m]
X_{CO_2}	CO_2 mass-fraction in gas phase, [-]
Γ	Temperature fraction, [-]
η	Efficiency, [-]
λ	Parasitic load fraction [-]
μ	Viscosity, [Pa s]
ρ	Density, [kg m^{-3}]
ϕ	Porosity, [-]

Chapter 6

Summary and Future Work

6.1 Summary

Here, I have summarised the conclusion section of each chapter to provide a more comprehensive view of the research outcomes.

- Chapter 2 presented a comprehensive sensitivity analysis that investigated the relationship between precipitated salt, reservoir damage, and imposed additional pumping requirements with capillary-driven backflow, covering a wide range of governing parameters. The 2D compositional numerical model used in this chapter was validated with that of [76]. The study involved 140 simulations, and a new backflow extent parameter was introduced, allowing for a more meticulous study of the relationship between governing parameters and water backflow. The results indicated that salt, out of all the minerals engaged in geochemical reactions, exerted the most significant impact on reservoir damage and porosity reduction, leading to a reduction of approximately 41% in porosity near the injection well. Moreover, by comparing the outcomes of scenarios with and without capillary effect, it was determined that capillary-driven backflow is the primary mechanism responsible for salt precipitation. Finally, salt precipitation reduced the porosity and permeability of the reservoir, leading to an increase in pressure drop by about 17-26% inside the aquifer [38].

- In chapter 3, an analytical solution was provided based on fractional flow theory and the definition of shocks in the presence of capillary pressure. A one-dimensional homogeneous two-phase model was used for this study, assuming a constant pressure and temperature distribution inside the aquifer, without considering the effects of the density gradient, temperature-dependent properties, and density-driven flow. The study found that capillary-driven backflow functions as a water provider to the dry-out region, leading to ongoing evaporation and precipitation processes as time progresses. This led to an increase in the average amount of the precipitated salt inside the aquifer by 14.71%, and an increase in the salt precipitation in the near injection well area by 58.73%. According to the results, the majority of salt precipitation occurred at a very close distance from the CO_2 injection well (22.81 m in the case considered in this chapter). The analytical solution provided here was capable of estimating the extent and the amount of precipitated salt at the injection well with an average error of about 13.70% compared to the computationally expensive numerical solution [175].

- In chapter 4, a series of simulations using 50 different braided fluvial realisations revealed an optimised doublet well spacing of approximately 400 to 500 metres ($L \approx 450$

m) for optimal performance of the CPG system. This chapter used 2D heterogeneous models, and the performance metrics were defined based on the aquifer (bottomhole) data. To reduce computational time and study a wide range of parameters, upward density-driven flow, and temperature and pressure drop in the production wells were not considered. The results from this chapter were then used to reduce the number of simulations in the next chapter, which included 3D aquifers coupled with well and power plant modelling. Additionally, an upscaling approach was performed on the heterogeneous realisations, and an optimum grid resolution was suggested that provided an average error of less than 10% and has the optimum computational time. The effects of heterogeneity were also investigated, and it was found that fluvial channels significantly reduce the performance of the CPG by a factor of 3 to 5. In other words, a homogeneous reservoir with an average permeability and porosity comparable to the channelised case outperforms the fluvial reservoir by a factor of 3 in terms of net power [157].

- Finally, in chapter 5, which constitutes the main contribution of this thesis, the performance, electric power generation, and limitations of a direct-CO_2 thermosiphon system combined with a direct-CO_2 expansion turbine cycle in 3D fluvial braided heterogeneous aquifers were studied. A total of 156 simulations were conducted on about 20 different fluvial aquifer models. The study identified two primary challenges that impact the thermosiphon: aquifer thermal depletion and the decrease in production temperature. Additionally, fluvial heterogeneity negatively affected thermal depletion, by a value ranging between 22% and 120%, depending on the channels' width. Moreover, in the homogeneous cases examined in this study, the CO_2 injection rate of 100 kg/s yielded the most optimal performance, resulting in cumulative power generation ranging from 0.15 to 0.20 TWh. The findings indicated that in order to achieve satisfactory electricity generation, a substantial mass flow rate ranging from 50 to 100 kg/s is necessary for a CPG system. However, these injection rates may not be feasible for a single injection/production well pair. One possible solution is to employ multiple injection and production wells. In this scenario, the arrangement of wells [53] and perforation costs are key to evaluate. Another aspect to take into account is the electricity generated by CPG, which was found to be around one-tenth of a TWh. Although this value may seem small, it is crucial to consider the potential expansion of CPG to encompass multiple wells and explore deeper, hotter systems. Additionally, the value of CCS and CCUS should be considered, specifically the sequestration of CO_2 at the end

of operations and the utilisation of CO_2 during the process [37].

6.2 Future work

The following areas are considered for future work:

- The calculation of the revenue from CCS and CCUS is not straightforward, and to understand whether CPG is financially beneficial, a detailed cost analysis is required, such as the one provided by Ezekiel et al. [190] for the hydrothermal doublet systems. There are some works on the evaluation of the achievable operating earnings from a CPG system [191, 158]. However, the simplifying assumptions in these studies, such as the homogeneity of the aquifers, not considering the well model, or the required CO_2 sequestration time, can result in considerable over-underestimations. Moreover, the performance metrics of CPG are highly dependent on each case, and parameters such as geological uncertainty significantly affect the net power output of these systems. Numerical modelling of 3D heterogeneous aquifers that include geochemical reactions and CO_2-brine interactions is computationally expensive and time-consuming. Therefore, to provide a comprehensive techno-economic model that includes all aspects of a CPG system, I suggest using machine learning methods.

- It has been argued that CPG systems have lower power output than water-based systems and cannot directly provide residential heating since they primarily use the high pressure produced by the fluid. To address these limitations, a new type of water-based geothermal system combined with carbon storage can be introduced. This proposed concept utilises two pairs of water injection and production wells with a single CO_2 injection well in the middle. The water injection wells act as barriers, preventing CO_2 from reaching the production wells. The injected CO_2 increases the reservoir pressure, subsequently increasing the production rates. This proposed concept ensures that no CO_2 or water is released at the surface and increases the carbon storage capacity of the system.

- Finally, in addition to power generation, closed-loop CPG cycles can supplement other power plants as sources of energy. For example, flue gas from gas-fired power plants in power CCS plants contains nitrogen, water vapour and CO_2. A CO_2 absorber tower uses a liquid solvent to extract CO_2 from the flue gas. However, the solvent must

release the CO_2 to inject it into a reservoir and store it underground. Conventionally, a CO_2 stripper tower heats the combined solvent-CO_2 mixture to around 100 °C, releasing CO_2 from the solvent. This process is energy-intensive and potentially increases the carbon footprint of power CCS systems. To address this, the concept of using geothermal heat to provide the thermal energy for CO_2 separation is proposed. The idea involves a closed-loop fluid cycle that absorbs heat from a deep underground reservoir and transfers it to the CO_2-solvent mixture to release the CO_2.

Chapter 7

Appendices

A Mathematical description

A1 Governing equations

Thermodynamic equilibrium is considered between phases at the continuum scale, and simulations are based on Darcy's law. General mass conservation equation and energy equation can be written as follows:

$$\frac{\partial}{\partial t}\left(\phi(\rho_w S_w + \rho_g S_g)\right) = \nabla\left(\rho_w q_w + \rho_g q_g\right) + Q_M \tag{A1a}$$

$$\frac{\partial}{\partial t}\left((1-\phi)\rho_m U_m + \phi(\rho_w S_w U_w + \rho_g S_g U_g)\right) = \nabla\left(\rho_w h_w q_w + \rho_g h_g q_g + K\nabla T\right) + Q_E \tag{A1b}$$

The description of the parameters of these equations is provided in the nomenclature table, and phase fluxes are calculated from Darcy's law, ($q_w = \frac{-kk_{rw}}{\mu_w}(\nabla P - \rho_w g)$ and $q_g = \frac{-kk_{rg}}{\mu_g}(\nabla P - \rho_g g)$). The components' mass conservation equation is considered as follows:

$$\frac{\partial}{\partial t}\left(\phi(c_{iw}\rho_w S_w + c_{ig}\rho_g S_g)\right) = \nabla\left(\frac{c_{iw}\rho_w k k_{rw}}{\mu_w}(\nabla P - \rho_w g \nabla D) + \frac{c_{ig}\rho_g k k_{rg}}{\mu_g}(\nabla P - \rho_g g \nabla D)\right) + q_i + F_{iw} + R_{iw} \tag{A2}$$

In this equation, q_i, F_{iw}, and R_{iw}, represent component variations due to injection or production, diffusion, and chemical reactions per unit volume and time, respectively.

A2 CO_2 and water solubility, diffusion, densities, and viscosities

During the injection procedure, CO_2 dissolves into the brine, and at the same time water vaporizes into the gaseous phase, *i.e.*, CO_2. Since the dissolution process happens quickly inside the aquifer, the whole system is considered to be in phase equilibrium condition [62]:

$$g_i = f_{i,g} - f_{i,w} = 0 \tag{A3}$$

where, $f_{i,g}$ represents the fugacity of the component i in the gaseous phase that can be calculated through the Peng-Robinson EoS [148] and $f_{i,w}$ shows the fugacity of the component i in the aqueous phase. Fugacity $f_{i,w}$ of the gaseous component in the aqueous phase can be obtained through Henry's law. Finally, the fugacity of water and CO_2 are calculated as

follows.

$$f_{CO_2,w} = y_{CO_2} H_{\text{salt},CO_2} \tag{A4a}$$

$$f_{H_2O,w} = y_{H_2O,w} f_{H_2O} \tag{A4b}$$

In Eqs A4a and A4b, H represents Henry's law constant, which is a function of pressure, temperature, and salinity and y denotes the component mole fraction. Here, the Henry coefficient of CO_2 in brine (H_{salt,CO_2}) is obtained from the relations reported in [192, 193, 194, 195], and f_{H_2O}, which is the fugacity of water at any temperature or pressure, can be calculated by utilising the equations reported by Canjar and Manning [196], aul and Wagner [193], and Rowe and Chou [145].

Another parameter that significantly affects the geochemical reactions is the diffusion of CO_2 into the brine, which increases the amount of CO_2 inside the brine and amplifies the CO_2-water-mineral reactions. For this purpose, the Stokes-Einstein law [197] is used to model the diffusion of aqueous components.

The Peng-Robinson EoS [148] is used to calculate CO_2 density, and its viscosity is estimated from the Jossi, Stiel, and Thodos correlation [149]. The brine density and viscosity are calculated respectively from the Rowe and Chou [145] and the Kestin et al. [146] correlations, whose applicability ranges are provided in Table A1. The Rowe-Chou correlation is a pressure-volume-temperature-concentration dependant equation reported for saline solutions.

Table A1: Applicability range of the correlations used for brine density and viscosity [147].

Correlation	**Fluid**	P (MPa)	T (°C)	$\hat{S}$ (mg.L^{-1})
Rowe and Chou [145]	NaCl solution	≤ 35	20-150	≤ 330000
Kestin et al. [146]	NaCl solution	0.1-35	20-150	≤ 460000

A3 Geochemical reactions, mineral precipitation, permeability, and porosity relations

Chemical reactions inside the reservoir are classified into intra-aqueous and mineral reactions. Aqueous reactions are the ones that only include soluble gaseous components, components that only exist in the aqueous phase, and H^+ and OH^-. These reactions happen at a relatively higher speed than the mineral ones, therefore they are represented as chemical equilibrium reactions. On the other hand, chemical kinetics is considered for mineral reactions and they

are represented as rate-dependent reactions [62]. Stoichiometry of the aqueous and mineral reactions is as follows:

$$\sum_{k=1}^{n_{aq}} \nu_{k\alpha}^{a} A_k = 0, \quad \alpha = 1, ..., R_{aq} \tag{A5}$$

In the above equation, n_{aq} is the number of components in the aqueous phase, R_{aq} is the number of intra-aqueous reactions, A_k is the chemical symbol of the aqueous species, and ν is the stoichiometric coefficient. With the same approach for the mineral equations:

$$\sum_{k=1}^{n_{ct}} \nu_{k\beta}^{m} A_k = 0, \quad \beta = 1, ..., R_{mn} \tag{A6}$$

Again, in Eq. A6, n_{ct} represents the total number of components and R_{mn} is the number of mineral reactions.

As mentioned previously, aqueous reactions are at chemical equilibrium and are modelled with chemical equilibrium constants [146].

$$Q_\alpha - K_{eq,\alpha} = 0, \quad \alpha = 1, ..., R_{aq} \tag{A7}$$

and

$$Q_\alpha = \prod_{k=1}^{n_{aq}} a_k^{\nu_{k\alpha}} \tag{A8}$$

In Eqs A7 and A8, $K_{eq,\alpha}$ represents the chemical equilibrium constant for each reaction, and $a_k, \nu_{k\alpha}$, and Q_α are the activity of component k, stoichiometry coefficient, and activity product, respectively. The activity coefficient is calculated through the B-dot model [146]. In addition, Bethke [198] provided $K_{eq,\alpha}$ as a function of temperature (°C) for most of the aqueous reactions. In the present work, a fourth-order correlation is used to calculate the $K_{eq,\alpha}$, whose constants are provided in Table A2.

$$\log(K_{eq,\alpha}) = \xi_0 + \xi_1 T + \xi_2 T^2 + \xi_3 T^3 + \xi_4 T^4 \tag{A9}$$

For mineral reactions occurring at a slower rate compared to aqueous ones, the rate law should be implemented [146]. Based on [199] and [200], salt reaction also requires more time compared to aqueous reactions. Therefore, NaCl reaction is considered as a rate-reaction as well.

$$r_\beta = \hat{A}_\beta k_\beta \left(1 - \frac{Q_\beta}{K_{eq,\beta}}\right), \quad \beta = 1, ..., R_{mn} \tag{A10}$$

In which, r_b is the reaction rate, $\hat{A}_\beta$ is the reactive surface area, k_β is the rate constant, $K_{eq,\beta}$ is the equilibrium constant (see Table A2), and Q_β is the active product of mineral component which resembles that of aqueous ones. The procedure for calculating each of these parameters is completely described by Nghiem et al. [62]. Also, rate law-related parameters are provided in Table A3. In Eq. A10, $\frac{Q_\beta}{K_{eq,\beta}}$ is the saturation index (SI) [62], where

$$
\begin{aligned}
&if: \ \text{SI} > 1, \quad \text{then mineral dissolution happens} \\
&if: \ \text{SI} = 1, \quad \text{reaction rate is zero} \\
&if: \ \text{SI} < 1, \quad \text{then mineral precipitation happens}
\end{aligned}
$$

Table A2: Chemical reactions equilibrium coefficients.

Reaction number	ξ_0	ξ_1	ξ_2	ξ_3	ξ_4
2.1a	14.9282	-0.0419	1.97×10^{-4}	-5.55×10^{-7}	7.58×10^{-10}
2.1b	-6.5492	0.0090	-1.02×10^{-4}	2.76×10^{-7}	-3.56×10^{-10}
2.1c	10.6080	-0.0128	1.20×10^{-4}	-3.02×10^{-7}	2.69×10^{-10}
2.1d	2.0689	-1.4267	-6.06×10^{-6}	1.46×10^{-7}	-4.19×10^{-10}
2.1e	3.1746	-0.2012	5.96×10^{-4}	-9.04×10^{-7}	9.15×10^{-11}
2.1f	9.72954	-0.0980	2.92×10^{-4}	-3.27×10^{-7}	-3.31×10^{-10}
2.1g	1.5686	0.0004	5.00×10^{-6}	-3.00×10^{-9}	-5.00×10^{-12}

Table A3: Parameters for mineral reactions' rate law [62].

Mineral	**log$k_{25°C}$** ($\mathbf{mol.m^{-2}s^{-1}}$)	**Activation energy** ($\mathbf{J.mol^{-1}}$)	**Initial specific reactive surface** ($\mathbf{m^2.m^{-3}}$)
Calcite	-8.8	41870	88
Anorthite	-12	67830	88
Kaolinite	-13	62760	17600
Halite [199, 200]	-5	2000	176

To implement the effects of mineral reactions on the porosity and permeability of the

reservoir, the following equations are used [62]:

$$\hat{\phi}^* \equiv \phi^* - \sum_{\beta=1}^{n_m} \left(\frac{N_\beta - N_\beta^0}{\rho_\beta} \right) \tag{A11}$$

$$\phi = \hat{\phi}^* [1 + c_\phi (P - P^*)] \tag{A12}$$

In the above equations, ϕ, ϕ^*, and $\hat{\phi}^*$ are the reservoir current porosity, reservoir initial porosity without mineral effects, and reservoir initial porosity including mineral effects, respectively. Also, N_β is the current moles of mineral β, N_β^0 is the initial moles of mineral per bulk volume inside the reservoir, ρ_β is the component's molar density, c_ϕ is the rock compressibility, and P^* is the reference pressure. To connect the minerals precipitation to reservoir permeability, the Kozeny-Carman equation [113, 114] with the exponent index of 5 is used.

$$\frac{k}{k_0} = \left(\frac{\phi}{\phi_0} \right)^{R_{exp}} \left(\frac{1 - \phi_0}{1 - \phi} \right)^2 \tag{A13}$$

In which, k_0, ϕ_0, and R_{exp} are the reservoir's initial permeability, reservoir's initial porosity, and the exponent index, respectively.

B Validation and grid resolution sensitivity

To validate the results and make sure of the accuracy of the simulations, four cases are considered, and results are compared with those of Cui et al. [76].

- Validation case 1 considers both the capillary pressure and the water evaporation with no mineral or geochemical reaction.
- Validation cases 2 and 3 only consider the effects of water evaporation and capillary pressure, respectively.
- Validation case 4 considers capillary, water vaporization, and geochemical reactions.

Water saturation is studied for the validation of cases 1, 2, and 3, and halite mole per unit volume and porosity are considered for the validation of case 4. Based on the validation results provided in Fig. B1, it is observed that the results are in perfect agreement with those of Cui et al. [76] with an average error of 0.8% for cases 1, 2, and 3 and an average error of 0.6% for porosity and 7% for halite in case 4.

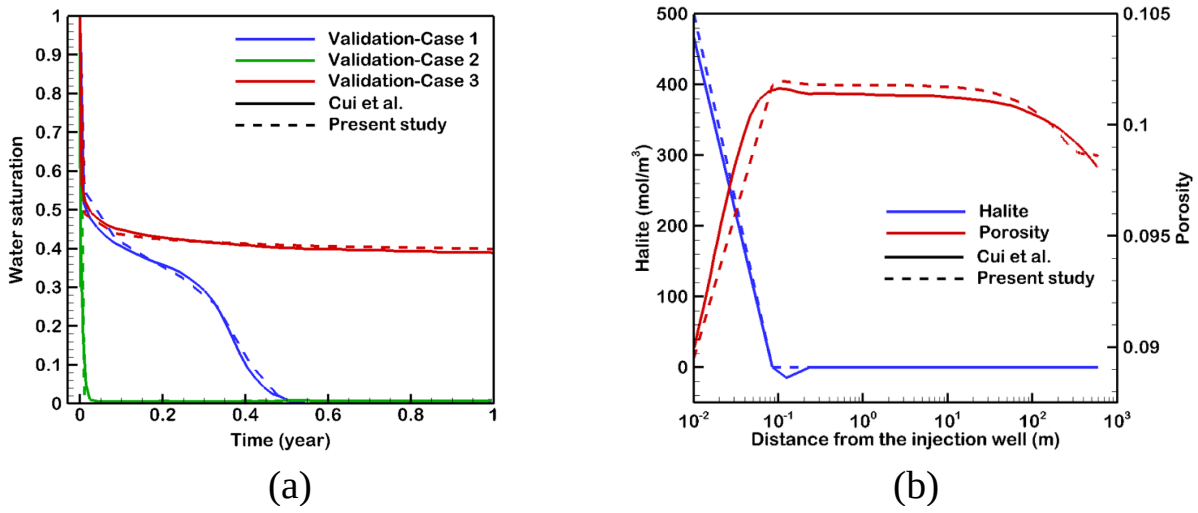

Figure B1: (a) Water saturation at the injection well grid block for validation cases 1, 2, and 3, and (b) validation case 4 results after 30 years.

To achieve a solution with minimum computational costs and the highest accuracy, a grid sensitivity analysis is performed. For this purpose, a more refined 1D grid with 605 grids and dx=0.05 to 1 m is generated and the most grid sensitive parameters, *i.e.*, water backflow velocity, salt precipitation, and porosity at the injection well are considered for the comparison. Based on the results, which are illustrated in Fig. B2, it is obvious that the

difference between the aforementioned parameters in the two geometry cases is negligible, however, the simulation time for the refined mesh was much higher. As a result, the grid with dx=0.05 to 10 m was chosen for this study.

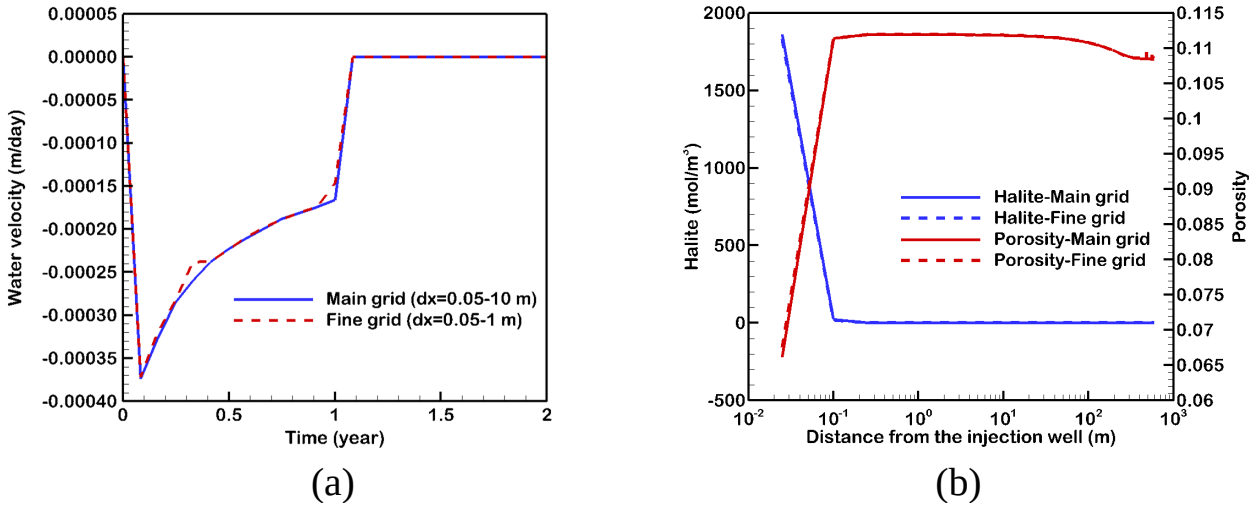

Figure B2: (a) Water backflow at the injection well grid block for different times, and (b) halite and porosity throughout the reservoir after 30 years.

C Capillary-driven backflow versus thermodynamics of the system

To compare the influence of the capillary-driven backflow on salt precipitation with the thermodynamics of the system, two high salinity cases (233,760 ppm) with the same thermodynamic conditions were considered. In these cases, water pressure was set to be similar, however, one of the cases included capillary pressure and the other did not. To make the water pressure the same ($P_{\text{water}} = P_{\text{CO}_2} - P_{\text{cap}}$) in both cases, the CO_2 injection rate in the no-capillary case was decreased to 5.7 kg.s^{-1} from 15 kg.s^{-1}. The results of these cases are illustrated in Fig. C1.

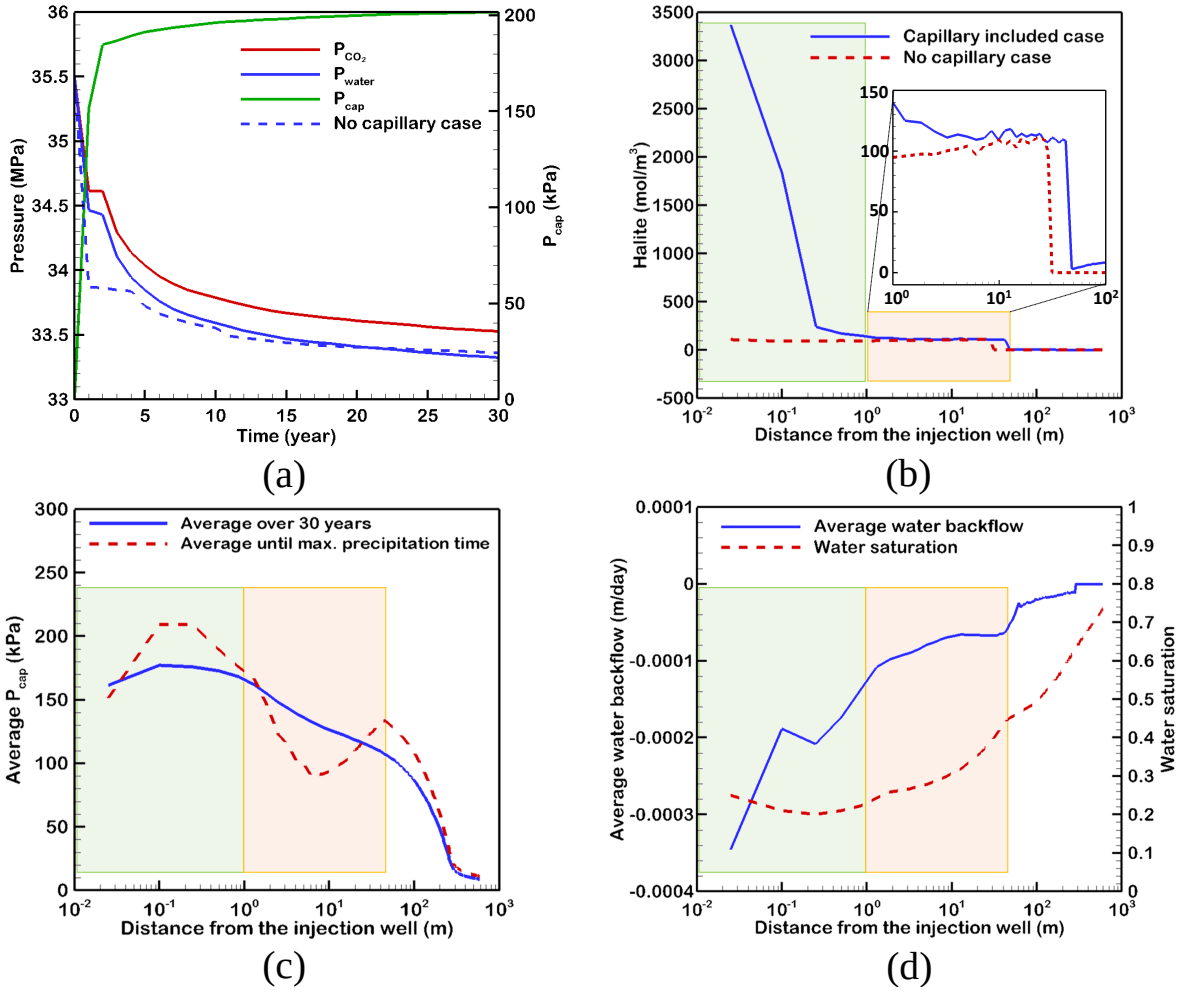

Figure C1: (a) Water, CO_2, and capillary pressure at the injection well, (b) salt precipitation over the reservoir after 30 years, (c) average capillary pressure, and (d) water backflow and saturation over the reservoir.

Based on these results, capillary-driven backflow is most intense and has the highest effect in the vicinity of the injection well (green zone in Fig. C1 $x < 1$ m). Therefore, it can be concluded that at the injection well and up to the zone shown in green, capillary backflow is the dominant driver of salt precipitation. However, as the distance from the injection well increases (red zone), the effect of capillary backflow fades and the thermodynamics of the system plays the key role in salt precipitation. Fig. C1(c) shows that for the capillary pressure-enabled case, the average capillary pressure (over time until maximum salt precipitation occurs) features steep negative gradients (dP_c/dx) behind which salt precipitations are observed at 30 years (zone green and zone red). The green zone near the well leads to strong capillary backflow (Fig. C1(d)) that significantly enhances salt precipitation near well (Fig. C1(b), blue curve in the green zone).

It is acknowledged that further investigation is required to provide a quantitative definition of the length, below which the capillary-driven backflow has a superior effect compared to the thermodynamics of the system. This investigation is crucial to define the proper grid resolution near the injection well.

D Mathematical description

D1 Fractional flow in presence of capillary effect

The first parameter that needs to be defined is the gas fractional flow inside the reservoir in presence of capillary pressure. Considering a control volume and writing the conservation equation ($\Delta M = M_{\text{in}} - M_{\text{out}}$) for it, the following mass conservation equation is achieved.

$$-\frac{\partial(\rho q)_{\text{a,g}}}{\partial r} = \frac{\partial}{\partial t}(A\phi\rho S)_{\text{a,g}} \tag{D1}$$

Using Darcy's equation to calculate flow rates, the total fluid volumetric flow rate inside the reservoir is defined as the following equation:

$$q_{\text{t}} = q_{\text{a}} + q_{\text{g}} = -\frac{kk_{\text{ra}}A}{\mu_{\text{a}}}\left(\frac{\partial P_{\text{a}}}{\partial r} - \rho_{\text{a}}g_{\text{x}}\right) - \frac{kk_{\text{rg}}A}{\mu_{\text{g}}}\left(\frac{\partial P_{\text{g}}}{\partial r} - \rho_{\text{g}}g_{\text{x}}\right) \tag{D2}$$

Neglecting the effect of gravity and having $P_{\text{cap}} = P_{\text{g}} - P_{\text{a}}$, Eq. D2 can be rewritten as below:

$$\begin{aligned} q_{\text{t}} &= -\frac{kk_{\text{ra}}A}{\mu_{\text{a}}}\left(\frac{\partial P_{\text{g}}}{\partial r} - \frac{\partial P_{\text{cap}}}{\partial r}\right) - \frac{kk_{\text{rg}}A}{\mu_{\text{g}}}\left(\frac{\partial P_{\text{g}}}{\partial r}\right) \\ &= -kA\left(\frac{k_{\text{ra}}}{\mu_{\text{a}}} + \frac{k_{\text{rg}}}{\mu_{\text{g}}}\right)\frac{\partial P_{\text{g}}}{\partial r} + kA\frac{k_{\text{ra}}}{\mu_{\text{a}}}\frac{\partial P_{\text{cap}}}{\partial r} \end{aligned} \tag{D3}$$

Defining fluid mobilities as $\lambda_{\text{a}} = \frac{k_{\text{ra}}}{\mu_{\text{a}}}$, $\lambda_{\text{g}} = \frac{k_{\text{rg}}}{\mu_{\text{g}}}$, and $\lambda_{\text{t}} = \lambda_{\text{a}} + \lambda_{\text{g}}$, we can write the above equation in a shorten form as:

$$q_{\text{t}} = -kA(\lambda_{\text{a}} + \lambda_{\text{g}})\frac{\partial P_{\text{g}}}{\partial r} + kA\lambda_{\text{a}}\frac{\partial P_{\text{cap}}}{\partial r} \tag{D4}$$

Now, by sorting the above equation for $\frac{\partial P_{\text{g}}}{\partial r}$, we obtain this parameter as a function of capillary pressure and fluid mobilities.

$$\frac{\partial P_{\text{g}}}{\partial r} = \frac{q_{\text{t}} - kA\lambda_{\text{a}}\frac{\partial P_{\text{cap}}}{\partial r}}{-kA(\lambda_{\text{a}} + \lambda_{\text{g}})} \tag{D5}$$

Implementing Eq. D5 in the Darcy's equation for gas phase velocity, we will obtain this parameter based on phases mobilities and the capillary pressure as below:

$$q_{\text{g}} = -\frac{kk_{\text{rg}}A}{\mu_{\text{g}}}\left(\frac{\partial P_{\text{g}}}{\partial r}\right) = \frac{\lambda_{\text{g}}}{\lambda_{\text{t}}}q_{\text{t}} - kA\frac{\lambda_{\text{g}}\lambda_{\text{a}}}{\lambda_{\text{t}}}\frac{\partial P_{\text{cap}}}{\partial r} \tag{D6}$$

Finally, from the definition of gas fractional flow ($f_g = \frac{q_g}{q_t}$):

$$f_g = \frac{\lambda_g}{\lambda_t} - \frac{kA\lambda_g\lambda_a}{q_t\lambda_t}\frac{\partial P_{cap}}{\partial r} \tag{D7}$$

where the permeability (k) unit is m^2.

D2 Capillary-driven backflow and drying front similarity variables in presence of capillary pressure

As in Eq. D7, it is analytically observed that capillary pressure acts against the gas flow inside the reservoir. Accordingly, in this section, based on the gas phase fractional flow calculated in Appendix D1, a similarity variable is derived for the capillary-driven backflow. It was previously proposed by Zeidouni et al. [103] that the solution to Eq. D1 (based on fractional flow) is as follows:

$$\eta_{\text{no cap}} = \left(\frac{r^2 - r_w^2}{t}\right)_{G_{CO_2}} = \frac{q_{inj}}{\pi H\phi}\left(q_D\frac{df_g}{dS_g}\right)_{G_{CO_2}} \tag{D8}$$

Considering $r_w = 0$ m, the solution for the capillary included case ($\eta_{cap} = (r^2/t)_{cap}$) is identical to Eq. D8. By defining the capillary-driven backflow similarity parameter as $\Delta\eta = \eta_{\text{no cap}} - \eta_{cap}$, the following equation is derived.

$$\begin{aligned}\Delta\eta &= \left(\frac{r^2}{t}\right)_{\text{no cap}} - \left(\frac{r^2}{t}\right)_{cap} \\ &= \left(\frac{q_{inj}}{\pi H\phi}q_D\frac{df_g}{dS_g}\right)_{\text{no cap}} - \left(\frac{q_{inj}}{\pi H\phi}q_D\frac{df_g}{dS_g}\right)_{cap}\end{aligned} \tag{D9}$$

Since S_g^c and f_g^c are almost constant in both capillary included and no-capillary cases, it can be assumed that q_D is the same for these two cases. Therefore, the above equation can be shortened as below:

$$\Delta\eta = \frac{q_{inj}}{\pi H\phi}q_D\left[\left(\frac{df_g}{dS_g}\right)_{\text{no cap}} - \left(\frac{df_g}{dS_g}\right)_{cap}\right] \tag{D10}$$

As in Eq. D10 and as discussed earlier, presence of capillary pressure in the solution only affects the fractional flow term in the equation. Now, considering Eq. D7, and having $I_1 = \frac{\lambda_g}{\lambda_t}$ and $I_2 = \frac{kA\lambda_g\lambda_w}{q_t\lambda_t}\frac{\partial P_{cap}}{\partial r}$, fractional flow derivatives versus gas saturation can be defined as below:

$$\left(\frac{df_g}{dS_g}\right)_{\text{No-cap}} = \frac{dI_1}{dS_g} \tag{D11a}$$

$$\left(\frac{df_g}{dS_g}\right)_{cap} = \frac{dI_1}{dS_g} - \frac{dI_2}{dS_g} \tag{D11b}$$

Knowing I_1 and I_2, and inserting Eqs D11a and D11b into Eq. D10, the capillary-driven backflow similarity variable versus capillary pressure is derived as below:

$$\begin{aligned}\Delta\eta &= \frac{q_{inj}q_D}{\pi H\phi}\left(\frac{dI_2}{dS_g}\right) \\ &= \frac{kAq_{inj}q_D}{\pi H\phi q_t}\frac{d}{dS_g}\left(\frac{\lambda_g\lambda_w}{q_t\lambda_t}\frac{\partial P_{cap}}{\partial r}\right)\end{aligned} \tag{D12}$$

Now, inserting the definition of capillary pressure $P_{cap} = P^0_{cap}(\hat{S}^{-1/\gamma} - 1)^{1-\gamma}$ into Eq. D12, and also considering $\frac{\partial P_{cap}}{\partial r} = \frac{dP_{cap}}{dS_g}\frac{\partial S_g}{\partial r}$, this equation is rewritten as:

$$\Delta\eta = \frac{kAq_{inj}q_DP^0_{cap}}{\pi H\phi q_t}\frac{d}{dS_g}\left(\frac{\lambda_a\lambda_g}{\lambda_a+\lambda_g}\frac{d}{dS_g}(\hat{S}^{-1/\gamma} - 1)^{1-\gamma}\frac{\partial S_g}{\partial r}\right) \tag{D13}$$

Finally, considering $\frac{\partial S_g}{\partial r}$ is constant at the drying shock, $q_D = q_t/q_{inj}$ (same as the no-capillary case), and $A = 2\pi r_c H$, the final equation for capillary backflow similarity variable is derived as below, in which $r_c = \sqrt{\eta t}$.

$$\Delta\eta = \frac{2r_ckP^0_{cap}}{\phi}\left(\frac{\partial S_g}{\partial r}\right)_{r=r_c,t}\frac{d}{dS_g}\left(\frac{\lambda_a\lambda_g}{\lambda_a+\lambda_g}\frac{d}{dS_g}(\hat{S}^{-1/\gamma} - 1)^{1-\gamma}\right) \tag{D14}$$

This equation defines the effect of capillary pressure and capillary-driven backflow on similarity variable inside the reservoir, which directly affects shocks' locations and salt precipitation inside the dry-out region.

E Parameters sensitivity analysis

In this section, the effects of three sets of parameters, including geochemical reactions, bottomhole temperature of the injected CO_2, and channels' porosity and permeability, on the system performance and power output are considered. The base case for the sensitivity analysis is a heterogeneous aquifer with a channel width of 50 m, a porosity of 0.25, a permeability of 1000 mD, and an injection rate of 50 kg/s.

E1 Geochemical reactions and salt precipitation

Geochemical reactions, specifically salt precipitation, can affect the aquifer injectivity and, therefore, the overall power output of the CPG system. However, it was shown that the dominant precipitation is due to water vaporization and salt precipitation near the injection well [38, 175]. The aquifer considered to study the effects of geochemical reactions is a heterogeneous high-salinity sandstone aquifer with a salinity of 15% by weight, channels' thickness of $w = 50$ m, and $k_{\text{avg}} = 250$ mD. Carbonate, silicate, and clay minerals, including calcite, anorthite, and kaolinite are among the most common components of such aquifers. To study the effects of geochemical reactions, both aqueous and mineral reactions are considered based on previous works by Norouzi et al. [38], Nghiem et al. [62], and Cui et al. [84]. Complete details of these reactions, including reactions' equilibrium coefficients and minerals' rate law equation parameters are provided in Appendix A of the work by Norouzi et al. [38].

$$H^+ + OH^- \rightleftharpoons H_2O \tag{E1a}$$

$$CO_2 + H_2O \rightleftharpoons HCO_3^- + H^+ \tag{E1b}$$

$$HCO_3^- \rightleftharpoons CO_3^{2-} + H^+ \tag{E1c}$$

$$\text{Calcite} + H^+ \rightleftharpoons Ca^{2+} + HCO_3^- \tag{E1d}$$

$$\text{Anorthite} + 8H^+ \rightleftharpoons 4H_2O + Ca^{2+} + 2Al^{3+} + 2SiO_{2,\text{aq}} \tag{E1e}$$

$$\text{Kaolinite} + 6H^+ \rightleftharpoons 5H_2O + 2Al^{3+} + 2SiO_{2,\text{aq}} \tag{E1f}$$

$$\text{Halite} \rightleftharpoons Na^+ + Cl^- \tag{E1g}$$

The initial composition of the brine and the aquifer are presented in Table E1.

Table E1: Aquifer and brine initial compositions.

Brine	**Ion**	H^+	Ca^{2+}	Al^{3+}	$SiO_{2,aq}$	Na^+	Cl^-
	mol.L^{-1}	1×10^{-7}	9.12×10^{-5}	2.32×10^{-11}	2.35×10^{-8}	1	1
	Ion	HCO_3^-	CO_3^{2-}	OH^-			
	mol.L^{-1}	2.5×10^{-2}	1.2×10^{-5}	5.45×10^{-7}			
Mineral	**Component**		Anorthite	Calcite	Kaolinite	Halite	
	Volume fraction		0.036	0.153	0.00135	0.00	

Here, two scenarios are considered. First, I have considered the heterogeneous cases that include CO_2 and brine, but no geochemical reaction happens between them, and second, I have considered the same cases with geochemical reactions occurring in the aquifer. The results are shown in Fig. E1. Fig. E1a shows the amount of the precipitated salt resulting from water vaporization. In agreement with the findings of previous works, such as [38, 175], salt is the main mineral that precipitates and affects aquifer injectivity. Salt precipitation mainly happens in the dry-out region close to the injection well and therefore reduces the injectivity in this area. From Fig. E1b it is observed that the precipitated salt near the injection well can reduce the aquifer porosity up to 0.01, which is about a 4% reduction in porosity near the injection well. Also, it is observed that far from the injection well, the aquifer porosity is slightly increased, which is mainly due to minerals' dissolution into water. Fig. E1c shows the instantaneous net power of the system for the cases with and without geochemical reactions. Geochemical reactions mainly affect the injectivity and therefore, pressure build-up near the injection well and CO_2 flow and distribution. However, in cases considered for the present study, since the injection mass flowrate is kept constant, the CO_2 and temperature distribution remain the same and only the pressure build-up at the injection well increases. An increase in the injection well bottomhole pressure will lead to an increase in injection wellhead pressure, *i.e.*, the required injection pressure increases. The increase in the required pumping pressure will reduce the amount of the excess pressure achieved from the surface, and therefore, reduces the system's output power. However, the scale of the reduction in excess pressure is small, and the average reduction in the CPG output power is about 4.8%.

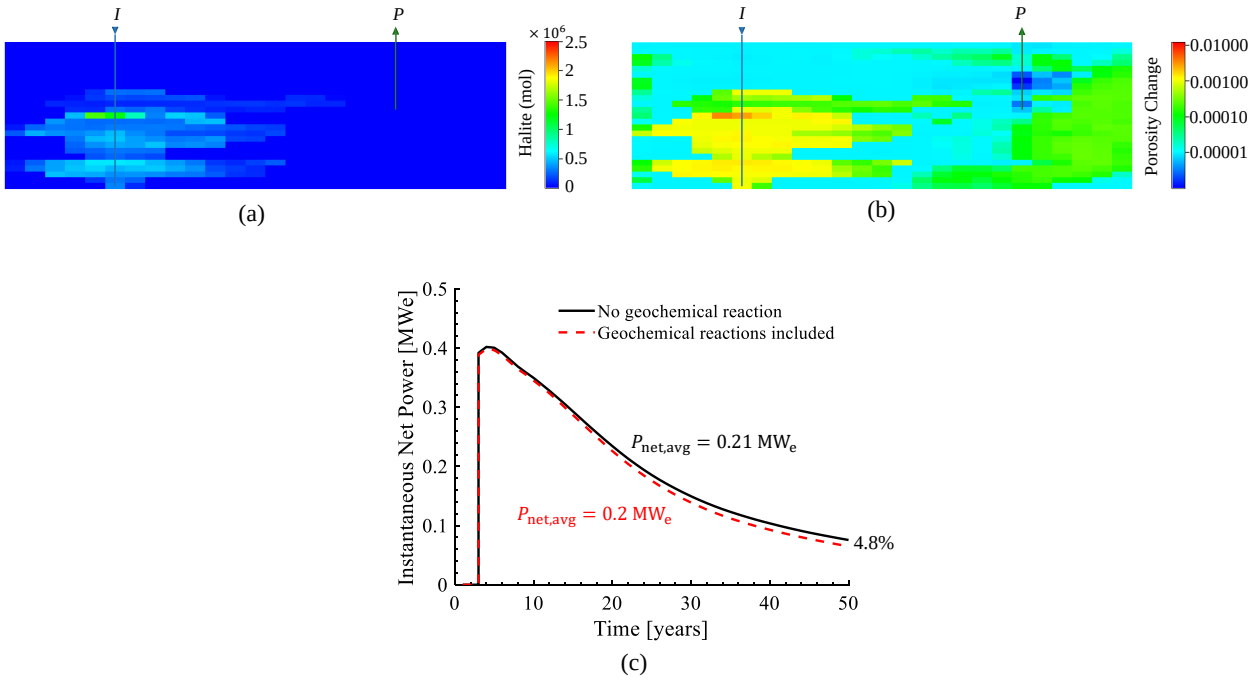

Figure E1: Geochemical reactions sensitivity analysis: (a) salt precipitation resulting from water vaporization in the dry-out region near the injection well after 50 years of injection, (b) variations in aquifer's porosity due to minerals' precipitation and dissolution after 50 years, and (c) the effect of geochemical reactions on the instantaneous power output of the system versus time.

E2 CO_2 bottomhole injection temperature

One of the parameters that can affect the temperature distribution, and consequently the system's performance, is the CO_2 injection temperature. CO_2 injection temperature is defined from the injection head temperature and the isentropic (adiabatic and reversible) compression process that occurs by reaching the aquifer depth. As a result, to increase the CO_2 injection temperature, higher temperature and pressure at the surface are required, meaning that the enthalpy gradient between the injection and production streams decreases and subsequently the system power production decreases as well.

Fig. E2a shows the temperature distribution in the aquifer for three different CO_2 injection temperatures. As the injection temperature increases, the temperature distribution becomes more uniform, and the temperature depletion rate decreases. This results in slightly higher bottomhole temperature at the production well, for instance, after 50 years, the production bottomhole temperature will be 72.9, 76.7, and 80.4 °C for the cases with injection temperatures of 40, 50, and 60 °C, respectively. Despite this increase in production bottom-

hole temperature, since the enthalpy gradient becomes smaller for cases with higher injection temperature, it is found that as the injection temperature increases, the average net power decreases (Fig. E2b).

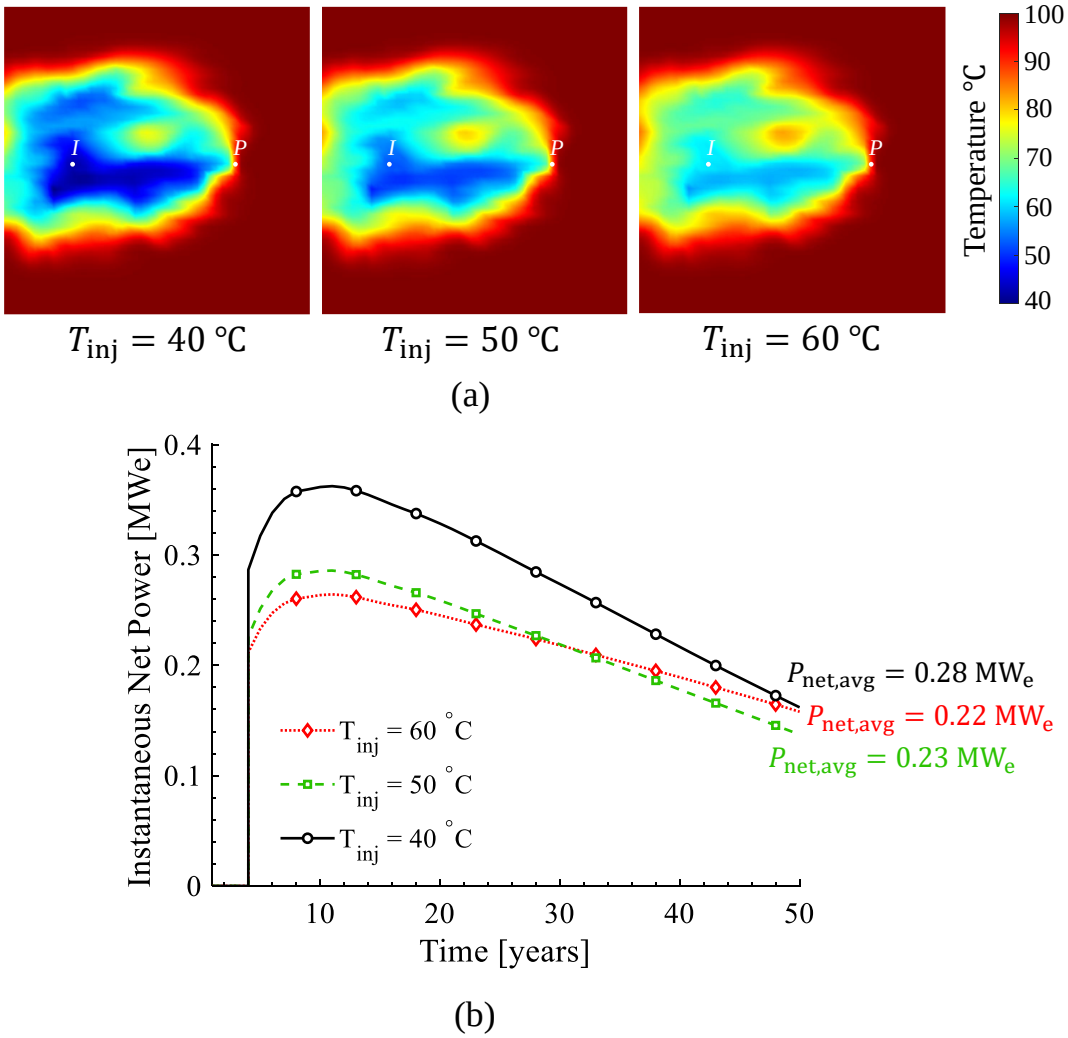

Figure E2: CO_2 bottomhole injection temperature sensitivity analysis: (a) temperature distribution at the mid-surface of the aquifer (2050 m) after 25 years of injection, and (b) instantaneous net power versus time.

E3 Channels' porosity and permeability

To study the effects of channels' porosity and permeability three sets of heterogeneous aquifers are considered as follows: (i) $\phi = 0.25$, $k = 1000$ mD, and k_{avg} =250 mD, (ii) $\phi = 0.23$, $k = 800$ mD, and k_{avg} =203 mD, and (iii) $\phi = 0.21$, $k = 600$ mD, and k_{avg} =157 mD.

Fig. E3 shows the CPG instantaneous net power for cases with different channels' permeability and porosity. Since the injection rate is kept constant at the rate of 50 kg/s, the CO_2-plume and the temperature distribution in the aquifer are almost the same for all these cases. However, as the aquifer transmissibility decreases, a higher parasitic pressure drop happens, resulting in lower excess pressure at the surface and consequently lower system output power. It is observed that a reduction of about 37% in the aquifer's average permeability results in a 7% reduction in output net power from 0.28 to 0.26 MW_e. Also, it is observed that as time goes on, the decrease in instantaneous net power increases. This is because CO_2 gradually disperses in the aquifer and as it reaches different layers of the aquifer, more pressure drop due to lower permeability and porosity occurs and therefore, the net power decreases more.

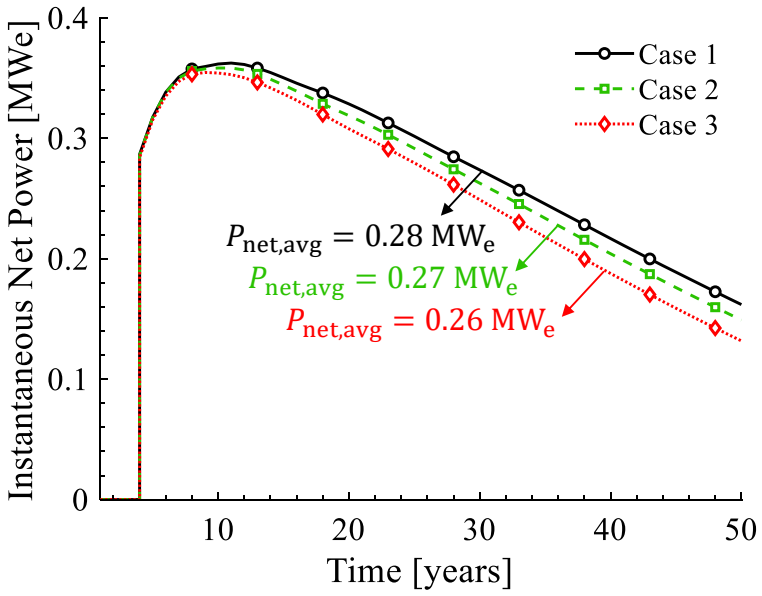

Figure E3: Effects of channels' porosity and permeability on the overall system performance and the instantaneous net power versus time.

Bibliography

[1] Office for National Statistics. COVID-19 restrictions cut household emissions [online] (2021). (accessed Jan. 15, 2023).

[2] BEIS. UK Energy in Brief 2020 [online] (2020). (accessed Jan. 15, 2023).

[3] BEIS. UK Energy in Brief 2022 [online] (2022). (accessed Jan. 15, 2023).

[4] SSE. INCREASED CCS CAN DECARBONISE GB ELECTRICITY FASTER ON ROUTE TO NET ZERO [online] (2022). (accessed Jan. 15, 2023).

[5] GT Energy UK Ltd. WHY GEOTHERMAL? [online]. (accessed Jan. 15, 2023).

[6] ARUP. Deep geothermal energy- Economic decarbonisation opportunities for the United Kingdom [online] (2021). (accessed Jan. 26, 2023).

[7] J. Busby, R. Terrington, Assessment of the resource base for engineered geothermal systems in Great Britain, Geothermal Energy 5 (1) (2017) 7.

[8] J. Busby, Geothermal Prospects in the United KingdomBritish Geological Survey, Keyworth, Nottingham, NG12 5GG, UK (2010).

[9] B. M. Adams, On the power performance and integration of carbon-dioxide plume geothermal (cpg) electrical energy production, A DISSERTATION SUBMITTED TO THE FACULTY OF THE UNIVERSITY OF MINNESOTA (2015).

[10] R. DiPippo, Geothermal Power Plants: Principles, Applications, Case Studies and Environmental Impact, 4th Edition, Butterworth-Heinemann, Amsterdam ; Boston, 2015.

[11] BGS © UKRI. Geothermal energy [online] (2023). (accessed Jan. 15, 2023).

[12] B.-H. Park, G.-O. Bae, K.-K. Lee, Importance of thermal dispersivity in designing groundwater heat pump (gwhp) system: Field and numerical study, Renewable energy 83 (2015) 270–279.

[13] B.-H. Park, B.-H. Lee, K.-K. Lee, Experimental investigation of the thermal dispersion coefficient under forced groundwater flow for designing an optimal groundwater heat pump (gwhp) system, Journal of hydrology 562 (2018) 385–396.

[14] G. C. Rau, M. S. Andersen, R. I. Acworth, Experimental investigation of the thermal dispersivity term and its significance in the heat transport equation for flow in sediments, Water Resources Research 48 (3) (2012).

[15] N. Molina-Giraldo, P. Bayer, P. Blum, Evaluating the influence of thermal dispersion on temperature plumes from geothermal systems using analytical solutions, International Journal of Thermal Sciences 50 (7) (2011) 1223–1231.

[16] W. Pophillat, G. Attard, P. Bayer, J. Hecht-Méndez, P. Blum, Analytical solutions for predicting thermal plumes of groundwater heat pump systems, Renewable Energy 147 (2020) 2696–2707.

[17] S. L. Russo, G. Taddia, G. Baccino, V. Verda, Different design scenarios related to an open loop groundwater heat pump in a large building: Impact on subsurface and primary energy consumption, Energy and Buildings 43 (2-3) (2011) 347–357.

[18] J. T. Chung, J. M. Choi, Design and performance study of the ground-coupled heat pump system with an operating parameter, Renewable Energy 42 (2012) 118–124.

[19] A. Casasso, R. Sethi, Sensitivity analysis on the performance of a ground source heat pump equipped with a double u-pipe borehole heat exchanger, Energy Procedia 59 (2014) 301–308.

[20] A.-M. Gustafsson, L. Westerlund, G. Hellström, Cfd-modelling of natural convection in a groundwater-filled borehole heat exchanger, Applied thermal engineering 30 (6-7) (2010) 683–691.

[21] A. Casasso, R. Sethi, Modelling thermal recycling occurring in groundwater heat pumps (gwhps), Renewable Energy 77 (2015) 86–93.

[22] A. Casasso, R. Sethi, Efficiency of closed loop geothermal heat pumps: a sensitivity analysis, Renewable Energy 62 (2014) 737–746.

[23] B. Piga, A. Casasso, F. Pace, A. Godio, R. Sethi, Thermal impact assessment of groundwater heat pumps (gwhps): Rigorous vs. simplified models, Energies 10 (9) (2017) 1385.

[24] A. García-Gil, S. M. Maya, E. G. Schneider, M. M. Moreno, E. Vázquez-Suñé, M. Á. Marazuela, J. M. Lázaro, J. Á. Sánchez-Navarro, Sustainability indicator for the prevention of potential thermal interferences between groundwater heat pump systems in urban aquifers, Renewable Energy 134 (2019) 14–24.

[25] D. Duchane, D. Brown, Hot dry rock (HDR) geothermal energy research and development at Fenton Hill, New Mexico, Geo-Heat Centre Quarterly Bulletin 23 (2002) 13–19.

[26] J. W. Tester, D. W. Brown, R. M. Potter, Hot Dry Rock geothermal energy— A new energy agenda for the twenty-first century, number: LA-11514-MS, Publisher: Los Alamos National Laboratory (Jan. 1989).

[27] K. Breede, K. Dzebisashvili, X. Liu, G. Falcone, A systematic review of enhanced (or engineered) geothermal systems: past, present and future, Geothermal Energy 1 (1) (2013) 4.

[28] D. Bonalumi, Enhanced geothermal system with captured co2, Energy Procedia 148 (2018) 744 – 750.

[29] K. Pruess, Enhanced geothermal systems (EGS) using CO2 as working fluid—A novel approach for generating renewable energy with simultaneous sequestration of carbon, Geothermics 35 (4) (2006) 351 – 367.

[30] Y. Wu, P. Li, The potential of coupled carbon storage and geothermal extraction in a CO2-enhanced geothermal system: a review, Geothermal Energy 8 (1) (2020) 19.

[31] S. Li, S. Wang, H. Tang, Stimulation mechanism and design of enhanced geothermal systems: A comprehensive review, Renewable and Sustainable Energy Reviews 155 (2022) 111914.

[32] W. Kumari, P. Ranjith, Sustainable development of enhanced geothermal systems based on geotechnical research – a review, Earth-Science Reviews 199 (2019) 102955.

[33] Z. Zhu, S. Yang, P. G. Ranjith, W. Tian, H. Tian, J. Zheng, G. Jiang, B. Dou, A comprehensive review on mechanical responses of granite in enhanced geothermal systems (egss), Journal of Cleaner Production 383 (2023) 135378.

[34] B. Avanthi Isaka, P. Ranjith, T. Rathnaweera, The use of super-critical carbon dioxide as the working fluid in enhanced geothermal systems (egss): A review study, Sustainable Energy Technologies and Assessments 36 (2019) 100547.

[35] D. Brown, A hot dry rock geothermal energy concept utilizing supercritical CO2 instead of water, Proceedings of the Twenty-Fifth Workshop on Geothermal Reservoir Engineering (01 2000).

[36] M. O. Saar, J. B. Randolph, T. H. Kuehn, Carbon dioxide-based geothermal energy generation systems and methods related thereto (Sep. 2010).

[37] A. M. Norouzi, F. Pouranian, A. Rabbani, N. Fowler, J. Gluyas, V. Niasar, J. Ezekiel, M. Babaei, Co2-plume geothermal: Power net generation from 3d fluvial aquifers, Applied Energy 332 (2023) 120546.

[38] A. M. Norouzi, M. Babaei, W. S. Han, K.-Y. Kim, V. Niasar, CO2-plume geothermal processes: A parametric study of salt precipitation influenced by capillary-driven backflow, Chemical Engineering Journal (2021) 130031.

[39] O. Kolditz, M. G. Blöcher, C. Clauser, H.-J. G. Diersch, T. Kohl, M. Kühn, C. I. McDermott, W. Wang, N. Watanabe, G. Zimmermann, D. Bruel, Geothermal Reservoir Simulation, John Wiley & Sons, Ltd, 2010, Ch. 5, pp. 245–301.

[40] R. Miri, H. Hellevang, Salt precipitation during CO2 storage—A review, International Journal of Greenhouse Gas Control 51 (2016) 136–147.

[41] C. E. Koltermann, S. M. Gorelick, Heterogeneity in Sedimentary Deposits: A Review of Structure-Imitating, Process-Imitating, and Descriptive Approaches, Water Resources Research 32 (9) (1996) 2617–2658.

[42] T. Beechie, H. Imaki, Predicting natural channel patterns based on landscape and geomorphic controls in the Columbia River basin, USA, Water Resources Research 50 (1) (2014) 39–57.

[43] J. Alshakri, G. J. Hampson, C. Jacquemyn, M. D. Jackson, D. Petrovskyy, S. Geiger, J. D. Machado Silva, S. Judice, F. Rahman, M. Costa Sousa, A screening assessment

of the impact of sedimentological heterogeneity on CO2 migration and stratigraphic-baffling potential: Sherwood and Bunter sandstones, UK, Geological Society, London, Special Publications 528 (1) (2023) SP528–2022–34, publisher: The Geological Society of London.

[44] J. Hornung, T. Aigner, Reservoir and aquifer characterization of fluvial architectural elements: Stubensandstein, upper triassic, southwest germany, Sedimentary Geology 129 (3) (1999) 215–280.

[45] J. Jensen, Statistics for Petroleum Engineers and Geoscientists, Gulf Professional Publishing, 2000.

[46] N. Abas, N. Khan, Carbon conundrum, climate change, CO2 capture and consumptions, Journal of CO2 Utilization 8 (2014) 39 – 48.

[47] R. M. Cuéllar-Franca, A. Azapagic, Carbon capture, storage and utilisation technologies: A critical analysis and comparison of their life cycle environmental impacts, Journal of CO2 Utilization 9 (2015) 82 – 102.

[48] M. Davarazar, D. Jahanianfard, Y. Sheikhnejad, B. Nemati, A. Mostafaie, S. Zandi, M. Khalaj, M. Kamali, T. M. Aminabhavi, Underground carbon dioxide sequestration for climate change mitigation – A scientometric study, Journal of CO2 Utilization 33 (2019) 179 – 188.

[49] R. Farajzadeh, A. Eftekhari, G. Dafnomilis, L. Lake, J. Bruining, On the sustainability of CO2 storage through CO2 – Enhanced oil recovery, Applied Energy 261 (2020) 114467.

[50] M. G. Rezk, J. Foroozesh, Determination of mass transfer parameters and swelling factor of CO2-oil systems at high pressures, International Journal of Heat and Mass Transfer 126 (2018) 380 – 390.

[51] M. Babaei, J. Mu, A. J. Masters, Impact of variation in multicomponent diffusion coefficients and salinity in CO2-EOR: A numerical study using molecular dynamics simulation, Journal of Petroleum Science and Engineering 162 (2018) 685–696.

[52] E. Mohagheghian, H. Hassanzadeh, Z. Chen, CO2 sequestration coupled with enhanced gas recovery in shale gas reservoirs, Journal of CO2 Utilization 34 (2019) 646 – 655.

[53] M. Babaei, Integrated carbon sequestration–geothermal heat recovery: performance comparison between open and close systems, Transport in Porous Media 126 (1) (2019) 249–273.

[54] T. A. Buscheck, T. R. Elliot, M. A. Celia, M. Chen, Y. Sun, Y. Hao, C. Lu, T. J. Wolery, R. D. Aines, Integrated geothermal-co2 reservoir systems: Reducing carbon intensity through sustainable energy production and secure co2 storage, Energy Procedia 37 (2013) 6587 – 6594, GHGT-11 Proceedings of the 11th International Conference on Greenhouse Gas Control Technologies, 18-22 November 2012, Kyoto, Japan.

[55] Y. Li, P. Ranjith, M. Perera, Q. Yu, Residual water formation during the CO2 storage process in deep saline aquifers and factors influencing it: A review, Journal of CO2 Utilization 20 (2017) 253 – 262.

[56] B. M. Adams, T. H. Kuehn, J. M. Bielicki, J. B. Randolph, M. O. Saar, On the importance of the thermosiphon effect in CPG (CO2 plume geothermal) power systems, Energy 69 (2014) 409–418.

[57] R. Ganjdanesh, G. A. Pope, K. Sepehrnoori, Production of energy from saline aquifers: A method to offset the energy cost of carbon capture and storage, International Journal of Greenhouse Gas Control 34 (2015) 97 – 105.

[58] N. Garapati, J. B. Randolph, J. L. Valencia, M. O. Saar, CO2-plume geothermal (CPG) heat extraction in multi-layered geologic reservoirs, Energy Procedia 63 (2014) 7631–7643.

[59] C. Pan, C. E. Romero, E. K. Levy, X. Wang, C. Rubio-Maya, L. Pan, Fully coupled wellbore-reservoir simulation of supercritical CO2 injection from fossil fuel power plant for heat mining from geothermal reservoirs, Journal of CO2 Utilization 27 (2018) 480 – 492.

[60] S. An, H. Erfani, H. Hellevang, V. Niasar, Lattice-boltzmann simulation of dissolution of carbonate rock during co2-saturated brine injection, Chemical Engineering Journal 408 (2021) 127235.

[61] H. Zhu, T. Xu, H. Tian, G. Feng, Z. Yang, B. Zhou, Understanding of Long-Term CO2-Brine-Rock Geochemical Reactions Using Numerical Modeling and Natural Analogue Study, Geofluids 2019 (2019) 1426061, publisher: Hindawi.

[62] L. Nghiem, P. Sammon, J. Grabenstetter, H. Ohkuma, Modeling CO2 storage in aquifers with a fully-coupled geochemical EOS compositional simulator, in: SPE/DOE symposium on improved oil recovery, Society of Petroleum Engineers, 2004.

[63] G. Baumann, J. Henninges, M. De Lucia, Monitoring of saturation changes and salt precipitation during CO2 injection using pulsed neutron-gamma logging at the Ketzin pilot site, International Journal of Greenhouse Gas Control 28 (2014) 134 – 146.

[64] S. Grude, M. Landrø, J. Dvorkin, Pressure effects caused by CO2 injection in the Tubåen Fm., the Snøhvit field, International Journal of Greenhouse Gas Control 27 (2014) 178 – 187.

[65] M. Nooraiepour, H. Fazeli, R. Miri, H. Hellevang, Effect of CO2 phase states and flow rate on salt precipitation in shale caprocks: A microfluidic study, Environmental Science & Technology 52 (10) (2018) 6050–6060.

[66] N. Muller, R. Qi, E. Mackie, K. Pruess, M. J. Blunt, CO2 injection impairment due to halite precipitation, Energy Procedia 1 (1) (2009) 3507 – 3514, greenhouse Gas Control Technologies 9.

[67] H. Ott, J. Snippe, K. De Kloe, H. Husain, A. Abri, Salt precipitation due to SC-gas injection: single versus multi-porosity rocks, Energy Procedia 37 (2013) 3319–3330.

[68] G. Bacci, A. Korre, S. Durucan, An experimental and numerical investigation into the impact of dissolution/precipitation mechanisms on CO2 injectivity in the wellbore and far field regions, International Journal of Greenhouse Gas Control 5 (3) (2011) 579–588.

[69] A. Berntsen, J. Todorovic, M. Raphaug, M. Torsæter, E. A. C. Panduro, K. Gawel, Salt clogging during supercritical CO2 injection into a downscaled borehole model, International Journal of Greenhouse Gas Control 86 (2019) 201–210.

[70] J. Oh, K.-Y. Kim, W. S. Han, T. Kim, J.-C. Kim, E. Park, Experimental and numerical study on supercritical CO2/brine transport in a fractured rock: Implications of mass transfer, capillary pressure and storage capacity, Advances in Water Resources 62 (2013) 442 – 453, computational Methods in Geologic CO2 Sequestration.

[71] Y. Tang, R. Yang, Z. Du, F. Zeng, Experimental study of formation damage caused by complete water vaporization and salt precipitation in sandstone reservoirs, Transport in Porous Media 107 (1) (2015) 205–218.

[72] M. Kim, A. Sell, D. Sinton, Aquifer-on-a-Chip: understanding pore-scale salt precipitation dynamics during CO2 sequestration, Lab Chip 13 (2013) 2508–2518.

[73] G. Cui, Y. Wang, Z. Rui, B. Chen, S. Ren, L. Zhang, Assessing the combined influence of fluid-rock interactions on reservoir properties and injectivity during CO2 storage in saline aquifers, Energy 155 (2018) 281–296.

[74] S. Parvin, M. Masoudi, A. Sundal, R. Miri, Continuum scale modelling of salt precipitation in the context of CO2 storage in saline aquifers with MRST compositional, International Journal of Greenhouse Gas Control 99 (2020) 103075.

[75] Y. Peysson, L. André, M. Azaroual, Well injectivity during CO2 storage operations in deep saline aquifers, Part 1: Experimental investigation of drying effects, salt precipitation and capillary forces, International Journal of Greenhouse Gas Control 22 (2014) 291–300.

[76] G. Cui, S. Ren, Z. Rui, J. Ezekiel, L. Zhang, H. Wang, The influence of complicated fluid-rock interactions on the geothermal exploitation in the CO2 plume geothermal system, Applied Energy 227 (2018) 49–63.

[77] K. Pruess, N. Müller, Formation dry-out from co2 injection into saline aquifers: 1. effects of solids precipitation and their mitigation, Water Resources Research 45 (3) (2009).

[78] H. Ott, K. de Kloe, F. Marcelis, A. Makurat, Injection of supercritical CO2 in brine saturated sandstone: Pattern formation during salt precipitation, Energy Procedia 4 (2011) 4425–4432.

[79] H. Ott, S. Roels, K. De Kloe, Salt precipitation due to supercritical gas injection: I. capillary-driven flow in unimodal sandstone, International Journal of Greenhouse Gas Control 43 (2015) 247–255.

[80] R. Miri, R. van Noort, P. Aagaard, H. Hellevang, New insights on the physics of salt precipitation during injection of CO2 into saline aquifers, International Journal of Greenhouse Gas Control 43 (2015) 10–21.

[81] S. M. Roels, N. El Chatib, C. Nicolaides, P. L. Zitha, Capillary-Driven Transport of Dissolved Salt to the Drying Zone During CO2 Injection in Homogeneous and Layered Porous Media, Transport in Porous Media 111 (2) (2016) 411–424.

[82] H. Yamamoto, C. Doughty, Investigation of gridding effects for numerical simulations of co2 geologic sequestration, International Journal of Greenhouse Gas Control 5 (4) (2011) 975 – 985.

[83] L. Zhang, G. Cui, Y. Zhang, B. Ren, S. Ren, X. Wang, Influence of pore water on the heat mining performance of supercritical CO2 injected for geothermal development, Journal of CO2 Utilization 16 (2016) 287 – 300.

[84] G. Cui, L. Zhang, C. Tan, S. Ren, Y. Zhuang, C. Enechukwu, Injection of supercritical CO2 for geothermal exploitation from sandstone and carbonate reservoirs: CO2–water–rock interactions and their effects, Journal of CO2 Utilization 20 (2017) 113–128.

[85] T. Xu, J. A. Apps, K. Pruess, Mineral sequestration of carbon dioxide in a sandstone–shale system, Chemical Geology 217 (3) (2005) 295–318, geochemical Aspects of CO2 sequestering.

[86] A. T. Corey, The interrelation between gas and oil relative permeabilities, Producers Monthly 19 (1) (1954) 38–41.

[87] M. I. Al-Mossawy, A simple approach to identify the proper relative permeability model, IOP Conference Series Materials Science and Engineering (Online) 495 (1) (2019) 8, place: United Kingdom INIS Reference Number: 52115573.

[88] M. Babaei, I. Pan, A. Alkhatib, Robust optimization of well location to enhance hysteretical trapping of CO2: Assessment of various uncertainty quantification methods and utilization of mixed response surface surrogates, Water Resources Research 51 (12) (2015) 9402–9424.

[89] S. Benson, R. Pini, C. Reynolds, S. Krevor, Relative permeability analysis to describe multi-phase flow in CO2 storage reservoirs, Global CCS Institute (2013).

[90] M. T. Van Genuchten, A closed-form equation for predicting the hydraulic conductivity of unsaturated soils, Soil Science Society of America Journal 44 (5) (1980) 892–898.

[91] W. S. Han, G. A. Stillman, M. Lu, C. Lu, B. J. McPherson, E. Park, Evaluation of potential nonisothermal processes and heat transport during CO2 sequestration, Journal of Geophysical Research: Solid Earth 115 (B7) (2010).

[92] W. S. Han, K.-Y. Kim, E. Park, B. J. McPherson, S.-Y. Lee, M.-H. Park, Modeling of Spatiotemporal Thermal Response to CO2 Injection in Saline Formations: Interpretation for Monitoring, Transport in Porous Media 93 (3) (2012) 381–399.

[93] K.-Y. Kim, W. S. Han, J. Oh, T. Kim, J.-C. Kim, Characteristics of salt-precipitation and the associated pressure build-up during CO2 storage in saline aquifers, Transport in Porous Media 92 (2) (2012) 397–418.

[94] L. André, Y. Peysson, M. Azaroual, Well injectivity during CO2 storage operations in deep saline aquifers–Part 2: Numerical simulations of drying, salt deposit mechanisms and role of capillary forces, International Journal of Greenhouse Gas Control 22 (2014) 301–312.

[95] Y. Tang, R. Yang, Z. Du, F. Zeng, Experimental study of formation damage caused by complete water vaporization and salt precipitation in sandstone reservoirs, Transport in Porous Media (2014) 1–14.

[96] M. Grimm Lima, P. Schädle, C. P. Green, D. Vogler, M. O. Saar, X.-Z. Kong, Permeability impairment and salt precipitation patterns during CO2 injection into single natural brine-filled fractures, Water Resources Research 56 (8) (2020) e2020WR027213.

[97] M. A. Hesse, H. A. Tchelepi, B. J. Cantwel, F. M. Orr, Gravity currents in horizontal porous layers: transition from early to late self-similarity, Journal of Fluid Mechanics 577 (2007) 363–383.

[98] B. McMillan, N. Kumar, S. L. Bryant, Time-dependent injectivity during CO2 storage in aquifers, in: SPE Symposium on Improved Oil Recovery, OnePetro, 2008.

[99] J. M. Nordbotten, M. A. Celia, Similarity solutions for fluid injection into confined aquifers, Journal of Fluid Mechanics 561 (2006) 307–327.

[100] M. H. Noh, L. W. Lake, S. L. Bryant, A. N. Araque-Martinez, Implications of Coupling Fractional Flow and Geochemistry for CO2 Injection in Aquifers, SPE Reservoir Evaluation & Engineering 10 (04) (2007) 406–414.

[101] E. Zuluaga, L. W. Lake, Modeling of Experiments on Water Vaporization for Gas Injection Using Traveling Waves, SPE Journal 13 (02) (2008) 248–256.

[102] K. Pruess, Formation dry-out from CO2 injection into saline aquifers: 2. Analytical model for salt precipitation, Water Resources Research 45 (3) (2009).

[103] M. Zeidouni, M. Pooladi-Darvish, D. Keith, Analytical solution to evaluate salt precipitation during CO2 injection in saline aquifers, International Journal of Greenhouse Gas Control 3 (5) (2009) 600–611.

[104] S. A. Mathias, J. G. Gluyas, G. J. González Martínez de Miguel, S. A. Hosseini, Role of partial miscibility on pressure buildup due to constant rate injection of CO2 into closed and open brine aquifers, Water Resources Research 47 (12) (2011).

[105] H. L. Kelly, S. A. Mathias, Capillary processes increase salt precipitation during CO2 injection in saline formations, Journal of Fluid Mechanics 852 (2018) 398–421.

[106] G. Cui, S. Ren, Z. Rui, J. Ezekiel, L. Zhang, H. Wang, The influence of complicated fluid-rock interactions on the geothermal exploitation in the CO2 plume geothermal system, Applied Energy 227 (2018) 49–63, Transformative Innovations for a Sustainable Future – Part III.

[107] K. Pruess, N. Spycher, ECO2N – A fluid property module for the TOUGH2 code for studies of CO2 storage in saline aquifers, Energy Conversion and Management 48 (6) (2007) 1761–1767, geologic Carbon Sequestration and Methane Hydrates Research from the TOUGH Symposium 2006.

[108] Buckley, S.E. and Leverett, M.C., Mechanism of Fluid Displacement in Sands, Transactions of the AIME 146 (01) (1942) 107–116.

[109] J. Dumore, J. Hagoort, A. Risseeuw, An Analytical Model for One-Dimensional, Three-Component Condensing and Vaporizing Gas Drives, Society of Petroleum Engineers Journal 24 (02) (1984) 169–179.

[110] J. Chang, Y. C. Yortsos, Effect of capillary heterogeneity on Buckley-Leverett displacement, SPE Reservoir Engineering 7 (02) (1992) 285–293.

[111] K. Ling, Fractional flow in radial flow systems: a study for peripheral waterflood, Journal of Petroleum Exploration and Production Technology 6 (3) (2016) 441–450.

[112] P. H. Nelson, Permeability-porosity Relationships In Sedimentary Rocks, The Log Analyst 35 (03) (05 1994).

[113] P. C. Carman, Fluid flow through granular beds, Chemical Engineering Research and Design 75 (1997) S32–S48.

[114] O. Izgec, B. Demiral, H. J. Bertin, S. Akin, Experimental and numerical modeling of direct injection of CO2 into carbonate formations, in: SPE annual technical conference and exhibition, Society of Petroleum Engineers, 2006.

[115] N. Spycher, K. Pruess, Co2-h2o mixtures in the geological sequestration of co2. ii. partitioning in chloride brines at 12-100oc and up to 600 bar (9 2004).

[116] A. Sayigh, Renewable energy — the way forward, Applied Energy 64 (1) (1999) 15–30.

[117] J. Ezekiel, A. Ebigbo, B. M. Adams, M. O. Saar, Combining natural gas recovery and CO2-based geothermal energy extraction for electric power generation, Applied Energy 269 (2020) 115012.

[118] E.-O. I. Obi, M. J. Blunt, Streamline-based simulation of carbon dioxide storage in a north sea aquifer, Water Resources Research 42 (3) (2006).

[119] H. Emami-Meybodi, H. Hassanzadeh, J. Ennis-King, Co2 dissolution in the presence of background flow of deep saline aquifers, Water Resources Research 51 (4) (2015) 2595–2615.

[120] A. W. Woods, T. Espie, Controls on the dissolution of CO2 plumes in structural traps in deep saline aquifers, Geophysical Research Letters 39 (8) (2012).

[121] C.-L. Wang, W.-L. Cheng, Y.-L. Nian, L. Yang, B.-B. Han, M.-H. Liu, Simulation of heat extraction from CO2-based enhanced geothermal systems considering CO2 sequestration, Energy 142 (2018) 157–167.

[122] J. B. Randolph, M. O. Saar, Combining geothermal energy capture with geologic carbon dioxide sequestration, Geophysical Research Letters 38 (10) (2011).

[123] E. L. Majer, R. Baria, M. Stark, S. Oates, J. Bommer, B. Smith, H. Asanuma, Induced seismicity associated with enhanced geothermal systems, Geothermics 36 (3) (2007) 185–222.

[124] Q. Gan, D. Elsworth, Production optimization in fractured geothermal reservoirs by coupled discrete fracture network modeling, Geothermics 62 (2016) 131–142.

[125] P. C. Myint, M. Bestehorn, A. Firoozabadi, Effect of permeability anisotropy on buoyancy-driven flow for CO2 sequestration in saline aquifers, Water Resources Research 48 (9) (2012).

[126] A. Atrens, H. Gurgenci, V. Rudolph, Exergy analysis of a CO2 thermosiphon, in: Workshop on Geothermal Reservoir Engineering, Stanford University, Stanford, CA, 2009.

[127] B. M. Adams, T. H. Kuehn, J. M. Bielicki, J. B. Randolph, M. O. Saar, A comparison of electric power output of CO2 Plume Geothermal (CPG) and brine geothermal systems for varying reservoir conditions, Applied Energy 140 (2015) 365–377.

[128] D. Bonté, J. . Van Wees, J. M. Verweij, Subsurface temperature of the onshore netherlands: New temperature dataset and modelling, Geologie en Mijnbouw/Netherlands Journal of Geosciences 91 (4) (2012) 491–515, cited By :44.

[129] B. M. Adams, D. Vogler, T. H. Kuehn, J. M. Bielicki, N. Garapati, M. O. Saar, Heat depletion in sedimentary basins and its effect on the design and electric power output of CO2 Plume Geothermal (CPG) systems, Renewable Energy 172 (2021) 1393–1403.

[130] M. R. Fleming, B. M. Adams, T. H. Kuehn, J. M. Bielicki, M. O. Saar, Increased Power Generation due to Exothermic Water Exsolution in CO2 Plume Geothermal (CPG) Power Plants, Geothermics 88 (2020) 101865.

[131] G. Medici, L. West, N. Mountney, Characterization of a fluvial aquifer at a range of depths and scales: the triassic st bees sandstone formation, cumbria, uk, Hydrogeology Journal 26 (11 2017).

[132] A. J. Newell, S. M. Shariatipour, Linking outcrop analogue with flow simulation to reduce uncertainty in sub-surface carbon capture and storage: an example from the sherwood sandstone group of the wessex basin, uk, Geological Society, London, Special Publications 436 (1) (2016) 231–246.

[133] C. J. Willems, H. M. Nick, M. E. Donselaar, G. J. Weltje, D. F. Bruhn, On the connectivity anisotropy in fluvial hot sedimentary aquifers and its influence on geothermal doublet performance, Geothermics 65 (2017) 222–233.

[134] C. Willems, H. Nick, T. Goense, D. Bruhn, The impact of reduction of doublet well spacing on the net present value and the life time of fluvial hot sedimentary aquifer doublets, Geothermics 68 (2017) 54–66.

[135] N. I. Gershenzon, R. W. Ritzi, D. F. Dominic, E. Mehnert, R. T. Okwen, C. Patterson, CO2 trapping in reservoirs with fluvial architecture: Sensitivity to heterogeneity in

permeability and constitutive relationship parameters for different rock types, Journal of Petroleum Science and Engineering 155 (2017) 89–99, energy Frontier Research Centers for Investigating Carbon Sequestration.

[136] B. Issautier, S. Viseur, P. Audigane, C. Chiaberge, Y.-M. Le Nindre, A new approach for evaluating the impact of fluvial type heterogeneity in CO2 storage reservoir modeling, Comptes Rendus Geoscience 348 (7) (2016) 531–539, modelling Approaches in Sedimentology.

[137] M. R. Soltanian, S. Hajirezaie, S. A. Hosseini, H. Dashtian, M. A. Amooie, A. Meyal, R. Ershadnia, W. Ampomah, A. Islam, X. Zhang, Multicomponent reactive transport of carbon dioxide in fluvial heterogeneous aquifers, Journal of Natural Gas Science and Engineering 65 (2019) 212–223.

[138] M. Babaei, H. M. Nick, Performance of low-enthalpy geothermal systems: Interplay of spatially correlated heterogeneity and well-doublet spacings, Applied Energy 253 (2019) 113569.

[139] E. A. Warren, C. P. Smalley, R. J. Howarth, Part 4: Compositional variations of North Sea formation waters, Geological Society, London, Memoirs 15 (1) (1994) 119–208.

[140] M. R. Gibling, Width and Thickness of Fluvial Channel Bodies and Valley Fills in the Geological Record: A Literature Compilation and Classification, Journal of Sedimentary Research 76 (5) (2006) 731–770.

[141] G. Liu, G. Wang, Z. Zhao, F. Ma, A new well pattern of cluster-layout for deep geothermal reservoirs: Case study from the dezhou geothermal field, china, Renewable Energy 155 (2020) 484–499.

[142] H. O. McLeod, Matrix Acidizing, Journal of Petroleum Technology 36 (12) (1984) 2055–2069.

[143] A. Sutter. Sedimentology, Depositional Environments and Sequence Stratigraphy [online] (2008). (accessed Oct. 14, 2021).

[144] F. N. Fritsch, R. E. Carlson, Monotone piecewise cubic interpolation, SIAM Journal on Numerical Analysis 17 (2) (1980) 238–246.

[145] A. M. Rowe, J. C. S. Chou, Pressure-volume-temperature-concentration relation of aqueous sodium chloride solutions, Journal of Chemical & Engineering Data 15 (1) (1970) 61–66, publisher: American Chemical Society.

[146] J. Kestin, H. E. Khalifa, R. J. Correia, Tables of the dynamic and kinematic viscosity of aqueous NaCl solutions in the temperature range 20–150°C and the pressure range 0.1–35 MPa, Journal of Physical and Chemical Reference Data 10 (1) (1981) 71–88.

[147] J. Adams, S. Bachu, Equations of state for basin geofluids: algorithm review and intercomparison for brines, Geofluids 2 (4) (2002) 257–271.

[148] D.-Y. Peng, D. B. Robinson, A New Two-Constant Equation of State, Industrial & Engineering Chemistry Fundamentals 15 (1) (1976) 59–64, publisher: American Chemical Society.

[149] R. C. Reid, J. M. Prausnitz, T. K. Sherwood, Properties of Gases & Liquids 3rd Edition, McGraw Hill, 1977.

[150] P. R. King, The use of renormalization for calculating effective permeability, Transport in Porous Media 4 (1) (1989) 37–58.

[151] P. R. King, Upscaling permeability: Error analysis for renormalization, Transport in Porous Media 23 (3) (1996) 337–354.

[152] International Energy Agency (IEA). CO2 Emissions from Fuel Combustion 2019 Edition [online] (2019). (accessed May 20, 2022).

[153] B. Metz, I. P. on Climate Change, I. P. on Climate Change. Working Group III., G. d'experts intergouvernemental sur l'évolution du climat. Working Group III, I. P. on Climate Change Working Group Technical Unit, P. Intergovernmental Panel on Climate Change. Working Group 3, O. Davidson, H. De Coninck, W. M. Organization, et al., Carbon Dioxide Capture and Storage: Special Report of the Intergovernmental Panel on Climate Change, 25 CM, Cambridge University Press, 2005.

[154] L. Pan, C. Doughty, B. Freifeld, How to sustain a CO2-thermosiphon in a partially saturated geothermal reservoir: Lessons learned from field experiment and numerical modeling, Geothermics 71 (2018) 274–293.

[155] N. Garapati, B. M. Adams, M. R. Fleming, T. H. Kuehn, M. O. Saar, Combining brine or co2 geothermal preheating with low-temperature waste heat: A higher-efficiency hybrid geothermal power system, Journal of CO2 Utilization 42 (2020) 101323.

[156] T. A. Buscheck, J. M. Bielicki, T. A. Edmunds, Y. Hao, Y. Sun, J. B. Randolph, M. O. Saar, Multifluid geo-energy systems: Using geologic CO2 storage for geothermal energy production and grid-scale energy storage in sedimentary basins, Geosphere 12 (3) (2016) 678–696.

[157] A. M. Norouzi, J. Gluyas, M. Babaei, Co2-plume geothermal in fluvial formations: A 2d numerical performance study using subsurface metrics and upscaling, Geothermics 99 (2022) 102287.

[158] C. Schifflechner, C. Wieland, H. Spliethoff, CO2 Plume Geothermal (CPG) Systems for Combined Heat and Power Production: an Evaluation of Various Plant Configurations, Journal of Thermal Science (Aug. 2022).

[159] C. Schifflechner, F. Dawo, S. Eyerer, C. Wieland, H. Spliethoff, Thermodynamic comparison of direct supercritical co2 and indirect brine-orc concepts for geothermal combined heat and power generation, Renewable Energy 161 (2020) 1292–1302.

[160] J. Ezekiel, B. M. Adams, M. O. Saar, A. Ebigbo, Numerical analysis and optimization of the performance of co2-plume geothermal (cpg) production wells and implications for electric power generation, Geothermics 98 (2022) 102270.

[161] P. A. Allen, J. R. Allen, Basin Analysis: Principles and Application to Petroleum Play Assessment, John Wiley & Sons, 2013, google-Books-ID: 77pjP0oJH3QC.

[162] G. Einsele, Sedimentary Basins: Evolution, Facies, and Sediment Budget, Springer Science & Business Media, 2000.

[163] J. Hartmann, N. Moosdorf, The new global lithological map database glim: A representation of rock properties at the earth surface, Geochemistry, Geophysics, Geosystems 13 (12) (2012).

[164] K. Ambrose, E. Hough, N. J. P. Smith, G. Warrington, Lithostratigraphy of the Sherwood Sandstone Group of England, Wales and south-west Scotland, num Pages: 50 Place: Nottingham, UK Publisher: British Geological Survey (2014).

[165] M. Olivarius, R. Weibel, H. Friis, L. O. Boldreel, N. Keulen, T. B. Thomsen, Provenance of the lower triassic bunter sandstone formation: implications for distribution and architecture of aeolian vs. fluvial reservoirs in the north german basin, Basin Research 29 (S1) (2017) 113–130.

[166] M. Kortekaas, U. Böker, C. Kooij, B. Jaarsma, Lower Triassic reservoir development in the northern Dutch offshore, Geological Society, London, Special Publications 469 (2018) SP469.19.

[167] Z. Tang, J. Parnell, F. J. Longstaffe, Diagenesis and Reservoir Potential of Permian–Triassic Fluvial/Lacustrine Sandstones in the Southern Junggar Basin, Northwestern China1, AAPG Bulletin 81 (11) (1997) 1843–1865.

[168] D. J. Cant, R. G. Walker, Development of a braided-fluvial facies model for the devonian battery point sandstone, québec, Canadian Journal of Earth Sciences 13 (1) (1976) 102–119.

[169] D. C. Swanson, The Importance of Fluvial Processes and Related Reservoir Deposits, Journal of Petroleum Technology 45 (04) (1993) 368–377.

[170] A. M. Norouzi, V. Niasar, J. G. Gluyas, M. Babaei, Analytical solution for predicting salt precipitation during co2 injection into saline aquifers in presence of capillary pressure, Water Resources Research 58 (6) (2022) e2022WR032612.

[171] R. Ershadnia, C. D. Wallace, S. Hajirezaie, S. A. Hosseini, T. N. Nguyen, D. M. Sturmer, Z. Dai, M. Reza Soltanian, Hydro-thermo-chemo-mechanical modeling of carbon dioxide injection in fluvial heterogeneous aquifers, Chemical Engineering Journal 431 (2022) 133451.

[172] N. Garapati, J. B. Randolph, M. O. Saar, Brine displacement by co2, energy extraction rates, and lifespan of a co2-limited co2-plume geothermal (cpg) system with a horizontal production well, Geothermics 55 (2015) 182–194.

[173] T. R. Elliot, T. A. Buscheck, M. Celia, Active co2 reservoir management for sustainable geothermal energy extraction and reduced leakage, Greenhouse Gases: Science and Technology 3 (1) (2013) 50–65.

[174] M. Babaei, A. M. Norouzi, H. M. Nick, J. Gluyas, Optimisation of heat recovery from low-enthalpy aquifers with geological uncertainty using surrogate response surfaces and

simple search algorithms, Sustainable Energy Technologies and Assessments 49 (2022) 101754.

[175] A. M. Norouzi, V. Niasar, J. G. Gluyas, M. Babaei, Analytical solution for predicting salt precipitation during co2 injection into saline aquifers in presence of capillary pressure, Water Resources Research 58 (6) (2022) e2022WR032612.

[176] H. Darcy, P. Bobeck, The Public Fountains of the City of Dijon: Exposition and Application of Principles to Follow and Formulas to Use in Questions of Water Distribution : the Book Ends with an Appendix on Water Supplies of Several Cities' Water Filtration and the Manufacture of Cast Iron, Lead, and Sheet Metal and Bitumen Pipes, Kendall/Hunt Publishing Company, 2004.

[177] A. Miall, A. A. of Petroleum Geologists, A. A. of Petroleum Geologists. Fall Education Conference, Analysis of Fluvial Depositional Systems, AAPG continuing education course note series, American Association of Petroleum Geologists, 1981.

[178] H. Aydin, S. Merey, Design of electrical submersible pump system in geothermal wells: A case study from west anatolia, turkey, Energy 230 (2021) 120891.

[179] Schlumberger, ECLIPSE Technical Description 2014.1 (2014).

[180] M. Pham, M. Sullera, M. J. Williams, R. Henneberger, ECLIPSE Geothermal-A Next-Generation Geothermal Reservoir Simulator, in: European Geothermal Congress, European Geothermal Conference, 2019.

[181] I. H. Bell, J. Wronski, S. Quoilin, V. Lemort, Pure and Pseudo-pure Fluid Thermophysical Property Evaluation and the Open-Source Thermophysical Property Library CoolProp, Industrial & Engineering Chemistry Research 53 (6) (2014) 2498–2508, publisher: American Chemical Society.

[182] Ofgem. Average gas and electricity use explained [online]. (accessed May 11, 2023).

[183] R. Chadwick, Offshore co2 storage: Sleipner natural gas field beneath the north sea, in: Geological Storage of Carbon Dioxide (CO2), Elsevier, 2013, pp. 227–253e.

[184] M. R. Soltanian, M. A. Amooie, D. R. Cole, D. E. Graham, S. A. Hosseini, S. Hovorka, S. M. Pfiffner, T. J. Phelps, J. Moortgat, Simulating the cranfield geological carbon sequestration project with high-resolution static models and an accurate equation of state, International Journal of Greenhouse Gas Control 54 (2016) 282–296.

[185] S. D. Hovorka, T. A. Meckel, R. H. Trevino, J. Lu, J.-P. Nicot, J.-W. Choi, D. Freeman, P. Cook, T. M. Daley, J. B. Ajo-Franklin, B. M. Freifeild, C. Doughty, C. R. Carrigan, D. L. Brecque, Y. K. Kharaka, J. J. Thordsen, T. J. Phelps, C. Yang, K. D. Romanak, T. Zhang, R. M. Holt, J. S. Lindler, R. J. Butsch, Monitoring a large volume co2 injection: Year two results from secarb project at denbury's cranfield, mississippi, usa, Energy Procedia 4 (2011) 3478–3485, 10th International Conference on Greenhouse Gas Control Technologies.

[186] S. A. Mathias, J. G. Gluyas, E. J. Mackay, W. H. Goldthorpe, A statistical analysis of well production rates from uk oil and gas fields–implications for carbon capture and storage, International Journal of Greenhouse Gas Control 19 (2013) 510–518.

[187] M. Arnaudo, M. Topel, P. Puerto, E. Widl, B. Laumert, Heat demand peak shaving in urban integrated energy systems by demand side management - a techno-economic and environmental approach, Energy 186 (2019) 115887.

[188] Z. Xin, S. U. N. Yuxiao, Z. Di, Z. Gaoxin, L. I. Jing, W. Xuwei, Z. Xiaozheng, Z. Jinlong, Benefit study of peak shaving energy systems using geothermal energy with storage in office buildings, Energy Storage Science and Technology 9 (3) (2020) 720.

[189] Climate Change Committee, Reducing uk emissions, 2018 progress report to parliament, Tech. rep., Committee on Climate Change (2018).

[190] J. Ezekiel, A. Ebigbo, I. Arifianto, A. Daniilidis, T. Finkbeiner, P. M. Mai, Techno-economic performance optimization of hydrothermal doublet systems: Application to the al wajh basin, western saudi arabia, Geothermics 105 (2022) 102532.

[191] M. Mahdi Rajabi, M. Chen, M. Reza Hajizadeh Javaran, A. Al-Maktoumi, A. Izady, Y. Dong, Probabilistic net present value analysis for designing techno-economically optimal sequential co2 sequestration and geothermal energy extraction, Journal of Hydrology 612 (2022) 128237.

[192] A. H. Harvey, Semiempirical correlation for Henry's constants over large temperature ranges, AIChE Journal 42 (5) (1996) 1491–1494.

[193] A. Saul, W. Wagner, International Equations for the Saturation Properties of Ordinary Water Substance, Journal of Physical and Chemical Reference Data 16 (4) (1987) 893–901, publisher: American Institute of Physics.

[194] J. E. Garcia, Density of aqueous solutions of CO2, No. LBNL-49023, Tech. rep., Lawrence Barkley Natioal Lab (2001).

[195] R. J. Bakker, Package FLUIDS 1. Computer programs for analysis of fluid inclusion data and for modelling bulk fluid properties, Chemical Geology 194 (1) (2003) 3 – 23, european Current Research on Fluid Inclusions.

[196] L. Canjar, F. Manning, Thermodynamic Properties and Reduced Correlations for Gases, Gulf Publishing Company, 1967.

[197] C. C. Miller, J. Walker, The Stokes-Einstein law for diffusion in solution, Proceedings of the Royal Society of London. Series A 106 (740) (1924) 724–749.

[198] C. M. Bethke, Geochemical Reaction Modeling: Concepts and Applications, Oxford University Press, Oxford, New York, 1996.

[199] M. Jin, A. Ribeiro, E. Mackay, L. Guimarães, U. Bagudu, Geochemical modelling of formation damage risk during CO2 injection in saline aquifers, Journal of Natural Gas Science and Engineering 35 (2016) 703 – 719.

[200] M. Alkattan, E. H. Oelkers, J.-L. Dandurand, J. Schott, Experimental studies of halite dissolution kinetics: II. The effect of the presence of aqueous trace anions and K3Fe(CN)6, Chemical Geology 143 (1997) 17–26.